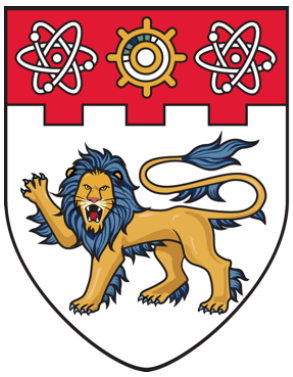

NANYANG TECHNOLOGICAL UNIVERSITY
SINGAPORE

INVESTIGATING THE BIOPHYSICAL INTERACTIONS OF ANTIMICROBIAL FATTY ACIDS AND LIPOSOMAL FATTY ACIDS WITH MODEL MEMBRANE PLATFORMS AND THEIR CORRELATION TO BIOLOGICAL ACTIVITY

SUNGMIN SHIN

SCHOOL OF MATERIALS SCIENCE AND ENGINEERING

2024

INVESTIGATING THE BIOPHYSICAL INTERACTIONS OF ANTIMICROBIAL FATTY ACIDS AND LIPOSOMAL FATTY ACIDS WITH MODEL MEMBRANE PLATFORMS AND THEIR CORRELATION TO BIOLOGICAL ACTIVITY

SUNGMIN SHIN

SCHOOL OF MATERIALS SCIENCE AND ENGINEERING

A thesis submitted to the Nanyang Technological University
in partial fulfilment of the requirement for the degree of
Doctor of Philosophy

2024

Statement of Originality

I hereby certify that the work embodied in this thesis is the result of original research, is free of plagiarised materials, and has not been submitted for a higher degree to any other University or Institution.

9 August 2024

. . . . . .
Date

. . . . . .
Sungmin Shin

Supervisor Declaration Statement

I have reviewed the content and presentation style of this thesis and declare it is free of plagiarism and of sufficient grammatical clarity to be examined. To the best of my knowledge, the research and writing are those of the candidate except as acknowledged in the Author Attribution Statement. I confirm that the investigations were conducted in accord with the ethics policies and integrity standards of Nanyang Technological University and that the research data are presented honestly and without prejudice.

19 August 2024

. . . . . .

Date

. . . . . .

Professor Nam-Joon Cho

Authorship Attribution Statement

This thesis contains material from one paper published in the following peer-reviewed journal.

Chapter 4 is published as S. Shin, H. Tae, N.-J. Cho. Lipid Membrane Remodeling by the Micellar Aggregation of Long-Chain Unsaturated Fatty Acids for Sustainable Antimicrobial Strategies. *Int. J. Mol. Sci.* **24**, 9639 (2023). DOI: 10.3390/ijms24119639.

The contributions of the co-authors are delineated as follows:

- Prof Cho provided the initial direction for the project.
- I prepared the manuscript drafts, which were reviewed and revised by Prof Cho and Mr. Tae.
- I co-designed the study with Mr. Tae, performed all the material synthesis, fluorescence spectroscopy, quartz crystal microbalance-dissipation (QCM-D) experiments, and fluorescence microscopy experiments. I also analyzed the data.
- Mr. Tae assisted with interpretation of the data.

9 August 2024

. . . . . .
Date

. . . . . .
Sungmin Shin

Abstract

The growing challenge posed by antimicrobial resistance (AMR) has prompted the exploration of innovative approaches to combat bacterial infections. Among these, long-chain fatty acids (LCFAs) and liposomes loaded with LCFAs (LipoFAs) have emerged as promising contenders against AMR. However, existing research primarily focuses on evaluating their antibacterial impacts on bacteria using biological methods. The design of these agents often relies on traditional assay methods that fail to accurately replicate the complexity of bacterial membranes, including the presence of charged phospholipids, nanometer dimensions, and other intricacies within the bacterial membranes. While it is known that LCFAs and LipoFAs exhibit membrane-active modes of action against the bacterial membranes, the detailed mechanisms of their interactions with membranes remain unclear. Herein, the development of a systematic analytical framework using supported lipid bilayer (SLB) platforms was reported to investigate how LCFAs, specifically linolenic acid (LNA), linoleic acid (LLA), and oleic acid (OA), and LipoFAs, including LNA-loaded liposomes (lipoLNA), LLA-loaded liposomes (LipoLLA), and OA-loaded liposomes (LipoOA), interact with model membrane systems. The central hypothesis of this thesis posits that SLBs can serve as predictive models for determining the antimicrobial efficacy and mechanisms of action (MOA) of LCFAs and LipoFAs. To test this hypothesis, single-component and multi-component SLBs, designed to closely mimic the composition and structure of bacterial membranes, were fabricated to study membrane interactions. Biophysical experimental findings revealed that LCFAs induce tubular formations and exhibit critical micelle concentration (CMC)-dependent membrane-disruptive behavior on single-component SLBs. Additionally, LNA and LLA exhibited interaction behaviors correlated with the CMC on multi-component bacterial membrane SLBs, leading to membrane remodeling and morphological changes at concentrations above CMC values. In contrast, OA exhibited CMC-independent activity, showing membrane insertion into the model membrane platform. LNA and LLA exhibited bactericidal effects, enhancing membrane permeability and ATP leakage, while OA, characterized by CMC-independent activity profile, exhibited potent bactericidal effects by penetrating the SLBs effectively,

increasing membrane permeability and ATP leakage. The observed activities of LCFAs on *S. aureus* correlated with their behavior on Gram-positive bacterial model membranes, highlighting the significance of multiple-component model systems in understanding antimicrobial activity. The study also explored the mechanistic interactions between LipoFAs and model bacterial membranes, revealing that LipoLNA and LipoLLA, encapsulated with FAs with higher degrees of unsaturation, induced a curved membrane surface morphology due to higher curvature stress, potentially increasing membrane permeability and leakage of intracellular ATP. These changes correlated with stronger bacteriostatic and bactericidal effects on *S. aureus* MW2. Overall, this research contributes to the ongoing efforts to combat AMR by elucidating the efficacy of antimicrobial agents and highlights the potential of using biologically relevant model membrane systems to develop innovative strategies for designing effective therapeutic agents in healthcare and biotechnology.

Lay Summary

Antimicrobial resistance (AMR) is an increasingly serious problem that is rendering antibiotics ineffective and obsolete, highlighting the urgent call for solutions to fight bacterial infections. While it is established that fatty acids (FAs) and FA-loaded liposomes (LipoFAs) can disrupt bacterial membranes, the precise mechanisms of these interactions remain largely unexplored. Long-chain fatty acids (LCFAs) and LipoFAs show promise against AMR, but existing research has predominantly focused on examining their effects on bacteria using conventional biological approaches. Moreover, the design of these agents, which primarily focuses on their interaction with bacterial membranes, often relies on traditional methods that struggle to replicate the complexity of these membranes accurately. The objective is to develop a screening platform that mimics bacterial membranes to understand how specific LCFAs (linolenic acid, linoleic acid, and oleic acid) and LipoFAs interact with these membrane platforms. This approach draws on principles from materials science, biophysics, chemistry, and engineering. The results indicate that LCFAs and LipoFAs interact differently with the model membranes. Importantly, the interactions observed on the membrane models mirrored those seen with actual bacteria. This result not only confirms the relevance of using model systems to understand antimicrobial activity but also proves the usefulness of this approach as a predictive model tool for identifying antimicrobial drugs. This research highlights the potential of engineered membrane platforms to provide useful information to better understand how antimicrobial agents interact with bacterial membranes, opening new avenues the development of innovative therapeutic strategies to address AMR in healthcare and biotechnology.

Acknowledgements

This dissertation would not have been possible without the generous support of Nanyang Technological University (NTU) and the invaluable research collaboration with Proctor & Gamble.

I am immensely grateful to my research supervisor, Professor Cho Nam-Joon, whose unwavering support and expert guidance have been crucial throughout my doctoral studies. Joining Professor Cho Nam-Joon's Translational Materials Innovation Group (TMIG) has been a transformative experience. It has allowed me to explore the profound intersections of engineering and biology in addressing global health and environmental challenges. I am deeply honored to have had Professor Cho Nam-Joon as my mentor, and I extend my sincere appreciation to all the members in the research group for their collaboration and camaraderie. Additionally, I wish to acknowledge the faculty and staff members at NTU who have supported me over the years.

My heartfelt thanks also goes to Professor Song Juha and Professor Tan Lay Poh, members of my Thesis Advisory Committee (TAC), for their invaluable guidance and feedback during my doctoral journey.

Finally, I am profoundly grateful to my beloved family: my father, mother, older brother and fiancé. Their unwavering support has been the cornerstone of my success, providing me with the strength and determination to persevere. To my family and my dear fiancé, your constant love, encouragement, and belief in me have been my greatest source of strength. I am eternally grateful for your presence in my life, and I love you all dearly.

Table of Contents

Abstract i

Lay Summary iii

Acknowledgements v

Table of Contents vii

Table Captions xiii

Figure Captions xv

Abbreviations xxv

Chapter 1 Introduction **1**

1.1 Hypothesis/Problem Statement 2

1.2 Objectives and Scope 6

1.3 Dissertation Overview 8

1.4 Findings and Outcomes/Originality 10

References 12

Chapter 2 Literature Review **15**

2.1 Antimicrobial Fatty Acids 16

2.1.1 History 16

2.1.2 Classes 17

2.1.3 Antibacterial Activity Spectrum 21

2.1.4 Antimicrobial Mechanisms 24

2.2 Biological and Biophysical Studies to Characterize Antimicrobial Fatty Acid Interactions **27**

2.2.1 Biological Assessment of Antimicrobial Fatty Acids 27

2.2.1.1 Bacteria Inhibition Assay 27

2.2.1.2 Time-Kill Kinetic Assay 29

2.2.1.3 Membrane Permeabilization and Intracellular Content Leakage Assays 30

2.2.1.4 Electron Microscopy 31

2.2.2 Biophysical Assessment of Antimicrobial Fatty Acids 33

2.2.2.1 Liposome Assays 33

2.2.2.2 Supported Lipid Bilayer Assays 34

2.3 Nanotechnology Formulations with Fatty Acids 36

2.3.1 Liposomes 36

2.3.2 Emulsions 37

2.3.3 Nanostructured Lipid Carriers 37

2.4 Outstanding Questions 39

2.4.1 Correlation between Biophysical Membrane Interaction Insights and Biological Experiments 38

2.4.2 Relationship Between the Physicochemical Property Differences of Fatty Acids, Liposomal Fatty Acids, and Model Bacterial Membranes 39

2.4.3 Comparison Between Bacterial Membranes and Supported Lipid Bilayers 40

References 41

Chapter 3 Experimental Methodology 47

3.1 Rationale for selection....48
3.2 Materials....49
3.2.1 Long-Chain Fatty Acids (LCFAs)....49
3.2.2 Phospholipid and Probe Reagents....50
3.2.3 Buffer Reagents....51
3.2.4 Bacterial Cell Strain and Biological Testing Reagents....52
3.3 Material Synthesis....53
3.3.1 Preparation of Antimicrobial Fatty Acid and Liposome Solutions....53
3.3.2 Preparation of Model Membrane Platforms....54
3.4 Experimental Techniques....56
3.4.1 Determination of Critical Micelle Concentration....56
3.4.2 Quartz Crystal Microbalance-Dissipation....57
3.4.3 Fluorescence Microscopy....59
3.4.4 Fluorescence Recovery After Photobleaching....61
3.4.5 Dynamic Light Scattering and Zeta-Potential....63
3.4.6 Minimum Inhibitory Concentration and Bactericidal Kinetics Testing....66
References....69

Chapter 4 Lipid Membrane Remodeling by the Micellar Aggregation of....73
4.1 Introduction....74
4.2 Materials and Methods....76
4.2.1 Materials....76
4.2.2 Preparation of Fatty Acid Solutions....76
4.2.3 Fluorescence Spectroscopy....77
4.2.4 Quartz Crystal Microbalance with Dissipation (QCM-D)....77

4.2.5 Time-lapse Fluorescence Microscopy 78

4.2.6 Statistical Analysis 79

4.3 Results and Discussion.....79

4.3.1 Determination of the Critical Micelle Concentration 79

4.3.2 Interaction between Long-Chain Unsaturated Fatty Acids and Supported Lipid Bilayers 80

4.3.3 Trend in Interaction Kinetics of Long-Chain Unsaturated Fatty Acids on Supported Lipid Bilayers 85

4.3.4 Observation of Membrane Morphological Responses in Supported Lipid Bilayers 87

4.4 Conclusion.....94

References.....95

Chapter 5 Exploring the Membrane-Active Interactions of 99

5.1 Introduction.....100

5.2 Experimental Methods 102

5.2.1 Reagents.....102

5.2.2 Antimicrobial Fatty Acids Solutions Preparation 103

5.2.3 Lipid Preparation for SLB Formation 103

5.2.4 Quartz Crystal Microbalance with Dissipation (QCM-D) Experiments ...104

5.2.5 Time-lapse Fluorescence Microscopy 105

5.2.6 Fluorescence Recovery after Photobleaching (FRAP) Measurements 105

5.3 Results and Discussion 106

5.3.1 Formation and Characterization of Model Bacterial Membranes.....106

5.3.2 Mass and Viscoelastic Property Changes Induced by Antimicrobial Long-Chain Fatty Acids on Model Bacterial Membranes.....109

5.3.3 Observation of Membrane Morphological Responses in Model Bacterial Membranes 118

5.4 Conclusion.....123

References.....125

Chapter 6 Interaction Dynamics of Liposomal Fatty Acids with.....129

6.1 Introduction.....130

6.2 Experimental Methods 132

6.2.1 Reagents.....132

6.2.2 Synthesis and Characterization of Antimicrobial Fatty Acids and Liposomes 133

6.2.3 Cryogenic Electron Microscopy (Cryo-EM) Imaging 134

6.2.4 Lipid Preparation for SLB Formation 134

6.2.5 Quartz Crystal Microbalance with Dissipation (QCM-D) Experiments ...134

6.2.6 Time-lapse Fluorescence Microscopy 135

6.2.7 Fluorescence Recovery after Photobleaching (FRAP) Measurements 136

6.2.8 Membrane Fluidity Assay 136

6.2.9 Liposome Fusion with S. aureus MW2.....137

6.3 Results and Discussion **137**

6.3.1 Synthesis and In Vitro Characterization of LipoFAs 137

6.3.2 Frequency and Dissipation Relations (F-D Curves) for LipoFAs on Gram-positive Model Membranes 139

6.3.3 Quantitative Analysis of Particle Formation in Gram-positive Model Membranes.....143

6.3.4 In Vitro Membrane Fluidity Changes Induced by LipoLNA, LipoLLA, and LipoOA on Gram-positive Bacterial Membranes 145

6.4 Conclusion....148

References....150

Chapter 7 Conclusions and Recommendations....155

7.1 Conclusions....156

7.2 Future Work....158

7.2.1 Antimicrobial Potency of the Membrane-Active Long-Chain Unsaturated Fatty Acids on S. aureus MW2....158

7.2.2 Antimicrobial Potency of the Membrane-Active Liposomal Long-Chain Fatty Acids on S. aureus MW2....162

7.2.3 In Vitro Cytotoxicity Evaluation of Long-Chain Fatty Acids and Liposomal Fatty Acids....166

References....168

Table Captions

Table 2.1 Data for melting points and solubility levels of fatty acids from literature

Table 2.2 Antibacterial efficacy of fatty acids against Gram-positive and Gram-negative bacterial pathogens

Figure Captions

Figure 1.1 Estimated Annual Deaths Attributable to Antibiotic Resistance in Comparison to Other Leading Causes of Mortality (Source: The Review on Antimicrobial Resistance, O'Neil 2016).

Figure 2.1 Chemical structures of saturated fatty acids (SFAs), monounsaturated fatty acids (MUFAs), and polyunsaturated fatty acids (PUFAs). SFAs; Capric acid (C10:0), Lauric acid (C12:0), Myristic acid (C14:0), Palmitic acid (C16:0), Stearic acid (C18:0). MUFAs; Palmitioleic acid (C16:1); Oleic acid (C18:1). PUFAs; Linoleic acid (C18:2), Linolenic acid (C18:3).

Figure 2.2 Schematic diagram illustrating antibacterial mechanisms of fatty acids. Reproduced with permission from reference [42].

Figure 2.3 SEM images showing effects of monoglyceride derivative against bacterial cell membranes. (A) B. subtilis cells treated with monocaprin. (B) E. coli cells treated with monocaprin. Reproduced with permission from reference [69].

Figure 2.4 TEM images showing effects of fatty acid against bacterial cell membranes. Clostridium difficile cells untreated (left) and treated (right) with 0.25x MBC of lauric acid for 15 minutes. Reproduced with permission from reference [70].

Figure 3.1 Chemical structures of long-chain fatty acids used in this thesis.

Figure 3.2 Chemical structures of the phospholipids, cholesterol, and probes used in this thesis.

Figure 3.3 Bottom-up fabrication formation process of supported lipid bilayer using solvent-assisted lipid bilayer method. Reproduced with permission from [29].

Figure 3.4 Schematic of the FRAP technique showing a fluorescence intensity curve

over time. Reproduced with permission from reference [48].

Figure 3.5 Schematic of the electrokinetic potential at the slipping plane, which represents the zeta-potential. Reproduced with permission from reference [58].

Figure 4.1 Overview of experimental strategy with materials used in this study. (A) Molecular structure and physicochemical properties of long-chain unsaturated fatty acids used in this study. (B) Schematic illustration of experimental strategy to characterize how long-chain unsaturated fatty acids interact with lipid membrane via supported lipid bilayer (SLB) platforms.

Figure 4.2 Determination of critical micelle concentration (CMC) values for linolenic acid (LNA), linoleic acid (LLA), and oleic acid (OA) using fluorescence spectroscopy. Peak wavelength is shown as a function of compound concentration in PBS buffer for (A) LNA, (B) LLA, and (C) OA. The CMC value is defined as the highest test concentration at which no peak shift occurs. Data are reported as mean ± standard deviation from six technical replicates (n = 6).

Figure 4.3 QCM-D investigation of concentration-dependent LNA treatment on SLBs at pH 7.5. Δf (blue line with squares) and ΔD (red line with triangles) shifts are presented as a function of time for (A) 500 μM, (B) 250 μM, (C) 125 μM, (D) 63 μM, (E) 31 μM, and (F) 16 μM LNA. The initial baseline values recorded at t = 0 min indicate the formation of an SLB on the silica surface. LNA was introduced at t = 5 min (arrow 1), followed by a buffer washing step (arrow 2) after the measurement signals stabilized.

Figure 4.4 QCM-D investigation of concentration-dependent LLA treatment on SLBs at pH 7.5. Δf (blue line with squares) and ΔD (red line with triangles) shifts are presented as a function of time for (A) 500 μM, (B) 250 μM, (C) 125 μM, (D) 63 μM, (E) 31 μM, and (F) 16 μM LLA. The initial baseline values recorded at t = 0 min indicate the formation of an SLB on the silica surface. LLA was introduced at t = 5 min (arrow 1), followed by a buffer washing step (arrow 2) after the measurement signals stabilized.

Figure 4.5 QCM-D investigation of concentration-dependent OA treatment on SLBs at pH 7.5. Δf (blue line with squares) and ΔD (red line with triangles) shifts are presented as a function of time for (A) 500 μM, (B) 250 μM, (C) 125 μM, (D) 63 μM, (E) 31 μM, and (F) 16 μM OA. The initial baseline values recorded at t = 0 min indicate the formation of an SLB on the silica surface. OA was introduced at t = 5 min (arrow 1), followed by a buffer washing step (arrow 2) after the measurement signals stabilized.

Figure 4.6 The trend in QCM-D measurement shifts for membrane remodeling behavior induced by different long-chain unsaturated fatty acids. Δf shifts are presented as functions of time for (A) LNA, (B) LLA, and (C) OA at 16 – 500 uM concentrations until 60 min. Fatty acids were added at t = 5 min (arrow). Column graph of the net |Δf| shifts (upper panel) and ΔD shifts (lower panel) at 60 min for (D) LNA, (E) LLA, and (F) OA, respectively. The net |Δf| and ΔD shifts are reported as |Δfmeasured − Δfbilayer| and ΔDmeasured − ΔDbilayer shifts, respectively. The dotted line in the lower panel represents above (to the left) and below (to the right) CMC ranges. Data are reported as mean ± standard deviation from n = 3 measurements.

Figure 4.7 Time-lapse microscopic observation of LNA-induced membrane morphological responses on SLBs at concentrations above CMC and below CMC, respectively. (A) Image snapshots at various time points depict nucleation sites from which aggregates proliferate upon treatment of SLB with 500 μM LNA at pH 7.5. (B) Image snapshots at various time points depict nucleation sites from which tubules grow upon treatment of SLB with 250 μM LNA at pH 7.5. At t = 0 min, LNA solution was added to the measurement chamber. The scale bar is 20 μm.

Figure 4.8 Time-lapse microscopic observation of LLA-induced membrane morphological responses on SLBs at concentrations above CMC and below CMC, respectively. (A) Image snapshots at various time points depict nucleation sites from which aggregates proliferate upon treatment of SLB with 250 μM LLA at pH 7.5. (B) Image snapshots at various time points depict nucleation sites from which tubules grow upon

treatment of SLB with 31 μM LLA at pH 7.5. At t = 0 min, LLA solution was added to the measurement chamber. The scale bar is 20 μm.

Figure 4.9 Time-lapse microscopic observation of OA-induced membrane morphological responses on SLBs at concentrations above CMC and below CMC, respectively. (A) Image snapshots at various time points depict nucleation sites from which aggregates proliferate upon treatment of SLB with 125 μM OA at pH 7.5. (B) Image snapshots at various time points depict nucleation sites from which tubules grow upon treatment of SLB with 16 μM OA at pH 7.5. At t = 0 min, LLA solution was added to the measurement chamber. The scale bar is 20 μm.

Figure 5.1 Experimental framework for investigating the interaction of antimicrobial long-chain fatty acids with model bacterial membrane platforms. (A) Schematics illustrating the membrane structure of Gram-positive bacteria with representative lipid compositions. (B) Chemical structure of the lipids utilized in model bacterial membrane platforms. Lysyl-PG is a bicationic membrane lipid, POPG and CL are anionic membrane lipids found in the plasma membranes of Gram-positive bacteria. (C) Schematics illustrating the experimental strategy used to investigate the interaction of long-chain fatty acids with model bacterial membranes, utilizing QCM-D and fluorescence microscopy.

Figure 5.2 Fluorescence recovery after photobleaching (FRAP) analysis for assessing the mobility of Gram-positive bacterial SLBs. (A) Mobile fractions and (B) lateral diffusivity values for the Gram-positive lipid membrane. Data are reported as the mean ± standard deviation from n = 3 measurements.

Figure 5.3 The formation of the model bacterial membrane using the SALB method on silicon dioxide and analyzed with QCM-D and fluorescence microscopy. (A) QCM-D monitoring of the SALB method using lipid compositions for the Gram-positive bacterial membrane. Arrows denote the injection of (1) buffer, (2) isopropanol, (3) lipid mixture, and (4) buffer exchange. The final values of Δf and ΔD for the membrane are reported, with all data shown as the mean ± standard deviation from n = 3 measurements. (B)

Fluorescence recovery after photobleaching (FRAP) analysis for the assessment of fluidity of the Gram-positive membrane. Photobleaching was carried out at t = 0 s, with the bleached area appearing as a dark spot in the center of the micrograph. The normalized fluorescence intensity (F.I.) across the bleached region (indicated by the white dotted line in the 0s images) is shown in the corresponding cases. The F.I. values were normalized to 0.0 and 1.0 au for the minimum and maximum fluorescence intensities throughout the time, respectively. The scale bar is 20 μm.

Figure 5.4 QCM-D investigation of LNA treatments on model bacterial membranes at pH 7.5. (A and C) Representative Δf and ΔD vs time plots of LNA-treated Gram-positive bacterial membranes at concentrations of 500 μM (above CMC) and 16 μM (below CMC), and (B and D) its respective Δf and ΔD plots. Fatty acid was added at t = 10 min, followed by a buffer washing step at t = 70 min. The dotted line in panels (A and C) represents the typical measurement responses for SLB formation.

Figure 5.5 QCM-D investigation of LNA treatment on model bacterial membranes at concentrations above and below CMC values at different overtones (from third-ninth). (A and B) Representative third through ninth harmonic Δf and ΔD vs time plots of LNA-treated Gram-positive bacterial membrane. Fatty acids were added at t = 10 min, followed by a buffer washing step at t = 70 min. The dotted line in panels (A and B) represents the typical measurement responses for SLB formation.

Figure 5.6 QCM-D investigation of LNA treatments on model bacterial membranes at pH 7.5. (A and C) Representative Δf and ΔD vs time plots of LNA-treated Gram-positive bacterial membranes at concentrations of 500 μM (above CMC) and 16 μM (below CMC), and (B and D) its respective Δf and ΔD plots. Fatty acid was added at t = 10 min, followed by a buffer washing step at t = 70 min. The dotted line in panels (A and C) represents the typical measurement responses for SLB formation.

Figure 5.7 QCM-D investigation of concentration-dependent LLA treatments on model Gram-positive bacterial membranes as functions of time at concentrations of 16 μM, 31

μM, 250 μM, and 500 μM until 70 min. Fatty acid was added at t = 10 min, followed by a buffer washing step at t = 70 min. The dotted line represents the typical measurement responses for SLB formation.

Figure 5.8 QCM-D investigation of LLA treatment on model bacterial membranes at concentrations above and below CMC values at different overtones (from third-ninth). (A and B) Representative third through ninth harmonic Δf and ΔD vs time plots of LLA-treated Gram-positive bacterial membrane. Fatty acids were added at t = 10 min, followed by a buffer washing step at t = 70 min. The dotted line in panels (A and B) represents the typical measurement responses for SLB formation.

Figure 5.9 QCM-D investigation of LLA treatments on model bacterial membranes at pH 7.5. (A and C) Representative Δf and ΔD vs time plots of LLA-treated Gram-positive bacterial membranes at concentrations of 500 μM (above CMC) and 16 μM (below CMC), and (B and D) its respective Δf and ΔD plots. Fatty acid was added at t = 10 min, followed by a buffer washing step at t = 70 min. The dotted line in panels (A and C) represents the typical measurement responses for SLB formation.

Figure 5.10 QCM-D investigation of concentration-dependent OA treatments on model Gram-positive bacterial membranes as functions of time at concentrations of 16 μM, 31 μM, 250 μM, and 500 μM until 70 min. Fatty acid was added at t = 10 min, followed by a buffer washing step at t = 70 min. The dotted line represents the typical measurement responses for SLB formation.

Figure 5.11 QCM-D investigation of OA treatment on model bacterial membranes at concentrations above and below CMC values at different overtones (from third-ninth). (A and B) Representative third through ninth harmonic Δf and ΔD vs time plots of OA-treated Gram-positive bacterial membrane. Fatty acids were added at t = 10 min, followed by a buffer washing step at t = 70 min. The dotted line in panels (A and B) represents the typical measurement responses for SLB formation.

Figure 5.12 QCM-D investigation of OA treatments on model bacterial membranes at pH 7.5. (A and C) Representative Δf and ΔD vs time plots of OA-treated Gram-positive bacterial membranes at concentrations of 500 μM (above CMC) and 16 μM (below CMC), and (B and D) its respective Δf and ΔD plots. Fatty acid was added at t = 10 min, followed by a buffer washing step at t = 70 min. The dotted line in panels (A and C) represents the typical measurement responses for SLB formation.

Figure 5.13 Time-lapse microscopic observation of membrane morphological responses in model Gram-positive bacterial membranes triggered by LNA, LLA, and OA at concentrations below CMC. Sequential image snapshots depicting the morphological change of Gram-positive bacterial membrane under (A) LNA treatment at 63 μM, (B) LLA treatment at 31 μM, and (C) OA treatment at 16 μM. At t = 0 min, the fatty acid solutions were added to the measurement chamber. The scale bar is 20 μm.

Figure 5.14 Time-lapse microscopic observation of membrane morphological responses in model bacterial membranes triggered by fatty acid treatments at concentrations below and above CMC. (A) Representative sequential image snapshots depicting the morphological change of Gram-positive bacterial membrane under LNA treatment at 500 μM. (B) Representative analysis for calculating spot area formed on SLBs. (C) Total area of spot formation on SLBs after buffer washing (n = 5, mean ± SD). The scale bar is 20 μm.

Figure 6.1 Schematic representation of the experimental approach for developing LipoFAs for antibacterial applications. Liposomes were prepared through the hydration of lipid and cholesterol mixtures, followed by sonication and extrusion techniques. (A) Membrane formation, (B) liposome fusion, and (C) membrane disruption activities of LipoFAs were evaluated.

Figure 6.2 Characterization of LipoFAs. (A-C) Change in hydrodynamic size (diameter, nm) and PDI of FFAs and LipoFAs with different compositions measured by DLS. (D-F) Change in surface zeta potential (mV) of FFAs and LipoFAs with different compositions

measured by DLS over 24 h (n = 3, mean ± SD). (G) Representative cryo-EM images of (1) BareLipo, (2) LipoLNA, (3) LipoLLA, and (4) LipoOA. The scale bar is 50 nm.

Figure 6.3 QCM-D curves for LipoFAs on Gram-positive model membranes. Δf and ΔD shifts as a function of time. (A-C) Frequency and dissipation shifts of BareLipo and LipoFAs on Gram-positive model membrane at varying concentrations. The dash line in panels (A-C) refer to initial SLB formation baseline.

Figure 6.4 Biophysical characterization of membrane interaction and fusion with S. aureus MW2. Viscoelastic fingerprints of interactions of LipoFAs with model Gram-positive bacterial SLBs. Frequency-dissipation (F-D) curves for (A) BareLipo, (B) 500 μg/mL LipoFAs, and (C) 15.625 μg/mL LipoFAs. Arrows in panel (A) highlight the stages of interaction, while the downward arrows in panels (B and C) denote the initiation of buffer washing. (D) Fluorescence images illustrating fusion activity between RhB-labeled LipoFAs (red) and DAPI-stained bacteria (blue). Control bacteria were incubated with PBS. The scale bar is 5 μm.

Figure 6.5 Quantitative analysis of particle formation in Gram-positive model membranes. Time-lapse microscopic observation of membrane morphological responses in SLBs induced by BareLipo, LipoOA, LipoLLA, and LipoLNA. (A) Sequential image snapshots depicting the morphological changes of SLBs upon interaction with BareLipo and LipoFAs at varying concentrations. The scale bar is 20 μm. The total number of particles (B) after sample treatment and (C) post-washing (n = 5, mean ± SD).

Figure 6.6 Membrane fluidity changes induced by LipoFAs on Gram-positive model membranes and in vitro bacterial fusion assays. (A) Summary of diffusion coefficients and mobile fractions for the Gram-positive model membrane before and after treatment with LipoFAs. Fluorescence micrographs at 0 min and 2 min after photobleaching for model membranes treated with (B) BareLipo, (C) LipoLNA, (D) LipoLLA, and (E) LipoOA. The scale bar is 20 μm. (F) Membrane fluidity of S. aureus MW2 treated with LipoFAs and BareLipo for 1h. Laurdan GP index = (I435 – I490)/(I435 + I490), where 435 and 490 are

the emission intensities at 435 nm and 490 nm, respectively, when excited at 350 nm (n = 3, mean ± SD). Statistical significance was determined with p values <0.05 as significant (*p < 0.05, **p < 0.01, and ***p < 0.001).

Figure 7.1 LNA, LLA, and OA penetrate the cell membrane bilayers of S. aureus MW2, demonstrating antimicrobial activity. (A) Exponential-phase S. aureus MW2 cells were treated with concentrations ranging from 16 μM to 500 μM for 4 h. Surviving cells were quantified by determining CFU (Colony Forming Units) counts through serial dilution and plating on MH agar plates every 2 h (n = 5, mean ± SD). Data points below the detection limit (2×10^2 CFU/mL) are indicated on the x-axis. (B) Membrane permeabilization was assessed after a 60 min treatment of S. aureus MW2 with LNA, LLA, and OA using SYTOX Green fluorescence (Ex 485 nm, Em 525 nm). The data represent the mean of three independent experiments. (C) Intracellular ATP leakage from S. aureus MW2 cells treated with LNA, LLA, and OA for 20 min was measured using an ATP luminescence assay. Individual data points are displayed, with error bars representing mean ± SD (n = 3). Statistical differences were analyzed using one-way ANOVA followed by Tukey's multiple comparisons test (**** p < 0.0001).

Figure 7.2 In vitro bactericidal activity of LCFAs and LipoFAs against S. aureus MW2. (A) A table showing the MIC values against S. aureus MW2. (B) CFU-time curves of liposomes against S. aureus MW2 plotted using exponential phase bactericidal kinetics analysis. Data are presented as mean ± standard deviation (n = 3), and data points on the x-axis fall below the detection limit of 2×10^2 CFU/mL.

Figure 7.3 Membrane permeability analysis and ATP leakage in bacterial cells. (A) Membrane permeability of S. aureus MW2 was assessed following treatment with LCFAs and LipoFAs for 60 min, using SYTOX Green (Ex 485 nm, Em 525 nm). Results represent the mean of three independent experiments. (B) ATP leakage from S. aureus MW2 was monitored for 10 min after treatment with FFAs and LipoFAs, using an ATP luminescence assay. Individual data points are displayed, and error bars indicate the mean ± standard deviation (n = 3). Statistical differences were determined by one-way ANOVA followed by

Tukey's multiple comparison test (* $p < 0.1$, ** $p < 0.001$, *** $p < 0.0001$, **** $p < 0.0001$).

Figure 7.4 In vitro cell viability assays for S. aureus MW2 after treatment with LCFAs and LipoFAs. (A) Cell viability analysis on (B) mouse fibroblast cells (L-929) and (C) human keratinocyte cells (HaCat) treated with LCFAs, BareLipos, and LipoFAs (n = 3, mean ± SD).

Abbreviations

AMR	Antimicrobial Resistance
ATP	Adenosine Triphosphate
CFU	Colony Forming Units
CA	Capric Acid
CL	Cardiolipin
CMC	Critical Micelle Concentration
DHA	Docosahexaenoic Acid
DLS	Dynamic Light Scattering
DOPC	1,2-dioleoyl-*sn*-glycero-3-phosphocholine
FFA	Free Fatty Acid
FRAP	Fluorescence Recovery After Photobleaching
GPB	Gram-Positive Bacteria
GRAS	Generally Recognized As Safe
LA	Lauric Acid
LCFA	Long-Chain Fatty Acid
LipoFA	Liposomal Fatty Acid
LipoLLA	Liposomal Linoleic Acid
LipoLNA	Liposomal Linolenic Acid
LipoOA	Liposomal Oleic Acid
LLA	Linoleic Acid
LNA	Linolenic Acid
MIC	Minimum Inhibitory Concentration
MBC	Minimum Bactericidal Concentration
MRSA	Methicillin-Resistant *Staphylococcus aureus*
MSSA	Methicillin-susceptible *Staphylococcus aureus*
OA	Oleic Acid
PBS	Phosphate-Buffered Saline
POPG	1-palmitoyl-2-oleoyl-sn-glycero-3-phospho-(1'-rac-glycerol)
PUFA	Polyunsaturated Fatty Acid

QCM-D	Quartz Crystal Microbalance-Dissipation
Rh-PE	1,2-dioleoyl-sn-glycero-3-phosphoethanolamine-N-(lissamine rhodamine B sulfonyl) (ammonium salt)
SALB	Solvent-Assisted Lipid Bilayer
SLB	Supported Lipid Bilayer
UFA	Unsaturated Fatty Acid

Chapter 1

Introduction

In recent years, antimicrobial fatty acids and liposomal fatty acids have gained significant attention as promising strategies to combat antimicrobial resistance, potentially serving as next-generation antibacterial agents. To fully leverage this potential and advance biotechnological applications, it is imperative to methodically comprehend the mechanisms underlying the interactions between these agents and model bacterial membranes. To achieve this objective, the integration of materials science and engineering tools with biophysical experiments offers exceptional advantages and introduces innovative approaches for studying antimicrobial fatty acids and liposomes. These combined methodologies allow for the exploration of the physicochemical mechanisms by which the molecular properties of these agents influence their biological activity. This chapter emphasizes the critical importance of understanding the interaction mechanisms to develop effective antimicrobial strategies.

1.1 Hypothesis/Problem Statement

The escalating threat of antimicrobial resistance (AMR), as highlighted by the World Health Organization (WHO), poses a significant challenge to global health [1]. With antibiotic resistance contributing to approximately 700,000 deaths each year worldwide, and forecasts indicate that this figure could exceed 10 million annually by 2050 without effective measures are not implemented [2, 3] (**Figure 1.1**). This antibiotic resistance crisis extends beyond healthcare to impact veterinary practices, food security, environmental well-being (e.g. water, soil), and agriculture, making it a critical public health concern [1-3]. To address this, a new Sustainable Development Goal (SDG) indicator for antibiotic resistance was included in the monitoring framework to monitor the frequency of bloodstream infections due to multi-drug resistant bacteria [1] .

While antibiotics have played a pivotal role in combating bacterial infections since their introduction over a century ago, significantly boosting human life expectancy by at least 23 years [4], their overuse in healthcare, agriculture, and animal rearing have exacerbated the issue of AMR. The increasing prevalence of antibiotic-resistant bacterial strains among human pathogens has further aggravated the problem [3, 4], resulting in ineffective antimicrobial treatments and higher morbidity and mortality rates [3]. This issue is compounded by the slow pace of new antibiotic development, partly due to low financial incentives and market pressures [4]. Recent efforts have largely focused on modifying the antibiotics rather than creating novel ones with unique mechanisms of action [3]. The emergence of “superbugs” has raised concerns about the future effectiveness of antibiotics [1], emphasizing the critical necessity to develop innovative antibacterial agents that are less vulnerable to antibiotic resistance.

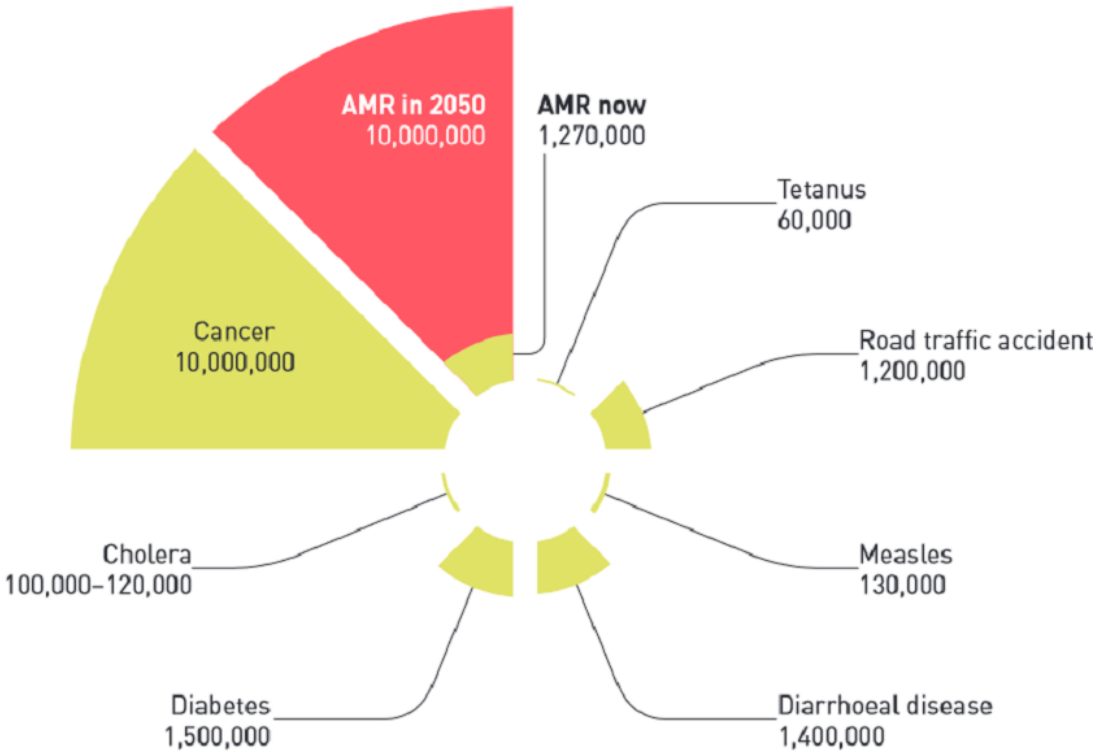

Figure 1.1 Estimated Annual Deaths Attributable to Antibiotic Resistance in Comparison to Other Leading Causes of Mortality. (Source: The Review on Antimicrobial Resistance, O'Neil 2016).

Antimicrobial fatty acids (FAs) and liposomes have gained attention as potential next-generation antibacterial agents. Although the antimicrobial properties of FAs were initially acknowledged in the late 19th century, with early studies demonstrating their effectiveness against *Bacillus anthracis* [5], their significance diminished with the advent of antibiotics. However, the resurgence of interest in these compounds is evident in antibacterial studies conducted in response to the growing threat of antibiotic-resistance bacteria, as evidenced by the antibacterial experiments performed by Weitzel on *Tubercle bacilli* using saturated FAs [6, 7]. FAs, characterized by a non-specific mechanism of action (MOA), are less likely to induce resistance [8]. Nonetheless, their limited solubility in aqueous media restricts their bioavailability and antibacterial efficacy [9]. Liposomes, first discovered in the 1960s by Bangham, offer a solution by enhancing solubility and delivery of FAs [10-12]. These nanocarriers, known for their biocompatibility and stability, can deliver high concentrations of FAs to bacterial membranes, leading to morphological

changes and cell death [13]. For example, liposomes containing oleic acid have demonstrated effectiveness against *Staphylococcus aureus* (*S. aureus*) and *Helicobacter pylori* (*H. pylori*), while those containing lauric acid exhibit potent antibacterial activity against *Propionibacterium acnes* (*P. acnes*) [14]. Despite these promising findings, there is a gap in biophysical investigations exploring the interactions between FAs and bacterial membranes when delivered via liposomes. Addressing this gap could provide critical insights into their MOA and optimize their use in combating bacterial infections.

In this thesis, particular attention is drawn to long-chain fatty acids (LCFAs), specifically linolenic acid (LNA), linoleic acid (LLA), and oleic acid (OA), and liposomes loaded with LNA (LipoLNA), LLA (LipoLLA), and OA (LipoOA), due to their potent antibacterial efficacy [15], low propensity for resistance development [16], high uptake of the agent by bacteria, and FDA "generally recognized as safe" (GRAS) status [17]. LCFAs have shown promise in controlling biofilm formation by *S. aureus* and other Gram-positive bacteria [18], exhibiting antibacterial effects against significant pathogens like methicillin-resistant *S. aureus* (MRSA) [19], *H. pylori* [20], and *mycobacteria* [21]. Given these benefits, the exploration of FAs and liposomes extends to various applications, including drug delivery [5], medical [5, 22], agricultural [23, 24] , and cosmetic uses [6, 23, 25, 26]. Nevertheless, it should be stressed that achieving a deeper understanding of how these agents influence the biological activities remains a key objective in the transition from prototypes to specific applications.

Comprehending the interactions between these agents and bacterial membranes is crucial for their practical utilization. Traditional methods for assessing antimicrobial efficacy, such as determining the minimum inhibitory concentration (MIC) and minimum bactericidal concentration (MBC), offer insights into structure-activity relationships and concentration-dependent effects [14, 27]. While these approaches elucidate the inhibitory effectiveness of antimicrobial agents at a biological level, they fall short in explaining the physicochemical interactions at a molecular level and how these properties influence the biological activities. This limitations hampers the understanding of the potency of specific compounds and the potential for optimization strategies [28]. Moreover, reported MIC and MBC values of the test compounds against the same bacteria often vary significantly. To

address this challenge, numerous studies have been performed to examine membrane morphology changes on bacterial cell membranes using electron microscopy and atomic force microscopy. However, these techniques require high FA concentrations, fixed samples, and post-treatment bacterial cell analysis.

To overcome these challenges and gain detailed understanding of molecular-level interactions, model biological membranes such as small unilamellar vesicles (SUVs) and giant unilamellar vesicles (GUVs) have been utilized. When paired with dynamic light scattering (DLS), these model systems allows for direct observation of membrane destabilization processes induced by antimicrobial FAs, including partial solubilization and membrane fission [29-32]. Additionally, supported lipid bilayers (SLBs), 2-D phospholipid bilayers studied with surface-sensitive techniques, have been extensively explored in antimicrobial research, offering valuable insights into the mechanistic interactions between antimicrobial agents and phospholipid membranes. While various SLBs have been investigated, each providing unique advantages for studying antimicrobial study, most single-component zwitterionic SLB and SLBs composed of bacterial cell membrane extracts [28, 33-37].

There is a pressing need to extend these approaches to investigate the interaction of LCFAs and liposomal fatty acids (LipoFAs) with SLBs that mimic bacterial membranes. By linking the physical and chemical attributes of these agents with their biophysical and biological characteristics, this research seeks to establish a comprehensive framework for understanding their antimicrobial mechanisms. This platform will be instrumental in exploring the mechanistic behavior of antimicrobial agents concerning bacterial membranes, offering insights crucial for advancing antimicrobial research and development. Several key questions remain unanswered:

1. How do LCFAs and LipoFAs interact with phospholipid membranes, and what morphological responses do they induce?
2. How do the physicochemical properties (e.g., critical micelle concentration, net charge, shape, tail volume, unsaturation degree) of these agents influence their interaction with phospholipid membranes?

3. How do these agents interact with biologically relevant membranes? Specifically, how do the interactions with antimicrobial agents vary with negatively versus positively charged phospholipid membranes?

To address these questions, this thesis will investigate single-component and multi-component SLBs to elucidate the interactions with LCFAs and FA-loaded liposomes, correlating these interactions with biological activities. The hypotheses guiding this thesis are as follows:

1. Single-component and multi-component supported lipid bilayers (SLBs) provide valuable insights into the mechanistic and kinetic interactions between long-chain fatty acids (LCFAs), liposomal long-chain fatty acids (LipoFAs), and bacterial membranes. Multi-component SLBs more accurately replicate the complexity of bacterial membranes, thereby yielding more reliable and predictive interaction signatures compared to single-component SLBs.
2. The concentration-dependent activity profiles of LCFAs correspond to the concentrations at which the test compounds induce antibacterial effect against the bacteria.
3. LCFAs and their corresponding liposomes induce distinct morphological changes in SLBs that correspond to their physicochemical properties and potency of the antimicrobial agents.

1.2 Objectives and Scope

The intricate interplay between antimicrobial agents and membranes holds great significance in understanding antibiotic resistance and developing novel therapeutic strategies [38-44]. Previous efforts have utilized Förster Resonance Energy Transfer (FRET) assays to study liposome interactions with model membranes, providing a valuable platform for investigating the biophysical properties and structural changes of lipid membranes in response to antimicrobial agents. This underscores the importance of leveraging biophysical methods, such as FRET, with well-controlled model membrane

systems to understand how these agents disrupt bacterial membranes [45, 46]. Recently, there has been notable interest in antimicrobial FAs and lipid-based antimicrobial delivery systems, such as liposomes, as potential solutions to this global challenge. These agents show promise as next-generation antimicrobial drugs due to their capacity to disrupt bacterial membranes, positioning them as promising antibacterial candidates [44]. The MOA of lipid-based liposomes involves a complex interplay of interactions, fusion, permeabilization, and modulation of bacterial membrane properties. Moreover, the permeabilization of bacterial membranes leads to increased membrane permeability and cell lysis. While these agents present a diverse and promising array of strategies for combating bacterial infections, limited information exists on how their physicochemical properties influence interactions with bacterial membranes. To address this research gap, SLBs that closely emulate the characteristics of bacterial membranes provide a valuable platform for investigating the MOA of LCFAs and LipoFAs, as well as the biophysical properties and structural changes of lipid membranes in response to these antimicrobial agents.

The key objective of this thesis was to establish a comprehensive experimental framework aimed at understanding the impact of the physicochemical characteristics of antimicrobial agents on their interactions with SLBs. SLB platforms offer enhanced versatility and numerous advantages over other model membrane platforms. Moreover, SLBs consisting of phospholipid blends with diverse shapes and charges can be readily produced utilizing the solvent-assisted lipid bilayer (SALB) method [47]. To accomplish this objective, the following studies were conducted:

Aim 1. To investigate how the physicochemical properties of long-chain fatty acids (LCFAs) influence their mechanisms of interaction with supported lipid bilayers (SLBs).

- Measured the critical micelle concentration (CMC) of LCFAs using fluorescence spectroscopy.
- Evaluated the concentration-dependent activity profiles of linoleic acid (LNA), linoleic acid (LLA), and oleic acid (OA) against single-component SLBs through

quartz crystal microbalance-dissipation (QCM-D) experiments and fluorescence microscopy at their respective CMC values.

- Established a foundation for understanding the relationship between LCFA physicochemical properties and their interaction mechanisms with SLBs.

Aim 2. To fabricate multi-component SLBs using the SALB method, incorporating charged phospholipids to mimic Gram-positive bacterial membranes and evaluate their interactions with LCFAs.

- Incorporated different proportions of charged phospholipids, such as Lysyl-phosphatidylglycerol (Lysyl-PG) and Cardiolipin (CL), into SLBs using the SALB method.
- Verified stable SLB formation using fluorescence recovery after photobleaching (FRAP) and quartz crystal microbalance-dissipation (QCM-D) techniques.
- Investigated the concentration-dependent activity profiles of linoleic acid (LNA), linoleic acid (LLA), and oleic acid (OA) against multi-component SLBs through QCM-D experiments and fluorescence microscopy at their respective CMC values.
- Performed antibacterial assays of LipoFAs on the S. aureus MW2 strain to correlate membrane interaction findings with biological activity.

Aim 3. To explore the role of lipid-based delivery systems in enhancing the solubility and antimicrobial activity of LCFAs against model membranes.

- Developed liposomal formulations containing LCFAs to overcome their limited solubility in aqueous solutions.
- Assessed the molecular interactions between liposome-encapsulated LCFAs and multi-component SLBs using QCM-D and fluorescence microscopy.
- Conducted antibacterial assays of LipoFAs on the *S. aureus* MW2 strain to link the concentration-dependent membrane interactions of the liposomal formulations with biological activity.

1.3 Dissertation Overview

Chapter 1 lays the foundation for this dissertation by presenting an in-depth background of the research field, elucidating the rationale behind selecting this Ph.D. research topic, and delineating the overarching goals and scope of the study.

Chapter 2 presents an overarching review of the current literature on antimicrobial FAs, liposomes, and various characterization methods employed to assess the biophysical and biological activities of antimicrobial lipids. This chapter delivers an extensive background on antimicrobial lipids, encompassing a detailed classification scheme and a thorough review of the antibacterial spectrum and potency of different molecules within this class. Furthermore, it explores the known mechanistic underpinnings of these agents, offering insights into their modes of action. In addition, this chapter discusses various characterization methods used to evaluate their biological and biophysical activities, highlighting the strengths and limitations of each technique. Potential strategies for nanoscale formulation of antimicrobial lipids are also examined. This chapter identifies the gaps that this thesis aims to address.

Chapter 3 offers a comprehensive description of the materials used in the study, the synthesis of these materials, and the experimental techniques employed. This chapter explains why specific methods were chosen and the underlying principles governing these techniques.

Chapter 4 presents empirical observations of the distinct membrane morphological responses induced by LFCAs, namely LNA, LLA, and OA in conventional zwitterionic SLB platforms. This chapter examines the effects of these FAs in concentrations above and below CMC values.

Chapter 5 examines the impact of charged lipids in SLBs that mimic Gram-positive bacterial membranes on the membrane morphology induced by LCFAs at concentrations above and below their CMC values. The chapter offers a fundamental analysis of how the molecular self-assembly of LCFAs relates to various membrane morphological responses in SLB platforms, identifying differences in membrane interactions between monomeric

and micellar states for the tested compounds. The chapter elucidates how the physicochemical properties of LCFAs determine the scope of their biophysical activities.

Chapter 6 explores the impact of charged lipids in SLB platforms on the membrane morphological responses induced by LipoFAs at concentrations above and below CMC values. It extends the investigation to assess how the tested compounds impact membrane fluidity and determines how the physicochemical attributes of LipoFAs determine the scope of their biophysical and biological activities.

Chapter 7 offers a comprehensive summary of the key findings from this research, highlighting significant results that contribute to advancing the field. The chapter also discusses potential future research opportunities, particularly focusing on *in vitro* biological experiments to establish correlations between the biophysical and biological experimental data. This detailed exploration aims to deepen the understanding of the specific mechanisms through which FAs exert their effects and to identify prospects for further investigation that could bolster the development of innovative antibacterial strategies.

1.4 Findings and Outcomes/Originality

The research conducted in this study has led to several novel advancements that enhance the measurement capabilities for investigating the activity profiles of antimicrobial LCFAs and LipoFAs. These advancements also facilitate the classification of the potency and MOA of various classes of lipids. The key findings of this thesis can be outlined as follows:

1. Single-component and charged multi-component SLB platforms that mimc bacterial membranes were established to elucidate the MOAs of LCFAs and LipoFAs. High-quality SLB formation was verified using characterization methods that employ surface-sensitive techniques. This research represents the first systematic investigation into how the physicochemical properties LCFAs and

liposomes loaded with LCFAs influence their biophysical and biological activities on SLB platforms with both zwitterionic and charged lipids.

2. It was identified that the molecular self-assembly emerged as a crucial physicochemical characteristic of LCFAs governing the extent of membrane morphological changes on SLBs. It was discerned that LCFAs predominantly exhibit membrane destabilization dynamics against zwitterionic SLBs at micellar state, leading to membrane remodeling, with minimal effects noted at concentrations below CMC values, displaying CMC-dependent activity profiles.
3. It was discovered that LCFAs exhibit distinct interactions with charged SLBs at neutral pH. Anionic FAs interact weakly with the SLB, forming tubules with a dark background, while neutral FAs penetrate deeper into the bilayer, inducing tubules with consistent fluorescence intensity. It was observed that LCFAs predominantly exert effects on charged SLBs above CMC values, except for oleic acid (OA), which self-aggregates into vesicles at physiological pH, enabling attachment to the SLB even at concentrations below CMC. Furthermore, the concentration-dependent behavior of LCFAs aligns with membrane permeabilization, intracellular ATP leakage, and bactericidal effects on *S. aureus* MW2, validating the model membrane system's utility in elucidating LCFA actions.
4. It was discovered that liposomes loaded with FAs were found to induce distinct alterations in membrane morphology on charged SLBs. This discovery holds significance due to the limited discussion on the details underlying the mechanistic interactions of LipoFAs. Previous comparisons have primarily focused on the biological activities, such as their bacteriostatic and bactericidal effects on bacteria. Using the SLB platform, it was identified that LipoFAs have the potential to influence membrane fluidity and trigger the development of morphological bud structures extending from the SLB. It was revealed that LipoFAs, particularly LipoLNA and LipoLLA, with higher degrees of unsaturation, led to high curvature stress on the SLBs, resulting in higher fluidity of the membrane and leakage of intracellular ATP, correlating with higher bactericidal effects on *S. aureus* MW2. These results consider how the physiochemical properties, such as structure and the tail volume of LCFAs, impact membrane fluidity and curvature upon incorporation

into the SLB.

References

[1] *Antimicrobial Resistance*. *World Health Organization (WHO)*. [accessed 2024 August 9).

[2] C. Willyard. *Nature*. **2017**, 543(7643), 15-15.

[3] *About Antibiotic Resistance*. *Centers for Disease Control and Prevention (CDC)*. [accessed 2024 August 9).

[4] R. Aminov. *Frontiers in Microbiology*. **2010**, 1.

[5] H. Thormar, H. Hilmarsson. *Chemistry and Physics of Lipids*. **2007**, 150(1), 1-11.

[6] A.P. Desbois, V.J. Smith. *Applied Microbiology and Biotechnology*. **2010**, 85(6), 1629-42.

[7] H. Thormar. *Lipids and Essential Oils as Antimicrobial Agents*. **2010**.

[8] A.P. Desbois, V.J. Smith. *Applied Microbiology and Biotechnology*. **2010**, 85, 1629-1642.

[9] A. Blanco, G. Blanco. In *Chapter 5 - Lipids: A. Blanco, G. Blanco (Eds.), Medical Biochemistry (Second Edition)*, Academic Press2022, pp. 105-129.

[10] L. Sercombe, T. Veerati, F. Moheimani, S.Y. Wu, A.K. Sood, S. Hua. *Frontiers in Pharmacology*. **2015**, 6, 286.

[11] A. Hafner, J. Lovrić, G.P. Lakoš, I. Pepić. *International Journal of Nanomedicine*. **2014**, 9, 1005-23.

[12] G.T. Noble, J.F. Stefanick, J.D. Ashley, T. Kiziltepe, B. Bilgicer. *Trends in Biotechnology*. **2014**, 32(1), 32-45.

[13] S.W. Jung, S. Thamphiwatana, L. Zhang, M. Obonyo. *PLoS One*. **2015**, 10(3), e0116519.

[14] J.A. Jackman, B.K. Yoon, D. Li, N.-J. Cho. *Molecules*. **2016**, 21(3), 305.

[15] H. Galbraith, T.B. Miller, A.M. Paton, J.K. Thompson. *Journal of Applied Bacteriology*. **1971**, 34(4), 803-13.

[16] L.L. Ling, T. Schneider, A.J. Peoples, A.L. Spoering, I. Engels, B.P. Conlon, A. Mueller, T.F. Schäberle, D.E. Hughes, S. Epstein. *Nature*. **2016**, 517(7535), 455-459.

[17] L. Acid. J. Am. Coll. *Toxicology*. **1987**, 6, 321-401.

[18] K.T. Yuyama, M. Rohde, G. Molinari, M. Stadler, W.R. Abraham. *Antibiotics*. **2020**.

[19] C.M. Huang, C.H. Chen, D. Pornpattananangkul, L. Zhang, M. Chan, M.F. Hsieh, L. Zhang. *Biomaterials*. **2011**, 32(1), 214-21.

[20] S. Thamphiwatana, W. Gao, M. Obonyo, L. Zhang. *PNAS*. **2014**, 111(49), 17600-5.

[21] M.V. Húmpola, M.C. Rey, N.M. Carballeira, A.C. Simonetta, G. Tonarelli. *Journal of Peptide Science*. **2016**.

[22] C.R. Cardoso, M.A. Souza, E.A. Ferro, S. Favoreto, Jr., J.D. Pena. *Wound Repair and Regeneration*. **2004**, 12(2), 235-43.

[23] A.P. Desbois. *Recent Patents on Anti-Infective Drug Discovery*. **2012**, 7(2), 111-22.

[24] J.J. Dibner, J.D. Richards. *Poultry Science*. **2005**, 84(4), 634-43.

[25] H. Maag. *Journal of the American Oil Chemists Society*. **1984**, 61(2), 259-267.

[26] T. Himeno, Y. Konno, N. Naito. In *Cosmetic Science and Technology*, Sakamoto, K., Lochhead, RY, Maibach, HI, Yamashita, Y., Eds. Elsevier2017, 539-549.

[27] M.I. Hutchings, A.W. Truman, B. Wilkinson. *Current Opinion in Microbiology*. **2019**, 51, 72-80.

[28] B.K. Yoon, J.A. Jackman, M.C. Kim, N.-J. Cho. *Langmuir*. **2015**, 31(37), 10223-10232.

[29] N. Berclaz, M. Müller, P. Walde, P.L. Luisi. *The Journal of Physical Chemistry B*. **2001**, 105(5), 1056-1064.

[30] S. Chungcharoenwattana. *Chemical and Pharmaceutical Bulletin*. **2004**, 52(9), 1058-1062.

[31] S. Lonchin, P.L. Luisi, P. Walde, B.H. Robinson. *The Journal of Physical Chemistry B*. **1999**, 103(49), 10910-10916.

[32] S. Rasi, F. Mavelli, P.L. Luisi. *The Journal of Physical Chemistry B*. **2003**, 107(50), 14068-14076.

[33] K.R. Flynn, L.L. Martin, M.L. Ackland, A.A.J. Torriero. *Langmuir*. **2016**, 32(45), 11717-11727.

[34] M. Hyldgaard, D.S. Sutherland, M. Sundh, T. Mygind, R.L. Meyer. *Applied and Environmental Microbiology*. **2012**, 78(8), 2957-65.

[35] D. Thid, J.J. Benkoski, S. Svedhem, B. Kasemo, J. Gold. *Langmuir*. **2007**, 23(11), 5878-81.

[36] B.K. Yoon, J.A. Jackman, M.C. Kim, T.N. Sut, N.-J. Cho. *Langmuir*. **2017**, 33(11) (2017) 2750-2759.

[37] B.K. Yoon, J.A. Jackman, E.R. Valle-González, N.J. Cho. *International Journal of Molecular Sciences*. **2018**, 19(4).

[38] A. Alghalayini, A. Garcia, T. Berry, C.G. Cranfield. *Antibiotics*. **2019**, 8(1).

[39] J. Davies, D. Davies. *Microbiology and Molecular Biology Reviews*. **2010**, 74(3), 417-33.

[40] N.K. Khadka, P. Teng, J. Cai, J. Pan. *Biochimica et Biophysica Acta (BBA)*. **2017**, 1859(5), 734-744.

[41] D.Y. Wang, H.C.v.d. Mei, Y. Ren, H.J. Busscher, L. Shi. *Frontiers in Chemistry*, **2020**.

[42] Y. Wang. *Journal of Applied Microbiology*. **2021**.

[43] K. Yang, B. Gitter, R. Rüger, G.D. Wieland, M. Chen, X. Liu, V. Albrecht, A. Fahr. *Photochemical & Photobiological Sciences*. **2011**.

[44] B.K. Yoon, J.A. Jackman, E.R. Valle-González, N.J. Cho. *International Journal of Molecular Sciences*. **2018**.

[45] H.R. Marsden, I. Tomatsu, A. Kros. *Chemical Society Reviews*. **2011**, 40(3), 1572-1585.

[46] J.R. Silvius. *Biophysical Journal*. **2003**, 85(2), 1034-1045.

[47] S.R. Tabaei, J.H. Choi, G. Haw Zan, V.P. Zhdanov, N.J. Cho. *Langmuir*. **2014**, 30(34), 10363-73.

Chapter 2

Literature Review

Naturally occurring antimicrobial fatty acids (FAs) and liposomal fatty acids (LipoFAs) have attracted considerable interest as promising antibacterial agents, owing to their broad-spectrum biological activities that involve membrane destabilization and potential to circumvent resistant mechanisms. Despite their long-standing recognition for antimicrobial properties, a comprehensive understanding of how these agents influence their biophysical and biological activities remains elusive. This chapter offers an in-depth overview of long-chain fatty acids (LCFAs) and LipoFAs, covering their classification, antibacterial activity spectrum, and current understanding of their mechanisms of actions (MOAs). Building on this foundation, the chapter delves into various experimental techniques used to assess the biophysical and biological activities of these compounds. This includes a critical examination of the limitations of current methodologies and reflections underscoring the necessity for future analytical advancements. Finally, the chapter formulates key outstanding questions that drive the objective of this thesis, underscoring the significance of linking biophysical and biological activities of LCFAs and LipoFAs with molecular self-assembly and interfacial properties to elucidate their interactions with phospholipid membranes.

2.1 Antimicrobial Fatty Acids

2.1.1 History

Antimicrobial lipids have a long history, beginning with Robert Koch's experiments in 1881, where the inhibitory effects of soaps containing fatty acids (FAs) on *Bacillus anthracis* were observed [1]. These initial observations laid the groundwork for recognizing the antibacterial properties of lipids, particularly in combating bacterial infections. Subsequent research conducted by Burtenshaw and colleagues in the 1940s further highlighted the importance of lipids as a natural barrier in human skin [2].

Despite the initial recognition of antimicrobial lipids, their prominence declined with the emergence of antibiotics, most notably with the discovery of penicillin in the 1930s, which revolutionized the treatment of bacterial infections by targeting specific bacterial enzymes [3]. While antimicrobial lipids possess broad-spectrum activity against diver microorganisms by targeting the cell membrane, antibiotics like penicillin operate by precisely targeting essential bacterial enzymes, leading to potent antibacterial effects. The effectiveness of antibiotics in treating bacterial infections led to their widespread adoption in therapeutic and preventative practices in human and veterinary medicine, contributing to their ubiquitous presence in modern healthcare practices.

The inappropriate use of antibiotics has resulted in the rise of antibiotic-resistant pathogens, presenting a substantial global health dilemma [4]. This surge in antibiotic resistance has rendered previously effective antibiotics ineffective against certain infections, thereby significantly affecting healthcare and medicine. Moreover, the dearth of new antibiotic classes in recent years, coupled with limited viable bacterial targets for drug development, has further exacerbated the crisis of antibiotic resistance. Current efforts in drug development primarily focus on combating resistant strains through the modification of existing antibiotics or the development of novel delivery strategies to enhance their efficacy.

In response to the escalating antibiotic resistance crisis, there is a growing recognition of the need to revisit antimicrobial lipids as potential candidates for

antibacterial agents [5]. Antimicrobial lipids offer several practical advantages, including a recognized safety profile endorsed by regulatory agencies [6], broad-spectrum efficacy against viruses, fungi, and bacteria [7-10], and a reduced risk of antibiotic resistance development due to their unique MOAs. Moreover, the mechanisms through which antimicrobial lipids operate, involving the disruption of bacterial cell membranes to induce cell death or inhibit bacterial growth [10], present a promising avenue for sustainable antibacterial interventions that can help mitigate the emergence of antibiotic resistance.

Despite the potential of antimicrobial lipids, a longstanding challenge has been the limited understanding of how their physicochemical properties correlate with their biological activities. While biological assays have been instrumental in assessing the antimicrobial efficacy of lipids, there remains a critical need to elucidate the intricate interplay between the physical chemistry of antimicrobial lipids and their biological functions. Establishing robust structure-activity relationships and delving deeper into the MOA of antimicrobial lipids are imperative for harnessing their full therapeutic potential in combating bacterial infections.

The renewed interest in antimicrobial lipids as alternative antibacterial agents underscores the urgent need to diversify the arsenal of antimicrobial treatments in response to the escalating antibiotic resistance crisis. By leveraging the inherent antimicrobial properties of LCFAS and LipoFAs and unraveling their MOAs, researchers can pave the way for innovative antimicrobial strategies that circumvent the challenges posed by antibiotic resistance, ushering in a new era in antibacterial therapeutics.

2.1.2 Classes

FAs are essential lipid molecules known for their various roles in biological processes and ability to combat various microorganisms due to their broad-spectrum activity and unique MOA. These molecules are characterized by amphiphilic structures, featuring long hydrocarbon chains (hydrophobic tail) and carboxylic acid groups (-COOH) (hydrophilic head). The carboxyl group is the functional moiety primarily responsible for determining the charge state of FAs. The charge state of FAs is affected by environmental

conditions like pH [11-13], where ionization occurs based on the acid dissociate constant (p*K*a) of the carboxyl group. This transition involves moving from non-ionized forms at low pH to fully ionized forms at high pH levels [14]. The p*K*a of FAs can vary depending on whether it is measured in bulk solution or at the surface of aggregates. The bulk p*K*a reflects the average value in a homogenous aqueous solution and is typically around 4.5 for most FAs [14]. In contrast, the surface p*K*a refers to the dissociation behavior at interfaces, such as the air-water interface or within structured systems like aggregates or solid particles. Surface p*K*a values are generally higher than bulk p*K*a values, indicating a weaker acidity at the air-water interface, due to reduced hydration and altered polarity at these interfaces. For instance, LCFAs discussed in this thesis have surface p*K*a values of approximately 8, 9, and 10 for LNA, LLA, and OA, respectively [15]. Furthermore, the ionization behavior of FAs changes when transitioning from an aqueous phase to a membrane environment. Coarse-grained models suggest that the p*K*a of FAs increases in hydrophobic environments, such as micelles and lipid bilayers. For example, p*K*a values can rise from 4.8 in bulk aqueous solutions to 6.5 in small micelles and 6.6 in bilayers [16]. This shift in p*K*a values is due to changes in hydration and water dynamics within the bilayer interior, leading to a higher p*K*a in the more hydrophobic environment [17]. Consequently, LCFAs predominantly exist in their anionic charge state for LCFAs when incorporated into bilayers, reflecting the influence of the hydrophobic environment on their ionization behavior [18].

FAs are typically classified based on their structural features and properties, which dictate their functions and roles in various biological systems. These molecules can be classified by the hydrocarbon chain length and unsaturation index. FAs generally consist of even number of carbon atoms, although exceptions with odd-numbered versions can be found in specific contexts or through synthetic production. As illustrated in **Figure 2.1**, FAs are divided into short-chain fatty acids (SCFAs) (<C8), medium-chain fatty acids (MCFAs) (C8-C12), and long-chain fatty acids (LCFAs) (C13-C21). Another classification method involves the number and type of bonds in their hydrocarbon chains: saturated fatty acids (SFAs) contain only single bonds, monounsaturated fatty acids (MUFAs) have one double bond, and polyunsaturated fatty acids (PUFAs) contain multiple double bonds. As illustrated in **Table 2.1**, the level of unsaturation plays a crucial role in determining the physiochemical attributes of FAs, including their melting points and solubility in aqueous

solutions. Furthermore, the arrangement of double bonds (*cis*- or *trans*-) can also impact these properties. Understanding FA classification is therefore crucial for exploring antibacterial trends related to molecular shape and structure. Studies have shown that MCFAs and LCFAs with double bonds show increased antimicrobial efficacy against Gram-positive bacteria (GPB) compared to Gram-negative bacteria (GNB), with GPB being particularly susceptible to these FAs [19-21]. Additionally, unsaturated fatty acids (UFAs) have shown to display higher antimicrobial effect compared to their saturated counterparts [20]. LCFAs, in particular, have been found to effectively eradicate major pathogenic microorganisms, such as MRSA and *Helicobacter pylori* (*H. pylori*) [22].

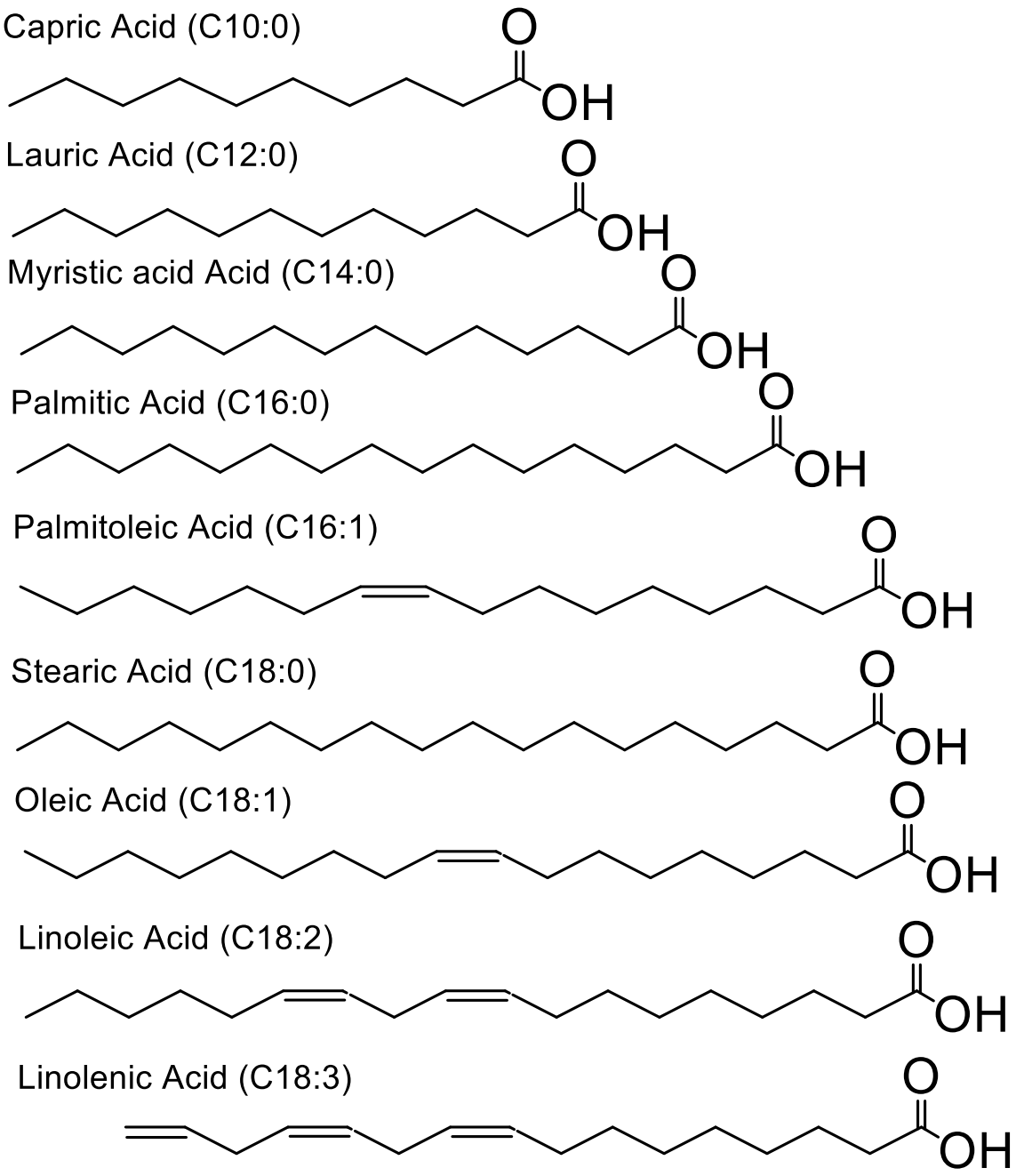

Figure 2.1 Chemical structures of saturated fatty acids (SFAs), monounsaturated fatty acids (MUFAs), and polyunsaturated fatty acids (PUFAs). SFAs; Capric acid (C10:0), Lauric acid (C12:0), Myristic acid (C14:0), Palmitic acid (C16:0), Stearic acid (C18:0). MUFAs; Palmitioleic acid (C16:1); Oleic acid (C18:1). PUFAs; Linoleic acid (C18:2), Linolenic acid (C18:3).

Table 2.1 Data for melting points and solubility levels of fatty acids from literature

Fatty acid	Melting Point (°C)	Solubility Level	Ref.
Capric acid (C10:0)	31.6	+	[23]
Lauric acid (C12:0)	44.8	+	[23]
Myristic acid (C14:0)	54.8	+	[23]
Palmitic acid (C16:0)	62.9	+	[23]
Palmitoleic acid (C16:1)	-0.1	+	[24]
Stearic acid (C18:0)	70.1	+	[23]
Oleic acid (C18:1)	16.0	++	[23]
Linoleic acid (C18:2)	-5	++	[23]
Linolenic acid (C18:3)	-11	+++	[23]

2.1.3 Antibacterial Activity Spectrum

FAs exert antimicrobial impact against a wide range of pathogens, encompassing viruses, GPB, GNB, fungi, and parasites. **Table 2.2** illustrates a detailed examination of the antibacterial of properties of FAs against GPB and GNB. Studies have shown that lauric acid (LA) among SFAs exhibits significant antibacterial effects against GPB [25]. Additionally, capric acid (CA), LA, LLA, and LNA have been evaluated against *S. aureus* and *streptococci* A, B, C, and G strains, with *S. aureus* strains showing lower susceptibility compared to streptoccal strains [26]. In a separate study, it was demonstrated that

unsaturated LCFAs, including LNA, LLA, and OA, demonstrated enhanced antibacterial activity in comparison to LA [20, 25, 27]. Notably, adding a second double bond to OA increased its antibacterial efficacy, while introducing a third double bond leads to reduced activity. Additionally, another study explored the antibacterial properties of PUFAs and discovered that essential FAs, such as arachidonic acid (AA), were effective against GPB strains like *Lactobacillus* and *S. epidermis* [28]. Recent studies have also highlighted the efficacy of LA against various GPB strains, including *Propionibacterium acnes* and *Bacillus anthracis Sterne*, with specific MIC values [29, 30]. However, as indicated in **Table 2.1**, no FAs exert antibacterial effect against *Escherichia coli* and *Salmonella* spp. at physiological pH [31]. Nevertheless, CA has been effective against *Campylobacter jejuni* at a specific concentration [32]. Studies have also demonstrated the antimicrobial effects of LA against *Helicobacter pylori* and other GNB [33], while CA, LA, myristic acid (MA), and palmitoleic acid (POA) have shown susceptibility against *H. pylori* and *Neisseria gonorrhoeae* [31, 34]. Additionally, lowering the pH from 6.5 to 5.2 has shown to inhibit *E. coli* by caprylic acid and CA, likely due to reduced outer membrane permeability, which allows the FAs to enter the inner membrane, caused by the acid [35].

Overall, the antibacterial effects of FAs differ across studies, influenced by variations in lipid concentrations, experimental conditions, and bacterial exposure duration. Generally, GPBs are more susceptible to unsaturated LCFAs, while GNBs are more susceptible to CA, LA, and POA. However, the exact mechanism underlying these effects remain incompletely understood.

Table 2.2 Antibacterial efficacy of fatty acids against Gram-positive and Gram-negative bacterial pathogens

Bacteria	Fatty Acids	Ref.
Staphylococcus aureus (+)	C10:0, C12:0, C18:2, C18:3, C20:4	[28, 36]
Methicillin-Susceptible *Staphylococcus aureus* (MSSA) (+)	C8:0, C10:0, C12:0, C14:0, C16:1, C18:0	[37]
Methicillin-Resistant *Staphylococcus aureus* (MRSA) (+)	C8:0, C10:0, C12:0, C14:0, C16:1, C18:0	[37]
Group A *Streptococcus* (GAS) (+)	C12:0, C16:1, C18:1	[36]
Group B *Streptococcus* (GAS) (+)	C12:0, C16:1, C18:1	[36]
Group D *Streptococcus* (GDS) (+)	C10:0, C12:0, C14:0	[36]
Listeria monocytogenes (+)	C12:0, C14:0, C16:0, C18:0, C18:1, C18:2, C18:3	[38]
Bacillus larvae (+)	C10:0, C11:0, C12:0, C13:0, C14:1, C16:1, C18:2	[39]
Helicobacter pylori (-)	C4:0, C5:0, C6:0, C7:0, C8:0, C9:0, C10:0, C11:0, C12:0, C13:0, C14:0, C15:0, C16:0, C17:0, C16:1, C18:1	[31, 33]
Neisseria gonorrhoeae (-)	C:10, C12:0, C16:1, C18:1, C20:4	[28, 34]
Campylobacter jejuni (-)	C10:0	[40]

2.1.4 Antimicrobial Mechanisms

The investigation into the antimicrobial mechanisms of FAs have been conducted through various experimental approaches, revealing their multifaceted and non-specific MOAs. Despite this, the precise mechanisms by which FAs exert their antibacterial activities remain unclear. It is evident that FAs primarily act on bacterial cell membranes, disrupting crucial cellular processes (**Figure 2.2**). The membrane-disruptive properties arise from the amphipathic property of FAs, allowing them to destabilize membranes and induce biophysical changes like membrane disruption and the formation of pores [10]. This destabilization leads to cell permeability, culminating in cell lysis and inhibition of bacterial growth, which can be reversible (bacteriostatic) or irreversible (bactericidal). Although antibacterial assays do not always distinguish between bacteriostatic and bactericidal effects, it is logical to infer that growth inhibition prevents cell division. Among the key cellular processes affected by FAs, the electron transport chain and oxidative phosphorylation play crucial roles in energy production. FAs can disrupt these processes by coupling with electron carriers, compromising membrane integrity, and disrupting oxidative phosphorylation, which in turn diminishes the proton gradient. Additionally, FAs have the ability to directly inhibit membrane enzymes and impede nutrient uptake of glucosyltransferase (GTase), potentially due to similarities in molecular structures [41]. Unlike traditional antibiotics, antimicrobial FAs are less susceptible to emergence of bacterial resistance owing to their unique MOAs. The schematic representation in **Figure 2.2** highlights the key antibacterial functions of FA, which focus on bacterial cell membranes and involves actions such as interference with the electron transport chain, uncoupling of oxidative phosphorylation, membrane destabilization, metabolite leakage, and enzyme activity inhibition. These mechanisms collectively contribute to the antibacterial effects of FAs, highlighting their potential as effective agents against bacterial infections.

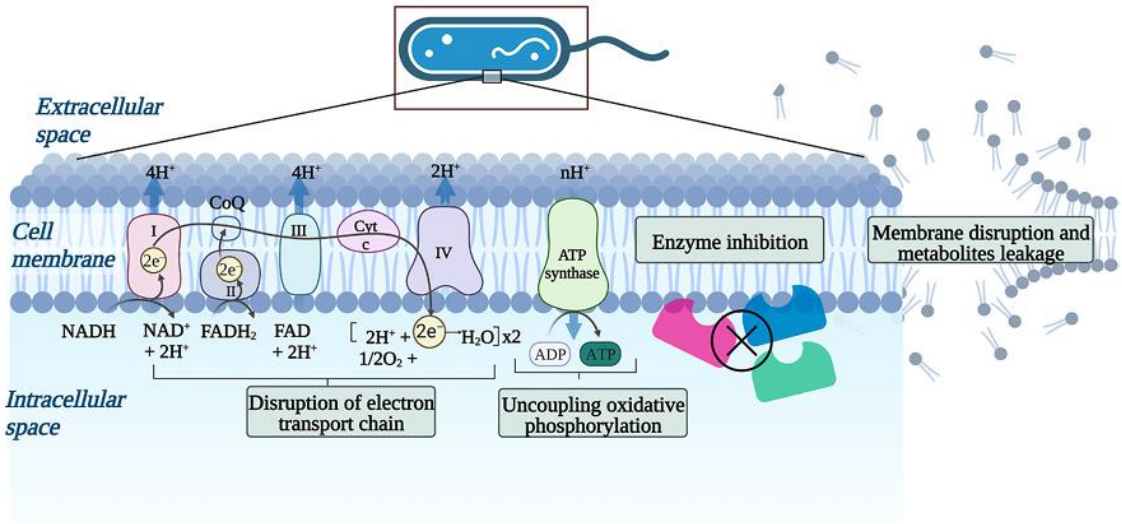

Figure 2.2 Schematic diagram illustrating antibacterial mechanisms of fatty acids. Reproduced with permission from reference [42].

Disruption of electron transport chain and uncoupling of oxidative phosphorylation

The electron transport chain and oxidative phosphorylation are crucial biological processes in the inner membranes of both GPB and GNB, essential for energy production. Within these processes, electrons traverse a series of carriers until they reach an oxygen molecule, where two protons combine to form water [43]. This electron transfer is essential as it drives the movement of protons from the bacterial cytoplasmic membrane to the exterior of the cell, creating a membrane potential that is critical for ATP production via ATP synthase. Integration of FAs into the bacterial cell membrane disrupts these processes significantly. FAs interact with the electron carriers in the membrane, displacing them and thereby interrupting the electron transport chain. This disruption results in inadequate energy production, leading to cell death. Additionally, the efficacy of ATP synthase is severely compromised as protons are able to bypass the enzyme, diminishing its ability to synthesize ATP [44, 45]. Empirical studies support these findings. For instance, Galbraith *et al.* revealed that LA, MA, and LLA significantly impacted the oxygen consumption of *Bacillus megaterium* and *Pseudomonas phaseolicola* [46]. Another study by Sheu and colleagues examined the impact of FAs on *Bacillus subtilis*, revealing a substantial decrease in oxygen uptake and ATP concentration due to membrane disintegration [47]. Particularly, UFAs have been demonstrated to decrease ATP synthesis due to increase in proton gradient as a result of higher membrane permeability [45, 48]. This increased

permeability allows protons to circumvent ATP synthase, further undermining energy production within the bacterial cell and leading to its eventual demise.

Membrane destabilization and metabolite leakage

Numerous studies have shown that FA interactions with bacterial membranes can lead to destabilization, increased permeability, metabolite leakage, and ultimately cell lysis. One study by Chamberlain *et al*. employed polarized fluorimetry to demonstrate that OA significantly increases membrane permeability, inducing cell death in *S. aureus* cells [49]. Similarly, high concentrations of LLA have been found to increase membrane fluidity in *S. aureus* cells, affecting macromolecule synthesis and oxygen uptake, which subsequently leads to cell lysis [50]. This finding underscores the multifaceted impact of LLA on bacterial cell membranes, affecting both the structural integrity and essential cellular functions. In a related investigation, Boyaval *et al*. demonstrated LLA increased membrane permeability, which in turn induced potassium efflux and decreaseed membrane potential [48]. These changes further highlight the complex biochemical disruptions caused by FAs, contributing to the overall antibacterial effect through multiple pathways. Additionally, studies have shown that SFAs can decrease membrane fluidity by inducing autolysis of bacterial cell membranes [51, 52]. This effect adds another layer to the understanding of how FAs can compromise bacterial cell integrity, emphasizing the broad-spectrum nature of their antimicrobial activity. Collectively, these findings reveal that FAs disrupt bacterial membranes through a variety of mechanisms, leading to a cascade of detrimental effects that ultimately inhibit bacterial growth and survival.

Inhibiting activity of bacterial enzymes

FAs demonstrate strong bactericidal effect by blocking essential membrane-associated enzymes crucial for growth and survival of bacterial cells. Various studies have delved into the enzyme-inhibiting properties of FAs, revealing significant findings. For instance, Zheng *et al.* reported that LLA displayed a remarkable antibacterial impact on *S. aureus* by targeting enoyl-acyl-carrier protein reductase (Fabl), a key enzyme involved in cytosolic activity, making it a vital target for antibacterial intervention [53]. Furthermore, another study highlighted how FAs impede glucan production via GTase, a vital

transmembrane protein responsible for glucan production in *Streptococcus sobrinus* [54]. This inhibition leads to a reduction in bacterial cell growth. Similarly, research has shown that LLA, OA, and AA also show strong antibacterial efficacy against *S. aureus* by inhibiting GTase [30], further substantiating the role of FAs in bacterial cell wall synthesis. These findings underscore the diverse modes of action through which antimicrobial FAs interact uniquely with bacterial membranes, disrupting enzymatic activities and exerting broad-spectrum antibacterial effects.

Despite these significant findings, comprehensively understanding how antimicrobial FAs directly or indirectly impact cell membranes remains a challenge. To address this gap, there is a need to develop a robust microbial membrane platform. Such a platform would enable a more comprehensive understanding of the different MOAs and antibacterial potencies of antimicrobial FAs. Subsequently, the primary experimental methodologies utilized to investigate the antimicrobial properties of FAs are explained using microbiological and biophysical approaches. These methodologies are vital for enhancing the comprehension of molecular-level mechanisms of antimicrobial FAs and for guiding the advancement of new antibacterial strategies.

2.2 Biological and Biophysical Studies to Characterize Antimicrobial Fatty Acid Interactions

2.2.1 Biological Assessment of Antimicrobial Fatty Acids

2.2.1.1 Bacteria Inhibition Assay

The assessment of bacterial inhibition by Antimicrobial FAs has been widely researched for their ability to deter bacterial growth, typically measured by bacteriostatic and bactericidal efficacy evaluations. The determination of bacteriostatic efficacy evaluation, also known as minimum inhibitory concentration (MIC), signifies the lowest effective concentration at which a substance hinders bacterial viability, is pivotal in gauging the susceptibility of antimicrobial agents. In the 1970's, Kabara *et al.* pioneered the study

of FAs' antimicrobial attributes by employing the broth dilution method to measure the MIC values of SFAs and MCFAs against *S. aureus* and other pathogens [55, 56]. Subsequent studies have expanded on these initial findings, evaluating the antibacterial potential of polyunsaturated LCFAs (LC-PUFAs) against bacteria such as *Cutibacterium acnes* and *S. aureus*, showcasing inhibitory effects at concentrations ranging from 32 to 1024 mg/L [57]. Additionally, extensive MIC studies have been performed by researchers such as Galbraith [27], Nakatsuji [58], and Kitahara [37]. More recently, researchers delved into the biological activities of FFAs and monoglycerides, accentuating their antimicrobial characteristics and therapeutic applications [5].

Determining the MIC of FAs involves employing diverse methodologies, with agar and broth dilution techniques being predominant. The agar dilution method integrates different FA concentrations into agar media, followed by inoculation with a standardized bacterial suspension. Subsequently, after incubation, MIC method is utilized to identify the lowest concentration of the drug at which visible bacteria are absent. Conversely, the broth dilution method encompasses both macrodilution and microdilution techniques. In broth macrodilution, larger volumes of media are employed, while broth microdilution utilizes microtiter plates for high-throughput screening with reduced volumes. The broth microdilution dilution method, aligned with the Clinical and Laboratory Standards Institute [59], is widely utilized for determining MIC today. Studies highlight the significance of standardized methods and conditions in MIC testing to ensure precise and reliable outcomes. However, MIC values for FAs can exhibit notable variations influenced by factors like broth composition, solvent usage, bacterial cell density, and incubation parameters (e.g., temperature, pH, and duration of incubation). For instance, MIC of LA against *S. aureus* strains has shown a tenfold difference across studies, highlighting the variability in MIC values for this antimicrobial agent [60]. Moreover, discrepancies in reported MIC values for LA in different solvents such as 1% ethanol or 5% dimethyl sulfoxide (DMSO) against *S. aureus* across research groups can exceed 100-fold difference, underscoring the imperative need for standardized testing protocols and appropriate utilization of broth, buffer, and organic solvents to achieve accurate and consistent MIC determinations. Furthermore, the low solubility of FAs and their sensitivity to temperature and pH necessitates meticulous experimental design and adjustments based on the test compound.

Despite the variability in MIC values, it is crucial to recognize that the MIC method does not provide mechanistic insights into the molecular interactions with the bacteria. Therefore, interpreting MIC values should be approached cautiously, considering the limitations and influencing factors inherent in their determination.

2.2.1.2 Time-Kill Kinetic Assay

The time-kill kinetic assay is a fundamental method used to evaluate the bactericidal potency of compounds over time. Hossain and colleagues highlighted the advantages of time-kill kinetics assays in continuously monitoring bacterial growth, offering insights into the kinetics and degree of bactericidal or bacteriostatic effects [61]. Typically, the results are represented as a logarithmic reduction in colony-forming units (CFUs) per milliliter over time, providing a visual representation of bactericidal kinetics. A key measure of bactericidal activity within the assay is the 4 log reduction, signifying a 99.99% decrease in the bacterial population from the initial inoculum. This metric is particularly crucial for assessing the potential efficacy of antimicrobial agents, as it denotes substantial bactericidal activity. Unlike the bacteriostatic measurements obtained from MIC assays, time-kill studies reveal the temporal dynamics of bacterial population changes in response to antimicrobial agents, enabling a more detailed evaluation of their efficacy. Studies have demonstrated effective bacterial eradication within minutes of exposure to specific FAs, showcasing rapid killing of GPB cocci and Chlamydia trachomatis by certain FAs and monoglycerides [62, 63]. Additionally, recent research by Le and colleagues discovered that PUFAs like eicosapentaenoic acid (EPA) swiftly eliminated two GPB bacteria, *Bacillus cereus* and *S. aureus*, within a short timeframe, accompanied by increased release of bacterial cell material [64].

However, while the bactericidal kinetics analysis provides time-dependent insight into the antimicrobial potency of compounds and determines whether the agent exerts a bacteriostatic or bactericidal effect on the bacteria, it encounters some limitations akin to the conventional MIC and MBC methods. In particular, it does not provide comprehensive information on the interactions between the agent and the bacteria at the atomic level.

Despite these challenges, this assay remains crucial for assessing the effectiveness of antimicrobial agents, offering a dynamic perspective that complements the static data from MIC and MBC measurements. It is essential to interpret the results of the kinetics analysis along with other complementary methods, which will be discussed in the next section, to further elucidate the mechanisms of antimicrobial action.

2.2.1.3 Membrane Permeabilization and Intracellular Content Leakage Assays

The membrane permeabilization and leakage assays are two primary biological methods employed to investigate the mechanism of membrane destabilization. Membrane permeabilization assays are used to scrutinize the impact of test agents on the bacterial membranes by quantifying the dye uptake. These assays offer quantitative insights into how the compounds disrupt or permeabilize bacterial membranes, leading to cell death or inhibition of growth. Several techniques have utilized these assays to evaluate the membrane integrity and permeability, focusing on the degree of membrane permeabilization and the discharge of intracellular contents as membrane damage indicators. Parsons *et al.* discovered that UFAs like OA and POA induced rapid membrane depolarization and the release of proteins [65]. Royce *et al.* explored the growth inhibitory impacts of SCFAs on *E. coli* and found that increasing the lipid chain length and the ratio of saturated/unsaturated FAs increases lipid packing efficiency within the membrane. This results in reduced membrane fluidity and intracellular metabolite leakage [66]. These biological assays are essential for understanding the antimicrobial properties of FAs, offering valuable information into the degree of membrane impairment and enhancing the comprehension of how FAs exert their bactericidal effects. However, while these assays offer perspectives on the antimicrobial potency of compounds over time, they do not furnish an intricate comprehension of the underlying interactions between FAs and bacterial membranes. To address this limitation, it is beneficial to combine these assays with biophysical studies. Such integrated approach would not only elucidate the physicochemical basis underlying the MOA but also assist in optimizing the effectiveness of antimicrobial compounds.

2.2.1.4 Electron Microscopy

Electron microcopy (EM) is a crucial imaging technique for studying the interactions between FAs h bacterial membranes due to its high-resolution imaging capabilities. The primary modalities employed in these studies are scanning electron microscopy (SEM) and transmission electron microscopy (TEM). SEM generates images by scanning the sample's surface with a concentrated electron beam, showing surface morphology and topographical changes in bacterial membranes. In contrast, TEM provides detailed images of thin samples by passing electrons through the specimen, revealing intricate details of bacterial membrane structure. These advanced imaging techniques have been instrumental in allowing researchers to observe and characterize the structural changes in bacterial membranes after exposure to various FAs. Several studies have shown that FAs can destabilize bacterial membranes, leading to structural damage and physiological changes. Studies have shown that FAs can disrupt and compromise bacterial membrane integrity [67, 68]. Investigations conducted by Yoon *et al.* have highlighted the morphological alterations induced by antibacterial FAs and their derivates on bacterial membranes, providing valuable insights into the MOAs of these compounds [60]. The use of SEM and TEM has enabled the visualization of specific mechanisms underlying the membrane disruptive effects of FAs. For example, the morphological alterations observed in the cell walls of *B. subtilis* and *E. coli* following exposure to monocaprin are presented in **Figure 2.4**. The distortion in the cell wall of GNB was more pronounced than in GPB, possibly due to monocaprin's ability to adhere to the hydrophobic tail chain of lipopolysaccharide (LPS), facilitating better penetration into the cell membrane and inhibiting bacteria growth [69]. Additionally, **Figure 2.5** illustrates TEM images confirming the leakage of cytoplasmic contents induced by LA [70]. Fischer *et al.* suggested that FAs can disrupt bacterial membranes through mechanisms such as membrane incorporation and lipid interactions, as elucidated through EM observations [71]. Furthermore, Lv *et al.* emphasized how FAs like LLA can lead to the destruction of bacterial cell membranes, a phenomenon directly observable and confirmable through EM imaging techniques [72].

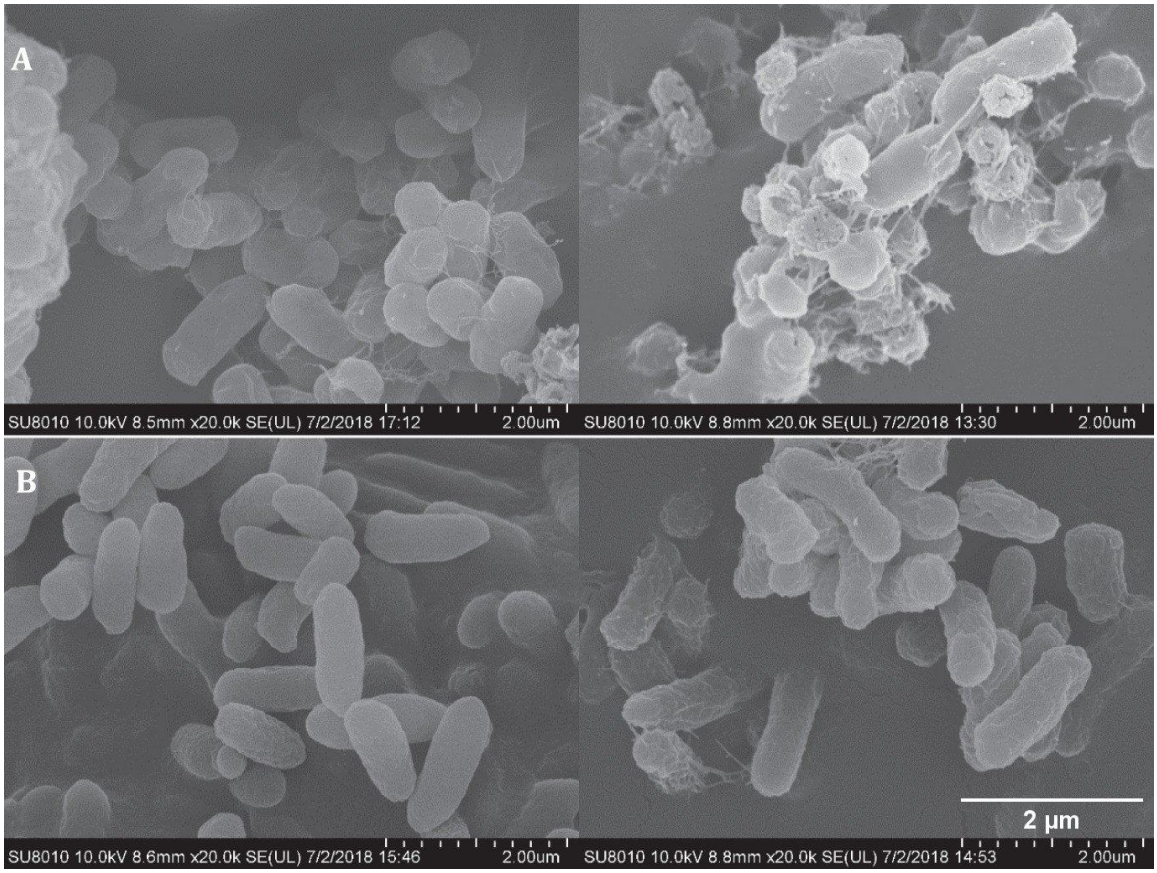

Figure 2.3 SEM images showing effects of monoglyceride derivative against bacterial cell membranes. (A) *B. subtilis* cells treated with monocaprin. (B) *E. coli* cells treated with monocaprin. Reproduced with permission from reference [69]. Scalr

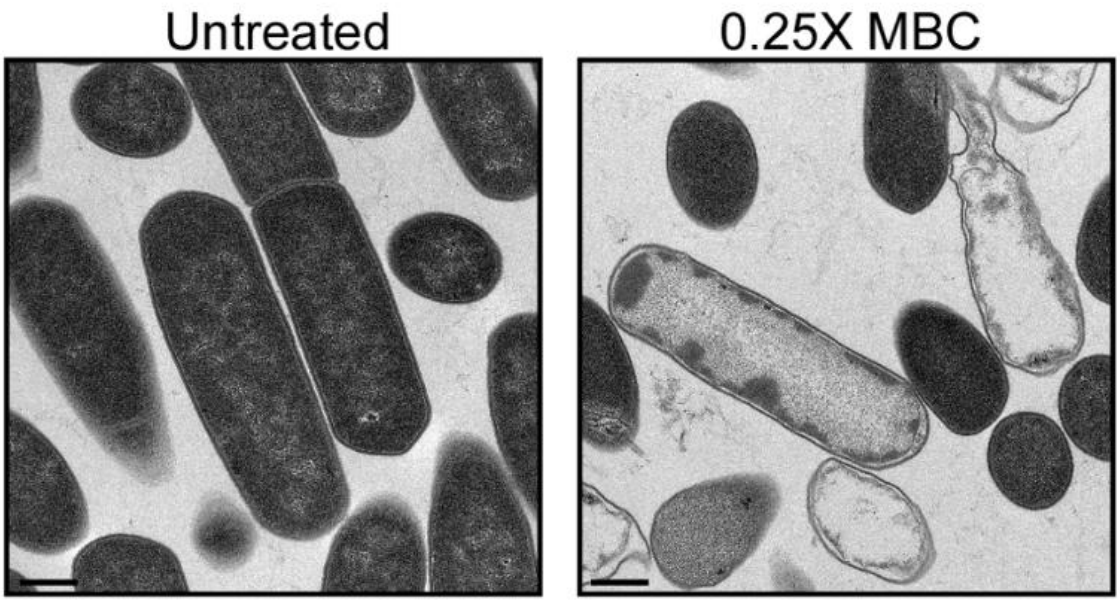

Figure 2.4 TEM images showing effects of fatty acid against bacterial cell membranes. *Clostridium difficile* cells untreated (left) and treated (right) with 0.25x MBC of lauric acid for 15 minutes. Reproduced with permission from reference [70].

Overall, EM techniques have substantially advanced the understanding of FA interactions with bacterial membranes, providing crucial mechanistic insights into morphological changes and mechanistic aspects of membrane disruption. However, gaining deeper mechanistic insights into the effects of FAs remains challenging. To address these limitations, biophysical techniques using model membrane platforms have been developed. These strategies, which will be discussed in the subsequent section, offer additional perspectives on the interactions between FAs and bacterial membranes.

2.2.2 Biophysical Assessment of Antimicrobial Fatty Acids

2.2.2.1 Liposome Assays

Biophysical studies using model lipid membranes, particularly liposomes, have been instrumental in unraveling the mechanisms involved in the interactions of antimicrobial compounds with bacterial cells. Liposomes are artificial vesicles composed of phospholipid bilayers, serving as valuable model membrane platforms for studying the

MOAs of antimicrobial compounds [73]. These model systems mimic the structural and functional characteristics of biological membranes, offering controlled environments for detailed investigations into antimicrobial activities. Liposomes are categorized by their lamellar structure and size into small (SUVs, between 20 and 50 nm), large (LUVs, between 50 and 100 nm), and giant (GUVs, between 10 and 100 μm) unilamellar vesicles, and are constructed from various lipids. These liposome platforms monitor changes in vesicle shape and size upon interaction with antimicrobial drugs using several biophysical techniques. Research by Suguna *et al.* delved into the formation of mixed vesicles containing phospholipids and FAs, specifically focusing on the interaction between specific FAs such as OA and oleate, and phosphocholine (PC) phospholipids. The research explores the impact of varying ratios of OA and oleate to PC on the kinetics and structural characteristics of the vesicles. A significant finding of the study was the observed kinetic effect even at high OA combined with oleate/PC ratios, highlighting the essential role of FA to phospholipid ratio in vesical formation kinetics. The research further delved into the matrix effect in vesicle formation, providing insights into the interaction dynamics inherent in the vesicle formation process [74]. Moreover, research by Rogerson *et al.* focused on investigating the interaction kinetics of FAs with PC vesicles to elucidate the mechanisms and rates of OA, LLA, and CA associations with an impact on phospholipid vesicles. These findings offer insights into the binding kinetics, structural changes, and stability alterations when FAs interact with phospholipid vesicles. Understanding the kinetics of these interactions is essential for comprehending how FAs may influence membrane properties, permeability, and overall membrane behavior. While liposomes serve as valuable instruments for research, they present obstacles for in-depth biophysical interaction investigations. Some of the challenges include controlling lipid composition [75] and difficulty in forming liposomes using lipids with high transition temperatures that are present in bacterial membranes [76].

2.2.2.2 Supported Lipid Bilayer Assays

Supported lipid bilayer assays, also known SLBs, are a robust model membrane system essential for exploring the interactions of antimicrobial agents with model

membranes. SLBs consist of a lipid bilayer anchored to a hydrophilic solid substrate, offering significant insights into the MOA of antimicrobial agents. SLBs offers a significant benefit in their ability to work seamlessly with a diverse range of surface-sensitive analytical methods, allowing for in-depth investigation into drug-membrane interaction kinetics. Numerous studies have utilized SLBs to study membrane-disruptive behaviors, lipid-membrane interactions, protein-membrane interactions, and other processes relevant to antimicrobial research. For instance, Thid *et al.* explored the impact of docosahexaenoic acid (DHA) on SLB membrane morphology using quartz crystal microbalance with dissipation (QCM-D). Their research emphasized the importance of employing multiple techniques to comprehensively characterize viscoelastic property alterations of the membrane induced by DHA. This highlights the need to comprehend DHA's influence on membrane morphology and the benefit of using complementary methods for a comprehensive analysis of membrane modifications [77]. Similarly, Yoon *et al.* investigated the diverse morphological changes triggered by FAs using QCM-D and fluorescence microscopy techniques. Their study explored how SFAs and related surfactants disrupt lipid bilayers, providing detailed insights into the mechanisms underlying these changes. This study enhances the understanding of how these compounds destabilize lipid membranes and offers valuable insights into the mechanisms governing the morphological responses of membranes to antibacterial agents. This investigation significantly contributes to enhancing the comprehension of how membrane-active compounds interact with lipid bilayers, elucidating the mechanisms through which these agents impact membrane morphology [78]. Valle-González *et al.* explored how low pH impact the membrane interactions of LA and GML using SLBs. This study underscores the importance of environmental factors in modulating antimicrobial activities and provides insights into the behavior of these compounds under acidic conditions. Moon *et al.* explored the impact of membrane activities of FAs on the membrane curvature of the SLBs and the utility of SLBs in evaluating membrane-disruptive mechanisms [79]. Collectively, these studies validate the utility of SLBs for investigating concentration-dependent interaction studies. Nevertheless, these findings motivate for further exploration of antimicrobial lipids, with future research opportunities outlined in subsequent section.

2.3 Nanotechnology Formulations with Fatty Acids

2.3.1 Liposomes

Despite the beneficial biological activities of antimicrobial FAs, several practical challenges hinder their clinical application. One major obstacle is their low aqueous solubility [80]. Nanoscale formulation strategies, such as liposomes, have been employed to enhance the antimicrobial potential of FAs and augment their interaction with bacterial membranes [81]. Liposomes, spherical vesicles comprised of lipid bilayers enclosing an aqueous core, can encapsulate FAs, thereby improving their solubility and antimicrobial efficacy. These vesicular systems, which typically rang in size from 50 to 300 nm, have emerged as promising strategies for combating bacterial infections as they are known to evade nonenzymatic resistance mechanism. Numerous studies have explored the antimicrobial potential of FA-loaded liposomes (LipoFAs), elucidating their MOAs and efficacy against various pathogens. Huang *et al.* gauged the therapeutic efficacy of OA-loaded liposomes (LipoOA) against MRSA [82]. Their study demonstrated that LipoOA fused with the membrane surface of the bacteria, improving the effectiveness of OA in killing MRSA compared to its free form. Jung *et al.* developed innovative LipoFA formulations, including SA (LipoSA), OA (LipoOA), and LNA (LipoLNA), which demonstrated strong capacity to eradicate antibiotic-resistant strains of *H. pylori* [83]. This study found that LipoLNA exhibited the strongest antimicrobial activity against *H. pylori*, increasing membrane permeability and causing cytoplasmic content leakage, as observed through TEM and SEM images. Pornpattananangkul *et al.* revealed the potency of LA loaded liposomes (LipoLA) in combating *Propionibacterium acnes* infections [84]. Their research demonstrated membrane fusogenic and disruptive activites of LipoLA at physiological pH, without causing toxicity to skin tissues. In comparison, benzoyl peroxide and salicylic acid caused mild to intense skin irritation. These observations indicate that LipoLA holds significant therapeutic promise as a treatment for acne and other conditions associated with *P. acnes.*

2.3.2 Emulsions

Nanoemulsions, which are oil-in-water (o/w) emulsion droplets ranging from 50-100 nm, are known for improving the solubility and stability of FAs. These emulsion systems have an oily core encased in a layer of surfactants that stabilize the system and maintain the small droplet size essential for effective antimicrobial action. Numerous studies have examined the antimicrobial capabilities of nanoemulsion-based FAs. For instance, Pimple *et al.* explored the antibacterial impact of nanoemulsion formulation based on plant essential oils against various pathogens, showcasing enhanced antimicrobial efficacy against pathogens like *E. coli*, *B. subtilis*, *Salmonella typhimurium* [85]. Another study investigated a new emulsion containing thymol and LA, discovering that the addition of LA boosted the antibacterial efficacy against *Listeria monocytogenes* [86]. Additionally, nanoemulsion formulations incorporating MA, liquid FAs, and surfactants were synthesized for antimicrobial purposes. Research by Rehman *et al.* demonstrated that the formulation containing both MA and OA exhibited the highest antimicrobial effect against both GPB and GNB [87]. However, a notable drawback of nanoemulsions is the substantial amount of surfactant required, which can potentially lead to toxicity [88].

2.3.3 Nanostructured Lipid Carriers

Nanostructured lipid carrier (NLCs) formulations incorporating FAs are an emerging nanotechnology-based strategy for combating bacterial infections. NLCs represent an advanced form of solid lipid nanoparticles (SLNs). Unlike SLNs, which are prone to solidification and gradual crystallization during storage, potentially leading to the expulsion of active substances[89], NLCs are synthesized from mixtures of SA derived solid lipids and OA derived liquid lipids with particle sizes ranging from 50-300 nm [90]. This composition imparts greater stability and versatility to NLCs, making them highly effective for antimicrobial applications. Several studies have explored the antimicrobial potential of FA-containing NLCs. Pires *et al.* developed NLCs containing essential oils that maintained high stability after long duration of storage at room temperature. These NLCs exhibited potent inhibitory effects against multidrug-resistant strains of

Campylobacter spp. [91]. This study highlights the potential of NLCs to maintain their antimicrobial efficacy over extended periods, which is crucial for practical applications. Another study examined NLCs loaded with DHA. These DHA-loaded NLCs demonstrated significantly stronger inhibitory effects against *H. pylori* compared to free DHA [92]. This increased efficacy is due to improve solubility of DHA when encapsulated in NCLs, which allows for better interaction with bacterial membranes and prolonged antimicrobial activity.

2.4 Outstanding Questions

2.4.1 Relationship between Biophysical Membrane Interaction Insights and Biological Experiments

Research on antimicrobial LCFAs and LipoFAs has primarily focused on their antibacterial activity against specific bacteria. These studies have aimed to characterize the antimicrobial potency based on FA structure. Despite employing diverse methods and experimental conditions, the field lacks a comprehensive understanding of the mechanisms through which antimicrobial lipids exert their effects. Although it is known that these lipids primarily target bacterial membranes, the precise mechanisms underlying their relative potencies and interactions with bacterial membranes remain unclear. Key questions include whether the effectiveness of an antimicrobial FA is linked to critical micelle concentration (CMC) and their affinity for phospholipid membranes relevant to bacterial membrane, and how this insight translates to the antimicrobial efficacy of liposomes when loaded with FAs. The interpretation of existing studies is further complicated by the diverse experimental designs, often influenced by the intended application of the antimicrobial lipid. Moreover, when these lipids are tested against clinically relevant bacteria, the focus is on determining either bacteriostatic and bactericidal effects. These differences in testing methods highlight the need for a more systematic approach that integrates biophysical and biological analyses to comprehend how the self-assembly properties of FAs affect their interactions with model membranes and real bacteria. It is also crucial to investigate how different FAs in liposomes affect the bacterial membrane upon incorporation. Further questions include how these biophysical membrane interaction insights correlate with biological activities like MIC,

membrane permeabilization, and intracellular ATP leakage. By establishing a model bacterial membrane platform and employing biophysical techniques to explain the MOAs of LCFAs and LipoFAs, it is possible to connect these findings to biological activities. Integrating biophysical and biological insights can greatly enhance the understanding of how antimicrobial lipids function, thereby improving their application in fighting bacterial infections.

2.4.2 Relationship Between the Physicochemical Property Differences of Fatty Acids, Liposomal Fatty Acids, and Model Bacterial Membranes

Research indicates that UFAs generally have greater antibacterial potency than SFAs, with OA being more effective than LNA. Additionally, liposomes containing OAs are reported to be more potent than liposomes containing LNA against certain bacterial strains. However, there is no clear explanation for why OA is more potent than LNA, or why LipOA is more potent than LipoLNA. One hypothesis is that at neutral pH, the carboxylic acid moiety of FAs becomes deprotonated, giving the FA surfactant-like properties that enable these acids to disrupt bacterial membranes. Another theory suggests that LipoLNA, with its highly kinked FA structure, has high antibacterial potency due to the increased membrane fluidity it causes when incorporated into the bacterial membrane through membrane fusion. However, these explanations do not fully account for the specific mechanisms by which FAs interact with bacterial membranes, how the different physicochemical attributes of bacterial membranes affect LCFA or LipoFA interactions, or the degree of impact these agents have on the bacterial membrane. To better address these gaps, it is crucial to employ biophysical approaches that can elucidate how the physicochemical attributes such as unsaturation degree, dissociation constant (p*K*a), and CMC values influence their antibacterial effectiveness. By exploring these connections, it is possible to gain deeper insights into how these properties translate into specific effects on bacterial membranes, thereby improving the comprehension of the antibacterial mechanisms of FAs.

2.4.3 Comparison Between Bacterial Membranes and Supported Lipid Bilayers

Supported lipid bilayers (SLBs) serve as simplified yet effective models for studying bacterial membrane interactions due to their structural and functional similarities. Both SLBs and bacterial membranes are phospholipid bilayers that maintain fluidity and semi-permeability, essential for cellular integrity and selective transport. SLBs can replicate critical features of bacterial membranes, including lipid lateral mobility and the incorporation of specific lipid types, enabling studies on lipid-protein interactions, membrane mechanics, and antimicrobial effects [93, 94]. Their utility is enhanced by compatibility with analytical methods such as quartz crystal microbalance (QCM-D) and fluorescence microscopy, allowing precise control over lipid composition to isolate factors such as charge, packing, and fluidity [100, 101]. However, bacterial membranes are more complex, comprising diverse lipid species (e.g., cardiolipin, phosphatidylglycerol, and phosphatidylethanolamine), asymmetric lipid distribution, and unique structural components like the peptidoglycan layer in Gram-positive bacteria or lipopolysaccharide-rich outer membranes in Gram-negative bacteria [94, 96, 97, 99]. These features, absent in SLBs, influence membrane properties and antimicrobial responses, highlighting SLB limitations as comprehensive models [98, 103]. Despite these differences, SLBs remain invaluable for dissecting specific membrane interactions. In this research, SLBs are employed to study long-chain fatty acids (LCFAs) and their interactions with membrane components, providing foundational insights into the physicochemical mechanisms underlying antimicrobial activity. Complementary studies on intact bacterial membranes are essential for capturing the complexity of natural systems, ensuring a robust understanding of membrane dynamics and informing the translation of findings to biological contexts [94, 104].

References

[1] R. Koch. *Mitt. ksl. Gesundheitsamt*. **1881**, 1, 234.

[2] J. Burtenshaw. *Epidemiology & Infection*. **1942**, 42(2), 184-210.

[3] R. Aminov. *Frontiers in Microbiology*. **2010**, 1.

[4] P. Kumar, S. Bag, T.S. Ghosh, P.K. Dey, M. Dayal, B. Saha, J. Verma, A. Pant, S. Saxena, A. Desigamani, P. Rana, D. Kumar, N. Sharma, P. Hanpude, T.K. Maiti, A.K. Mukhopadhyay, R.K. Bhadra, G.B. Nair, T. Ramamurthy, B. Das. *Scientific Reports*. **2017**, 7(1).

[5] B.K. Yoon, J.A. Jackman, E.R. Valle-González, N.J. Cho. *International Journal of Molecular Sciences*. **2018**, 19(4), 1114.

[6] J.J. Kabara. *Journal of Food Protection*. **1981**, 44(8), 633-647.

[7] B.K. Yoon, J.A. Jackman, E.R. Valle-González, N.-J. Cho. *International Journal of Molecular Sciences*. **2018**, 19(4), 1114.

[8] L. McGaw, A. Jäger, J. Van Staden. *South African Journal of Botany*. **2002**, 68(4), 417-423.

[9] H. Thormar. *Lipids and essential oils as antimicrobial agents*. **2010**.

[10] A.P. Desbois, V.J. Smith. *Appl Microbiol Biotechnol*. **2010**, 85(6), 1629-42.

[11] C.P. Churchward, R.G. Alany, L.A.S. Snyder. *Critical Reviews in Microbiology*. **2018**, 44(5), 561-570.

[12] S. Wolfrum, J. Marcus, D. Touraud, W. Kunz. *Advances in Colloid and Interface Science*. **2016**, 236, 28-42.

[13] A. Arnould, A.A. Perez, C. Gaillard, J.-P. Douliez, F. Cousin, L.G. Santiago, T. Zemb, M. Anton, A.-L. Fameau. *Journal of Colloid and Interface Science*. **2015**, 445, 285-293.

[14] D.P. Cistola, J.A. Hamilton, D.S. Jackson, D. *Biochemistry*. **1988**, 27(6), 1881-1888.

[15] J.R. Kanicky, D.O. Shah. *Journal of Colloid and Interface Science*. **2002**, 256(1), 201-207.

[16] W.F. Bennett, A.W. Chen, S. Donnini, G. Groenhof, D.P. Tieleman. *Canadian Journal of Chemistry*. **2013**, 91(9), 839-846.

[17] S. Škulj, M. Vazdar. *Physical Chemistry Chemical Physics*. **2019**, 21(19), 10052-10060.

[18] A.A. Pashkovskaya, M. Vazdar, L. Zimmermann, O. Jovanovic, P. Pohl, E.E. Pohl. *Biophysical Journal*. **2018**, 114(9), 2142-2151.

[19] G. Bergsson, J. Arnfinnsson, Ó. Steingrímsson, H. Thormar. *APMIS*. **2001**, 109(10), 670-678.

[20] J.J. Kabara, D.M. Swieczkowski, A.J. Conley, J.P. Truant. *Antimicrobial Agents and Chemotherapy*. **1972**, 2(1), 23-28.

[21] E. Freese, C.W. Sheu, E. Galliers. *Nature*. **1973**, 241(5388), 321-325.

[22] C.J. Zheng, J.-S. Yoo, T.-G. Lee, H.-Y. Cho, Y.H. Kim, W.G. Kim. *FEBS Letters*. **2005**, 579(23), 5157-5162.

[23] K. Siram, S.M. Habibur Rahman, K. Balakumar, N. Duganath, R. Chandrasekar, R. Hariprasad. In *Chapter 4 - Pharmaceutical nanotechnology: Brief perspective on lipid drug delivery and its current scenario, A.M. Grumezescu (Ed.), Biomedical Applications of Nanoparticles*, William Andrew Publishing2019, pp. 91-115.

[24] M.P. Doss. In *Properties of the principal fats, fatty oils, waxes, fatty acids, and their salts*, The Texas Company1952.

[25] A.J. Conley, J.J. Kabara. *Antimicrob Agents Chemother*. **1973**, 4(5), 501-6.

[26] P.B. Heczko, R. Lütticken, W. Hryniewicz, M. Neugebauer, G. Pulverer. *J Clin Microbiol*. **1979**, 9(3), 333-5.

[27] H. Galbraith, T.B. Miller, A.M. Paton, J.K. Thompson. *Journal of Applied Bacteriology*. **1971**, 34(4), 803-813.

[28] H.R. Knapp, M.A. Melly. *J Infect Dis*. **1986**, 154(1), 84-94.

[29] T. Nakatsuji, M.C. Kao, J.Y. Fang, C.C. Zouboulis, L. Zhang, R.L. Gallo, C.M. Huang. *J Invest Dermatol*. **2009**, 129(10), 2480-8.

[30] H.G. Preuss, B. Echard, M. Enig, I. Brook, T.B. Elliott. *Mol Cell Biochem*. **2005**, 272(1-2), 29-34.

[31] G. Bergsson, O. Steingrímsson, H. Thormar. *Int J Antimicrob Agents*. **2002**, 20(4), 258-62.

[32] H. Thormar, G. Bergsson, E. Gunnarsson, G. Georgsson, M. Witvrouw, O. Steingrímsson, E. De Clercq, T. Kristmundsdóttir. *Sex Transm Infect*. **1999**, 75(3), 181-5.

[33] B.W. Petschow, R.P. Batema, L.L. Ford. *Antimicrob Agents Chemother*. **1996**, 40(2), 302-6.

[34] G. Bergsson, O. Steingrímsson, H. Thormar. *Antimicrob Agents Chemother*. **1999**, 43(11), 2790-2.

[35] G. Bergsson, H. Hilmarsson, H. Thormar. In *Antibacterial, Antiviral and Antifungal Activities of Lipids, Lipids and Essential Oils*, Antimicrobial Agents2011, pp. 47-80.

[36] G. Bergsson, J. Arnfinnsson, O. Steingrímsson, H. Thormar. *APMIS*. **2001**, 109(10), 670-8.

[37] T. Kitahara, N. Koyama, J. Matsuda, Y. Aoyama, Y. Hirakata, S. Kamihira, S. Kohno, M. Nakashima, H. Sasaki. *Biological and Pharmaceutical Bulletin*. **2004**, 27(9), 1321-1326.

[38] L.L. Wang, E.A. Johnson. *Appl Environ Microbiol*. **1992**, 58(2), 624-9.

[39] M. Feldlaufer, D. Knox, W. Lusby, H. Shimanuki. *Apidologie*. **1993**, 24(2), 95-99.

[40] H. Thormar, H. Hilmarsson, G. Bergsson. *Appl Environ Microbiol*. **2006**, 72(1), 522-6.

[41] S.-R. Won, M.-J. Hong, Y.-M. Kim, C.Y. Li, J.-W. Kim, H.-I. Rhee. *FEBS Letters*. **2007**, 581(25), 4999-5002.

[42] H. Arellano, V. Nardello-Rataj, S. Szunerits, R. Boukherroub, A.-L. Fameau. *Advances in Colloid and Interface Science*. **2023**, 318, 102952.

[43] P. Mitchell. *Nature*. **1961**, 191(4784), 144-148.

[44] P. Borst, J.A. Loos, E.J. Christ, E.C. Slater. *Biochim Biophys Acta*. **1962**, 62, 509-18.

[45] M.R. Wieckowski, L. Wojtczak. *FEBS Letters*. **1998**, 423(3), 339-42.

[46] M. Marounek, V. Skřivanová, O. Savka. *Journal of Animal and Feed Sciences*. **2002**, 11(3), 507-516.

[47] C.W. Sheu, E. Freese. *J Bacteriol*. **1972**, 111(2), 516-24.

[48] P. Boyaval, C. Corre, C. Dupuis, E. Roussel. *Le Lait*. **1995**, 75(1), 17-29.

[49] N.R. Chamberlain, B.G. Mehrtens, Z. Xiong, F.A. Kapral, J.L. Boardman, J.I. Rearick. *Infect Immun*. **1991**, 59(12), 4332-7.

[50] D.L. Greenway, K.G. Dyke. *J Gen Microbiol*. **1979**, 115(1), 233-45.

[51] T. Tsuchido, T. Hiraoka, M. Takano, I. Shibasaki. *J Bacteriol*. **1985**, 162(1), 42-6.

[52] M.C. Mansilla, L.E. Cybulski, D. Albanesi, D. de Mendoza. *J Bacteriol*. **2004**, 186(20), 6681-8.

[53] C.J. Zheng, J.S. Yoo, T.G. Lee, H.Y. Cho, Y.H. Kim, W.G. Kim. *FEBS Letters*. **2005**, 579(23), 5157-62.

[54] H. Kurihara, Y. Goto, M. Aida, M. Hosokawa, K. Takahashi. *Fisheries Science*. **1999**, 65(1), 129-132.

[55] J.J. Kabara, R. Vrable. *Lipids*. **1977**, 12(9), 753-9.

[56] J.J. Kabara. *J Soc Cosmet Chem*. **1978**, 29:733–741..

[57] A.P. Desbois, K.C. Lawlor. *Marine Drugs*. **2013**, 11(11), 4544-4557.

[58] T. Nakatsuji, M.C. Kao, J.-Y. Fang, C.C. Zouboulis, L. Zhang, R.L. Gallo, C.-M. Huang. *Journal of Investigative Dermatology*. **2009**, 129(10), 2480-2488.

[59] M.A. Wikler. *CLSI (NCCLS)*. **2006**, 26.

[60] B.K. Yoon, J.A. Jackman, M.C. Kim, N.J. Cho. *Langmuir*. **2015**, 31(37), 10223-10232.

[61] T.J. Hossain. *European Journal of Microbiology and Immunology*. **2024**, 14(2), 97-115.

[62] G. Bergsson, J. Arnfinnsson, Ó. Steingrímsson, H. Thormar. *APMIS*. **2001**, 109(10), 670-678.

[63] G. Bergsson, J. Arnfinnsson, S.M. Karlsson, Ó. Steingrímsson, H. Thormar. *Antimicrobial Agents and Chemotherapy*. **1998**, 42(9), 2290-2294.

[64] P.N.T. Le, A.P. Desbois. *Marine Drugs*. **2017**, 15(11), 334.

[65] J.B. Parsons, J. Yao, M.W. Frank, P. Jackson, C.O. Rock. *Journal of Bacteriology*. **2012**, 194(19), 5294-5304.

[66] L.A. Royce, P. Liu, M.J. Stebbins, B.C. Hanson, L.R. Jarboe. *Applied Microbiology and Biotechnology*. **2013**, 97(18), 8317-8327.

[67] S.K. Yang, K. Yusoff, M. Ajat, C.-Y. Wee, P.S.X. Yap, S.H.E. Lim, K.S. Lai. *Frontiers in Microbiology*. **2021**, 12.

[68] H. Galbraith, T.B. Miller. *Journal of Applied Bacteriology*. **1973**, 36(4), 647-658.

[69] W. Wang, R. Wang, G. Zhang, F. Chen, B. Xu. *Journal of Food Protection*. **2020**, 83(2), 331-337.

[70] H.-T. Yang, J.-W. Chen, J. Rathod, Y.-Z. Jiang, P.-J. Tsai, Y.-P. Hung, W.-C. Ko, D. Paredes-Sabja, I.-H. Huang. *Frontiers in Microbiology*. **2018**, 8.

[71] C.L. Fischer, K.S. Walters, D.R. Drake, D.V. Dawson, D.R. Blanchette, K.A. Brogden, P.W. Wertz. *International Journal of Oral Science*. **2013**, 5(3), 130-140.

[72] H. Lv, D. Ren, W. Yan, Y. Wang, H. Liu, M. Shen. *Journal of the Science of Food and Agriculture*. 2020, 100(5), 2057-2064.

[73] G. Sessa, G. Weissmann. *Journal of Lipid Research*. **1968**, 9(3), 310-318.

[74] L. Suguna, P.L. Luisi, P. Walde, B.H. Robinson. *The Journal of Physical Chemistry B*. **1999**, 103(49), 10910-10916.

[75] E. Rideau, R. Dimova, P. Schwille, F.R. Wurm, K. Landfester. *Chemical Society Reviews*. **2018**, 47(23), 8572-8610.

[76] M.d. Vestergaard, T. Hamada, M. Takagi. *Biotechnology and Bioengineering*. **2008**, 99(4), 753-763.

[77] D. Thid, J.J. Benkoski, S. Svedhem, B.H. Kasemo, J. Gold. *Langmuir*. **2007**, 23(11), 5878-5881.

[78] B.K. Yoon, J.A. Jackman, M.C. Kim, N.-J. Cho. *Langmuir*. **2015**, 31(37), 10223-10232.

[79] S. Moon, B.K. Yoon, J.A. Jackman. *Langmuir*. **2022**, 38(15), 4606-4616.

[80] Q. Zhang, W. Wu, J. Zhang, X. Xia. *Journal of Drug Targeting*. **2020**, 28(3), 271-281.

[81] R. Ghosh, M. De. *ACS Omega*. **2023**, 8(39), 35442-35451.

[82] C.M. Huang, C.H. Chen, D. Pornpattananangkul, L. Zhang, M.D. Chan, M.F. Hsieh, L. Zhang. *Biomaterials*. **2011**, 32(1), 214-221.

[83] S.W. Jung, S. Thamphiwatana, L. Zhang, M. Obonyo. *PLOS ONE*. **2015**, 10(3), e0116519.

[84] D. Pornpattananangkul, V. Fu, S. Thamphiwatana, L. Zhang, M. Chen, J. Vecchio, W. Gao, C.-M. Huang, L. Zhang. *Advanced Healthcare Materials*. **2013**, 2(10), 1322-1328.

[85] V. Pimple*, A.G. Kulkarni, S. Patil, S.J. Dhoble. *International Journal of Innovative Technology and Exploring Engineering*. **2019**, 9(1), 4800-4808.

[86] Q. Cai, Y. Zhang, X. Fang, S. Lin, Z. He, S. Peng, W. Liu. *Front Nutr*. **2022**, 9, 859293.

[87] M. Rehman, A. Arshad, M.A. Madni. *Global Pharmaceutical Sciences Review*. **2017**, 2, 1-9.

[88] S. Begum Jp, P. Sahu, R. Vinode, A. Patel, M.N. Alomary, M.Y. Begum, Y.F. Jamous, A. Siddiqua, A.A. Fatease, M.A. Ansari. *Journal of Saudi Chemical Society*. **2024**, 28(4), 101896.

[89] K. Westesen, H. Bunjes, M.H.J. Koch. *Journal of Controlled Release*. **1997**, 48(2), 223-236.

[90] B. Subramaniam, Z.H. Siddik, N.H. Nagoor. *Journal of Nanoparticle Research*. **2020**, 22, 1-29.

[91] H.M. Pires, L.M. Bastos, E.F. da Silva, B.B. Fonseca, S. Sommerfeld, R.J. de Oliveira Junior, L.N.d.M. Ribeiro. *Pharmaceutics*. **2024**, 16(7), 922.

[92] C.L. Seabra, C. Nunes, M. Gomez-Lazaro, M. Correia, J.C. Machado, I.C. Gonçalves, C.A. Reis, S. Reis, M.C.L. Martins. *International Journal of Pharmaceutics*. **2017**, 519(1-2), 128-137.

[93] N. Paracini, P. Gutfreund, R. J. L. Welbourn, J. F. Gonzalez-Martinez, K. Zhu, Y. Miao, N. R. Yepuri, T. A. Darwish, C. J. Garvey, S. Waldie. *ACS Applied Materials & Interfaces*. **2023**, 15 (3), 3772-3780.

[94] X. Li, A. W. Smith. *The Journal of Physical Chemistry B*. **2019**, 123 (49), 10433-10440.

[95] A. Poursoroush, M. M. Sperotto, M. Laradji. *The Journal of Chemical Physics*. **2017**, 146 (15).

[96] Q. Wang, B. Peng, M. Song, M. A. Khan, J. Li, J. Miao, K. Feng, F. Chen, X. Zhai, Y. Cao. *Frontiers in Nutrition*. **2021**, 8.

[97] J. Li, Z. Shen, D. Wang, B.Z. Tang. *ACS Nano*. **2023**, 17 (5), 4239-4249.

[98] S. Varma, M. Teng, H. L. Scott. *Langmuir*. **2012**, 28 (5), 2842-2848.

[99] A. Mai‐Prochnow, M. Clauson, J. Hong, A. B. Murphy. *Scientific Reports*. **2016**, 6 (1).

[100] B. Bechinger. *Encyclopedia of Biophysics*. **2013**, 2522-2528.

[101] S.F. Gilmore, H. Nanduri, A. N. Parikh. *PLOS One*. **2011**, 6 (12), e28517.

[102] F. Harb, B. Tinland. *Langmuir*. **2013**, 29 (18), 5540-5546.

[103] J. Zhong, D. He. *Chemistry - A European Journal*. **2012**, 18 (14), 4148-4155.

[104] A. H. Kycia, J. Wang, A. R. Merrill, J. Lipkowski. *Langmuir*. **2011**, 27 (17), 10867-10877.

Chapter 3

Experimental Methodology

Chapter 3 outlines the research approach employed in this thesis, encompassing materials, materials synthesis, and experimental techniques. This chapter begins with explaining the rationale for the selected experimental strategies, followed by a summary of the materials used. The chapter then thoroughly describes the various experimental techniques used to measure critical micelle concentrations of unsaturated long-chain fatty acids, the interaction of antimicrobial fatty acids and fatty acid loaded liposomes with neutral and charged supported lipid bilayers, and their biological effects against antibiotic-resistant bacteria, including their killing effect, membrane permeabilization, and ATP leakage. The chapter also delves into the optimization process for fabricating a model bacterial membrane and the analysis of membrane interaction using complementary surface-sensitive techniques. By integrating these approaches, the research seeks to provide a holistic comprehension of the interactions between these antimicrobial agents and bacterial membranes, ultimately contributing to the advancement of more effective antimicrobial strategies.

3.1 Rationale for Selection

In this thesis, the experimental approach revolves around Materials, Materials Synthesis, and Experimental Methodologies. The main objective is to develop a testing platform for antimicrobial lipids that closely resembles clinically relevant GPB. This platform is designed to enhance the biophysical comprehension of the mechanisms of antimicrobial lipids and establish connections between these mechanisms and their biological impacts on bacteria. While existing research has primarily concentrated on investigating structure-activity relationships and their inhibitory or bactericidal effects on bacteria, as well as the morphological impacts on bacterial membrane physiology, these approaches often fall short in characterizing and explaining the underlying atomic-level interactions with membranes. By establishing a membrane platform relevant to bacteria, it becomes feasible to monitor the drug-membrane interactions in real-time. Past research has validated the utility of SLBs as an interfacial science platform tool for investigating the MOAs of antimicrobial FAs such as LA, CA, and DHA. However, these studies have predominantly utilized single-component SLBs, which may not accurately represent bacterial membranes. This project aims to use multiple-component SLBs that mirror the lipid compositions of GPB, specifically *S. aureus*, to understand how the physicochemical factors govern the antimicrobial effectiveness of antimicrobial FAs and liposomes. A critical component of this study is the inclusion of Lysyl-PG in the SLBs, which is a key lipid in the cell membranes of GPB. Lysyl-PG imparts a positive charge to the bacterial cell envelope, creating an electrostatic barrier that helps bacteria resist cationic compounds. By incorporating Lysyl-PG into the SLB model, the study aims to better replicate the unique physicochemical properties of GPB membranes and explore how this lipid influences the interactions of antimicrobial agents with bacterial membranes, providing deeper insights into their MOA.

The materials used in this project encompass amphiphilic LCFAs, phospholipids, cholesterol, functional lipids, buffer reagents, bacterial cell strain, and consumables for antibacterial testing, membrane permeabilization testing, and ATP leakage testing. Sample preparation involves FA solutions, liposome solutions, SLB fabrication, and bacterial cell cultures. Phospholipids and cholesterol were used to make liposomes, phospholipids with

different charges are used to fabricate SLBs, and methicillin-resistant strains of *S. aureus* for biological studies.

Detailed descriptions of the experimental techniques and their principles are provided. CMC values of LCFAs are measured using fluorescence probe spectroscopy method. The utilization of QCM-D enables the exploration of the concentration-dependent interactions of FAs and FA-loaded liposomes with SLBs, with a correlation made between the former observations and the CMC values. Morphological changes in SLBs induced by these agents are monitored using fluorescence microscopy, which complements the results obtained from QCM-D. FRAP technique is utilized to assess changes in membrane fluidity of SLBs upon interaction with LipoFAs. Additionally, QCM-D and FRAP methods are utilized to optimize and characterize the membrane formation of model bacterial SLBs. Biological activities, such as MICs, time-killing assays, membrane permeabilization, and intracellular leakage are determined to complement the biophysical experiments. Establishing correlations between biophysical membrane interactions and biological activities provides insights into the underlying physicochemical behavior of antimicrobial FAs and LipoFAs, providing a systematic approach to enhance and optimize antimicrobial efficacy for future applications in combating bacterial infections.

3.2 Materials

3.2.1 Long-Chain Fatty Acids (LCFAs)

LNA, LLA, and OA were obtained from Sigma-Aldrich (St Louis, MO) and stored at –20°C to main stability until needed for experiments. These LCFAs, LNA, LLA, and OA, each have 18-carbon long unsaturated hydrocarbon chains that are susceptible oxidation and may have altered biological activity. Just before each experiment, precise quantities of LCFAs are measured. After transferring them to vials, they are promptly stored back in the freezer to minimize exposure to light and air. The mentioned FA's chemical structures are illustrated in **Figure 3.1**, showing them in their protonated state, though they can also exist in a deprotonated form depending on environmental conditions.

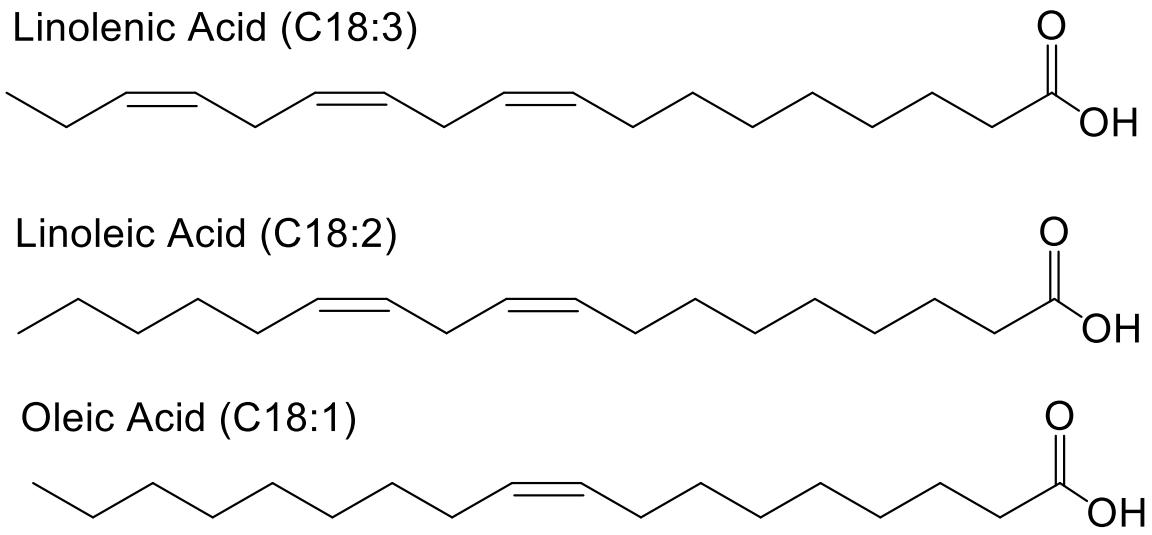

Figure 3.1 Chemical structures of long-chain fatty acids used in this thesis

3.2.2 Phospholipid and Probe Reagents

1,2-dioleoylsn-glycero-3-phosphocholine (DOPC), 1-palmitoyl-2-oleoyl-*sn*-glycero-3-phospho-(1′-*rac*-glycerol) (POPG), 1,2-dipalmitoyl-sn-glycero-3-[phospho-rac-(3-lysyl(1-glycerol))] (Lysyl-PG), 1′,3′-bis[1-Palmitoyl-2-oleoyl-sn-glycero-3-phospho]-glycerol (Cardiolipin, CL), 1,2-dioleoyl-sn-glycero-3-phosphoethanolamine-N-(lissamine rhodamine B sulfonyl) (ammonium salt) (Rh-PE), L-α-phosphatidylcholine (Egg PC), cholesterol (ovine wool, >98%), and 6-Dodecanoyl-N,N-dimethyl-2-naphthylamine (Laurdan) were obtained from Avanti Polar Lipids (Alabaster, AL) (**Figure 3.2**). Neutrally charged single-component SLBs were fabricated using neutrally charged DOPC lipids (phase transition temperature (T_m) = -17 °C [1]) at room temperature. Multi-component SLBs that mimic the bacterial membrane of *S. aureus* were fabricated using anionic POPG lipids (T_m = -2 °C [2]), cationic Lysyl-PG lipids (T_m = 40 °C [3]), and anionic CL lipids (T_m = 62.2 °C [4]). Tabaei and colleagues previously employed solvent-assisted lipid bilayer (SALB) method to produce SLBs with charged lipids [5]. Building on their work, this thesis also utilizes the SALB method to fabricate bacterial membranes. Egg PC, cholesterol, and LCFAs were used to prepare LipoFA samples. For fluorescence microscopy studies, Rh-PE fluorophore, a negatively charged synthetic lipid that shares similar structure as DOPC, was incorporated into the SLBs. Laurdan, a polarity-sensitive

fluorescent dye, was employed to quantify changes in the membrane bilayer fluidity of *S. aureus* bacteria before and after treatment with LipoFAs. All phospholipids and probes were kept at freezer temperature condition (-20 °C), either in powder form or dissolved in either ethanol or chloroform.

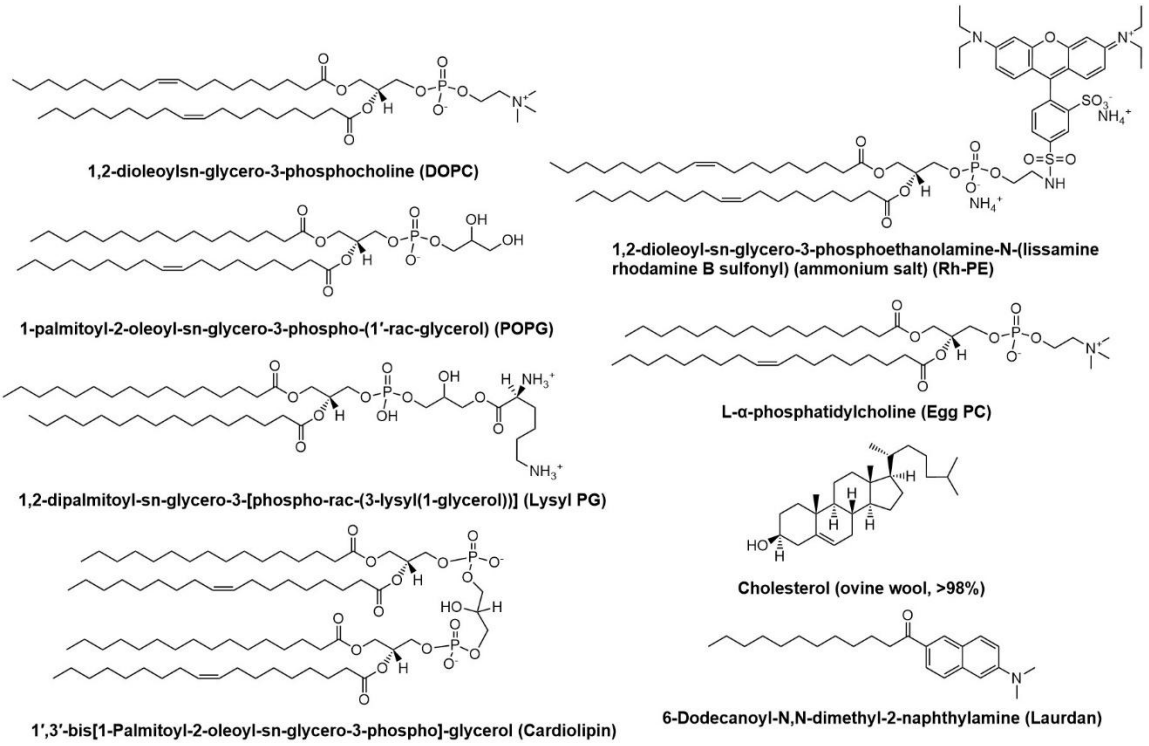

Figure 3.2 Chemical structures of the phospholipids, cholesterol, and fluorescent probes used in this thesis

3.2.3 Buffer Reagents

Previously, Tabaei *et al.* demonstrated successful SLB fabrication using tris(hydroxymethyl)aminomethane (Tris) buffer [5-7]. The primary amine group in Tris, with a high buffering capacity (pKa = 8.06) within the pH range of 7-9, enables it to form stable complexes and interact with molecules effectively [8]. Leveraging this property, Tris buffer solution containing NaCl (10 mM of Tris, 150 mM of NaCl, and pH 7.5) was utilized to produce SLBs. These two reagents were sourced from VWR (Singapore) and Merck (Singapore), respectively. Phosphate-buffered saline (PBS) buffer solution (pH 7.5), certified by the National Bureau of Standards (NBS) as a physiological pH standard [9],

was used for washing the formed SLBs and treating the antimicrobial lipids for QCM-D and fluorescence microscopy experiments, as well as for all sample preparations. PBS was obtained from Gibco (Carlsbad, CA). Tris and PBS buffers were prepared in Milli-Q-treated water (>18 MΩ·cm).

3.2.4 Bacterial Cell Strain and Biological Testing Reagents

Traditionally, MRSA infections were primarily associated with healthcare facilities and immunocompromised individuals. However, there has been a significant rise in community-acquired MRSA (CA-MRSA), which exhibits increased antibiotic resistance and virulence. This has become a global concern, with CA-MRSA surpassing healthcare-acquired infections in prevalence, particularly in North America [10, 11]. CA-MRSA has become a leading cause of infections affecting the skin and soft tissues, known for its quick resistance to multiple antibiotic drugs and its ability to cause severe infections in otherwise healthy minors [12]. Hence, there is a pressing need to develop innovative antimicrobial strategies.

For this study, *S. aureus* MW2, a type of CA-MRSA strain, provided by Ewha Womans University in Seoul, South Korea, was used as the quality control bacterial strain. Previous research has highlighted the effectiveness of FAs against *S. aureus*, making them ideal for studying interactions with model bacterial membranes and linking biophysical observations with biological activities. *S. aureus* MW2 cells were cultivated with tryptic soy broth (TSB) and stored in a 16% (v/v) glycerol stock solution at temperatures between -70 and -80 °C. TSB broth was used for bacterial propagation, culture, and served as the medium for OD_{600} measurements [13].

To assess the bacterial inhibitory effects of antimicrobial lipids, the microdilution method with Mueller-Hinton (MH) broth was employed, complying with the guidelines set by Clinical and Laboratory Standards Institute (CLSI). However, due to poor solubility of FAs in water [14, 15], the microdilution technique using OD_{600} measurement was unsuitable for this study. Instead, bacterial kinetics were evaluated by plating the diluted samples on MH agar.

To evaluate the permeabilization of bacterial cell membranes, SYTOX Green dye was utilized. This DNA-binding dye is known for its inability to permeate intact cell membranes. When the cell membranes are disrupted, SYTOX Green is able to enter the cells, where it binds to DNA and emits fluorescence. The bacterial suspension, which contained SYTOX Green, was treated with various antimicrobial agents, and the resulting fluorescence intensity was determined to quantify the extent of membrane permeabilization [16].

The quantification of the release of enveloped ATP from *S. aureus* MW2 was measured using an ATP assay technique [16]. Furthermore, Laurdan dye was used to assess water penetration levels in the bacterial membrane when exposed to LipoFAs, which served as an indicator of membrane fluidity. However, Laurdan dye is limited by its low photostability and high internalization rates [17]. Therefore, experiments involving this dye were handled with extra care, using brown-tinted glass vials or covering transparent vials with aluminum foil to shield the dye from light exposure.

3.3 Material Synthesis

3.3.1 Preparation of Antimicrobial Fatty Acid and Liposome Solutions

The solubility of FAs exhibit varies significantly depending on the solvent used. Ethanol has been identified as the suitable solvent for FAs due to its favorable solubility properties [18, 19]. It has been reported that 1% ethanol concentration marks the threshold boundary between non-toxic and toxic levels [20]. Therefore, precise amounts of each LNA, LLA, and OA were dissolved in ethanol to achieve 50 mM. These solutions were then diluted with PBS buffer to achieve 500 µM, maintaining the ethanol concentration at 1%. The test samples were heated and vortexed to ensure thorough solubilization, then cooled to room temperature and further diluted before each experiment. All solutions were immediately prepared prior to each experiment.

Despite the beneficial biological properties of antimicrobial FAs, their limited solubility in aqueous solution presents a challenge for practical use. To address this limitation, liposomes can be used to encapsulate FAs, improving the solubility and delivery

into cells or bacteria through membrane fusion [21-23]. Liposomes, consisting of enclosed lipid bilayers, can be prepared using several methods such as solvent injection, stirring, surfactant removal, and reverse phase evaporation [24]. Among these techniques, the vesicle extrusion method is highlighted as a straightforward approach to liposome preparation [25]. This method involves creating a thin film through solvent evaporation, rehydrating the film with a PBS solution to form MLVs, and then extruding the MLVs through polycarbonate membranes to generate small SUVs. The vesicle extrusion technique, known for its reproducibility and simplicity, does not require organic solvents. Therefore, this method was selected for the preparation of LipoFAs in this study, with modifications to a previously established protocol [23]. LipoLNA, LipoLLA, and LipoOA were formulated by mixing Egg PC, cholesterol, and LCFA in a chloroform solution at specific weight ratios. The lipid film was initially dried with nitrogen and then vacuum desiccated to eliminate any remaining solvents. It was subsequently rehydrated with PBS buffer to create an opaque MLV solution. This solution was then vortexed, subjected to bath sonication (RS PRO, Kuala Lumpur, Malaysia), and further processed using a 20 kHz ultrasonic probe (QSonica, Newton, CT) with a 12 mm tip diameter, operating at 20 kHz, 500 W, and 40% amplitude for 10 minutes to produce SUVs. To avoid excessive heat that could potentially degrade the phospholipids or cause metal contamination, careful monitoring during sonication was essential. Finally, the resulting lipid suspension was passed through polycarbonate (PC) membranes with pores ranging from 100 to 400 nm using an extruder, with each membrane being used 11 times. LipoFA stability was assessed by measuring the hydrodynamic size and zeta potential of the particle surface with dynamic light scattering (DLS), with all measurements performed three times at 25 °C.

3.3.2 Preparation of Model Membrane Platforms

Previous studies have utilized model cell membranes, such as liposomes and SLBs, to examine how biomolecules interact with FAs. SLBs are particularly advantageous for studying membrane interactions and is the preferred option for this thesis due to several reasons such as their stability under various solution conditions [26], compatibility with other surface-sensitive techniques like microfluidics, and, importantly, the flexibility to

incorporate diverse lipid compositions with different charges and shapes. For this thesis, SLBs on solid supports were selected to investigate the membrane interactions of LCFAs and LipoFAs.

There are multiple methods to create planar SLBs, including surface-mediated liposome fusion [27] and Langmuir-Blodgett (LB) deposition [28] methods. However, these methods have drawbacks, including the specialized equipment, multiple steps to transfer lipid monolayers onto the substrate, and complex procedures for vesicle fusion and rupture. To address this issue, a simpler and more robust fabrication method was utilized in this thesis, which allows for the production of stable, high-quality SLBs with significant amount of charged lipids. Thus, the solvent-assisted lipid bilayer (SALB) method was used to create SLBs that replicate bacterial membranes, following a well-established protocol [7]. As illustrated in **Figure 3.3**, the SALB method entails applying a 0.5 mg/mL lipid mixture and isopropanol (IPA) onto a support. Subsequently, the solvent is promptly replaced with Tris buffer, which triggers phase transitions and lipid rearrangements. This procedure leads to the formation of planar lamellar-phase SLBs on various substrate surfaces [7].

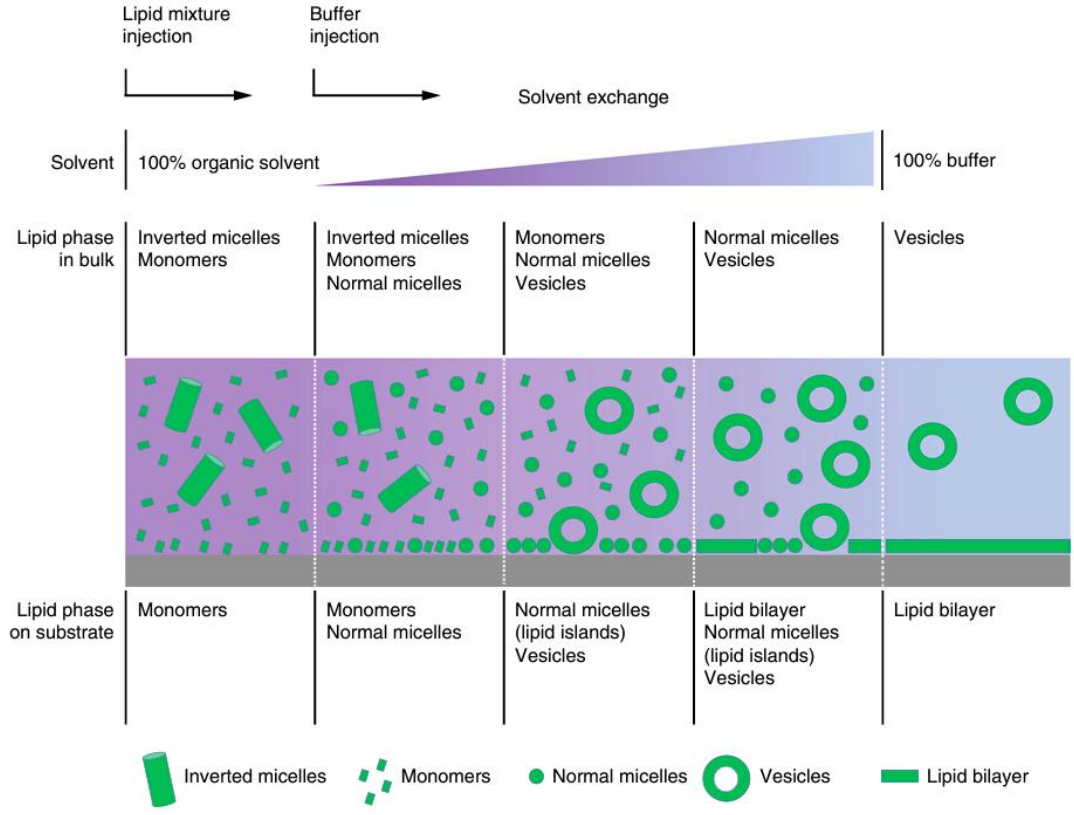

Figure 3.3 Bottom-up fabrication formation process of supported lipid bilayer using solvent-assisted lipid bilayer method. Reproduced with permission from [29].

Another benefit of the SALB method is its capability to produce high-quality charged SLB membranes. Tabaei *et al*. have previously shown that negatively charged lipid molecules can be fabricated on silicon dioxide and aluminum oxide substrates using the SALB technique. In their work, phospholipid self-assembly is primarily governed by electrostatic interactions [5]. In this thesis, a rigorous optimization process was conducted to produce homogenous charged SLBs that mimic bacterial membrane.

3.4 Experimental Techniques

3.4.1 Determination of Critical Micelle Concentration

A fundamental metric in the examination of micelles is the CMC. This concentration signifies the point at which amphiphilic molecules in a solution start to assemble into supramolecular structures known as micelles. Comprehending the CMC is essential for thermodynamic evaluation and for elucidating the behavior of surfactants. Many approaches, such as conductivity measurements [30], fluorescence-based techniques [31], and hyper-Raleigh scattering [32], can be used to calculate the CMC. The sensitivity, precision, and prior validation of the fluorescence-based method in earlier studies [33] made it the preferred choice for measuring the CMC values of LCFAs. This method utilizes the principles of fluorescence, specifically the behavior or ground-state electrons, their excitation to higher energy levels, and the resultant Stokes shift. A fluorescence probe, 1-pyrenecaroxaldehyde (1-PyCHO), known for its high sensitivity to alterations in polarity within its environment, with a pyrene moiety and an aldehyde group, was used to monitor the formation in micelles in solution [34].

The Stokes shift, defined as the shift distance between the excitation and emission wavelengths of the probe, is a crucial aspect of this method. As the concentration of the FA nears the threshold level, the probe transitions from a nonpolar (monomeric) state to a polar environment within the micelle. This transition is detected through observable changes in the fluorescence emission spectrum. Specifically, as the probe moves from a nonpolar to a

polar environment, the Stokes shift becomes evident as a noticeable change or shift in the fluorescence emission spectrum. At concentrations below the self-assembly threshold, the probe exists in a monomeric state with distinct characteristic fluorescence properties. When light is absorbed by the probe, ground-state electrons in the probe are excited to higher energy levels, resulting in fluorescence emission. As FA micelle formation commences upon reaching the critical concentration point, the probe experiences a shift in its emission wavelength due to changes in its surroundings within the micelle. This wavelength shift in the fluorescence emission spectrum serves as an indicator of micelle formation. In this study, the maximum emission wavelength of 1-PyCHO in PBS was recorded at 473 nm using a microplate reader, consistent with literature values at room temperature [35]. This shift in the emission wavelength as the surfactant concentration reaches the CMC provides a reliable signal for the onset of micelle formation. This fluorescence-based technique, utilizing the sensitivity of the 1-pyrenecarboxaldehyde probe and the observable Stokes shift, is a robust method for investigating the self-aggregation properties of LCFAs in solution, offering valuable insights into their biophysical interactions and potential applications.

To prepare the samples, a specific amount of 1-PyCHO was dissolved in methanol to achieve 5 mM, and the stock solution was kept at 4 °C. For sample preparation, a specific volume of the stock solution was added to a vial. Methanol was then evaporated using nitrogen, resulting in a thin film of the probe. PBS containing the FA was then transferred to the vial to reach a concentration of 0.1 µM. The mixture was vortexed to ensure thorough mixing, and residual nitrogen gas was allowed to evaporate. The resulting test samples, containing both the FA solution and the 1-PyCHO probe, were then subjected to fluorescence analysis using the microplate reader. The samples were excited at 365.5 nm [35], and their fluorescence emission spectra were measured between 420 nm and 580 nm. Each sample underwent a minimum of eight scans for accuracy, and the final emission spectrum was obtained by averaging the results.

3.4.2 Quartz Crystal Microbalance-Dissipation

In this study, QCM-D technique using the Q-Sense E4 instrument (Biolin Scientific,

Stockholm, Sweden) was used to analyze the properties and interaction kinetics of SLBs following treatment with LCFAs and LipoFAs. QCM-D operates on the principle of the piezoelectric effect, where a quartz crystal resonator generates an electrical signal in response to mechanical stress. When a biomolecule film is deposited onto the surface of a quartz crystal sensor chip (5 MHz AT-cut) [36, 37], the resonance frequency of the sensor shifts in proportion to the mass of the adsorbed material. This change is quantified by the Sauerbrey equation, where Δm represents the mass change per unit area, n denotes the harmonics (overtone number), Δf is the frequency shift, and C the is mass sensitivity constant, approximately 17.7 ng·cm^{-2}·Hz^{-1} for a 5 MHz crystal [38]:

$$\Delta m = -\frac{\Delta f}{n} C$$

Frequency changes are measured and correlated with the absorbed mass, forming the fundamental basis of the QCM-D mass detection technique. However, accurate application of the Sauerbrey equation requires several conditions: the adsorbed material must be firmly adsorbed to the crystal surface without significant movement or deformation during oscillation, the mass must be uniformly distributed across the crystal surface for consistent frequency measurements, and the mass should be less than that of the crystal sensor itself. If the mass of the adsorbed mass is comparable to or exceeds that of the sensor crystal, the Sauerbrey equation's assumptions may not hold. While this equation allows for estimation of the mass change of a rigidly adbsorbed layer, QCM-D also evaluates the viscoelasticity of the adsorbed material through the dissipation factor, D, as outlined in previous studies [39]:

$$D = \frac{1}{Q} = \frac{E_D}{2\pi E_S}$$

where Q is the quality factor, E_D is the energy dissipated per cycle, and E_s is the stored energy. D is measured by the output of voltage over the crystal that decays when the piezoelectric oscillator voltage is switched off after excitation at the crystal's resonance frequency. D is calculated as [40]:

$$D = \frac{1}{\pi f \tau}$$

where f is the frequency and τ is the decay time constant, providing a dimensionless number that describes the oscillation energy losses [39].

In this study, QCM-D was instrumental in characterizing model bacterial membrane SLBs and understanding the effects of LCFAs and LipoFAs on these SLBs. QCM-D's sensitivity to both the mass of adsorbed material and the coupled solvent makes it highly responsive to changes in membrane properties.

Experimental data for QCM-D experiments were obtained at the third (n = 3), fifth (n = 5), seventh (n = 7), and ninth (n = 9) overtones. For representative data, the fifth overtone was used to display frequency and dissipation plots. The sensor chips, featuring a 50-nm-thick silicon dioxide coating and a resonance frequency of 5 MHz, underwent a rigorous cleaning process. This involved rinsing with SDS (sodium dodecyl sulfate), DI water, and ethanol, followed by drying with nitrogen. Additionally, the chips were treated with oxygen plasma using a plasma cleaner before each experiment. Single-component and multi-component SLBs were formed on the plasma-treated sensors using the SALB method. The measurements began with stabilization in Tris buffer to establish baseline values, followed by IPA injection until equilibration. For single-component SLBs, a 0.5 mg/ml DOPC lipid mixture in IPA was introduced for 5 to 10 minutes. For multi-component SLBs, a 0.3 mg/mL of POPG, Lysyl-PG, and CL lipid mixture in IPA was injected for 5 – 10 minutes, followed by Tris buffer exchange. The quality of SLBs was assessed based on final net frequency (Δf) and dissipation shifts (ΔD) with optimal values around -28 Hz and 0.9×10^{-6}, respectively. After successful SLB formation, the Tris buffer was replaced with PBS to simulate biological conditions. Antimicrobial FAs and liposomes loaded with FAs were then injected, and their interactions with SLBs were tracked by monitoring shifts in mass and viscoelastic properties. Samples, buffers, and solvents were all injected at a controlled flow rate of 50 μL/min, while maintaining room temperature. This meticulous protocol ensured the accuracy and reliability of QCM-D measurements, offering useful mechanistic insights into how antimicrobial agents interact with model membrane systems.

3.4.3 Fluorescence Microscopy

Fluorescence microscopy is a highly sensitive optical imaging technique extensively used in biological research to visualize and study cellular processes at the molecular scale [41, 42]. This technique works by exciting fluorophores within a sample with a particular

wavelengths of light, which causes these fluorophores to emit light at extended wavelengths. The emitted light is then detected and visualized, while the excitation light is filtered out. This method provides exceptional sensitivity and spatial resolution for observing specific molecules or cell structures. Fluorescence microscopy encompasses various techniques, each with its own approach for measurement. Common types include epifluorescence microscopy, confocal microscopy, and total internal reflection fluorescence (TIRF) microscopy. TIRF microscopy is noted for its exceptional sensitivity and minimal background signal, providing detailed, high-contrast imaging of subcellular regions [43]. This technique selectively excites fluorophores close to the glass-lid interface by utilizing the rapid decay of evanescent waves, which penetrate only a few hundred nanometers (typically 100-200 nm) into the specimen. This selective excitation effectively suppresses signals from deeper layers, allowing for precise imaging of membrane associated processes [44]. Confocal microscopy, on the other hand, restricts illumination and detection to a diffraction-limited area within the sample through the use of a pinhole. This approach enhances resolution and reduces background signals. By collecting light from the focal plane, confocal microscopy can construct 3-D images by compiling serial optical sections, providing detailed structural information of the sample. Epifluorescence microscopy involves illuminating the entire sample with light and collecting the emitted fluorescence to form the image. The excitation light and emitted fluorescence are both directed through the same objective lens, allowing for simple and rapid imaging of fluorescently labeled samples in real-time [45]. In this thesis, this technique was utilized to monitor changes in membrane morphology of fluorophore-labeled SLBs caused by LCFAs and LipoFAs. It offers visual morphological information of membrane destabilization and fusion. Furthermore, fluorescence microscopy was applied to measure the degree of morphological changes and to determine localization of molecules within the membrane.

For the experiments in this thesis, epifluorescence microscopy technique was used to visually probe the interactions between FAs and LipoFAs with SLBs in real-time. An inverted optical microscope, equipped with a 60× magnification (NA = 1.49) oil-immersion objective lens (Nikon, Japan) and a fiber-coupled mercury lamp (Intensilight C-HGFIE, Nikon) for fluorescence excitation via a TRITIC filter, was utilized. Images

were captured using the iXon 512 pixel × 512 pixel EMCCD camera (Andor Technology, Northern Ireland), featuring a pixel size of 0.267 × 0.267 μm^2. SLBs were prepared using a lipid solution of 0.5 mg/mL containing 99.5 mol% DOPC lipid and 0.5 mol% Rh-PE lipid in IPA, as well as a lipid solution of 0.3 mg/mL containing 99.5 mol% POPG, Lysyl-PG, and CL lipids with 0.5 mol% Rh-PE lipid in IPA. These solutions were applied to a glass slide within a flow-through chamber using the SALB method, where SLBs formed on the glass surface through vesicle adsorption and spontaneous rupture. Following SLB establishment, PBS was used to rinse the chamber, and antimicrobial agents were introduced at a flow rate of 50 μl/min. Micrographs were captured every 5 seconds for 60-minute period, capturing both above and below CMC concentrations during the treatment and buffer washing phases. Fluorescence intensity data were normalized during the analysis.

3.4.4 Fluorescence Recovery After Photobleaching

FRAP is a prevalent experimental technique in biological research, especially for examining membrane dynamics using SLBs platforms. FRAP involves using a high-intensity laser beam (30-50 mW or higher) to photobleach a specific region within the SLB, where fluorescent molecules are concentrated. This technique monitors how fluorescence intensity recovers in this photobleached area over time as unbleached fluorescent molecules diffuse back into the bleached zone (**Figure 3.4**). This method provides quantitative information on the rate and extent of fluorescence recovery, which can be evaluated to understand the lateral diffusion and mobility of molecules within SLB membranes [46]. The resulting fluorescence recovery curve, which tracks the intensity of fluorescence in the bleached area over time, provides information on the diffusion

coefficient and the proportion of mobile molecules [47].

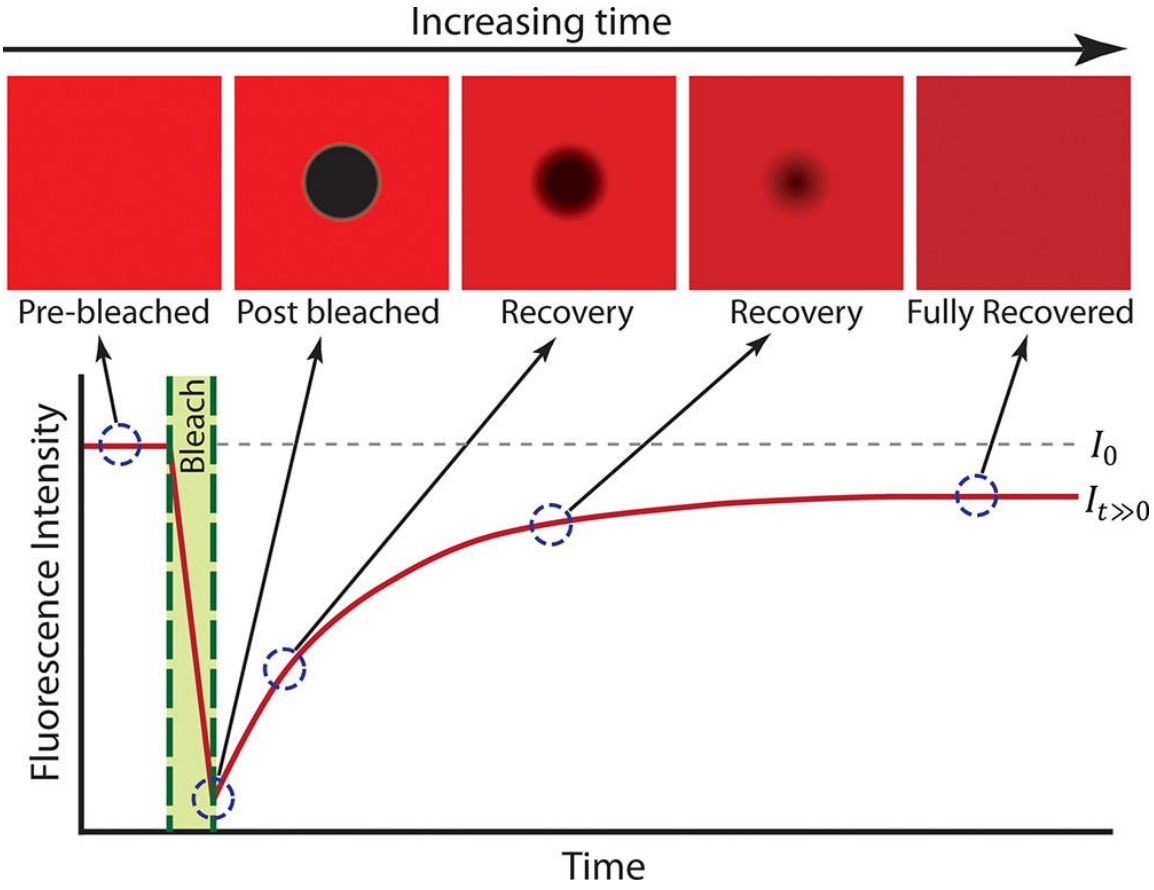

Figure 3.4 Schematic of the FRAP technique showing a fluorescence intensity curve over time. Reproduced with permission from reference [48].

Fick's law of diffusion is a fundamental principle in diffusion that was first posited by Adolf Flick. This law is essential for understanding the diffusion of molecules through a medium, such as lipid bilayers, based on concentration gradients and diffusion coefficients [49]. By applying Fick's law, researchers can predict and analyze the movement of molecules within the SLB, providing insights into how different factors, such as lipid composition, cholesterol content, or the presence of specific molecules, influence diffusion rates and membrane dynamics [50]. In an isotropic system like an SLB, where properties are uniform in all directions [51], Fick's law is foundational for studying 2-D diffusion processes. Applying Fick's law in FRAP experiments on SLBs enables the measurement of lateral diffusion rates and the characterization of membrane properties [50]. After photobleaching, the system behaves according to Fick's second law:

$$\frac{\partial}{\partial t}C = D\nabla^2 C$$

where *C* represents the concentration of the unbleached fluorophores over time *t* and radial distance *r* after photobelaching. *C i*s proportional to diffusion coefficient *D*. ∇^2 represents the Laplacian operator, which can be simplified to spherical symmetry assuming the gradient is along the radial direction [52]:

$$\frac{\partial}{\partial t}C = D\left(\frac{\partial^2}{\partial r^2}C + \frac{2}{r}\frac{\partial}{\partial r}C\right)$$

The Hankel transformation is a mathematical tool that can be applied to analyze diffusion phenomena and the diffusion coefficient from Fick's equation. Previous work by Jönsson *et al.* applied the Hankel transformation to Fick's second law, demonstrating its accuracy in FRAP analysis, including diffusion coefficient determination [51]. Therefore, the Hankel transform method was utilized in this thesis for FRAP measurements and evaluation of SLB quality.

In the FRAP experiments, SLBs underwent photobleaching for 5 seconds utilizing a 532 nm, 100 mW laser to generate a spot with a diameter of 20 μm. After photo-bleaching, the fluorescence recovery was monitored, and images were captured every 2 seconds for 120 seconds for both single-component and multi-component SLBs, unless specified otherwise. The lateral diffusion coefficients were derived from the FRAP data using the Hankel transform method, with computations performed in Matlab [53].

3.4.5 Dynamic Light Scattering and Zeta-Potential

DLS is an experimental technique for determining particle size and size distribution profile of molecules in a suspension by analyzing random changes in scattered light fluctuations due to Brownian motion [54], while zeta potential characterizes the surface charge of nanoparticles. DLS analyzes intensity fluctuations rather than average light intensity to gain information about the particle dynamics. By applying the Stokes-Einstein formula to the autocorrelation function of the scattered light, DLS quantifies particle diffusion coefficients and dynamics [55]. The correlation between particle size and diffusion coefficient is expressed as follows [56]:

$$D = \frac{k_B T}{6\pi\eta R}$$

where D is the concentration-dependent diffusion coefficient, k_B is the Boltzmann coefficient (1.380×10^{-23} J/K), T is the absolute temperature, η is the solution's viscosity, R is the particle's hydrodynamic radius. According to this formula, larger particles exhibit slower diffusion and longer correlation times.

DLS analysis uses different weighted distributions like intensity-weighted, volume-weighted, and number-weighted to characterize particle size distribution within a sample [56]. These distributions offer insights into the relative contributions of particle of different sizes to the overall scattering signal, facilitating a comprehensive understanding of the particle population in the system. In this thesis, the size distribution of micelles and liposomes was analyzing both the average size and polydispersity index (PDI). Light scattering is influenced by particle refractive index, and the intensity-weighted distribution ($\%I_a$), which assumes a monodisperse sample of spherical particles solubilized in suitable buffer solution, corresponds to the sixth power of the particle diameter, based on Rayleigh approximation [57]:

$$\%I_a = \frac{a^6 N_a 100}{N_a a^6 + N_b b^6}$$

This can be to volume-weighted distribution ($\%V_a$), assuming uniform density, with size proportional to the third power:

$$\%V_a = \frac{a^3 N_a 100}{N_a a^3 + N_b b^3}$$

Finally, $\%I_a$ can also be converted into number-weighted distribution:

$$\%N_a = \frac{N_a 100}{N_a + N_b}$$

where N_a and N_b represent particles with sizes a and b, respectively. In this study, intensity-weighted distributed was employed to measure the size of FA micelles and liposomes, as they displayed lognormal size distribution.

Zeta potential is a critical parameter in colloidal systems that defines the surface charge of particles and is crucial in determining their stability and behavior in suspensions [58]. The process of measuring zeta potential with DLS involves evaluating the electrophoretic mobility (μ_e) of particles dispersed in a solution. When an electric field is

introduced, charged particles move toward the electrode with the opposite charge. As presented in **Figure 3.5**, zeta potential reflects the electrical potential gradient at the slipping plane of the particle-fluid interface and is derived from μ_e using:

$$\mu_e = \frac{V}{E}$$

where *V* is the velocity of the particle in μm/s and *E* denotes the electric field strength in V/cm. Henry's equation is used to calculate zeta potential:

$$\mu_e = \frac{2\varepsilon\zeta f(Ka)}{3\eta}$$

where η is viscosity, ε is dielectric constant, *f(Ka)* is a function defined for different particle sizes and salt concentrations. For large particles (up to 1 μm) in high salt concentration, f*(Ka)* is 1.5, while for small particles in low salt concentration, it simplifies to 1, yielding the Helmholtz-Smoluchowski (HS) equation and Hückel equation, respectively:

$$\mu_e = \frac{\varepsilon\zeta}{\eta} \text{ and } \mu_e = \frac{2\varepsilon\zeta}{3\eta}$$

The velocity of the charged particles moving towards opposite charge is directly proportional to zeta potential. Zeta potential classifications for colloidal dispersions are as follows: ± 0-10 mV indicates instability, ± 10–20 mV suggests relative stability, and ± 20–30 mV denotes moderate stability, and values exceeding $> \pm 30$ mV are considered highly unstable [59].

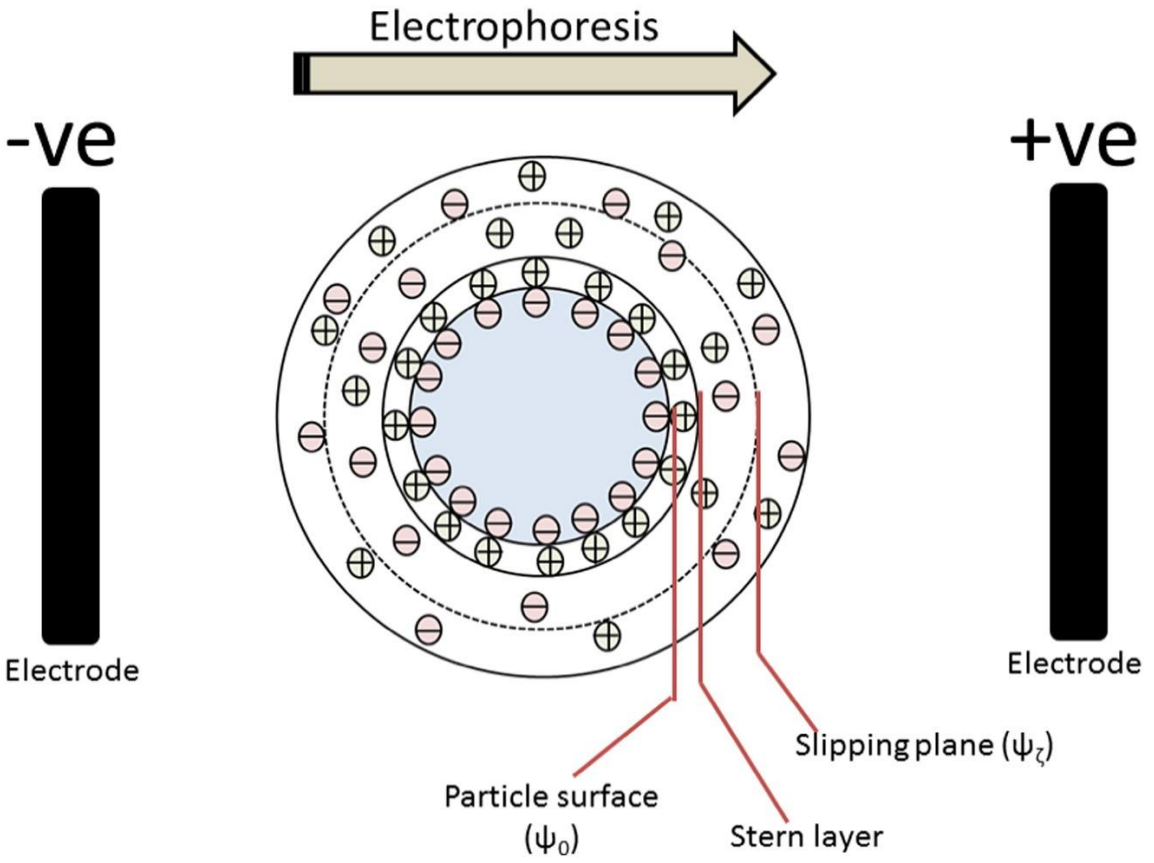

Figure 3.5 Schematic of the electrokinetic potential at the slipping plane, which represents the zeta-potential. Reproduced with permission from reference [58].

Surface zeta potential and average size of LCFAs and extruded LipoFAs in PBS were characterized using the zeta PALS analyzer. To abate reflection artifacts, the angle of the scattering light was set at orthogonal direction. Samples were diluted tenfold in DI water and analyzed with an average count rate ranging between 100 and 450 kcps, a PDI ranging from 0.1 to 0.4, and a zeta potential exceeding ±25 mV to ensure sample quality. The autocorrelation data obtained were subjected to analysis using the standard cumulants method and were fitted to lognormal distribution(s) to accurately determine size distributions. Moreover, to prevent any contamination, cuvettes were utilized with lids, and no precipitation was observed at the bottom of the cuvette.

3.4.6 Minimum Inhibitory Concentration and Bactericidal Kinetics Testing

MIC testing determines the minimal concentration of an antimicrobial agent needed

to inhibit visible bacterial growth. This test is typically performed in batch cultures with various concentrations of the antimicrobial agent to evaluate its efficacy against different bacterial strains [60]. MIC testing can be carried out using either the agar dilution method or broth dilution method [61]. In the agar dilution method, the antimicrobial agent is mixed with a nutrient agar medium, and a standardized bacterial inoculum is spread across the agar plate's surface. In contrast, the broth dilution method involves inoculating bacteria in a liquid medium that contains varying amounts of the antimicrobial agents. MIC is assessed using a microtiter plate by measuring OD_{600}, which indicates the level of bacterial turbidity. The MIC is identified as the point at which no increase in turbidity is observed. This method is often favored for antibacterial testing due to its straightforward procedure and minimal sample requirements. Given the poor solubility of FAs in water, this method was chosen to assess the MIC of LipoFAs. MIC was determined following the microdilution technique in line with the guidelines outlined by the Clinical and Laboratory Standards Institute (CLSI) [62], with MH broth serving as the standard medium for growing *S. aureus* [63].

Bactericidal kinetics testing is used to evaluate the temporal dynamics of bactericidal activity, specifically measuring its ability to achieve a reduction of ≥3 log10 (CFU/mL). This testing assesses the rate at which a bacterial population diminishes over a specified period, providing insights into the time required for complete bacterial inactivation. The broth dilution technique is employed for this purpose, allowing the assessment of antimicrobial effectiveness across a spectrum of concentrations. This assay can determine not only the minimum concentration needed to exert a bactericidal effect but also the time-dependent behavior of the antimicrobial agent at varying concentrations. This is crucial for comprehending the kinetics of bacterial killing and optimizing dosage for therapeutic applications. In this study, to main consistency with the buffer conditions used in the biophysical assays, PBS was used for all dilution procedures during MIC and time-kill assays. This selection ensures that the environmental conditions in the assays closely match those of the biophysical analyses, providing more relevant and comparable data regarding the antimicrobial activity of tested compounds.

MIC of the antimicrobial lipids was assessed using the microdilution method. An overnight culture of *S. aureus* MW2 was prepared and diluted to a concentration of 1×10^6

CFU/mL in MH broth. Test compounds were serially diluted in MH broth across a 96-well microtiter plate, with concentrations ranging from 8 μM to 500 μM for LCFAs and 8 μg/mL to 500 μg/mL for LipoFAs. A specific volume of the bacterial suspension was then dispensed into each well containing the diluted test compounds, while wells without the test compound served as negative controls. The plates were incubated overnight at 37°C, and OD_{600} was measuring using a multimode reader. Bacterial growth was indicated by an OD_{600} reading of ≥0.1. For the bactericidal kinetics analysis of MRSA during the exponential phase, an overnight culture of *S. aureus* MW2 was diluted in TBS and incubated at 37°C until the OD_{600} reached 0.05, indicating exponential growth. Subsequently, the culture was mixed with an equivalent volume of pre-warmed TSB containing double the target concentrations of the test compounds. Samples were collected hourly, serially diluted tenfold in PBS, and plated onto MH agar. Following an overnight incubation, the colonies were counted to ascertain the quantity of viable cells. Each experiment was carried out independently three times.

References

[1] T.-H. Lee, D.J. Hirst, K. Kulkarni, M.P. Del Borgo, M.-I. Aguilar. *Chemical Reviews*. **2018**. 118(11), 5392-5487.

[2] T. Wiedmann, A. Salmon, V. Wong. *Lipids and Lipid Metabolism*. **1993**, 1167(2), 114-120.

[3] E. Nagamachi, R. Kariyama, Y. Kanemasa. *Physiological Chemistry and Physics and Medical NMR*. **1985**, 17(3), 255-60.

[4] S. Danner, G. Pabst, K. Lohner, A. Hickel. *Biophysical Journal*. **2008**, 94(6), 2150-9.

[5] S.R. Tabaei, S. Vafaei, N.-J. Cho. *Physical Chemistry Chemical Physics*. **2015**, 17(17), 11546-11552.

[6] S.R. Tabaei, J.H. Choi, G. Haw Zan, V.P. Zhdanov, N.J. *Langmuir*. **2014**, 30(34), 10363-73.

[7] S.R. Tabaei, J.A. Jackman, M. Kim, S. Yorulmaz, S. Vafaei, N.J. Cho. *JoVE*. **2016**, (106).

[8] L. Samuelsen, R. Holm, A. Lathuile, C. Schönbeck. *International Journal of Pharmaceutics*. **2019**, 560, 357-364.

[9] R.N. Roy, L.N. Roy, M.S. Fuge, C.N. Roy, C.A. Himes, P.A. Bryant, K.T. Robinson, D.A. Kaufmann, 2nd, C.H. Grove, T. Ghosh, A. Bwashi. *Journal of Solution Chemistry*. **2009**, 38(4), 471-483.

[10] C. Cuny, L.H. Wieler, W. Witte. *Antibiotics*. **2015**, 4(4), 521-543.

[11] J. Zhang, J. Conly, J. McClure, K. Wu, B. Petri, D. Barber, S. Elsayed, G. Armstrong, K. Zhang. *Microorganisms*. **2021**, 9(2), 287.

[12] F.R. DeLeo, M. Otto, B.N. Kreiswirth, H.F. Chambers. *The Lancet*. **2010**, 375(9725), 1557-1568.

[13] F. Widdel. *Di dalam Grundpraktikum Mikrobiologie*. **2007**, 4(11).

[14] H. Vorum, R. Brodersen, U. Kragh-Hansen, A.O. Pedersen. *Biochimica et Biophysica Acta (BBA)*. **1992**, 1126(2), 135-142.

[15] H. Arellano, V. Nardello-Rataj, S. Szunerits, R. Boukherroub, A.-L. Fameau. *Advances in Colloid and Interface Science*. **2023**, 318, 102952.

[16] H.Y. Heo, G. Zou, S. Baek, J.-S. Kim, E. Mylonakis, F.M. Ausubel, H. Gao, W. Kim. *Advanced Science*. **2024**, 11(9), 2306112.

[17] E. Sezgin, T. Sadowski, K. Simons. *Langmuir*. **2014**, 30(27), 8160-8166.

[18] A.W. Ralston, C.W. Hoerr. *The Journal of Organic Chemistry*. **1942**, 07(6), 546-555.

[19] S. Shiozawa, L.C.B.A. Bessa, M.C. Ferreira, A.J.A. Meirelles, E.A.C. Batista. *Journal of Chemical & Engineering Data*. **2015**, 60(8), 2371-2379.

[20] N. Kar, D. Gupta, J. Bellare. *Toxicology Reports*. **2021**, 8, 1054-1066.

[21] G.A. Castro, L.A. Ferreira. *Expert Opinion on Drug Delivery*. **2008**, 5(6), 665-79.

[22] V.P. Torchilin. *Nature Reviews Drug Discovery*. **2005**, 4(2), 145-60.

[23] D. Yang, D. Pornpattananangkul, T. Nakatsuji, M. Chan, D. Carson, C.M. Huang, L. Zhang. *Biomaterials*. **2009**, 30(30), 6035-40.

[24] D. Lombardo, M.A. Kiselev. *Pharmaceutics*. **2022**, 14(3).

[25] L.D. Mayer, M.J. Hope, P.R. Cullis. *Biochimica et Biophysica Acta (BBA)*. **1986**, 858(1), 161-8.

[26] K. Giger, E.R. Lamberson, J.S. Hovis. *Langmuir*. **2009**, 25(1), 71-74.

[27] L.K. Tamm, H.M. McConnell. *Biophysical Journal*. **1985**, 47(1), 105-13.

[28] N. Vila, M. Puggelli, G. Gabrielli. *Colloids and Surfaces A*. **1996**, 119(2), 95-104.

[29] A.R. Ferhan, B.K. Yoon, S. Park, T.N. Sut, H. Chin, J.H. Park, J.A. Jackman, N.-J. Cho. *Nature Protocols*. **2019**, 14(7), 2091-2118.

[30] N. Shahi, A. Bhattarai. *Bibechana*. **2017**, 15, 85-89.

[31] L.N. K, S. Jagadeeshan, S.A. Nair, G.S.V. Kumar. *Journal of Nanobiotechnology*. **2011**, 9(1).

[32] S. Ghosh, A. Krishnan, P.K. Das, S. Ramakrishnan. *Journal of the American Chemical Society*. **2003**, 125(6), 1602-1606.

[33] A. Dominguez, A. Fernandez, N. Gonzalez, E. Iglesias, L. Montenegro. *Journal of Chemical Education*. **1997**, 74(10), 1227.

[34] M. Osa, Y. Itoda, Y. Suzuki, T. Yumoto, A. Yoshida. *Polymer Journal*. **2015**, 47(1), 59-65.

[35] M. Ashaduzzaman, M. Kunitake. *International Letters of Chemistry, Physics and Astronomy*. **2013**, 6, 55-62.

[36] M. Rodahl, F. Höök, C. Fredriksson, C. A. Keller, A. Krozer, P. Brzezinski, M. Voinova, B. Kasemo. *Faraday Discussions*. **1997**, 107(0), 229-246.

[37] K.D. Esmeryan, C.E. Castano, M. Abolghasemibizaki, R. Mohammadi. *Sensors and Actuators B: Chemical*. **2017**, 243, 910-918.

[38] F. Höök, B. Kasemo, T. Nylander, C. Fant, K. Sott, H. Elwing. *Analytical Chemistry*. **2001**, 73(24), 5796-5804.

[39] M. Rodahl, F. Höök, A. Krozer, P. Brzezinski, B. Kasemo. *Review of Scientific Instruments*. **1995**, 66(7), 3924-3930.

[40] M. Rodahl, B. Kasemo. *Review of Scientific Instruments*. **1996**, 67(9), 3238-3241.

[41] M.J. Rust, M. Bates, X. Zhuang. *Nature Chemical Biology*. **2006**, 3(10), 793-796.

[42] P. Rodríguez-Sevilla, S. Thompson, D. Jaque. *Advanced Nanobiomed Research*. **2022**, 2(5).

[43] V. Dubey, A. Ahmad, R. Singh, D.L. Wolfson, P. Basnet, G. Acharya, D.S. Mehta, B.S. Ahluwalia. *Optics Express*. **2018**, 26(16), 19864.

[44] J. Fan, X. Huang, L. Li, C. Liang-yi, S. Tan. *Biomedical Optics Express*. **2019**, 10(3), 1097.

[45] A. Baumstummler, R. Chollet, H. Meder, C. Rofel, A. Venchiarutti, S. Ribault. *Letters in Applied Microbiology*. **2010**, 51(6), 671-677.

[46] L.R. Jordan, M. Blauch, A. Baxter, J. Cawley, N.J. Wittenberg. *Biointerfaces*. **2019**, 183, 110442.

[47] H. Ishikawa-Ankerhold, R. Ankerhold, G. Drummen. *eLS*. **2014**.

[48] J. Kurniawan, J.F. Ventrici de Souza, A.T. Dang, G.-y. Liu, T.L. Kuhl. *Langmuir*. **2018**, 34(51), 15622-15639.

[49] J.V.D. Steene, H. Verplancke. *European Journal of Soil Science*. **2005**, 57(2), 106-121.

[50] S. Ladha, A. Mackie, L.J. Harvey, D. Clark, E.J.A. Lea, M. Brullemans, H. Duclohier. *Biophysical Journal*. **1996**, 71(3), 1364-1373.

[51] P. Jönsson, M.P. Jonsson, J.O. Tegenfeldt, F. Höök. *Biophysical Journal*. **2008**, 95(11), 5334-48.

[52] H.-I. Yoo, In *Diffusion in Continuum*, Springer International Publishing2020, pp. 1-71.

[53] P. Jönsson, M.P. Jonsson, J.O. Tegenfeldt, F. Höök. *Biophysical Journal*. **2008**, 95(11), 5334-5348.

[54] V.A. Hackley, J.D. Clogston. *Methods in Molecular Biology*. **2010**, 35-52.

[55] J.H. Lee, W.C. Wu, J. Jiang, B. Zhu, D.A. Boas. *Optics Express*. **2012**, 20(20), 22262.

[56] H.Z. Cummins, E.R. Pike. In *Photon correlation and light beating spectroscopy*, New York1974.

[57] C.E. Barnett. *The Journal of Physical Chemistry*. **1942**, 46(1), 69-75.

[58] S. Bhattacharjee. *Journal of Controlled Release*. **2016**, 235, 337-351.

[59] V.R. Patel, Y.K. Agrawal. *Journal of Advanced Pharmaceutical Technology & Research*. **2011**, 2(2), 81-7.

[60] J.M. Andrews. *Journal of Antimicrobial Chemotherapy*. **2001**, 48(suppl 1), 5-16.

[61] I. Wiegand, K. Hilpert, R.E. Hancock. *Nature Protocols*. **2008**, 3(2), 163-75.

[62] M.A. Wikler. *CLSI (NCCLS)*. **2006**, 26..

[63] T. Baba, F. Takeuchi, M. Kuroda, H. Yuzawa, K.-i. Aoki, A. Oguchi, Y. Nagai, N. Iwama, K. Asano, T. Naimi, H. Kuroda, L. Cui, K. Yamamoto, K. Hiramatsu. *The Lancet*. **2002**, 359(9320), 1819-1827.

Chapter 4*

Lipid Membrane Remodeling by the Micellar Aggregation of Long-Chain Unsaturated Fatty Acids for Sustainable Antimicrobial Strategies

Antimicrobial fatty acids are promising surface-active substances with a wide range of applications. Their ability to target bacterial membrane in multiple mechanisms offer a promising antimicrobial approach for combating bacterial infections. However, the interaction of bacterial cell membranes by these amphiphilic compounds are not yet fully understood. Here, we investigated the concentration-dependent and time-dependent membrane interaction between linolenic acid (LNA), linoleic (LLA), and oleic acid (OA) and the supported lipid bilayers (SLBs) using quartz crystal microbalance-dissipation (QCM-D) and fluorescence microscopy. We first determined the critical micelle concentration (CMC) of each compound and discovered that all micellar fatty acids elicited membrane-active behavior and induced tubular morphological change primarily above their respective CMC values. Fatty acids with a higher degree of unsaturation induced more significant changes in the membrane but required higher concentrations to initiate these effects. Taken together, our findings highlight the critical role of self-aggregation properties and degree of unsaturated bonds in long-chain unsaturated fatty acids on modulating membrane destabilization.

*This chapter is published as S.M. Shin, H.H. Tae, S.H. Park, and N.J. Cho. Lipid Membrane Remodeling by the Micellar Aggregation of Long-Chain Unsaturated Fatty Acids for Sustainable Antimicrobial Strategies. *Int. J. Mol. Sci.* **24**, 9639. https://doi.org/10.3390/ijms24119639. (No written permission from MDPI is necessary for thesis purposes.)

4.1 Introduction

Antimicrobial FAs have been widely applied to various applications such as pharmaceutical, cosmetic, detergent, food science, and nanotechnology [1-7]. As the global demand for surfactants has increased, the surfactants market is expected to grow at a compound annual growth rate (CAGR) of 4.5% between 2022 and 2030 [3]. However, most surfactant-based products are principally derived from petroleum through a chemical process and leave residues that can be detrimental to the environment [3, 8]. Due to the increasing market demand for environmentally friendly and safer ways to produce surfactants, the surfactant industry has shifted away from using synthetic surfactants to replace them with more sustainable alternatives directly derived from natural FAs, also known as green surfactants or biosurfactants [1, 8-10].

Compared to their synthetic counterparts, natural FAs have superior physicochemical properties such as lower critical micelle concentration and high toleration to high temperatures as well as pH and ionic strength [1, 11-14]. Moreover, FAs can target bacterial cell membranes in multiple mechanisms, which can lead to the inhibition of bacterial growth or cell death [15]. They accomplish this by destabilizing the lipid membrane through their amphiphilic properties, which disrupts metabolic regulation and prevents bacterial growth [15, 16]. Some of them can even cause complete membrane lysis, resulting in irreversible damage and leading to bacterial death in a matter of minutes [17]. As a result, natural FAs offer a promising antimicrobial approach for combating bacterial infections and preventing the development of drug-resistant strains [2, 18, 19], as well as a sustainable strategy along with growing environmental awareness [1, 3, 8, 9].

Among the various natural FAs, LCFAs have been classified as Generally Recognized as Safe (GRAS) according to the US Food and Drug Administration (FDA) classification system [20] and are widely used as commercial formulations in food, medicine, cosmetic, and agriculture industries [2, 21-24]. In addition to their potential as antimicrobial agents against a wide range of bacteria, unsaturated FAs have been found to be more effective than saturated ones with the same carbon chain [18, 25, 26]. In line with thoughts that antimicrobial lipids are principally active in the micellar state [27], their

antimicrobial activities may be linked to the ability to form micelles or aggregates in solution. However, although extensive *in vitro* studies revealed the structural effect of long-chain unsaturated FAs on antibacterial activity [18], it remains unknown how they interact and destabilize membranes in real-time.

Herein, we systematically investigated the molecular self-assembly and membrane interaction of LCFAs—linolenic acid (LNA, C18:3), linoleic (LLA, C18:2), and oleic acid (OA, C18:1)— on supported lipid bilayer (SLB) platforms in real-time (**Figure 4.1**). SLB platforms were selected as model cell membranes because they are well-suited for accessing the interfacial activity of membrane-active molecules, as well as being compatible with a diverse array of surface-sensitive methods. We first investigated the molecular aggregation of these compounds at various concentrations using fluorescence spectroscopy. Then, the real-time membrane remodeling by long-chain unsaturated FAs was monitored with the quartz crystal microbalance-dissipation (QCM-D). Finally, time-lapsed fluorescence microscopy imaging techniques were performed for scrutinizing membrane morphological responses between LCFAs and model cell membranes.

A

	Long-chain Unsaturated Fatty Acids		
	Linolenic Acid (LNA)	**Linoleic Acid (LLA)**	**Oleic Acid (OA)**
Carbon: Unsaturated bonds	C18:3	C18:2	C18:1
Chemical structure	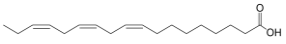	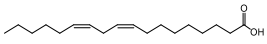	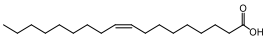
3D molecular structure	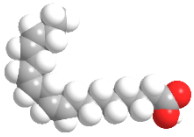	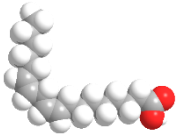	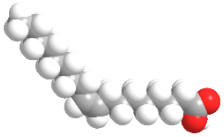
Melting point (℃)	-11.0 [28]	-5.0 [28]	13.4 [29]
Surface p*K*a at 25℃	8.28 [30]	9.24 [30]	9.85 [30]

B

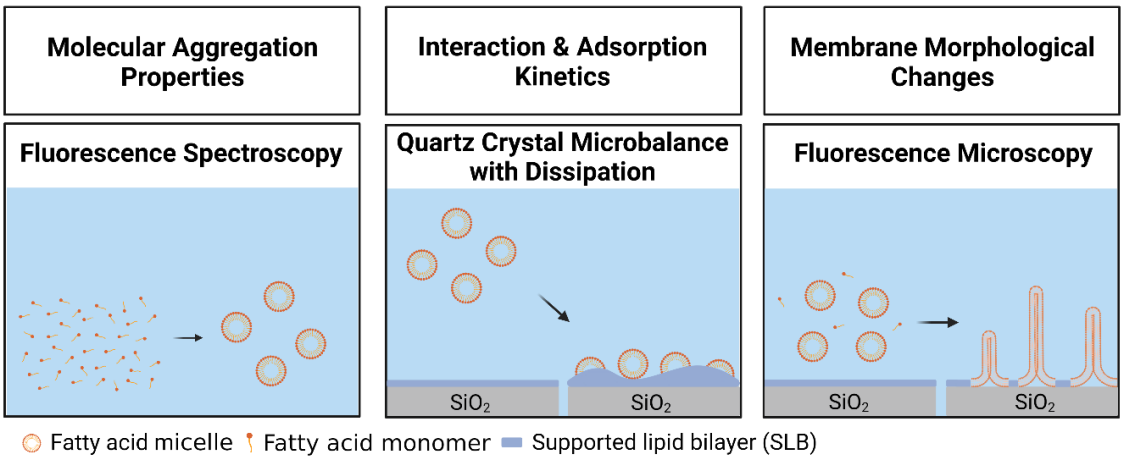

Figure 4.1 Overview of experimental strategy with materials used in this study. (A) Molecular structure and physicochemical properties of long-chain unsaturated fatty acids used in this study. (B) Schematic illustration of experimental strategy to characterize how long-chain unsaturated fatty acids interact with lipid membrane via supported lipid bilayer (SLB) platforms.

4.2 Materials and Methods

4.2.1 Materials

1,2-Dioeloyl-sn-glycero-3-phosphocholine (DOPC) and 1,2-dioleoyl-sn-glycero-3-phosphoethanolamine-N-(lissamine rhodamine B sulfonyl) (ammonium salt) (Rh-PE) were purchased from Avanti Polar Lipids, Inc. (Alabaster, Al). 1-Pyrenecarboxaldehyde was purchased from Sigma-Aldrich (St Louis, MO). Linolenic acid, linoleic acid, and oleic acid were obtained from Sigma-Aldrich (St. Louis, MO). Phosphate-buffered saline (PBS) was procured from Gibco (Carlsbad, CA). All solutions were prepared using Milli-Q-treated deionized water (>18 MΩ·cm) (Millipore, Billerica, MA).

4.2.2 Preparation of Fatty Acid Solutions

Stock solutions of linolenic acid (LNA), linoleic acid (LLA), and oleic acid (OA) were prepared by dissolving the weighed amount of the compound in ethanol to a concentration of 50 mM. Aliquots of the stock solution were diluted 100-fold with PBS

solution to a final concentration of 500 μM. Complete solubilization was promoted by heating the test samples to 70 °C for 15 min. Subsequently, the solutions were cooled down to room temperature and further diluted in 2-fold steps. Given the p*K*a values of linolenic acid (~8), linoleic acid (~ 9), and oleic acid (~10), all FAs are presumed to be protonated under the test conditions. The incorporation of these LCFAs into zwitterionic liposomes introduces a negative charge on the liposome surface [31, 32]. Consequently, the charge state of these FAs are anionic relative to the membrane. All solutions were freshly prepared prior to each experiment.

4.2.3 Fluorescence Spectroscopy

Experiments were conducted with a multimode microplate reader (Tecan Spark®, Tecan Trading AG, Switzerland) to determine the critical micelle concentration (CMC) values of the tested compounds at room temperature (21 °C). The test samples were excited at 365.5 nm, and the fluorescence emission spectrum of the probe in PBS was recorded from 400 nm to 600 nm in the presence of increasing concentrations of the samples [33]. The stock solution of the probe was initially prepared in methanol at a concentration of 5 mM. The test samples were prepared by adding a certain amount of the probe stock to a glass vial, and then the methanol was fully evaporated using nitrogen gas. A PBS solution containing an appropriate amount of test compound was then added to the vial, followed by vortexing and nitrogen gas evaporation. The final concentration of the probe was 0.1 μM. All measurements for each sample were scanned ten times and averaged.

4.2.4 Quartz Crystal Microbalance with Dissipation (QCM-D)

QCM-D experiments were conducted to characterize the SLB formation process and the interaction between the antimicrobial lipids and the SLB with a four-channel Q-Sense E4 instrument (Q-Sense AB, Gothenburg, Sweden). The QCM-D technique monitors the shifts in the frequency (Δf) and energy dissipation (ΔD) of an oscillating, piezoelectric quartz crystal sensor chip as a function of time, and these shifts reflect the mass and viscoelastic properties, respectively, of the adsorbed phospholipid film on the surface [34].

The sensor chips had a fundamental frequency of 5 MHz [34-36] and were coated with a sputter-coated, 50 nm-thick layer of silicon dioxide (model no. QSX 303, Biolin Scientific). For cleaning purposes, the sensor chips were sequentially washed with SDS 1% (wt/vol), water, and ethanol, and then dried with a gentle stream of nitrogen gas, followed by oxygen plasma treatment for 1 min with an Expanded Plasma Cleaner (PDC-002, Harrick Plasma, Ithaca, NY). In the experiments, SLBs composed of a 1,2-dioleoylsn-glycero-3-phosphocholine (DOPC) lipid were initially formed using the solvent-assisted lipid bilayer (SALB) technique [37]. The SLBs were single-use for each experiment. A baseline signal in aqueous buffer solution (10 mM Tris, 150 mM NaCl, pH 7.5) was recorded, followed by the exchange to isopropanol solution, addition of 0.5 mg/mL DOPC lipid in isopropanol solution, and finally solvent exchange with PBS buffer solution to form the SLB. Subsequently, after the stabilization of a baseline signal in aqueous Tris buffer solution, 0.1 mg/mL bovine serum albumin (BSA) in an aqueous solution was added as a blocking agent to prevent the nonspecific protein adsorption onto the SLB-coated surface [38]. After completing the bilayer formation, the test compound in PBS solution was added under a continuous flow rate. A washing step with PBS solution completed the procedure. All liquid samples were added into the measurement chamber under continuous flow conditions using a peristaltic pump (Reglo Digital, Ismatec, Glattbrugg, Switzerland) and the flow rate was set at 50 μL/min. During the experiments, the temperature in the measurement cell was maintained at 25.0 ± 0.5 °C. Measurement data were collected at the third (n = 3), fifth (n = 5), and seventh (n = 7) overtones using the Q-Soft software program (Biolin Scientific). All presented data were collected at the fifth (n = 5) overtone. Data processing was performed in the Q-Tools (Biolin Scientific) and OriginPro (OriginLab, Northampton, MA) software programs.

4.2.5 Time-lapse Fluorescence Microscopy

Epifluorescence microscopy experiments were conducted to directly observe real-time membrane morphological changes in the SLBs on glass surfaces upon treatment with LNA, LLA, and OA. The experiments were conducted using an Eclipse TI-E inverted microscope (Nikon, Tokyo, Japan) with a 60× magnification (NA = 1.49) oil-immersion

objective lens (Nikon), and the micrograph images were collected with an iXon 512 pixel × 512 pixel EMCCD camera (Andor Technology, Belfast, Northern Ireland). The pixel size was 0.267 × 0.267 μm2. A fiber-coupled mercury lamp (Intensilight C-HGFIE, Nikon) was used to illuminate fluorescently labeled DOPC phospholipids (0.5 mol % Rh-PE) through a TRITC filter [39]. SLBs were fabricated using the solvent-assisted lipid bilayer (SALB) method [37, 40] on a glass slide that was enclosed within a microfluidic flow-through chamber (sticky slide VI 0.4, Ibidi, Germany). After complete lipid bilayer formation, the measurement chamber was rinsed with PBS buffer solution, and then the test compound was introduced to the chamber at a continuous flow rate of 50 μL/min. Time-lapse micrographs were recorded every 5 s for a total duration of 60 min at concentrations above CMC and below CMC, under room temperature (21 °C). The initial time, t = 0 s, was defined by when the test compound was initially injected. Image analysis was conducted using the ImageJ software program (National Institutes of Health, Bethesda, MD, USA).

4.2.6 Statistical Analysis

All experiments were performed in triplicate unless otherwise stated. A two-tailed T-test was carried out to analyze statistical significances of the measurements by using Microsoft Excel (Microsoft, Redmond, WA, USA). Correlations with p-value < 0.05 were considered statistically significant (*p < 0.05, **p < 0.01, and ***p < 0.001).

4.3 Results and Discussion

4.3.1 Determination of the Critical Micelle Concentration

We first measured the critical micelle concentration (CMC) values of LNA, LLA, and OA, as the single-chain antimicrobial lipids (e.g., FAs) are suggested to disrupt the phospholipid membrane by forming a micellar structure [27]. To determine the CMC values, fluorescence spectroscopy experiments were conducted with the fluorescent probe technique by measuring the fluorescence emission spectrum of 1-pyrenecarboxaldehyde in different concentrations of the test compounds. When present in an aqueous environment,

1-pyrenecarboxaldehyde exhibits a peak emission wavelength of 473 nm, and in the presence of micelle aggregates, the peak wavelength decreases as a result of the probe intercalating into the hydrophobic region of the micelle, which corresponds to a decrease in dielectric constant [41, 42]. Thus, CMC is defined as the lowest concentration at which the peak wavelength begins to decrease, and the formation of micelles becomes energetically favorable. The CMC experiments were performed under the typical physiological value of pH 7.5. The CMC value of LNA in PBS was determined to be 160 μM, which is consistent with the literature value [43] (**Figure 4.2A**). Similarly, the CMC of LLA was determined to be 60 μM, which also agrees with the literature value [44] (**Figure 4.2B**). Finally, the CMC value of OA was found to be 20 μM, which agrees with the value reported in the literature [43, 44] (**Figure 4.2C**). Together, lower CMC values were observed when there are few unsaturated bonds. This trend in CMC values can be attributed to the lower hydrophobicity of the LCFA with more C=C bonds. When one -CH_2- group is lost, it results in the formation of one double bond, which reduces hydrophobicity and increases solubility, leading to higher CMC values [14]. Taken together, the results indicate that the unsaturation degree affects the self-assembly of the FAs and therefore LNA has a higher CMC value than other long-chain unsaturated FAs.

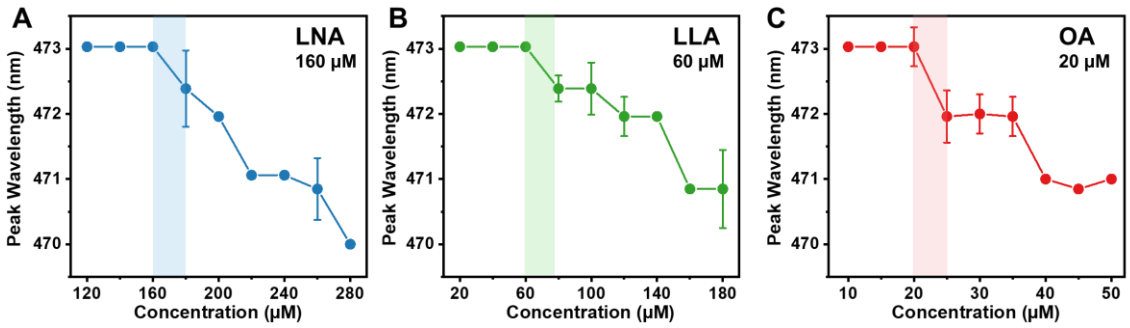

Figure 4.2 Determination of critical micelle concentration (CMC) values for linolenic acid (LNA), linoleic acid (LLA), and oleic acid (OA) using fluorescence spectroscopy. Peak wavelength is shown as a function of compound concentration in PBS buffer for (A) LNA, (B) LLA, and (C) OA. The CMC value is defined as the highest test concentration at which no peak shift occurs. Data are reported as mean ± standard deviation from six technical replicates (n = 6).

4.3.2 Interaction between Long-Chain Unsaturated Fatty Acids and Supported Lipid Bilayers

We then performed QCM-D experiments to probe the membrane remodeling behavior of LNA, LLA, and OA against zwitterionic DOPC supported lipid bilayer (SLBs) under physiological conditions. The QCM-D technique measures the changes in frequency (*Δf*) and energy dissipation (*ΔD*) signals that occur due to the mechanistic interaction between SLBs and antimicrobial lipids that are reflected as mass and viscoelastic properties. Zwitterionic DOPC lipid compositions were used to fabricate the SLB platform for two reasons. First, phosphocholine lipids are widely found in biological membranes, and second, the lipid composition has demonstrated distinct membrane morphological responses in previous studies [45-50]. The single-component SLBs with zwitterionic DOPC lipids were formed by the solvent-assisted lipid bilayer (SALB) method [37]. As for complete SLB formation, an initial baseline recording was obtained in an aqueous buffer solution, after which the solution was exchanged for a water-miscible isopropanol solution. Next, 0.5 mg/mL DOPC lipid in isopropanol was deposited on the silicon dioxide-coated sensor surface. The solution was then exchanged back to the aqueous buffer solution. The homogenous SLB formation was confirmed by the final resonance frequency (*Δf*) and energy dissipation (*ΔD*) shifts of -26.4 ± 0.6 Hz and $0.3 \pm 0.1 \times 10^{-6}$, respectively, as reported in the literature [51, 52]. The bilayer was further confirmed to be defect-free by a bovine serum albumin (BSA) blocking step, which resulted in a negligible change in frequency of less than 1 Hz and a significant reduction in protein adsorption to the SLB-coated silica substrate by over 94%. Subsequently, SLBs were exposed to LNA, LLA, and OA at fixed concentrations under continuous flow conditions, followed by a washing step with an equivalent buffer solution, and QCM-D measurements for *Δf* and *ΔD* shifts were tracked in real-time. Of note, t = 0 min denotes SLB formation and t = 5 min indicates the addition of the test compounds under continuous flow conditions in the measurement chamber. The binding dynamics obtained for the test compounds are presented below.

Linolenic Acid (LNA). Figure 4.3 presents the effects of LNA on membrane remodeling of SLBs. Upon treatment with 500 μM LNA, there was a rapid decrease in Δf to around -39.2 ± 1.8 Hz and an increase in ΔD to $8.6 \pm 0.2 \times 10^{-6}$ (**Figure 4.3A**). The increase in mass and dissipation showed that LNA was attached to the SLB right after the treatment. Upon reaching the critical point, the measurement responses began to reverse,

with a swift rise in *Δf* and decline in *ΔD* and ultimately stabilizing at -5.3 ± 2.5 Hz and 6.3 ± 0.4 × 10^{-6}, respectively. The rapid increase in frequency and large residual dissipation shift may suggest that the LNA treatment had partially destabilized the lipid membrane. Interestingly, a buffer washing step led to a decrease in *Δf* shift to around −31.0 ± 2.4 Hz and *ΔD* shift to 0.2 ± 0.1 × 10^{-6}. This intricate behavior parallels with capric acid treatment on SLBs at high concentrations in which similar QCM-D signals were observed for the lipid−membrane interaction with a net *Δf* and *ΔD* decrease but contrasts with lauric acid treatment on SLBs at concentrations above CMC with a net *Δf* and *ΔD* increase [48, 49]. LNA produced a similar activity profile at the concentration of 250 μM (**Figure 4.3B**). The *Δf* signal gradually decreased to -38.1 ± 3.4 Hz and then increased before finally stabilizing at -28.0 ± 1.7 Hz. At the same time, the signal *ΔD* followed the same pattern, reaching a critical point at 12.2 ± 0.5 × 10^{-6} before decreasing and stabilizing at 7.9 ± 0.3 × 10^{-6}. During the buffer washing step, there was a sharp decrease in both the *Δf* and *ΔD* signals, with final values of -28.0 ± 2.1 Hz and 0.3 ± 0.4 × 10^{-6}, respectively. When treated with LLA at lower concentrations (125 μM and below), there were either insignificant or minimal changes in both *Δf* and *ΔD* signals (**Figure 4.3C-F**). This observation is consistent with previous reports in which the micellar form of lipids facilitates membrane disruption [46]. Collectively, the QCM-D findings suggest that LNA micelles are active against SLBs, whereas LNA monomers are primarily inactive against SLBs at concentrations below CMC value (160 μM).

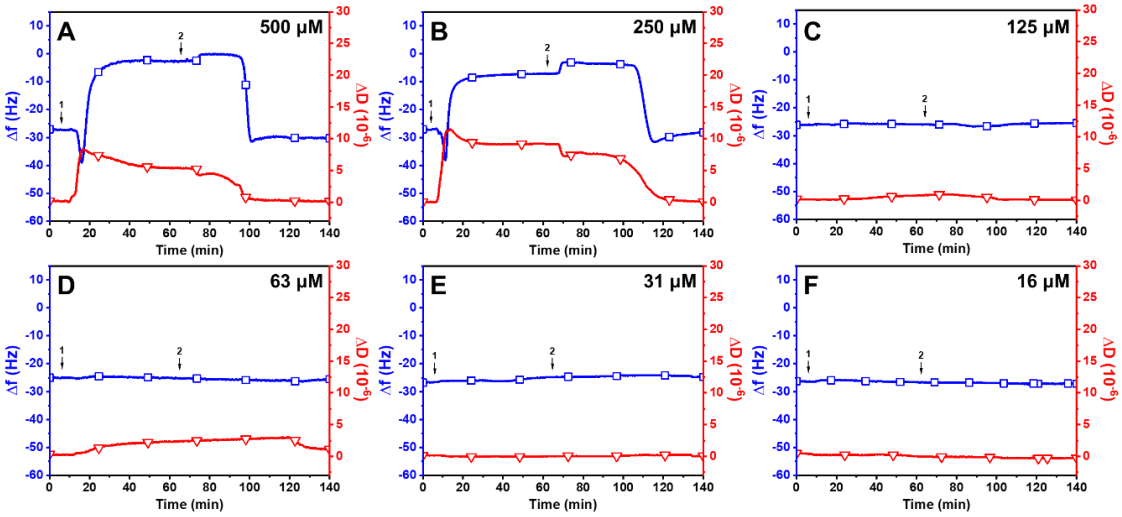

Figure 4.3 QCM-D investigation of concentration-dependent LNA treatment on SLBs at pH 7.5. *Δf* (blue line with squares) and *ΔD* (red line with triangles) shifts are presented as a function of time for (A) 500 μM, (B) 250 μM, (C) 125 μM, (D) 63 μM, (E) 31 μM, and (F) 16 μM LNA. The initial baseline values recorded at t = 0 min indicate the formation of an SLB on the silica surface. LNA was introduced at t = 5 min (arrow 1), followed by a buffer washing step (arrow 2) after the measurement signals stabilized.

Linoleic Acid (LLA). **Figure 4.4** displays the effects of LLA on the membrane remodeling of SLBs. Treatment with 500 μM LLA resulted in a rapid reduction in *Δf* shift to -39.3 ± 2.7 Hz and an increase in *ΔD* shift to 9.8 ± 0.4 × 10^{-6} (**Figure 4.4A**). The *Δf* signal subsequently began to increase to -11.0 ± 2.0 Hz and *ΔD* signal reached around 4.5 ± 0.2 × 10^{-6} before gradually increasing. After a buffer washing step, the *Δf* measurement began to increase with a decrease in *ΔD* and stabilize at around -1.5 ± 1.0 Hz and 5.1 ± 0.4 × 10^{-6}. Similar results were observed when SLBs were treated with 250 μM LLA with values around -4.5 ± 0.9 Hz and 4.2 ± 0.6 × 10^{-6} (**Figure 4.4B**). Notably, unlike LNA, no significant alterations were noticed in *Δf* and *ΔD* shifts after buffer washing for up to 140 minutes at 500 uM and 250 uM of LLA treatment. Due to LLA having a straighter hydrophobic tail compared to LNA, LNA may not bind as strongly to the membrane as LLA [16, 53]. Conversely, rapid changes were measured in *Δf* and *ΔD* shifts following buffer washing at 125 uM of LLA treatment, leading to the final values of *Δf* shift of -31Hz and *ΔD* shift of 1.62 × 10^{-6} (**Figure 4.4C**). The same trend was detected at 63 uM of LLA following buffer washing, even though the changes in *Δf* and *ΔD* shifts transpired faster than in 125 uM of LLA treatment (**Figure 4.4D**). It is noteworthy that LLA had a slow binding rate to the membrane at lower concentrations, and the changes of *Δf* and *ΔD* shifts occurred rapidly after buffer washing. This result indicates that the binding strength between LLA micelles and membrane diminishes as the concentration of LLA decreases [54]. Similar to the activity profile of LNA, there were negligible changes in both measurement responses at lower concentrations (31 μM and 16 μM, **Figure 4.4E and F**). Thus, LLA was not active against SLBs at concentrations below the CMC value of 60 μM.

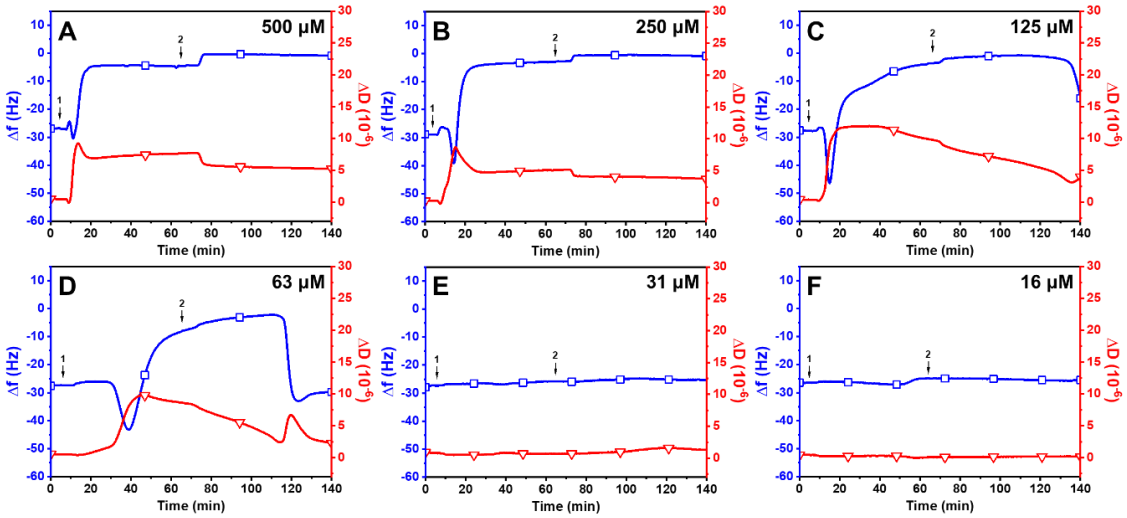

Figure 4.4 QCM-D investigation of concentration-dependent LLA treatment on SLBs at pH 7.5. *Δf* (blue line with squares) and *ΔD* (red line with triangles) shifts are presented as a function of time for (A) 500 μM, (B) 250 μM, (C) 125 μM, (D) 63 μM, (E) 31 μM, and (F) 16 μM LLA. The initial baseline values recorded at t = 0 min indicate the formation of an SLB on the silica surface. LLA was introduced at t = 5 min (arrow 1), followed by a buffer washing step (arrow 2) after the measurement signals stabilized.

Oleic Acid (OA). The effects of OA on the remodeling of SLBs are presented in **Figure 4.5**. Upon treatment with 500 μM OA, there was an immediate decrease in *Δf* shift to -43 Hz and an increase in *ΔD* shift to 11.3 × 10^{-6} (**Figure 4.5A**). Subsequently, the *Δf* signal increased to around -12.7 ± 0.4 Hz, while the *ΔD* signal decreased to around 9.8 ± 1.2 × 10^{-6} and gradually decreased thereafter. After buffer washing, the *Δf* signal began to increase to -2.1 ± 0.2 Hz and the *ΔD* began to decrease to 3.4 ± 0.9× 10^{-6}. Similar profiles were observed at 250 μM OA with final *Δf* and *ΔD* values around -1.3 ± 0.2 Hz and 4.6 ± 0.5 × 10^{-6} (**Figure 4.5B**). Interestingly, OA causes membrane remodeling at a slower rate than LNA and LLA at equivalent concentrations. The 125 μM of OA induced slow membrane remodeling on SLB compared to higher OA concentrations (**Figure 4.5C**). A similar trend was observed after treatment with 63 μM OA (**Figure 4.5D**). 31 μM of OA did not cause much change in membrane mass and viscoelasticity although the concentration was above CMC (**Figure 4.5E**). Instead, the OA micelles moderately attached to the SLB, leading to a gradual decrease in *Δf* shift and an increase in *ΔD* shift, even after buffer washing. Even though low concentrations of OA micelles can trigger

membrane remodeling due to its lower CMC value compared to LNA and LLA, the impact of OA on the alteration of the membrane's structure was not as significant as that of LNA and LLA. This is likely due to the fact that OA's unsaturated tails have a limited degree of conformational flexibility in their shape, resulting in a more rigid packing and reduced fluidity in the membrane [55]. When SLBs were treated with OA monomer at below CMC, there was negligible change in *Δf* and *ΔD* shifts (**Figure 4.5F**), demonstrating that OA monomer does not induce membrane destabilization.

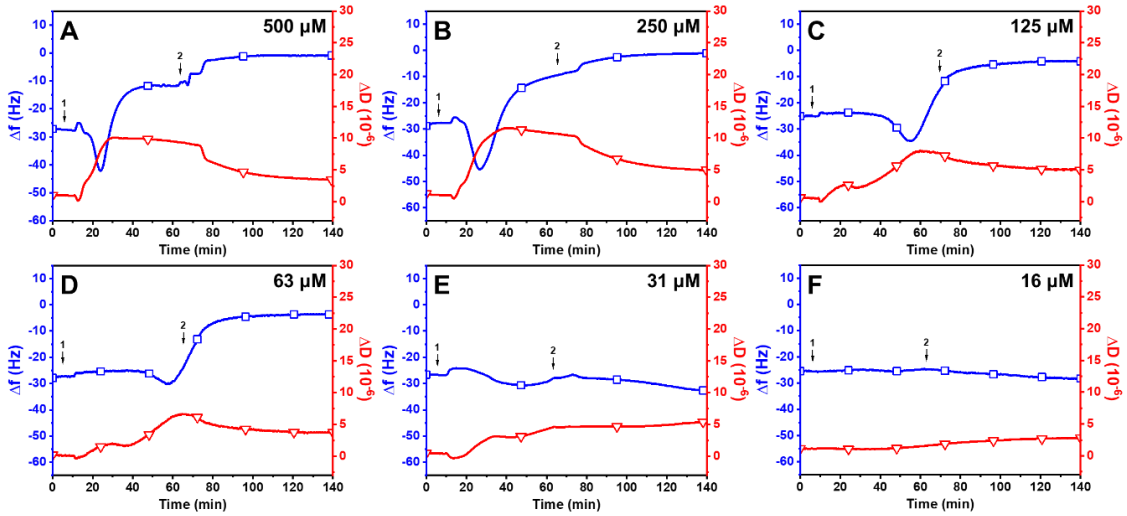

Figure 4.5 QCM-D investigation of concentration-dependent OA treatment on SLBs at pH 7.5. *Δf* (blue line with squares) and *ΔD* (red line with triangles) shifts are presented as a function of time for (A) 500 μM, (B) 250 μM, (C) 125 μM, (D) 63 μM, (E) 31 μM, and (F) 16 μM OA. The initial baseline values recorded at t = 0 min indicate the formation of an SLB on the silica surface. OA was introduced at t = 5 min (arrow 1), followed by a buffer washing step (arrow 2) after the measurement signals stabilized.

4.3.3 Trend in Interaction Kinetics of Long-Chain Unsaturated Fatty Acids on Supported Lipid Bilayers

To better understand the membrane-active mechanism of long-chain unsaturated FAs, we examined the trends in the interaction between 3 FAs (LNA, LLA, and OA) and SLBs at concentrations above and below their respective CMC values. Treatment with 250-500 μM LNA resulted in rapid binding and membrane remodeling (**Figure 4.6A**). LLA

showed similar response profiles above CMC, but the interaction kinetics slowed down at lower concentrations (**Figure 4.6B**). OA exhibited slower kinetics compared to LNA and LLA across all concentrations (**Figure 4.6C**). At high concentrations above CMC, it appears that LCFAs with a higher degree of unsaturation require fewer molecules to drive the system to a non-lamellar phase and induce curvature, possibly due to the increased kinkiness structure and the greater intermolecular distance between the FA molecules [56]. The double bond-induced negative curvature increases concentration dependently and this leads to an increase in bending rigidity, which is determined by the trade-off between born energy and hydrophobic interaction energy [14]. Conversely, when the concentrations of FAs are below their respective CMC in which they are predominantly in the monomer state, none of them induce membrane remodeling with negligible change of Δf and ΔD shifts compared to those induced by FAs above their CMC values (**Figure 4.6D-F**). This highlights the importance of micelle formation for the antimicrobial membrane-active functionality of FAs. It is noteworthy that long-chain unsaturated FAs with a higher degree of unsaturation led to significant changes in the membrane, but also that they require high concentrations to initiate the membrane remodeling, as CMC values are generally proportional to the degree of unsaturation. Moreover, it is important to note that the concentrations above CMC align with the minimum inhibitory concentration (MIC) values reported for these FAs; 200-400 μM for LNA against *Staphylococcus aureus* and *Streptococcus pyogenes* [57], 114-125 μM for LLA against *Bacillus cereus* [58], and 53 μM for OA against *Porphyromonas gingivalis* [59]. Although the MIC values may vary in the literature due to the different experimental conditions, it can be inferred that long-chain unsaturated FAs primarily induce concentration-dependent membrane remodeling behavior *in vitro*, particularly above their respective CMC values. Taken together, the observed trends support that the degree of unsaturation of LCFAs has a significant effect on the self-assembly properties and the differential membrane remodeling behavior on phospholipid membranes.

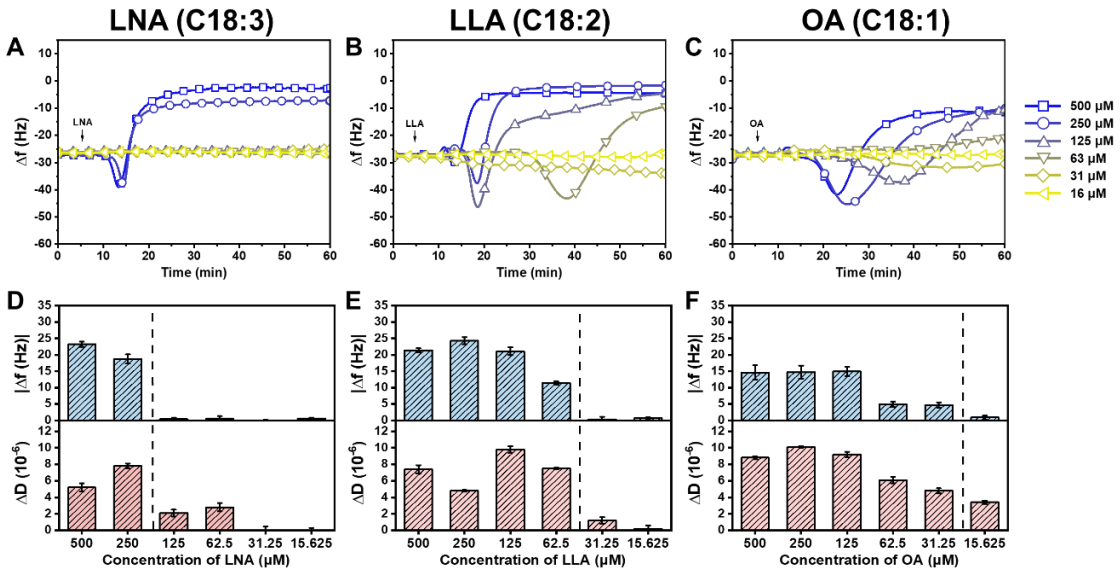

Figure 4.6 The trend in QCM-D measurement shifts for membrane remodeling behavior induced by different long-chain unsaturated fatty acids. *Δf* shifts are presented as functions of time for (A) LNA, (B) LLA, and (C) OA at 16 – 500 uM concentrations until 60 min. Fatty acids were added at t = 5 min (arrow). Column graph of the net $|\Delta f|$ shifts (upper panel) and *ΔD* shifts (lower panel) at 60 min for (D) LNA, (E) LLA, and (F) OA, respectively. The net $|\Delta f|$ and *ΔD* shifts are reported as $|\Delta f_{measured} - \Delta f_{baseline}|$ and $\Delta D_{measured} - \Delta D_{baseline}$ shifts, respectively. The dotted line in the lower panel represents above (to the left) and below (to the right) CMC ranges. Data are reported as mean ± standard deviation from n = 3 measurements. The asterisk indicates a statistically significant difference between the initial concentration below CMC and the individual above CMC values (* for p-value < 0.05, ** for p-value < 0.01, and *** for p-value < 0.001).

4.3.4 Observation of Membrane Morphological Responses in Supported Lipid Bilayers

To further characterize membrane remodeling, we performed time-lapsed fluorescence microscopy to directly observe the response in membrane morphology induced by the FAs. The SLBs, which comprises 99.5 mol % DOPC and 0.5 mol % Rh-PE, were fabricated on a hydrophilic silicon dioxide surface using the SALB method at pH 7.5. Once the baseline signal was established to signify bilayer formation, the test compounds in an equivalent PBS buffer solution were introduced under continuous flow conditions. Of note, t = 0 min corresponds to the time when the solution containing the test compounds

reached the measurement chamber. Based on the fluorescence spectroscopy and QCM-D measurement results, we tested LNA, LLA, and OA at one concentration above CMC and one below CMC. The selected concentrations were 500 μM and 63 μM for LNA, 250 μM and 31 μM for LLA, and 125 μM and 16 μM for OA.

Linolenic acid (LNA). Figure 4.7A presents the time-lapsed morphological responses in the SLB induced by 500 μM LNA (above CMC). Within 2.8 min of treatment, a profuse number of short tubules protruded from the SLBs, in which the bright spots represent the nucleation sites. Shortly after, within 11.4 min, the tubules started to aggregate with higher fluorophore concentrations, and small dark patches started to emerge in the background. As the time scale reached the final mark, aggregated tubules became more prominent with the fluorescence intensity of the background decreasing significantly. This discrepancy may be attributed to the tubules growing out of the focal plane [60]. Upon buffer washing, the tubules were removed, and the various sizes of dark patches appeared with very few bright spots of fluorescence, indicating that LNA induced membrane disruption in the SLB membrane. In marked contrast, minimal morphological responses were observed with only a few long tubules protruding from the SLB when treated with 63 μM LNA (**Figure 4.7B**). Upon buffer washing, most tubules were removed with negligible morphological changes in the SLB, which agrees with QCM-D results.

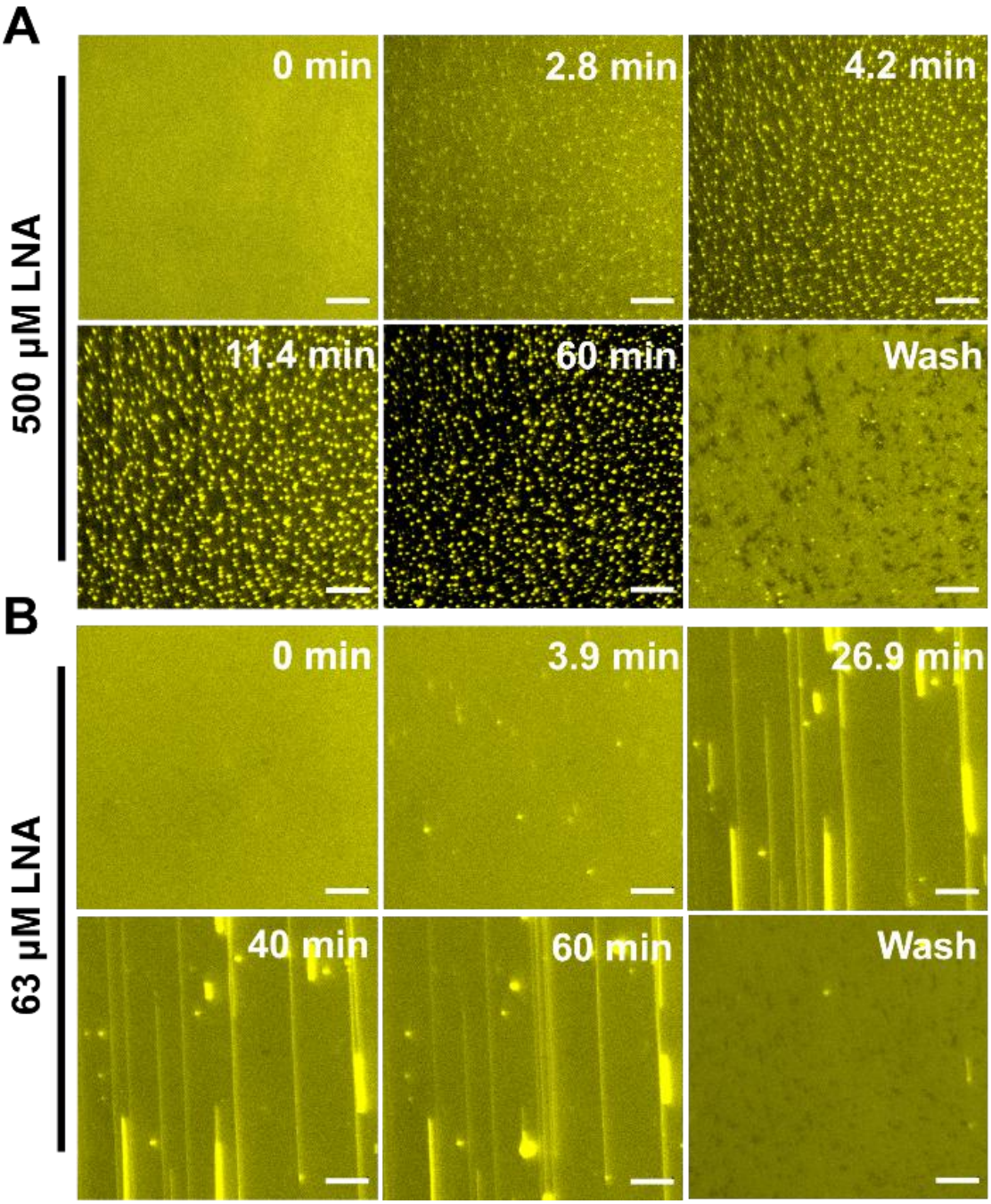

Figure 4.7 Time-lapse microscopic observation of LNA-induced membrane morphological responses on SLBs at concentrations above CMC and below CMC, respectively. (A) Image snapshots at various time points depict nucleation sites from which aggregates proliferate upon treatment of SLB with 500 μM LNA at pH 7.5. (B) Image snapshots at various time points depict nucleation sites from which tubules grow upon treatment of SLB with 250 μM LNA at pH 7.5. At t = 0 min, LNA solution was added to the measurement chamber. The scale bar is 20 μm.

Linoleic acid (LLA). **Figure 4.8A** shows the morphological change in the SLB over time when treated with 250 μM LLA under continuous flow conditions. Initially, many elongated tubules protruded from the SLBs within 5.6 min, and shortly after, the tubules started to lose their fibrils and aggregate with small dark patches emerging from the SLB. As time passed, aggregated tubules with fibrils (approximately 2 μm in length) became more prominent, and the fluorescence intensity of the background decreased significantly like LNA treatments. Interestingly, compared to LNA treatments, the number of nucleation sites (indicated by bright spots) was lower, and the size of tubules was larger when treated with LLA. This implies that a higher amount of LLA is required to attach to the membrane to induce morphological remodeling, resulting in large lipid aggregations. These findings are consistent with the interaction kinetics of FAs measured in QCM-D. Upon buffer washing, the tubules were removed and various sizes of dark patches with very few bright spots of fluorescence appeared. It appears that LLA induced membrane remodeling in the SLB membrane. **Figure 4.8B** presents the morphological responses in an SLB upon treatment with 31 μM LLA (below CMC). In this case, a relatively smaller number of tubules protruded from the SLB, and a decrease in fluorescence intensity in the background was not observed, indicating that there was less membrane morphological change compared to LLA treatments above CMC. After buffer washing, most of the aggregates were removed from SLBs, which is in agreement with QCM-D results.

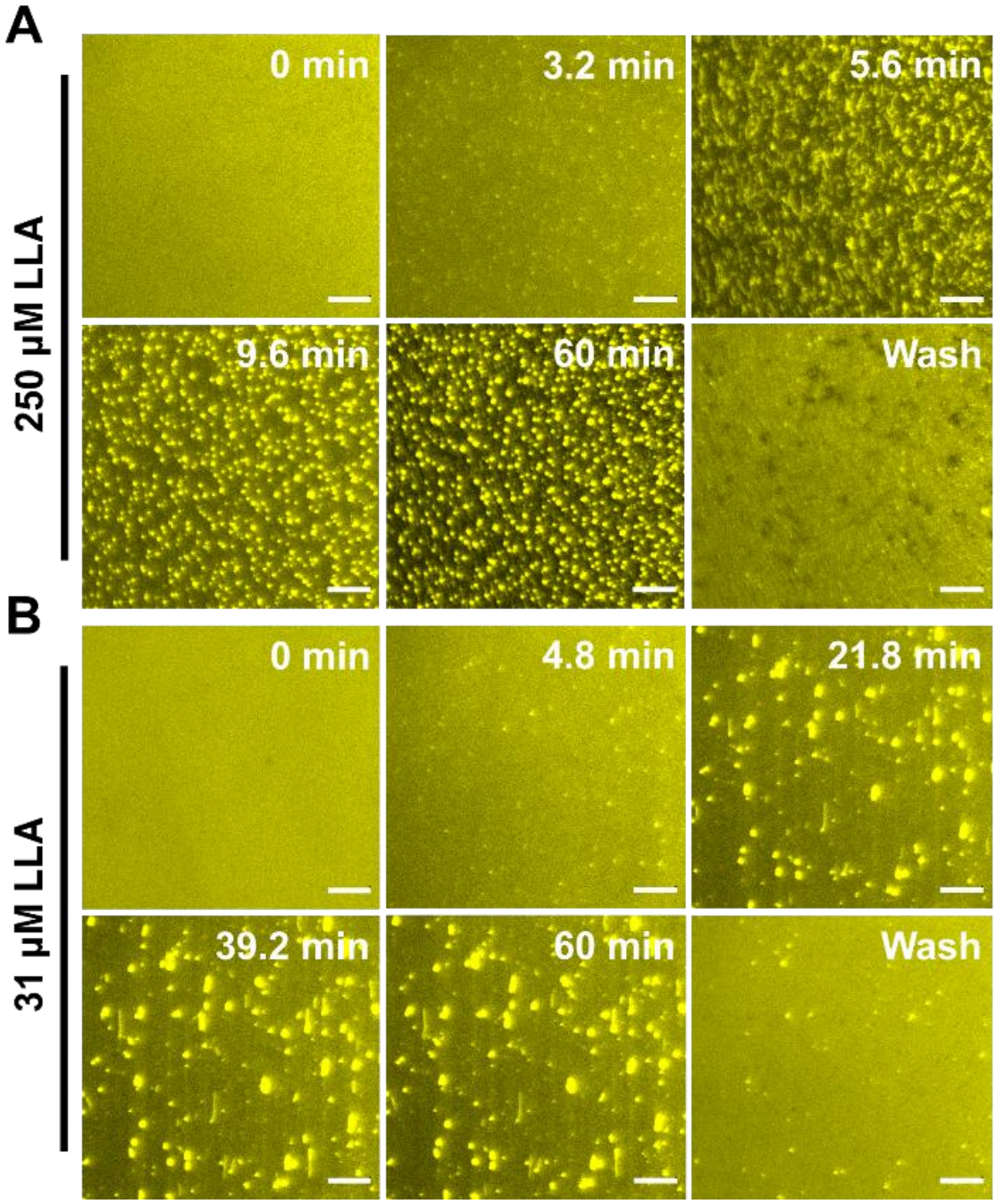

Figure 4.8 Time-lapse microscopic observation of LLA-induced membrane morphological responses on SLBs at concentrations above CMC and below CMC, respectively. (A) Image snapshots at various time points depict nucleation sites from which aggregates proliferate upon treatment of SLB with 250 μM LLA at pH 7.5. (B) Image snapshots at various time points depict nucleation sites from which tubules grow upon treatment of SLB with 31 μM LLA at pH 7.5. At t = 0 min, LLA solution was added to the measurement chamber. The scale bar is 20 μm.

Oleic acid (OA). **Figure 4.9A** presents the time-lapsed snapshots of the SLB morphological response induced by 125 μM OA (above CMC). Within a few minutes, elongated tubules began to form and varied in length between 2-30 μm. The tubules remained stagnant until 14.6 min when the fibrils got absorbed and led to the increase in the tubule size, which may be a result of potential aggregation. Of note, the tubules formed by OA were bigger than those induced by LNA and LLA, suggesting that decreased kinkiness of OA requires large aggregation for membrane remodeling. Upon the buffer washing step, the tubules remained attached to the lipid bilayer but decreased in size. It appears that the highest saturation degree and hydrophobicity of OA resulted in strong insertion in the membrane. At 16 μM OA (below CMC), dense coverage of tubules with fibrils protruded from the SLB after OA treatments (**Figure 4.9B**). Upon buffer washing, most tubules were removed but a few bright spots of tubules that are bigger than the tubules produced by 31 μM LLA remained translocated in the SLB. This may suggest that due to the smaller kink molecular structure of OA, the packing between phospholipids increases and decreases the membrane fluidity, resulting in bigger tubules remaining adsorbed in the membrane [61, 62].

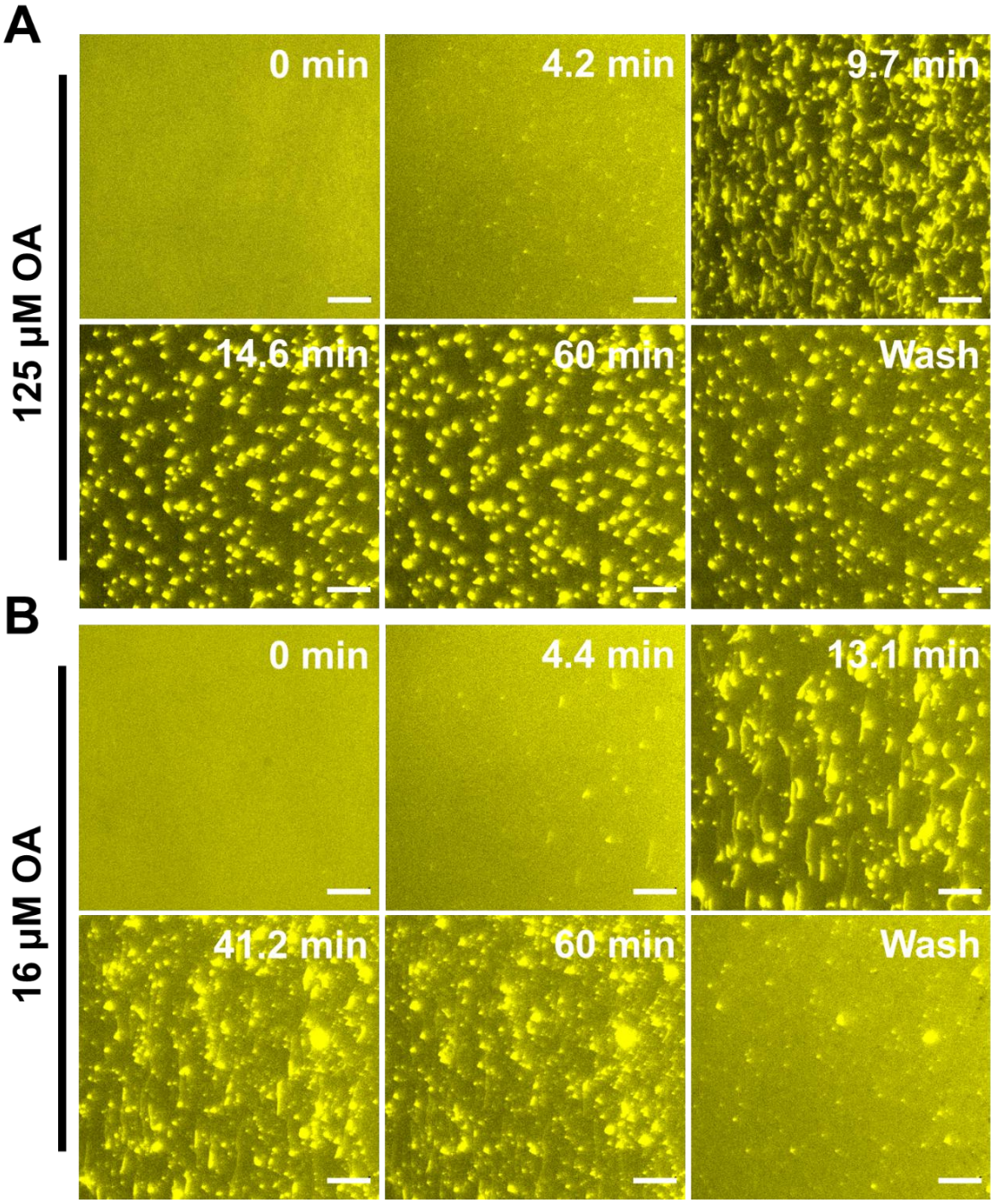

Figure 4.9 Time-lapse microscopic observation of OA-induced membrane morphological responses on SLBs at concentrations above CMC and below CMC, respectively. (A) Image snapshots at various time points depict nucleation sites from which aggregates proliferate upon treatment of SLB with 125 μM OA at pH 7.5. (B) Image snapshots at various time points depict nucleation sites from which tubules grow upon treatment of SLB with 16 μM OA at pH 7.5. At t = 0 min, LLA solution was added to the measurement chamber. The scale bar is 20 μm.

4.4 Conclusion

In this work, we investigated the real-time membrane remodeling effects of long-chain unsaturated FAs—linolenic acid (LNA, C18:3), linoleic (LLA, C18:2), and oleic acid (OA, C18:1)— using model membranes and systematic biophysical measurements. LNA had a higher CMC value than other UFAs, indicating the unsaturation degree affects the self-assembly property of the FAs. Using the combination of QCM-D and fluorescence microscopy, we discovered that the FAs caused distinct changes in membrane morphology in a concentration-dependent manner, which was characterized by the development of tubules protruding from the lipid bilayer membrane. We also identified that the compounds induced membrane remodeling activity against SLBs at concentrations primarily above their respective CMC values. The results showed that LNA exhibited the highest membrane remodeling ability, suggesting that the FAs with a higher degree of unsaturation lead to significant change in the membrane remodeling process, but that they also required high concentrations to initiate the remodeling due to the increased CMC values.

The distinct membrane interaction behaviors of these FAs can be attributed to their molecular structures, which govern their physicochemical interactions with lipid bilayers. The degree of unsaturation plays a crucial role: LNA and LLA, with multiple double bonds, introduce kinks in their hydrocarbon chains, disrupting tight lipid packing and enhancing their ability to destabilize membranes. These kinks generate curvature stress, promoting membrane remodeling processes such as tubule formation and aggregation. In contrast, OA, with a single double bond, has a straighter hydrocarbon chain, resulting in more rigid packing and reduced membrane perturbation.

Overall, this study provides valuable insights into the molecular mechanisms underlying the membrane interaction behaviors of long-chain unsaturated FAs. By highlighting the role of self-aggregation properties and unsaturation degrees, these findings contribute to a deeper understanding of how these compounds destabilize membranes, paving the way for the development of effective antimicrobial strategies.

References

[1] S. De, S. Malik, A. Ghosh, R. Saha, B. Saha. *RSC Advances*. **2015**, 5(81), 65757-65767.

[2] A.P. Desbois. *Recent Pat Antiinfect Drug Discov*. **2012**, 7(2), 111-22.

[3] C.B.B. Farias, F.C.G. Almeida, I.A. Silva, T.C. Souza, H.M. Meira, R.d.C.F. Soares da Silva, J.M. Luna, V.A. Santos, A. Converti, I.M. Banat, L.A. Sarubbo. *Electronic Journal of Biotechnology*. **2021**, 51, 28-39.

[4] I. Mnif, D. Ghribi. *J Sci Food Agric*. **2016**, 96(13), 4310-20.

[5] P.J. Naughton, R. Marchant, V. Naughton, I.M. Banat. *J Appl Microbiol*. **2019**, 127(1), 12-28.

[6] M. Nitschke, C.A. Marangon. *Critical Reviews in Biotechnology*. **2022**, 42(2), 294-310.

[7] A. Varvaresou, K. Iakovou. *Letters in Applied Microbiology*. **2015**, 61(3), 214-223.

[8] A. Bhadani, K. Iwabata, K. Sakai, S. Koura, H. Sakai, M. Abe. *RSC Advances*. **2017**, 7(17), 10433-10442.

[9] A. Bhadani, A. Kafle, T. Ogura, M. Akamatsu, K. Sakai, H. Sakai, M. Abe. *Current Opinion in Colloid & Interface Science*. **2020**, 45, 124-135.

[10] C. Verma, C.M. Hussain, M.A. Quraishi, A. Alfantazi. *Advances in Colloid and Interface Science*. **2023**, 311, 102822.

[11] H.L. Halliday. *Journal of Perinatology*. **2008**, 28(1), S47-S56.

[12] R. Jahan, A.M. Bodratti, M. Tsianou, P. Alexandridis. *Advances in Colloid and Interface Science*. **2020**, 275, 102061.

[13] N. Lourith, M. Kanlayavattanakul. *International Journal of Cosmetic Science*. **2009**, 31(4), 255-261.

[14] Z. Shen, Q. Zhang, X. Li, Q. Chen. *Minerals*. **2020**, 10(10), 905.

[15] G. Casillas-Vargas, C. Ocasio-Malavé, S. Medina, C. Morales-Guzmán, R.G. Del Valle, N.M. Carballeira, D.J. Sanabria-Ríos. *Prog Lipid Res*. **2021**, 82, 101093.

[16] A.P. Desbois, V.J. Smith. *Applied Microbiology and Biotechnology*. **2010**, 85(6), 1629-1642.

[17] H. Thormar. In *Lipids and Essential Oils as Antimicrobial Agents*. **2011**, pp. 25-45.

[18] A.P. Desbois, V.J. Smith. *Appl Microbiol Biotechnol*. **2010**, 85(6), 1629-42.

[19] H. Thormar, H. Hilmarsson. *Chem Phys Lipids*. **2007**, 150(1), 1-11.

[20] R. Clark. *Substances Generally Recognized as Safe (GRAS) Contents*. **2015**.

[21] T.-H. Huang, P.-W. Wang, S.-C. Yang, W.-L. Chou, J.-Y. Fang. *Marine Drugs*. **2018**, 16(8), 256.

[22] G.R. Kelm, R.R. Wickett. In *The Role of Fatty Acids in Cosmetic Technology, in: M.U. Ahmad (Ed.), Fatty Acids*, AOCS Press. **2017**, pp. 385-404.

[23] X. Vecino, L. Barbosa-Pereira, R. Devesa-Rey, J.M. Cruz, A.B. Moldes. *Journal of the Science of Food and Agriculture*. **2015**, 95(2), 313-320.

[24] A.M. Lykke, S.B. Gregersen, E.A. Padonou, I.H.N. Bassolé, T.K. Dalsgaard. *Lipids*. **2021**, 56(4), 357-390.

[25] A.P. Desbois, T. Lebl, L. Yan, V.J. Smith. *Appl Microbiol Biotechnol*. **2008**, 81(4), 755-64.

[26] H. Galbraith, T.B. Miller, A.M. Paton, J.K. Thompson. *J Appl Bacteriol*. **1971**, 34(4), 803-13.

[27] C.Q. Sun, C.J. O'Connor, A.M. Roberton. *FEMS Immunol Med Microbiol*. **2003**, 36(1-2), 9-17.

[28] A. Zotos, V.A. Bampidis. *Journal of Food Composition and Analysis*. **2014**, 33(2), 181-186.

[29] J. Yang, K. Gan, S. Li, Y. Gai, Z. Zhang, S. Yan, Y. Chen, X. Zhang, Y. Lu, J. Xu. *Ceramics International*. **2017**, 43(14), 11361-11366.

[30] J.R. Kanicky, D.O. Shah. *Journal of Colloid and Interface Science*. **2002**, 256(1), 201-207.

[31] M.C. Dixon. *J Biomol Tech*. **2008**, 19(3), 151-8.

[32] P. Jönsson, M.P. Jonsson, J.O. Tegenfeldt, F. Höök. *Biophys J*. **2008**, 95(11), 5334-48.

[33] M. Ashaduzzaman, M. Kunitake. *International Letters of Chemistry, Physics and Astronomy*. **2013**, 6, 55-62.

[34] M. Rodahl, F. Höök, A. Krozer, P. Brzezinski, B. Kasemo. *Review of Scientific Instruments*. **1995**, 66(7), 3924-3930.

[35] M. Rodahl, F. Höök, C. Fredriksson, C.A. Keller, A. Krozer, P. Brzezinski, M. Voinova, B. Kasemo. *Faraday Discussions*. **1997**, 107, 229-246.

[36] M. Rodahl, B. Kasemo. *Review of Scientific Instruments*. **1996**, 67, 3238-3241.

[37] S.R. Tabaei, J.H. Choi, G. Haw Zan, V.P. Zhdanov, N.J. Cho. *Langmuir*. **2014**, 30(34), 10363-73.

[38] K. Glasmästar, C. Larsson, F. Höök, B. Kasemo. *Journal of Colloid and Interface Science*. **2002**, 246(1), 40-47.

[39] J.A. Jackman, Z. Zhao, V.P. Zhdanov, C.W. Frank, N.J. Cho. *Langmuir*. **2014**, 30(8), 2152-60.

[40] A.R. Ferhan, B.K. Yoon, S. Park, T.N. Sut, H. Chin, J.H. Park, J.A. Jackman, N.J. Cho. *Nat Protoc*. **2019**, 14(7), 2091-2118.

[41] K. Chandrasekaran, J.K. Thomas. *Journal of the American Chemical Society*. **1983**, 105(21), 6383-6389.

[42] K. Kalyanasundaram, J.K. Thomas. *Journal of the American Chemical Society*. **1977**, 99(7), 2039-2044.

[43] Y. Wang, L. Jiang, Q. Shen, J. Shen, Y. Han, H. Zhang. *RSC Advances*. **2017**, 7(66), 41561-41572.

[44] K.S. Tang. *Lipids Health Dis*. **2014**, 13, 197.

[45] L.M. Kawakami, B.K. Yoon, J.A. Jackman, W. Knoll, P.S. Weiss, N.-J. Cho. *Langmuir*. **2017**, 33(51), 14756-14765.

[46] D. Thid, J.J. Benkoski, S. Svedhem, B. Kasemo, J. Gold. *Langmuir*. **2007**, 23(11), 5878-81.

[47] E.R. Valle-González, J.A. Jackman, B.K. Yoon, S. Park, T.N. Sut, N.-J. Cho. *Langmuir*. **2018**, 34(45), 13745-13753.

[48] B.K. Yoon, J.A. Jackman, M.C. Kim, N.J. Cho. *Langmuir*. **2015**, 31(37), 10223-32.

[49] B.K. Yoon, J.A. Jackman, M.C. Kim, T.N. Sut, N.-J. Cho. *Langmuir*. **2017**, 33(11), 2750-2759.

[50] B.K. Yoon, J.A. Jackman, E.R. Valle-González, N.J. Cho. *Int J Mol Sci*. **2018**, 19(4).

[51] N.J. Cho, C.W. Frank, B. Kasemo, F. Höök. *Nat Protoc*. **2010**, 5(6), 1096-106.

[52] C.A. Keller, B. Kasemo. *Biophys J*. **1998**, 75(3), 1397-1402.

[53] M. Ikawa, J.J. Sasner, J.F. Haney. *Hydrobiologia*. **1997**, 356(1), 143-148.

[54] D.L.A. Greenway, K.G.H. Dyke. *Journal of General Microbiology*. **1979**, 115(1), 233-245.

[55] G.L. Nicolson, M.E. Ash. *Biochimica et Biophysica Acta (BBA)-Biomembranes*. **2014**, 1838(6), 1657-1679.

[56] A.I.I. Tyler, J.L. Greenfield, J.M. Seddon, N.J. Brooks, S. Purushothaman. *Frontiers in Cell and Developmental Biology*. **2019**, 7.

[57] C.J. Zheng, J.-S. Yoo, T.-G. Lee, H.-Y. Cho, Y.H. Kim, W.G. Kim. *Febs Letters*. **2005**, 579(23), 5157-5162.

[58] K.T. Yuyama, M. Rohde, G. Molinari, M. Stadler, W.-R. Abraham. *Antibiotics*. **2020**, 9(11), 788.

[59] S.A. Eltigani, M.M. Eltayeb, A. Ishihara, J. Arima. *Journal of Food Biochemistry*. **2019**, 43(11).

[60] J.C. Waters. *J Cell Biol*. **2009**, 185(7), 1135-48.

[61] P.C. Calder, P. Yaqoob, D.J. Harvey, A. Watts, E.A. *Biochem J*. **1994**, 300(2), 509-18.

[62] S. Leekumjorn, H.J. Cho, Y. Wu, N.T. Wright, A.K. Sum, C. Chan. *Biochim Biophys Acta*. **2009**, 1788(7), 1508-16.

Chapter 5

Exploring the Membrane-Active Interactions of Antimicrobial Long-Chain Fatty Acids Using a Supported Lipid Bilayer Model for Gram-Positive Bacterial Membranes

The complexity of bacterial lipid membranes poses challenges for traditional antimicrobial assays, necessitating innovative approaches. Herein, we successfully fabricated model bacterial supported lipid bilayers (SLBs) that closely replicate the characteristics of Gram-positive bacteria using the solvent-assisted lipid bilayer (SALB) technique. By employing quartz crystal microbalance with dissipation and fluorescence microscopy, we investigated the interactions between these bacterial mimetic membranes and long-chain unsaturated fatty acids. Specifically, linolenic acid (LNA) and linoleic acid (LLA) demonstrated interaction behaviors correlated with the critical micelle concentration (CMC) on Gram-positive membranes, resulting in membrane remodeling and removal at micellar state. In contrast, oleic acid (OA), exhibited membrane insertion and CMC-independent activity on the Gram-positive membranes. These findings shed light on the intricate molecular mechanisms governing the interactions between long-chain unsaturated fatty acids and model bacterial membranes. Importantly, this study underscores the potential of using biologically relevant model bacterial membrane systems to develop innovative strategies for combating bacterial infections and designing effective therapeutic agents.

5.1 Introduction

The bacterial lipid membrane, a vital structural component of bacterial cells, is essential for numerous biological functions and has garnered significant attention in the fields of microbiology, drug development, and antimicrobial research [1-5]. This lipid bilayer membrane enveloping the bacterial cells not only acts as a protective barrier against external threats but also serves as a dynamic interface for crucial biomolecular interactions [2, 6-8]. Therefore, understanding the intricate nature of these interactions is paramount for advancing our knowledge of bacterial resistance mechanisms, combating bacterial infections, and developing novel therapeutic agents, such as FAs-based drugs [9, 10]. Furthermore, as the emergence of antibiotic-resistant bacterial strains has underscored the pressing need to devise innovative strategies to address bacterial infections, the design of antibacterial agents relies heavily on comprehending how these molecules disrupt the bacterial membrane, which offers a wide array of lipid and protein targets that can be exploited without leading to multi-drug resistance [11-14]. This knowledge not only aids in the development of more effective treatments but also allows for the prediction and prevention of resistance mechanisms that bacteria may employ. However, the study of bacterial membrane interactions presents its own set of challenges. Traditional *in vitro* biological assay methods often fall short in accurately replicating the complex nature of bacterial membranes [15, 16]. The presence of charged lipids, the nanometre dimensions, and other intricacies within bacterial membranes makes it difficult to mimic their properties faithfully [17]. As a result, there is a pressing need for innovative approaches to investigate membrane interactions more accurately.

Supported lipid bilayers (SLBs) have great potential for advancing research in bacterial membranes as their planar geometry allows compatibility with various surface sensing techniques and high-resolution imaging tools [16]. However, creating fluid and stable SLBs that faithfully mimic bacterial membranes, particularly those of complex compositions with a high percentage of charged lipids, remains challenging as the success of SLB formation by commonly used vesicle fusion methods heavily relies on the preparation of high-quality vesicles and is typically limited to specific substrate supports and lipid composition [18]. Specifically, bacterial membranes consist of intricate lipid

mixtures that encompass anionic phospholipids such as cardiolipin (CL) and phosphatidylglycerol (PG), and cationic phospholipids like Lysyl-PG [17, 19]. The Gram-positive membrane contains approximately 80% charged lipids, while the phospholipid membrane of Gram-negative bacteria has around 30% charged lipids [20, 21]. This disparity in charged lipid contents results in strong electrostatic interactions between the lipids and the substrate surface, which, in turn, influences lipid motion within the model membrane [22, 23].

To overcome these challenges, we utilized the solvent-assisted lipid bilayer (SALB) method to fabricate SLBs that mimic the characteristics of Gram-positive bacterial membrane (**Figure 5.1A-B**). The SALB method represents an advanced and meticulously engineered approach that enables the precise fabrication of SLBs featuring various lipids including highly charged lipids, applied to a diverse range of substrates [24, 25]. Upon successful fabrication of model bacterial membrane, we then systematically investigated the real-time interactions between long-chain unsaturated FAs and the bacterial SLB platform (**Figure 5.1C**). Herein, our aim is to capture the physicochemical properties of the Gram-positive bacterial membranes, considering that LCFAs typically exhibit limited efficacy against Gram-negative bacteria [26]. The selection of long-chain unsaturated FAs was predicated on their potential as natural and effective entities with low probability for developing resistance for developing novel antimicrobial agents [27, 28]. Our previous research has focused on the intermolecular self-assembly of FAs and the FA-lipid membrane interactions with zwitterionic SLB platforms, providing valuable insights into their interactions with lipid bilayers [29]. Building upon this foundation, the scope of the SLB platforms is expanded to emulate bacterial membranes, thereby establishing a more biologically relevant model system. This expansion provides detailed insights into the molecular interactions of long-chain unsaturated FAs with Gram-positive bacterial membranes.

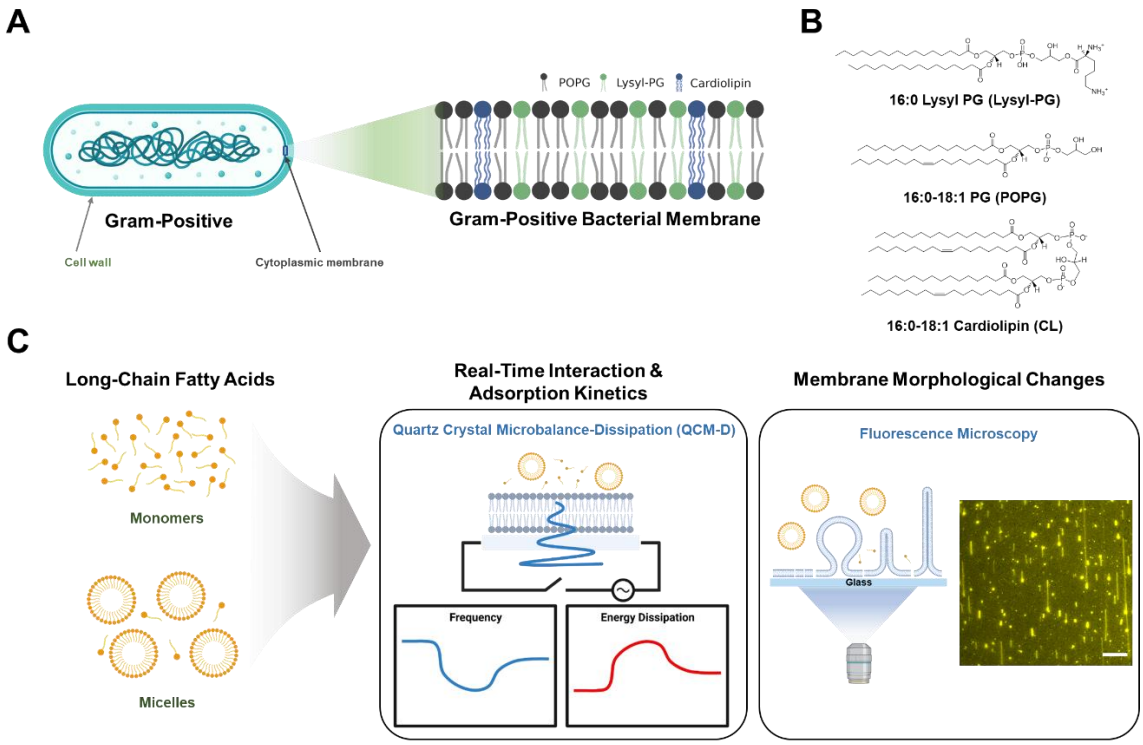

Figure 5.1 Experimental framework for investigating the interaction of antimicrobial long-chain fatty acids with model bacterial membrane platforms. (A) Schematics illustrating the membrane structure of Gram-positive bacteria with representative lipid compositions. (B) Chemical structure of the lipids utilized in model bacterial membrane platforms. Lysyl-PG is a bicationic membrane lipid, POPG and CL are anionic membrane lipids found in the plasma membranes of Gram-positive bacteria. (C) Schematics illustrating the experimental strategy used to investigate the interaction of long-chain fatty acids with model bacterial membranes, utilizing QCM-D and fluorescence microscopy.

5.2 Experimental Methods

5.2.1 Reagents

1-palmitoyl-2-oleoyl-sn-glycero-3-phospho-(1′-rac-glycerol) (POPG), 1,2-dipalmitoyl-sn-glycero-3-[phospho-rac-(3-lysyl(1-glycerol))] (Lysyl-PG), 1′,3′-bis[1-Palmitoyl-2-oleoyl-sn-glycero-3-phospho]-glycerol (Cardiolipin, CL), and 1,2-dioleoyl-sn-glycero-3-phosphoethanolamine-N-(lissamine rhodamine B sulfonyl) (ammonium salt) (Rh-PE) were obtained from Avanti Polar Lipids, Inc. (Alabaster, AL). Linolenic acid (LNA), linoleic acid (LLA), and oleic acid (OA) were purchased from Sigma-Aldrich (St. Louis, MO). Phosphate-buffered saline (PBS) buffer was purchased from Gibco (Carlsbad,

CA). All solutions were prepared using Milli-Q-treated deionized water (>18 MΩ·cm) (Millipore, Billerica, MA).

5.2.2 Antimicrobial Fatty Acids Solutions Preparation

To prepare stock solutions of LNA, LLA, and OA, precise quantities of each compound were dissolved in ethanol to achieve concentration of 50 mM. These stock solutions were then diluted by a factor of 100 using a PBS solution to a concentration of 500 μM. The test samples underwent heating to 60-70 °C for 5 min to improve solubility, followed by cooling to room temperature. Subsequent dilutions were made in 2-fold increments, and all test samples were freshly prepared just prior to each experiment.

Previous research has shown that the pKa of the carboxyl group (~4.75) increases in a hydrophobic environment near physiological pH [30]. Moreover, the incorporation of LCFAs into zwitterionic liposomes imparts a negative charge on the liposome [31, 32]. Therefore, the charge state of LNA and LLA is considered to be anionic in relation to the membrane, while OA is considered to be neutral with a protonated carboxylic acid moiety due to its high pKa and its capacity to adjust the charge based on the solution's pH. This charge state information was used to elucidate the mechanistic interactions with model bacterial membranes.

5.2.3 Lipid Preparation for SLB Formation

Lipids for Gram-positive biomimetic model membrane composed of anionic POPG lipid, cationic Lysyl-PG lipid, and anionic CL lipid were mixed in a molar ratio of 65:30:5 in chloroform at a final concentration of 0.3 mg/mL. In the context of fluorescence microscopy experiments, 0.5 mol% of Rh-PE, a negatively charged fluorescent DOPC analogue, was doped in SLBs. To prepare SALB experiments, lipid films were initially desiccated using nitrogen gas and subsequently subjected to overnight storage to eliminate the organic solvent. This was followed by dissolution in ethanol at 70 °C for 3 min to achieve concentration of 1 mg/mL. Before each experiment, the solution was additionally

diluted in isopropanol.

5.2.4 Quartz Crystal Microbalance with Dissipation (QCM-D) Experiments

Formation of supported lipid bilayers (SLBs) and characterization of the interaction of the antimicrobial FAs were assessed using QCM-D using a four-channel Q-Sense E4 instrument (Q-Sense AB, Gothenburg, Sweden). QCM-D tracks changes in the frequency (Δf) and energy dissipation (ΔD) of a piezoelectric quartz crystal sensor chip with a frequency of 5 MHz, which oscillates over time, and these responses provide quantitative insights into the mass and viscoelastic property changes of the phospholipid film adsorbed on the chip surface coated with 50 nm-thick layer of silicon dioxide (model no. QSX 303, Biolin Scientific). Prior to each experiment, the sensors underwent sequential washing with SDS 1% (wt/vol), water, and ethanol. Subsequently, they were dried with nitrogen and oxygen plasma treated for 1 min using an Expanded Plasma Cleaner (PDC-002, Harrick Plasma, Ithaca, NY). In the experimental procedures, Gram-positive SLBs were established using the solvent-assisted lipid bilayer (SALB) technique [18], with heating at 70 °C. Each SLB was used only once per experiment. Initially, a baseline signal was recorded in an aqueous Tris buffer solution (10 mM Tris, 150 mM NaCl, pH 7.5). The solution was then substituted with an isopropanol solution, followed by the addition of 0.3 mg/mL Gram-positive mimetic membrane lipids in isopropanol solution, and finally, the solvent was exchanged with a PBS solution to form the SLB. Once the lipid bilayer formation was complete, the test sample in PBS solution was introduced, and the procedure was concluded with a final washing step using PBS solution. All liquid samples were introduced into the chamber via a peristaltic pump (Reglo Digital, Ismatec, Glattbrugg, Switzerland) at a flow rate set at 50 μL/min. The temperature of the cells was set at room temperature (25.0 ± 0.5 °C). Measurement data was obtained at the third (n = 3), fifth (n = 5), seventh (n = 7), and ninth (n=9) overtones using the Q-Soft software program (Biolin Scientific). The data presented was obtained at the fifth overtone, and all data processing was carried out using the Q-Tools (Biolin Scientific) and OriginPro (OriginLab, Northampton, MA) software programs.

5.2.5 Time-lapse Fluorescence Microscopy

Epifluorescence microscopy was used to examine membrane morphology alterations after treatment with LCFAs. The observations were made using an Eclipse TI-E inverted microscope (Nikon, Tokyo, Japan) with a 60× magnification (NA = 1.49) oil-immersion objective lens (Nikon) and images were captured using an iXon 512 × 512-pixel EMCCD camera (Andor Technology, Belfast, Northern Ireland). Each image had a pixel size of 0.267 × 0.267 μm^2. Fluorescently labeled phospholipids (0.5 mol % Rh-PE) were illuminated with a fiber-coupled mercury lamp (Intensilight C-HGFIE, Nikon) using a TRITC filter. The SLBs were fabricated on a glass coverslip (sticky slide VI 0.4, Ibidi, Germany) through the SALB method [18, 30, 31]. After forming the SLBs, the PBS buffer was used to rinse the chamber, and the test compounds were introduced at a flow rate of 50 μL/min. To examine the time-dependence of the effect of the FAs on the SLBs, sequential images were taken every 5 s for for 60 min at room temperature. The starting time, t = 0 s, was designated as the time when the test solution was administered. The captured images are displayed with false-color visualizations, where yellow highlights the lipid bilayer regions. The proportionate surface area of membrane defects in SLBs was measured and analyzed using the ImageJ software application (National Institutes of Health, Bethesda, MD, USA).

5.2.6 Fluorescence Recovery after Photobleaching (FRAP) Measurements

FRAP techniques were used to assess the lateral diffusivity of SLBs labeled with Rh-PE lipids, both before and after treatment with the FAs. A 532 nm, 100 mW laser (Klastech Laser Technologies, Dortmund, Germany) was employed to photobleach circular spots with a diameter of 20-μm. The photobleaching process lasted for 5 s, and fluorescence micrographs were taken every 2 s for 120 s to monitor the recovery of fluorescence. The lateral diffusion coefficients were derived from the FRAP data using a Hankel transform method [33], implemented with using Matlab (MathWorks, USA).

5.3 Results and Discussion

5.3.1 Formation and Characterization of Model Bacterial Membranes

Bacteria are known to have limited capacity to modify their fundamental membrane lipid compositions compared to other targets, which contributes to a reduced likelihood of developing drug resistance [34-36]. Therefore, understanding how antimicrobial agents interact with and disrupt bacterial membranes is crucial for developing effective therapies, as it provides insights into their mechanism of action. Many previous studies have utilized PG, PC, and PE as lipid compositions for model bacterial membranes. While such investigations have enhanced our knowledge of membrane biophysics and the effects of specific lipid components on antimicrobial function, it is imperative to consider model membranes that reproduce actual bacterial membranes. Therefore, we began by creating SLBs that closely mimic the plasma membranes of Gram-positive bacteria using the SALB method. The lipid compositions selected for the bacterial membranes matched those found in *S. aureus*. The Gram-positive bacterial SLBs were composed of POPG:Lysyl-PG:CL at the molar ratio of 65:30:5 [37], with anionic to cationic lipid proportions around 2:1 [38], at physiological pH. The significance of Lysyl-PG lipid lies in its ability to confer a positive charge to the cell envelope, creating a barrier against cationic compounds [39], including antibiotics like daptomycin and host defense antimicrobial peptides (AMPs) [38], and the significance of CL lipid lies in its capability to resist mechanisms against membrane curvature-dependent AMPs, potentially rendering the bacteria susceptible to some of the novel antimicrobial agents [40, 41]. Prior to implementing the SALB method, lipids with a high gel-to-liquid transition temperature (T_m) (e.g., Lysyl-PG has a T_m of 40℃ and CL has a T_m of 62.5℃ [42, 43]) were mixed with ethanol at a temperature of 70 °C to enhance the solubility of the lipid mixture, thus enabling the reinstatement of fluidity within the SLBs. Seyed et al previously reported that isopropanol is the most effective organic solvent for depositing charged lipids onto a SiO_2 substrate using the SALB method [18, 44]. Building upon this foundation, isopropanol was selected as the solvent medium to facilitate the solvent exchange step for the fabrication of model membranes, aligning with established protocols in the field.

To confirm the formation of SLB, QCM-D experiments were performed. The results indicated that the final resonance frequency (*Δf*) and energy dissipation (*ΔD*) responses were -26.8 ± 1.1 Hz and $0.7 \pm 0.4 \times 10^{-6}$, respectively, for Gram-positive bacterial SLB (**Figure 5.3A**), which were within the expected range for successful SLB formation [45, 46]. To evaluate membrane structural integrity, FRAP analysis was utilized to track the lateral diffusion of fluorescently labelled Rh-PE lipids in Gram-positive bacterial SLB. The photobleached spots were near-completely recovered within 2 min with over 80% mobile fraction (**Figure 5.3B**), confirming the intact fluidity of the lipid bilayer membrane [47]. Moreover, the lateral diffusivity yielded a value of 0.47 ± 0.23 $\mu m^2 s^{-1}$ (**Figure 5.2B**), indicating the slower lateral diffusion of Gram-positive bacterial membrane compared to a DOPC bilayer, which can be attributed to the existence of charged lipid species like Lysyl-PG and CL. The reduced lateral diffusion of Gram-positive bacterial SLB can most likely be attributed to tighter lateral packing induced by the four-alkyl chain structure of CL [48].

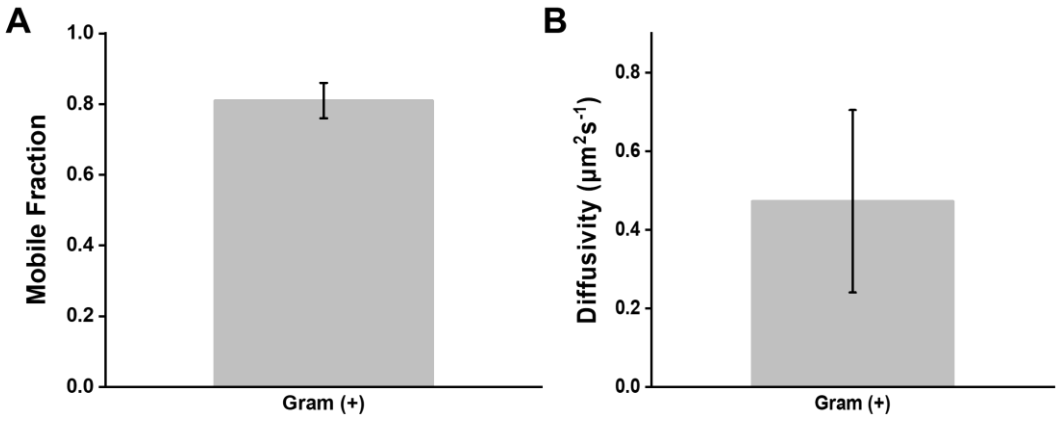

Figure 5.2 Fluorescence recovery after photobleaching (FRAP) analysis for assessing the mobility of Gram-positive bacterial SLBs. (A) Mobile fractions and (B) lateral diffusivity values for the Gram-positive lipid membrane. Data are reported as the mean ± standard deviation from n = 3 measurements.

This structural characteristic increases the average area occupied by each lipid molecules, thereby affecting the mobility of the SLB. Moreover, the low mobility value is not significantly influenced by Lysyl-PG due to its structural similarity to PG, resulting in negligible electrostatic interactions with other phospholipids. Taken together, these

findings demonstrate that Gram-positive biomimetic SLBs, composed of anionic and cationic phospholipids with high transition temperature, can be successfully formulated using the SALB method in a near physiological pH environment.

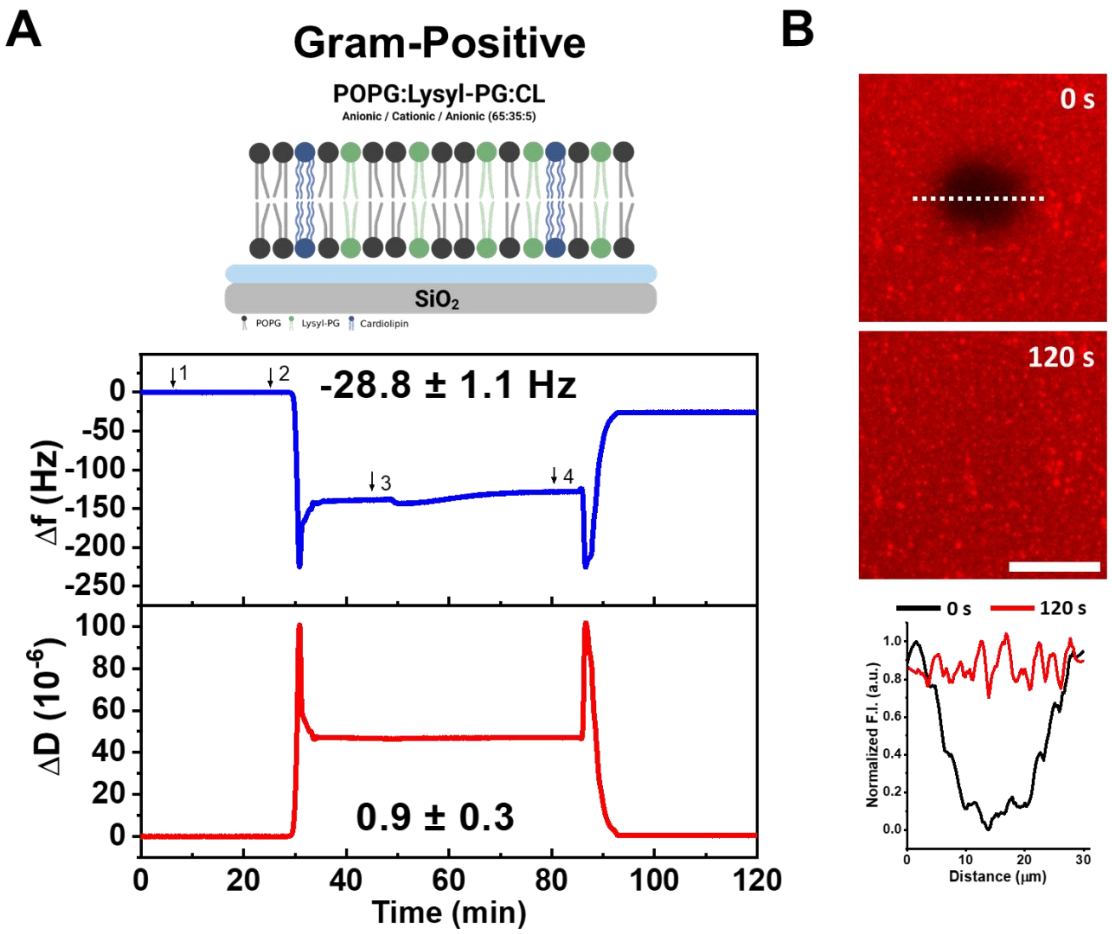

Figure 5.3 The formation of the model bacterial membrane using the SALB method on silicon dioxide and analyzed with QCM-D and fluorescence microscopy. (A) QCM-D monitoring of the SALB method using lipid compositions for the Gram-positive bacterial membrane. Arrows denote the injection of (1) buffer, (2) isopropanol, (3) lipid mixture, and (4) buffer exchange. The final values of Δf and ΔD for the membrane are reported, with all data shown as the mean ± standard deviation from n = 3 measurements. (B) Fluorescence recovery after photobleaching (FRAP) analysis for the assessment of fluidity of the Gram-positive membrane. Photobleaching was carried out at t = 0 s, with the bleached area appearing as a dark spot in the center of the micrograph. The normalized fluorescence intensity (F.I.) across the bleached region (indicated by the white dotted line in the 0s images) is shown in the corresponding cases. The F.I. values were normalized to 0.0

and 1.0 au for the minimum and maximum fluorescence intensities throughout the time, respectively. The scale bar is 20 μm.

5.3.2 Mass and Viscoelastic Property Changes Induced by Antimicrobial Long-Chain Fatty Acids on Model Bacterial Membranes

QCM-D experiments on the model bacterial membrane platforms were performed to examine the interaction between model bacterial SLBs and antimicrobial long-chain unsaturated FAs. The QCM-D method monitors alterations in frequency (Δf) and energy dissipation (ΔD) responses resulting from the dynamic interplay between model bacterial SLBs and antimicrobial FAs. These changes manifest as shifts in mass and modifications in viscoelastic characteristics. This study extends the previous research using single-component SLBs containing zwitterionic DOPC lipids [29] to model Gram-positive bacterial membrane SLBs. The aim was to enhance the understanding of membrane behaviors and mechanisms of actions of potential antimicrobial LCFAs, particularly against Gram-positive bacteria, by targeting bacterial FA synthesis and disrupting bacterial membranes [49]. Model Gram-positive bacterial SLBs were treated with linolenic acid (LNA), linoleic acid (LLA), and oleic acid (OA) at specific concentrations, and then subjected to a 60 min wash with an equivalent buffer solution. Real-time tracking of the temporal Δf and ΔD shifts with QCM-D measurements was carried out. Notably, t = 0 min marks the formation of the bacterial SLB, and t = 10 min signifies the introduction of FAs into the measurement chamber. The time-dependent binding and interaction kinetics observed for LCFAs, are detailed below.

Linolenic Acid (LNA) on Gram-Positive bacterial SLBs. Figure 5.4-5.6 illustrates the interaction dynamics of model bacterial SLBs induced by LNA. Upon exposure to 500 μM LNA was applied to Gram-positive SLBs, a sharp decrease in both Δf to approximately -63.8 ± 0.8 Hz and ΔD to $12.8 \pm 0.5 \times 10^{-6}$ occurred (**Figure 5.5A**). For the zwitterionic membranes, the maximum binding amount was approximately -39.2 ± 1.8 Hz and $8.6 \pm 0.2 \times 10^{-6}$ [29]. With the charged membranes, the binding substantially increased, which may suggest that LNA attached onto the charged membrane together with the large amount of solvent through stronger electrostatic attraction, leading to considerable membrane

remodeling. After reaching the critical juncture, measurement responses commenced to exhibit a reversal, characterized by a swift increase in Δf and a decrease in ΔD, eventually reaching a stable state at -29.6 ± 2.1 Hz and $23.8 \pm 1.6 \times 10^{-6}$, respectively. Subsequent buffer washing led to partial membrane removal with a change in Δf to around -17.0 ± 0.6 Hz and ΔD to $6.2 \pm 0.2 \times 10^{-6}$, resulting in a net Δf increase of 10.1 ± 1.4 Hz and net ΔD increase of $5.4 \pm 0.7 \times 10^{-6}$. Similarly, LNA exhibited a comparable attachment-detachment pattern on the Gram-positive membrane at 250 μM (**Figure 5.4**). The Δf signal decreased to -58.2 ± 1.9 Hz, increased after the critical point, and stabilized at -16.6 ± 2.1 Hz after buffer rinsing. The ΔD signal concomitantly increased to $15.5 \pm 0.7 \times 10^{-6}$ before stabilizing at $5.3 \pm 0.5 \times 10^{-6}$ after buffer washing.

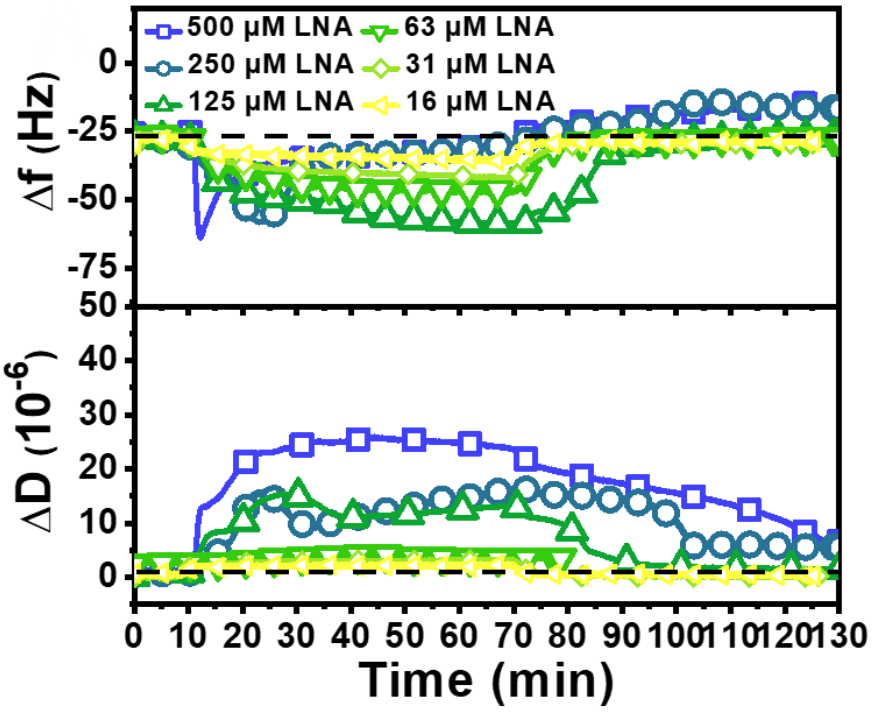

Figure 5.4 QCM-D investigation of concentration-dependent LNA treatments on model Gram-positive bacterial membranes as functions of time at concentrations of 16 μM, 31 μM, 250 μM, and 500 μM until 70 min. Fatty acid was added at t = 10 min, followed by a buffer washing step at t = 70 min. The dotted line represents the typical measurement responses for SLB formation.

Figure 5.5B illustrates a three-stage Δf vs ΔD plot after LNA treatment. An increase in mass and a decrease in rigidity occurs in the initial phase, indicating that LNA is rapidly

integrating into the membrane and subsequent membrane rearrangement between phospholipids and LNA molecules [50]. The second phase shows a reduction in mass and a further decline in rigidity, which may suggest ongoing rearrangement and expulsion of entrapped solvent or material removal. Moreover, the lower harmonics exhibit higher frequency values, suggesting that the top layer is denser, possibly due to additional LNA molecules or the displacement of more phospholipids from the bottom layer in exchange for LNA. This is promptly succeeded by a slight mass reduction and higher rigidity, implying the near-completion of membrane rearrangement and the commencement of phospholipid removal. During this stage, the shift from a relatively small spreading to the overlap of the third to ninth harmonics is evident upon buffer washing (**Figure 5.5A**), which indicates that the membrane removal affects both the bottom and top SLB layers similarly. In the final stage, there is a notable reduction in mass and an increase in rigidity upon buffer washing, signifying the removal of weakly interacting LNA attached on the phospholipids and a portion of the membrane. LNA, with the highest number of double bonds and the lowest p*K*a, is more likely to be deprotonated, reducing hydrophobic interaction energy and promoting the shift of its anionic form into the aqueous phase through hydrogen bonding with water molecules [51], resulting in weak interaction with the membrane.

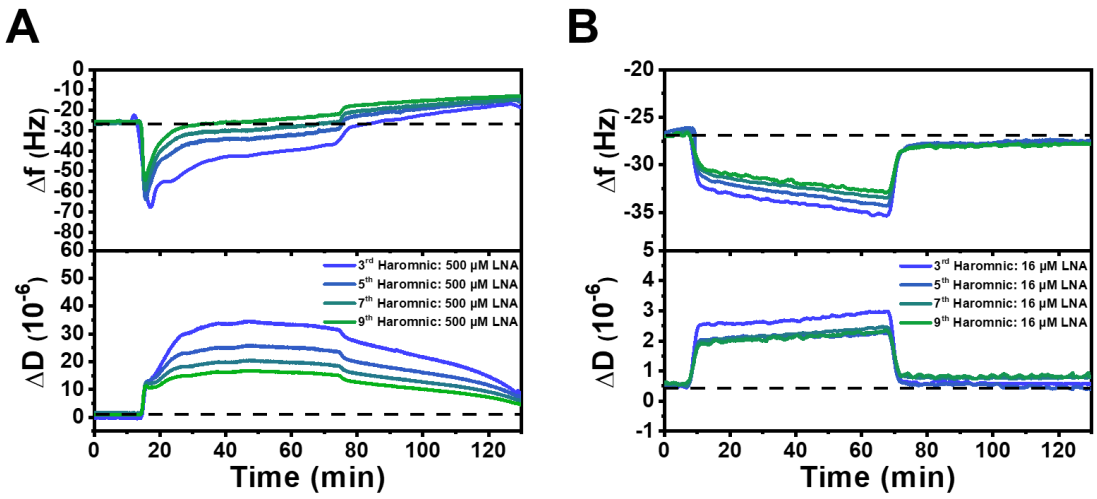

Figure 5.5 QCM-D investigation of LNA treatment on model bacterial membranes at concentrations above and below CMC values at different overtones (from third-ninth). (A and B) Representative third through ninth harmonic Δ*f* and Δ*D* vs time plots of LNA-treated Gram-positive bacterial membrane. Fatty acids were added at t = 10 min, followed by a buffer washing

step at t = 70 min. The dotted line in panels (A and B) represents the typical measurement responses for SLB formation.

By contrast, at concentrations below CMC (160 μM), LNA exhibited slow attachment to the Gram-positive membrane (**Figure 5.4**, **Figure 5.6C**), followed by rapid detachment without inducing discernible Δ*D* shift, indicating the integrity of rigid membrane without membrane remodeling. Figure 3D shows a two-stage Δ*f* vs Δ*D* plot after LNA treatment at low concentration. Stage one shows moderate mass increase and rigidity reduction, directly followed a mass reduction and rigidity increase, indicating negligible interaction between LNA and the membrane.

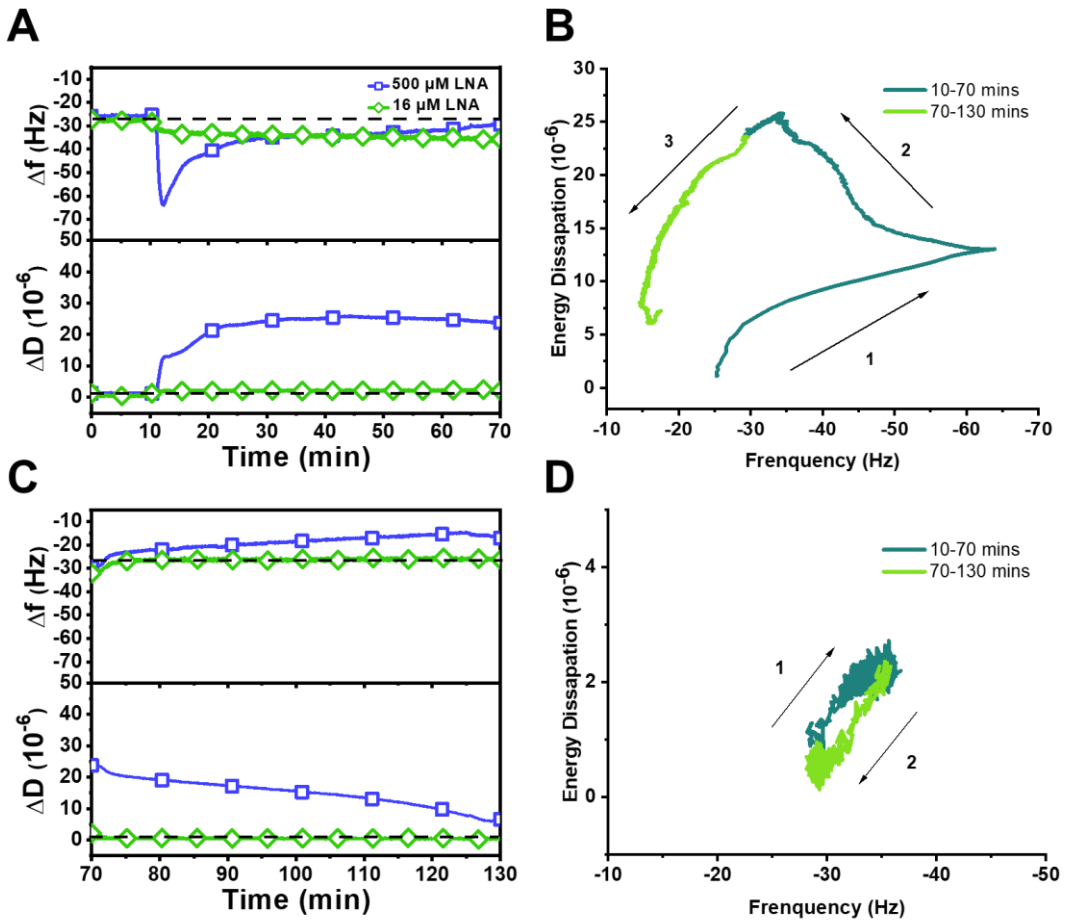

Figure 5.6 QCM-D investigation of LNA treatments on model bacterial membranes at pH 7.5. (A and C) Representative Δ*f* and Δ*D* vs time plots of LNA-treated Gram-positive bacterial membranes at concentrations of 500 μM (above CMC) and 16 μM (below CMC), and (B and D) its respective Δ*f* and Δ*D* plots. Fatty acid was added at t = 10 min, followed by a buffer washing step

at t = 70 min. The dotted line in panels (A and C) represents the typical measurement responses for SLB formation.

Linoleic Acid (LLA) on Gram-Positive bacterial SLBs. **Figure 5.7-5.9** presents the mass and viscoelastic changes of model bacterial SLBs as functions of LLA concentration. Exposure to 500 μM LLA led to a sharp drop in Δ*f* to −59.0 ± 3.0 Hz and a corresponding rise in Δ*D* to 17.4 ± 2.3 × 10^{-6} onto Gram-positive SLBs (**Figure 5.8A**). Following buffer rinsing, the Δ*f* and Δ*D* signals gradually reached equilibrium at around −18.7 ± 2.8 Hz and 26.8 ± 3.4 × 10^{-6}, respectively, resulting in a net Δ*f* increase of 9.1 ± 1.0 Hz and net Δ*D* increase of 26.7 ± 3.6 ×10^{-6}. This observed trend was consistent across varying LLA concentrations, including 250 μM, 125 μM, and 62.5 μM (**Figure 5.7**), albeit at a slower rate than LNA.

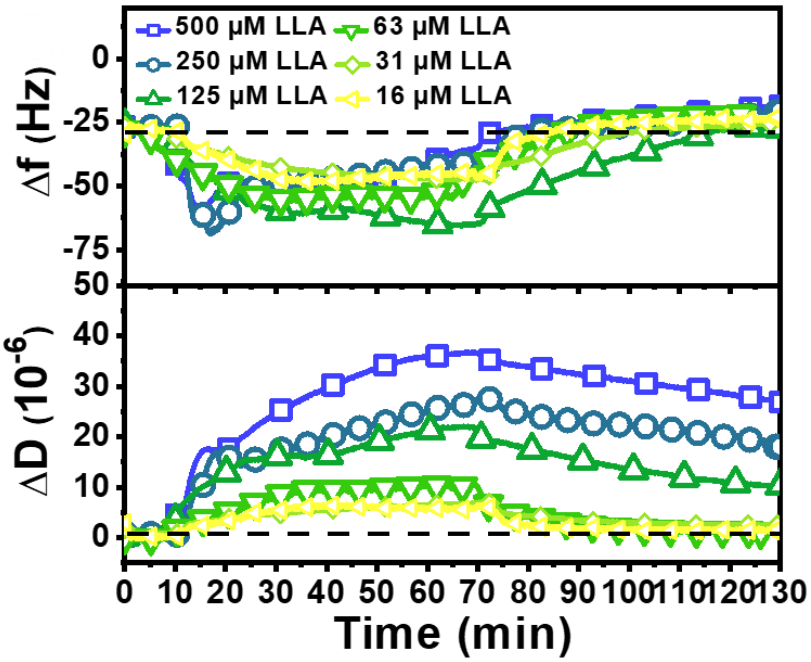

Figure 5.7 QCM-D investigation of concentration-dependent LLA treatments on model Gram-positive bacterial membranes as functions of time at concentrations of 16 μM, 31 μM, 250 μM, and 500 μM until 70 min. Fatty acid was added at t = 10 min, followed by a buffer washing step at t = 70 min. The dotted line represents the typical measurement responses for SLB formation.

The lowest harmonics recorded the greatest increase of mass and reduction in rigidity, indicating that LLA predominantly attaches to the upper section of the SLB layer (**Figure 5.8A**). Conversely, the higher harmonics, which correspond to the bottom layer, observed the most significant decrease in mass. This suggests that phospholipids may be primarily displaced from the bottom later in favor of LLA.

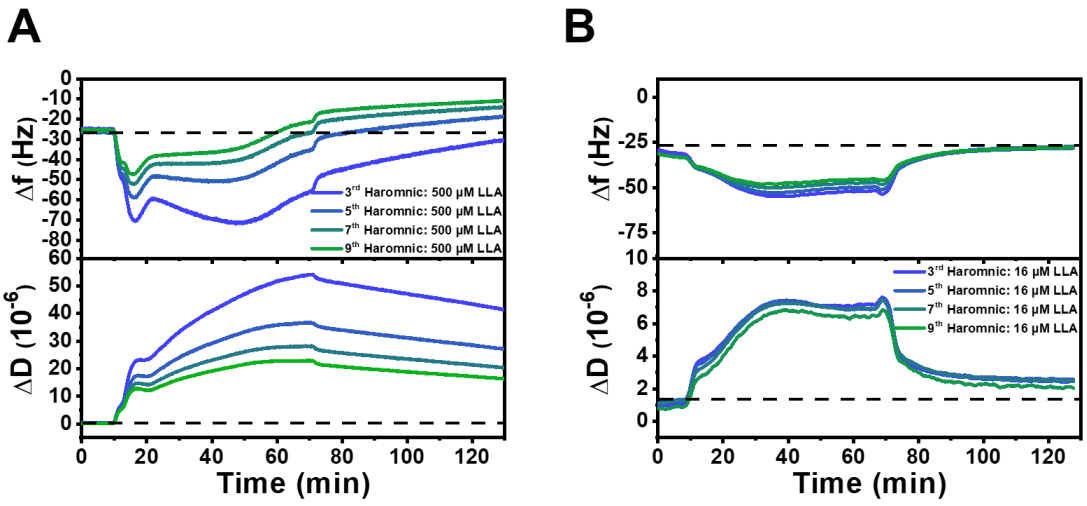

Figure 5.8 QCM-D investigation of LLA treatment on model bacterial membranes at concentrations above and below CMC values at different overtones (from third-ninth). (A and B) Representative third through ninth harmonic Δ*f* and Δ*D* vs time plots of LLA-treated Gram-positive bacterial membrane. Fatty acids were added at t = 10 min, followed by a buffer washing step at t = 70 min. The dotted line in panels (A and B) represents the typical measurement responses for SLB formation.

In **Figure 5.9B**, the Δ*f* vs Δ*D* plot illustrates a three-stage process following 500 μM LLA treatment. Similar to LNA, stage one showed mass increase and a rigidity reduction, signifying the gradual integration of LLA into the membrane, albeit at a slower rate. After reaching the turning point, stage two involved a concomitant decrease in both mass and rigidity, indicating membrane rearrangement. In the final stage, a further decrease in mass combined with an increase in rigidity is observed. Notably, the net mass change was smaller in magnitude and the net dissipation change was almost negligible with evident increased harmonic spreading after buffer washing (**Figure 5.8B**). This behavior indicates that the enhanced incorporation of LLA resulted in a more fluidic SLB, leading to reduced membrane removal.

Conversely, at concentrations below CMC (60 μM), LLA monomers had negligible effect on the Gram-positive membrane. However, the longer trend line of LLA with higher frequency and dissipation responses signifies that LLA had more impact on the membrane even at concentrations below CMC due to its physiochemical property differences (**Figure 5.9D**).

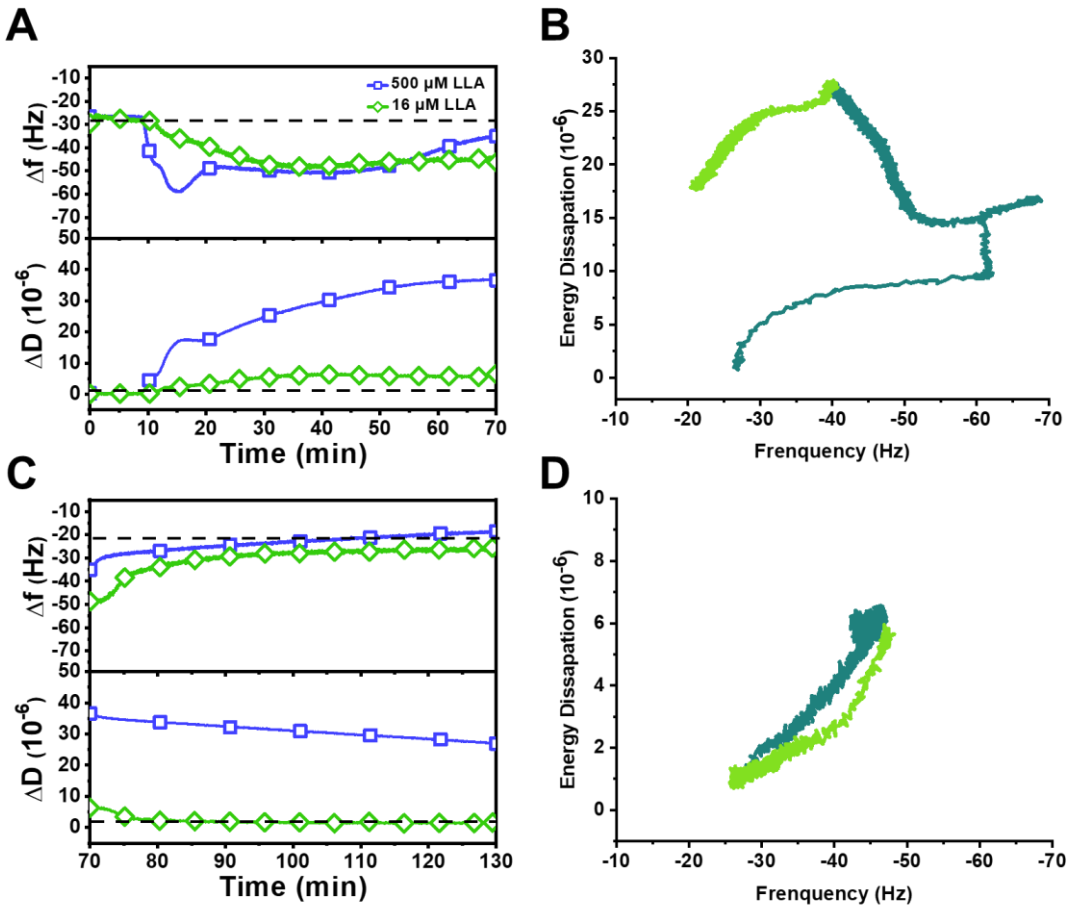

Figure 5.9 QCM-D investigation of LLA treatments on model bacterial membranes at pH 7.5. (A and C) Representative Δ*f* and Δ*D* vs time plots of LLA-treated Gram-positive bacterial membranes at concentrations of 500 μM (above CMC) and 16 μM (below CMC), and (B and D) its respective Δ*f* and Δ*D* plots. Fatty acid was added at t = 10 min, followed by a buffer washing step at t = 70 min. The dotted line in panels (A and C) represents the typical measurement responses for SLB formation.

Oleic Acid (OA) on Gram-Positive bacterial SLBs. **Figure 5.10-5.12** illustrates the impact of OA on the changes in Δ*f* and Δ*D* signals within model bacterial membranes.

Treatment with 500 µM OA led to reduction in Δ*f* signal to −68.5 ± 6.0 Hz and an increase in Δ*D* to 18.5 ± 1.8 × 10^{-6} (**Figure 5.12A**). After the buffer washing step, the Δ*f* and Δ*D* signals reach equilibrium at around −38.5 ± 4.3 Hz and 22.1 ± 1.7 × 10^{-6}, respectively, resulting in a net Δ*f* decrease of 11.3 ± 0.9 Hz and net Δ*D* increase of 21.4 ± 0.5 × 10^{-6}. Among the three tested agents, OA induced the most substantial changes in physiochemical properties of the Gram-positive bacterial SLBs. The significant harmonic spreading seen with OA treatment indicates considerable changes in dissipation, indicating the development of a softer and thicker SLB. This effect was evident in both the top and bottom layers of the membrane.

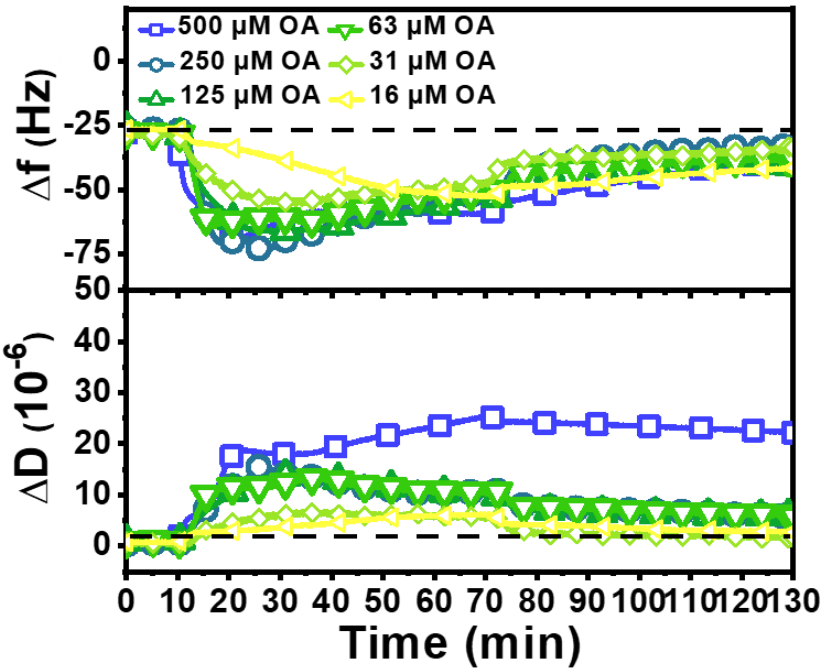

Figure 5.10 QCM-D investigation of concentration-dependent OA treatments on model Gram-positive bacterial membranes as functions of time at concentrations of 16 µM, 31 µM, 250 µM, and 500 µM until 70 min. Fatty acid was added at t = 10 min, followed by a buffer washing step at t = 70 min. The dotted line represents the typical measurement responses for SLB formation.

Figure 5.12B depicts the three distinctive stages for the OA-treated SLB. In the initial stage, treatment with 500 µM OA led to mass increase and rigidity reduction. Upon reaching the inflection point, there was mass loss followed by subsequent gain in mass, while rigidity continued to decrease (stage two). This pattern may suggest molecule

rearrangement, resulting in the development of a thicker and more fluidic membrane, as supported by the extensive harmonic spreading shown in **Figure 5.11A**. After buffer washing, stage three involved a decrease in mass with negligible viscoelastic property change, potentially indicating the incorporation of protonated form of OA into the bilayer membrane to reach energetic minimum [51]. Previous reports suggest that the protonated carboxylic acid moiety enables deeper lipid bilayer penetration and plays a crucial role in membrane disruption [52].

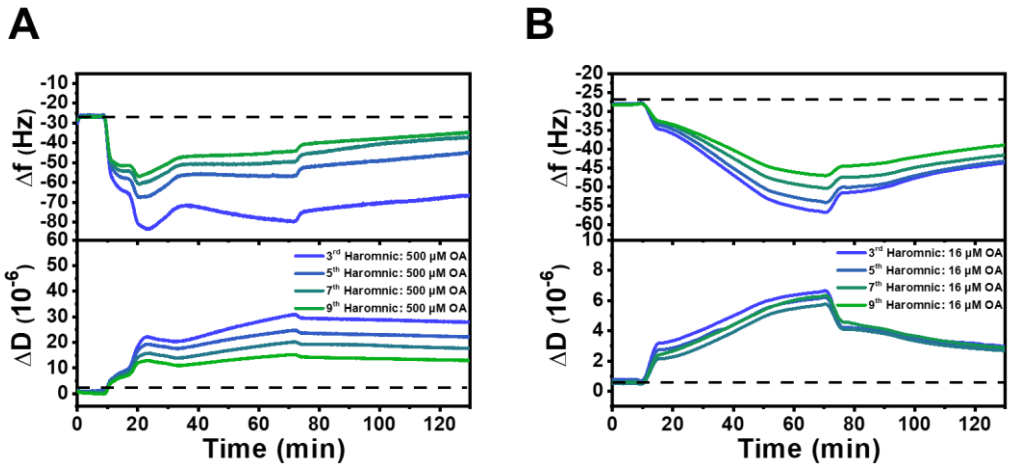

Figure 5.11 QCM-D investigation of OA treatment on model bacterial membranes at concentrations above and below CMC values at different overtones (from third-ninth). (A and B) Representative third through ninth harmonic Δ*f* and Δ*D* vs time plots of OA-treated Gram-positive bacterial membrane. Fatty acids were added at t = 10 min, followed by a buffer washing step at t = 70 min. The dotted line in panels (A and B) represents the typical measurement responses for SLB formation.

Interestingly, at concentrations below micelle-forming threshold (20 μM), OA displayed gradual attachment to Gram-positive membranes with minimal changes in dissipation, even after buffer washing (**Figure 5.12C**). This phenomenon may be attributed to the ability of OA to self-aggregate into vesicles even at concentrations below CMC [53], allowing it to attach to the membrane even at low concentrations. As evidenced by the uniform spreading of the harmonics in **Figure 5.11B**, OA produced similar effects on both sides of the SLB, indicating its influence on the entire bilayer structure.

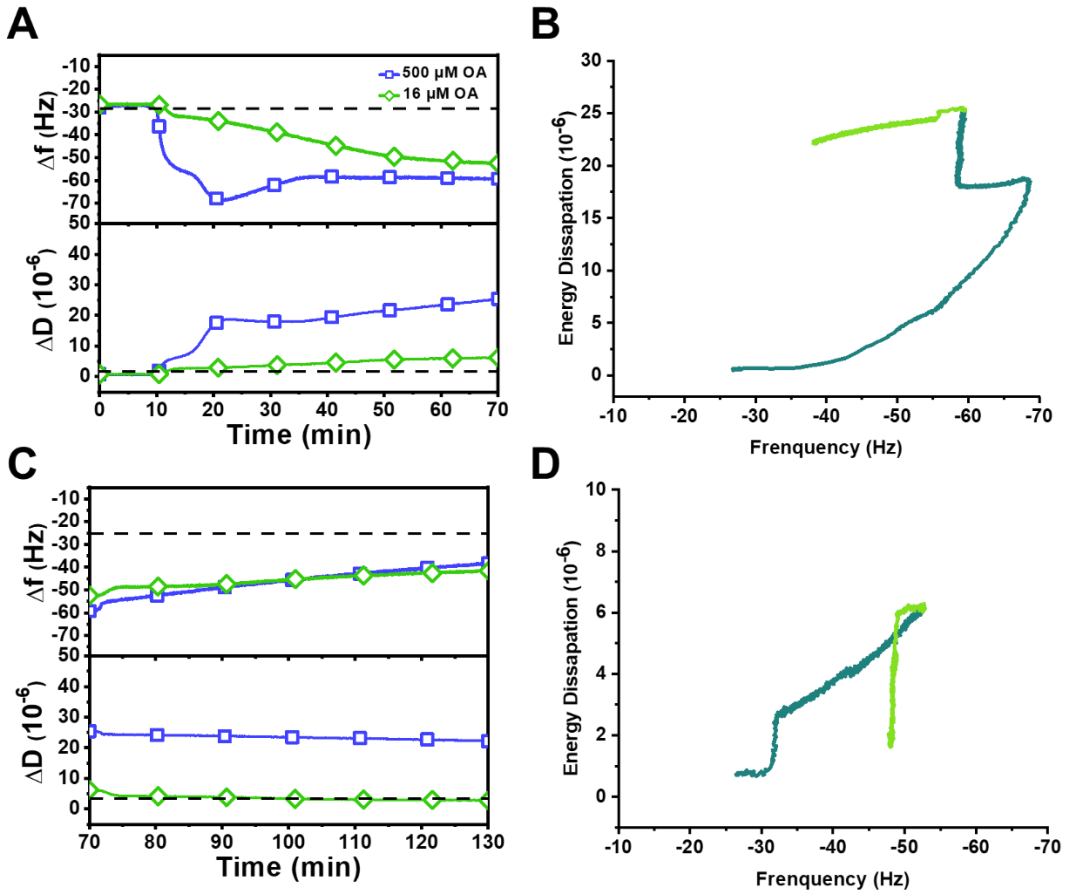

Figure 5.12 QCM-D investigation of OA treatments on model bacterial membranes at pH 7.5. (A and C) Representative Δ*f* and Δ*D* vs time plots of OA-treated Gram-positive bacterial membranes at concentrations of 500 μM (above CMC) and 16 μM (below CMC), and (B and D) its respective Δ*f* and Δ*D* plots. Fatty acid was added at t = 10 min, followed by a buffer washing step at t = 70 min. The dotted line in panels (A and C) represents the typical measurement responses for SLB formation.

5.3.3 Observation of Membrane Morphological Responses in Model Bacterial Membranes

We employed fluorescence microscopy to examine the morphological alterations in Gram-positive bacterial SLBs induced by antimicrobial LCFAs (**Figure 5.14**). Following the establishment of the bacterial biomimetic SLB, LCFAs were injected under continuous flow. The moment the FA solution entered the measurement chamber was marked as t = 0 min. The FA concentrations used were selected based on their CMC values measured by

fluorescence spectroscopy [29, 54, 55]. The results obtained for these compounds are presented below.

Treatment with 500 μM LNA, above its CMC, induced the rapid formation of static nucleation sites with bright spots on the Gram-positive SLB. These sites developed into short tubules that remained stable over time and persisted on the membrane even after buffer washing, resulting in a total spot area of 1489.0 ± 104.7 μm^2 (**Figure 5.14C**). Notably, the size of the short tubules and aggregates was small, and there was a reduction in fluorescence intensity of the background. This observation potentially indicates a weak interaction between LNA and the membrane and suggests signs of membrane removal after buffer washing, as observed in QCM-D experiments. In contrast, 63 μM LNA, below its CMC, led to minimal morphological changes, with only a few short tubules observed on the SLB surface, covering a total area of 2.2 ± 0.4 μm^2. This indicates minimal morphological changes on the SLB membrane at concentrations below CMC (**Figure 5.13A**).

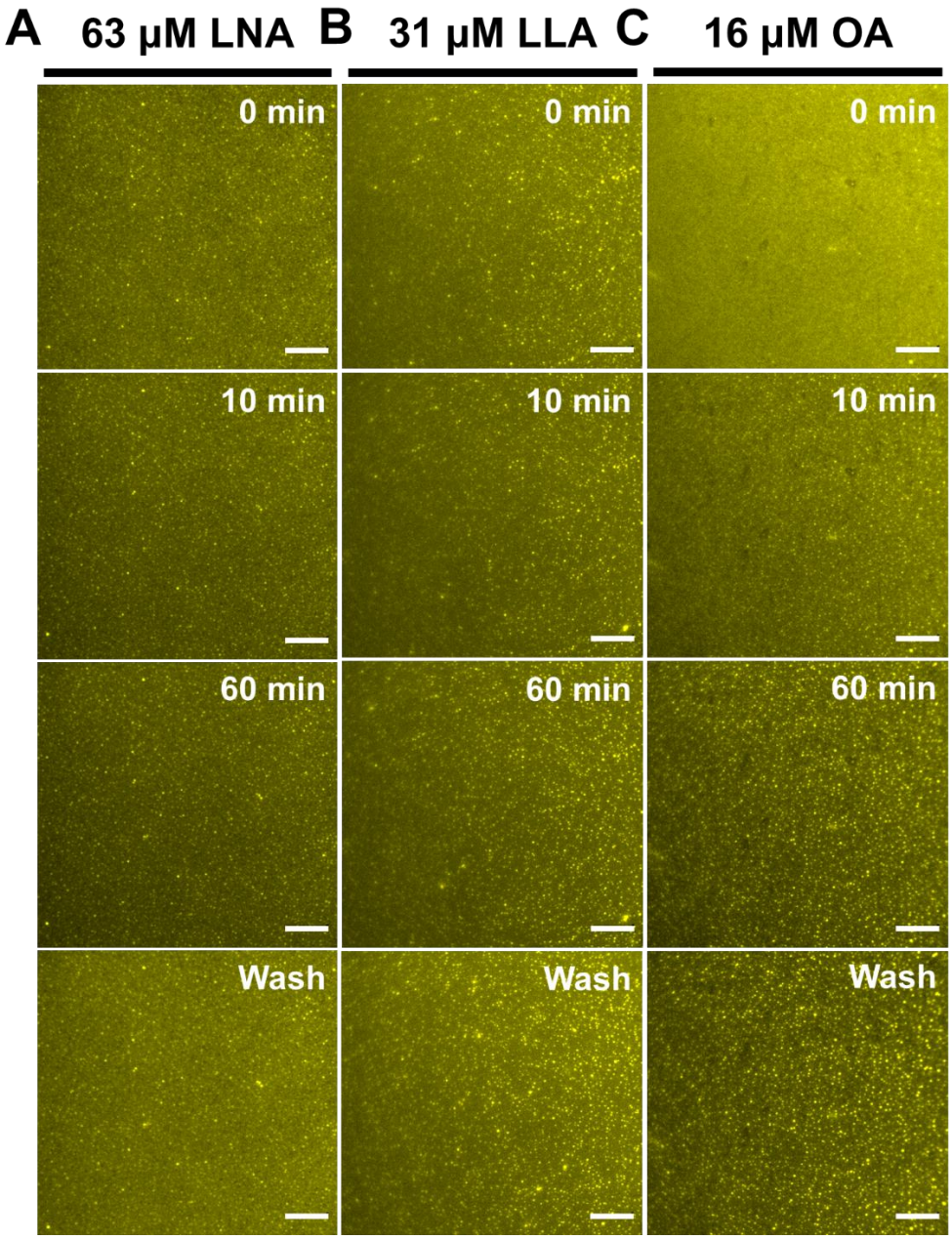

Figure 5.13 Time-lapse microscopic observation of membrane morphological responses in model Gram-positive bacterial membranes triggered by LNA, LLA, and OA at concentrations below CMC. Sequential image snapshots depicting the morphological change of Gram-positive bacterial membrane under (A) LNA treatment at 63 μM, (B) LLA treatment at 31 μM, and (C) OA treatment at 16 μM. At t = 0 min, the fatty acid solutions were added to the measurement chamber. The scale bar is 20 μm.

Upon exposure to 250 μM LLA, a dense array of bright spots protruded from the membrane, remaining relatively unchanged for 60 min. Following the buffer washing step, these bright spots became notably more pronounced, covering an area of 2158.0 ± 77.8 μm^2. Compared to LNA, the aggregates formed by LLA were visibly larger, with areas of higher fluorescence intensity in the background after buffer washing. This observation is consistent with the smaller net mass change and the detection of highest mass decrease in the higher harmonics, resulting in the removal of the bottom layer in exchange for LLA molecules (**Figure 5.8A**). When exposed to 31 μM LLA, there was marginal morphological changes on the membrane, indicated by few discernible spots. LLA exhibited CMC-dependent membrane remodelling and removal on the Gram-positive membrane. This trend is closely aligned with the interaction kinetics of LNA with the Gram-positive membrane as observed through QCM-D signal responses, which revealed the attachment and detachment kinetics of FAs are observed at concentrations above the CMC, accompanied by significant changes in energy dissipation. Notably, the membrane underwent less property changes with LLA than with LNA, likely due to LLA's straighter hydrophobic tail, which confers a stronger insertion capacity [51].

Similar morphological responses and attachment phenomena were observed on the membrane throughout the 60 min when treated with 125 μM of OA, resulting in the highest spot area of 2434.9 ± 125.7 μm^2. Notably, the fluorescence intensity of the background remained relatively unchanged throughout the treatment and the washing steps, consistent with the conclusions of the QCM-D fingerprinting analysis. OA displayed membrane attachment and remodeling patterns similar to those observed with LNA and LLA, but without membrane removal and with deeper insertion into the bilayer membrane, as indicated by smaller aggregates. At a concentration of 16 μM, OA instigated the formation of conspicuous spot protrusions on the membrane surface, and these protrusions remained unaffected even after the buffer washing step, providing evidence of OA's insertion into the membrane. Notably, the number of persistent bright spots (781.5 ± 51.4 μm^2) surpassed those observed with LNA and LLA treatments at concentrations below CMC, underscoring the CMC-independent activity profile of OA. This phenomenon may be attributed to OA having the highest p*K*a value among the three FAs, thereby increasing the probability of the FA being protonated [51]. This results in higher electrostatic interaction force between

OA and anionic phospholipids within the bacterial membrane, potentially pulling a larger fraction of OA deep into the lipid bilayer. Consequently, OA can interact with the Gram-positive membrane at both concentrations above and below its respective CMC value. Notably, OA exhibited membrane activity even at concentrations below CMC, suggesting robust adhesion, likely attributed to its efficient integration into CL lipids [56].

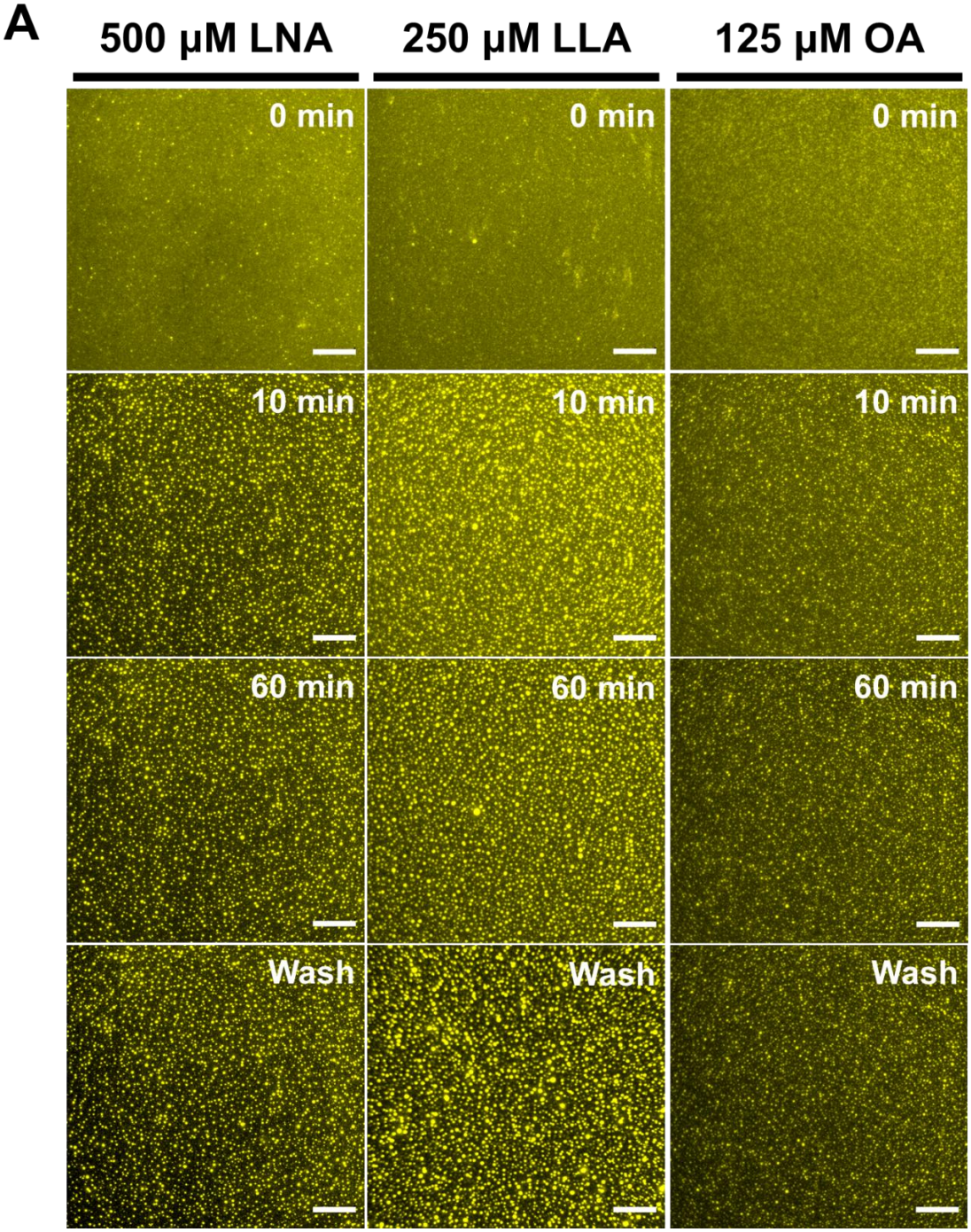

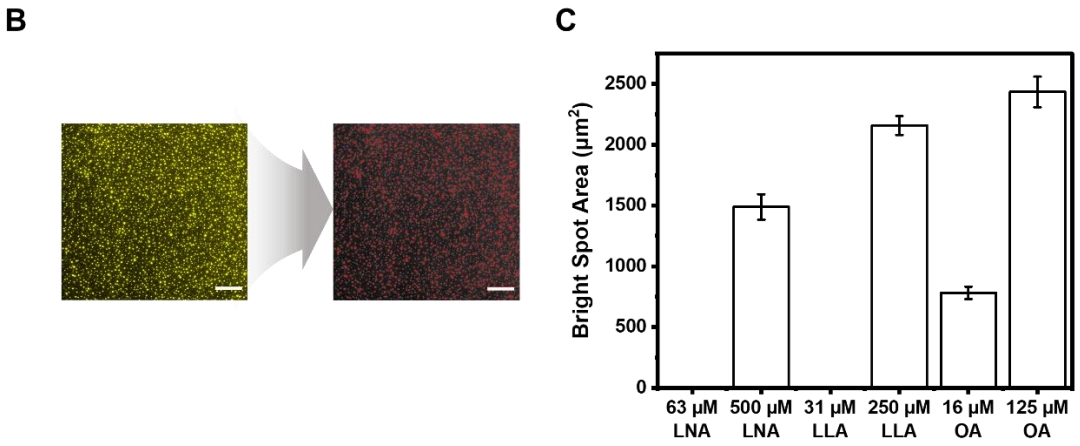

Figure 5.14 Time-lapse microscopic observation of membrane morphological responses in model bacterial membranes triggered by fatty acid treatments at concentrations below and above CMC. (A) Representative sequential image snapshots depicting the morphological change of Gram-positive bacterial membrane under LNA treatment at 500 μM. (B) Representative analysis for calculating spot area formed on SLBs. (C) Total area of spot formation on SLBs after buffer washing (n = 5, mean ± SD). The scale bar is 20 μm.

5.4 Conclusion

In conclusion, our study explored the intricate interactions between antimicrobial LCFAs (LNA, LLA, and OA) and Gram-positive bacterial membranes using model bacterial lipid bilayers fabricated via the solvent-assisted lipid bilayer (SALB) method. By integrating QCM-D measurement and fluorescence microscopy imaging, we elucidated that LNA and LLA exhibit CMC-dependent interactions with Gram-positive membranes, leading to significant membrane remodeling and removal at concentrations exceeding their respective CMC values. In contrast, OA demonstrated a CMC-independent activity characterized by penetration into the membrane across all concentrations tested. These results offer critical insights into the diverse mechanisms through which long-chain unsaturated FAs exert their effects on Gram-positive bacterial membranes. Moreover, they underscore the importance of utilizing biologically relevant model systems to advance our understanding of antimicrobial mechanisms and to contribute to the development of effective antibacterial treatments. Furthermore, the potential of LCFAs in combating antibiotic-resistant strains is highlighted. Nevertheless, further research is warranted to

assess their *in vitro* and *in vivo* efficacy and potential cytotoxicity, ensuring their safety and efficacy for clinical applications.

References

[1] H.I. MacDermott-Opeskin, V. Gupta, M.L. O'Mara. *Biophysical Reviews*. **2022**, 14(1), 145-162.

[2] S. Li, R. Ren, L. Lyu, J. Song, Y. Wang, T.-W. Lin, A.L. Brun, H.-Y. Hsu, H.-H. Shen. *Membranes*. **2022**, 12(10), 906.

[3] N. Ganesan, B. Mishra, L. Felix, E. Mylonakis. *Microbiology and Molecular Biology Reviews*. **2023**, 87(2), e00037-22.

[4] C.D. Fjell, J.A. Hiss, R.E.W. Hancock, G. Schneider. *Nature Reviews Drug Discovery*. **2012**, 11(1), 37-51.

[5] A.P. Desbois, V.J. Smith. *Applied Microbiology and Biotechnology*. **2010**, 85(6), 1629-1642.

[6] J. Sarkis, V. Vié. *Frontiers in Bioengineering and Biotechnology*. **2020**, 8.

[7] J. Lombard. *Biology Direct*. **2014**, 9(1).

[8] F. Ramos-Martín, N. D'Amelio. *Biochimie*. **2022**, 203, 118-138.

[9] B.K. Yoon, J.A. Jackman, M.C. Kim, T.N. Sut, N.-J. Cho. *Langmuir*. **2017**, 33(11), 2750-2759.

[10] B.K. Yoon, J.A. Jackman, M.C. Kim, N.-J. Cho. *Langmuir*. **2014**, 31(37), 10223-10232.

[11] M. Frieri, K. Kumar, A. Boutin. *Journal of Infection and Public Health*. **2017**, 10(4), 369-378.

[12] M.F. Chellat, L. Raguž, R. Riedl. *Angewandte Chemie International Edition*. **2016**, 55(23), 6600-6626.

[13] T.J. Silhavy, D. Kahne, S. Walker. *Cold Spring Harb Perspect Biol*. **2010**, 2(5), a000414.

[14] C. Dias, A.P. Rauter. *Future Med Chem*. **2019**, 11(3), 211-228.

[15] H. Behuria, N. Pal, R. Munda, S. Sahu. In *Preparation of Giant Unilamellar Vesicles (GUVS) from Bacterial Polar Lipid Extract: Developing a Prokaryotic Model Membrane System,* Biotechnology for Sustainable Utilization of Bioresources. **2020**, pp. 309-320.

[16] B.K. Yoon, J.A. Jackman, E.R. Valle-González, N.-J. Cho. *International Journal of Molecular Sciences*. **2018**, 19(4), 1114.

[17] E. Krok, M. Stephan, R. Dimova, L. Piatkowski. *Biochimica et Biophysica Acta (BBA) - Biomembranes*. **2023**, 1865(7), 184194.

[18] S.R. Tabaei, J.H. Choi, G. Haw Zan, V.P. Zhdanov, N.J. Cho. *Langmuir*. **2014**, 30(34), 10363-73.

[19] A.B. Carey, A. Ashenden, I. Köper. *Biophys Rev*. **2022**, 14(1), 111-143.

[20] W. Dowhan. *Annu Rev Biochem*. **1997**, 66, 199-232.

[21] C. Sohlenkamp, O. Geiger. *FEMS Microbiol Rev*. **2016**, 40(1), 133-59.

[22] P. Kékicheff, S. Marčelja, T.J. Senden, V.E. Shubin. *The Journal of Chemical Physics*. **1993**, 99(8), 6098-6113.

[23] T. Mukhina, A. Hemmerle, V. Rondelli, Y. Gerelli, G. Fragneto, J. Daillant, T. Charitat. *The Journal of Physical Chemistry Letters*. **2019**, 10(22), 7195-7199.

[24] S.R. Tabaei, S. Vafaei, N.-J. Cho. *Physical Chemistry Chemical Physics*. **2015**, 17(17), 11546-11552.

[25] H. Tae, C. Yang, N.-J. Cho. *Accounts of Materials Research*. **2022**, 3(12), 1272-1284.

[26] C.J. Zheng, J.S. Yoo, T.G. Lee, H.Y. Cho, Y.H. Kim, W.G. Kim. *FEBS Lett*. **2005**, 579(23), 5157-62.

[27] E.E. Pohl, O. Jovanovic. *Molecules*. **2019**, 24(24).

[28] N. Togashi, A. Shiraishi, M. Nishizaka, K. Matsuoka, K. Endo, H. Hamashima, Y. Inoue. *Molecules*. **2007**, 12(2), 139-148.

[29] S. Shin, H. Tae, S. Park, N.-J. Cho. *International Journal of Molecular Sciences*. **2023**, 24(11), 9639.

[30] S. Di Leone, M. Kyropoulou, J. Köchlin, R. Wehr, W.P. Meier, C.G. Palivan. *Langmuir*. **2022**, 38(21), 6561-6570.

[31] M.C. Dixon. *J Biomol Tech*. **2008**, 19(3), 151-8.

[32] P. Jönsson, M.P. Jonsson, J.O. Tegenfeldt, F. Höök. *Biophys J*. **2008**, 95(11), 5334-48.

[33] P. Jönsson, M.P. Jonsson, J.O. Tegenfeldt, F. Höök. *Biophys J*. **2008**, 95(11), 5334-5348.

[34] M.L. Mangoni, Y. Shai. *Cell Mol Life Sci*. **2011**, 68(13), 2267-80.

[35] K. Matsuzaki. *Biochim Biophys Acta*. **1999**, 1462(1-2), 1-10.

[36] M. Zasloff. *Nature*. **2022**, 415(6870), 389-95.

[37] R.P. Rehal, H. Marbach, A.T.M. Hubbard, A.A. Sacranie, F. Sebastiani, G. Fragneto, R.D. Harvey. *Chem Phys Lipids*. **2017**, 206, 60-70.

[38] E.M. Kilelee, A. Pokorny, M.R. Yeaman, A.S. Bayer. *Antimicrobial Agents and Chemotherapy*. **2010**, 54(10), 4476-4479.

[39] W.J. Perry, C.M. Grunenwald, R. Van de Plas, J.C. Witten, D.R. Martin, S.S. Apte, J.E. Cassat, G.B. Pettersson, R.M. Caprioli, E.P. Skaar, J.M. Spraggins. *Cell Chem Biol*. **2022**, 29(7), 1209-1217.e4.

[40] D. Poger, S. Pöyry, A.E. Mark. *J Biol Chem*. **1999**, 274(13), 8405-10.

[42] E. Nagamachi, R. Kariyama, Y. Kanemasa. *Physiol Chem Phys Med NMR*. **1985**, 17(3), 255-60.

[43] S. Danner, G. Pabst, K. Lohner, A. Hickel. *Biophys J*. **2008**, 94(6), 2150-9.

[44] S.R. Tabaei, S. Vafaei, N.J. Cho. *Physical Chemistry Chemical Physics*. **2015**, 17(17), 11546-11552.

[45] N.J. Cho, C.W. Frank, B. Kasemo, F. Höök. *Nat Protoc*. **2010**, 5(6), 1096-106.

[46] T.K. Lind, H. Wacklin, J. Schiller, M. Moulin, M. Haertlein, T.G. Pomorski, M. Cárdenas. *PLoS One*. **2015**, e0144671.

[47] M. Przybylo, J. Sýkora, J. Humpolíckova, A. Benda, A. Zan, M. Hof. *Langmuir*. **2006**, 22(22), 9096-9.

[48] B.A. Wilson, A. Ramanathan, C.F. Lopez. *Biophys J*. **2019**, 117(3), 429-444.

[49] C.J. Zheng, J.-S. Yoo, T.-G. Lee, H.-Y. Cho, Y.-H. Kim, W.-G. Kim. *FEBS Letters*. **2005**, 579(23), 5157-5162.

[50] K.R. Flynn, L.L. Martin, M.L. Ackland, A.A. Torriero. *Langmuir*. **2016**, 32(45), 11717-11727.

[51] A.A. Pashkovskaya, M. Vazdar, L. Zimmermann, O. Jovanovic, P. Pohl, E.E. Pohl. *Biophysical Journal*. **2018**, 114(9), 2142-2151.

[52] S.M. Kim, G. Zou, H. Kim, M. Kang, S. Ahn, H.Y. Heo, J.S. Kim, K.M. Lim, F.M. Ausubel, E. Mylonakis, H. Gao, W. Kim. *Biomed Pharmacother*. **2022**, 150, 112977.

[53] J.J. Janke, W.F.D. Bennett, D.P. Tieleman. *Langmuir*. **2014**, 30(35), 10661-10667.

[54] K. Kalyanasundaram, J.K. Thomas. *Journal of the American Chemical Society*. **1977**, 99(7), 2039-2044.

[55] K. Kalyanasundaram, J.K. Thomas. *The Journal of Physical Chemistry*. **1977**, 81(23), 2176-2180.

[56] H.-C. Ting, L.-T. Chen, J.-Y. Chen, Y.-L. Huang, R.-C. Xin, J.-F. Chan, Y.-H.H. Hsu. *Lipids in Health and Disease*. **2019**, 18(1), 53.

Chapter 6

Interaction Dynamics of Liposomal Fatty Acids with Gram-Positive Bacterial Membranes

While existing studies of liposomal fatty acids (LipoFAs) have focused on in vitro assessment of the biological activities of LipoFAs, the mechanistic interactions between the test compounds and model membranes remains limited. Herein, we investigate the interactions between liposomal linolenic acid (LipoLNA), liposomal linoleic acid (LipoLLA) and liposomal oleic acid (LipoOA) and model Gram-positive bacterial membranes using quartz crystal microbalance with dissipation monitoring (QCM-D) and fluorescence microscopy. QCM-D revealed that LipoOA exhibited the fastest fusion rate with the model membrane. Fluorescence microscopy revealed that LipoLNA induced large bud structures, while LipoOA caused rapid incorporation with dense spotting. Furthermore, fluorescence recovery after photobleaching (FRAP) analysis showed that LipoOA significantly reduced lipid mobility and diffusion coefficient within the membrane. The assessment of membrane rigidity using Laurdan generalized polarization (GP) confirmed the highest rigidity induced by LipoOA. The degree of fatty acid unsaturation significantly impacted interaction mechanisms, with fewer double bonds facilitating faster fusion and incorporation into the model bacterial membrane. These findings provide valuable insights into how LipoFAs structurally disrupt model Gram-positive membranes, offering mechanistic understanding of their antibacterial properties and potential therapeutic applications.

6.1 Introduction

Bacterial infections have long posed significant challenges to public health [1, 2], and this situation has been exacerbated by swift spread of resistant strains. Consequently, it is crucial to devise new approaches to combat this escalating threat. FAs (FAs) have gained significant interest recently for their wide-ranging effectiveness against bacterial infections [3-5]. Previous studies have highlighted the interactions of FFAs with bacterial membranes and their antibacterial properties [6-17]. Among FAs, LCFAs have drawn wide attention due to their significant antimicrobial activities against Gram-positive bacterial strains [3, 18-22]. This interest is driven by their intrinsic antimicrobial properties, widespread availability [23], and cost-effectiveness [24-26]. However, FFAs face challenges such as solubility constraints, micelle destabilization [27], and vulnerability to oxidation [28, 29]. Therefore, to enhance their practical applications, it is essential to encapsulate the LCFAs with other materials.

Currently, various strategies have been developed for antibacterial applications using FAs including emulsion [30, 31], liposomes [32-34], and hydrogels [35, 36]. These strategies offer benefits such as higher loading efficiency [37] and controlled release [38] of the loaded FAs. Among these carrier systems, liposomes present distinct advantages in facilitating the delivery of amphiphilic antimicrobial agents [39]. This is notably achieved through the process of membrane fusion [40-42], which significantly enhances the efficacy of FA delivery. Furthermore, liposomes enable the integration of FAs into the membrane structure [43], consequently altering its properties.

Since membrane fluidity is crucial for bacterial metabolic functions, particularly affecting membrane-associated proteins [44], lipid bilayer fluidity [45], and intracellular vesicular transport [46], any disruption in this fluidity can interfere with vital cellular processes such as cytokinesis [47]. Therefore, changes in the membrane's physicochemical properties can impact the requisite structural integrity for sustaining biological activities [48]. The impact of LipoFAs on bacteria has been investigated previously. Liposomal oleic acid, for instance, demonstrates rapid fusion with the membrane of *Staphylococcus aureus* MW2, thereby impeding its growth [49]. Similarly, liposomal linolenic acid exhibits fusion

behavior with *Helicobacter pylori*, even when the bacterium is in a dormant state [51]. Additionally, research indicates that FAs can modulate the fluidity of bacterial membranes inhibiting their growth [51-53]. Nevertheless, the physical mechanisms by which FA-loaded liposomes disrupt bacterial membranes and induce membrane alterations at molecular level remain elusive, owing to the intricate nature of biological membranes.

Herein, we investigated the interactions between liposomal linolenic acid (LipoLNA), liposomal linoleic acid (LipoLLA), and liposomal oleic acid (LipoOA) with Gram-positive model membrane by means surface-sensitive measurement techniques, including quartz crystal microbalance with dissipation monitoring (QCM-D) and fluorescence microscopy, which offers real-time molecular insights into the interaction kinetics of liposomal adsorption, fusion, and changes in membrane fluidity. These findings elucidate the structural and fluidity changes induced in the model bacterial membrane (**Figure 6.1**), offering valuable mechanistic insights into the antibacterial potency and potential clinical applicability of these liposomes in combating bacterial infections.

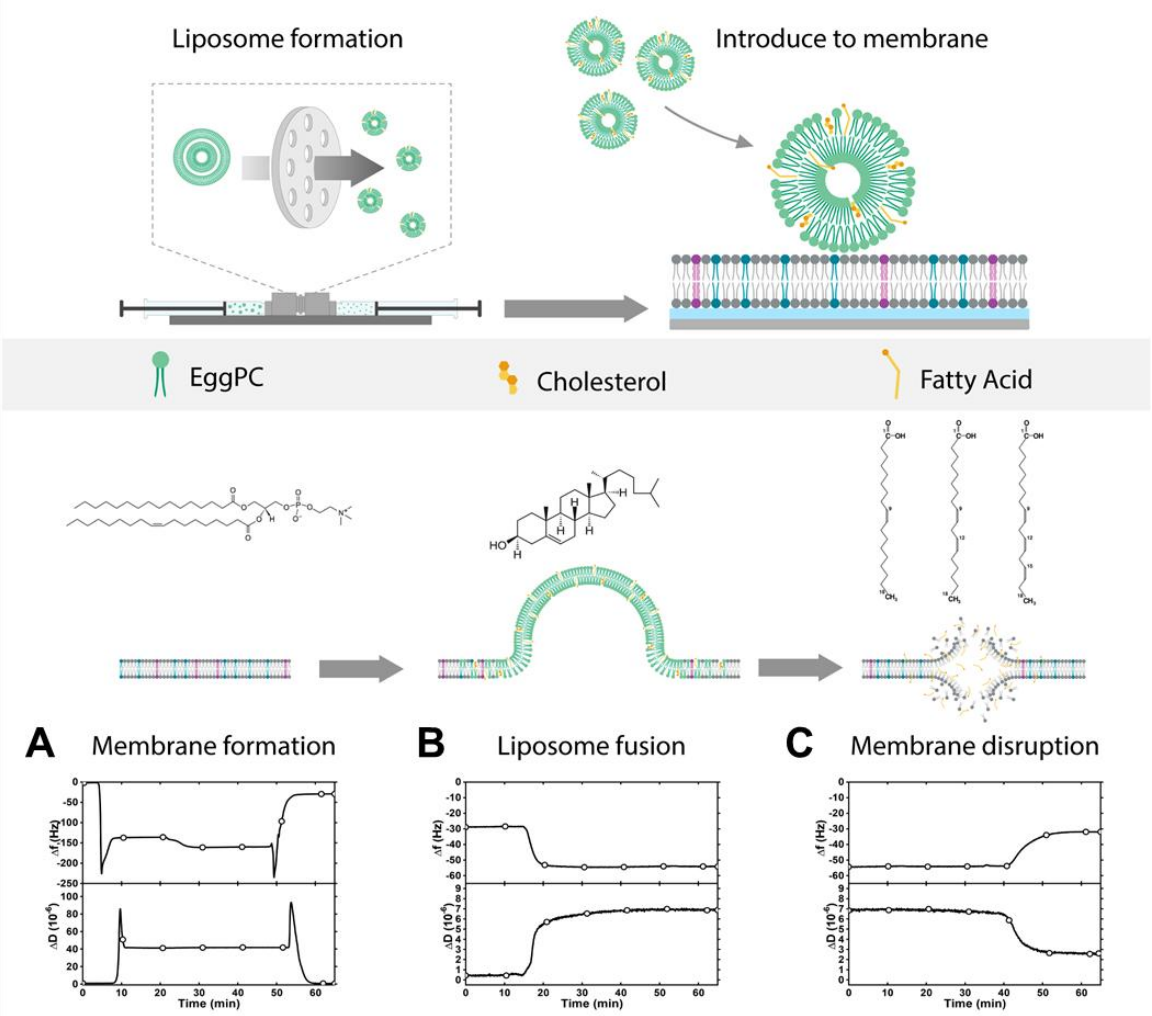

Figure 6.1 Schematic representation of the experimental approach for developing LipoFAs for antibacterial applications. Liposomes were prepared through the hydration of lipid and cholesterol mixtures, followed by sonication and extrusion techniques. (A) Membrane formation, (B) liposome fusion, and (C) membrane disruption activities of LipoFAs were evaluated. Image credit: Batika Saxena.

6.2 Experimental Methods

6.2.1 Reagents

L-α-phosphatidylcholine (Egg PC), cholesterol (ovine wool, >98%), 1-palmitoyl-2-oleoyl-sn-glycero-3-phospho-(1′-rac-glycerol) (POPG), 1,2-dipalmitoyl-sn-glycero-3-[phospho-rac-(3-lysyl(1-glycerol))] (Lysyl-PG), 1′,3′-bis[1-Palmitoyl-2-oleoyl-sn-

glycero-3-phospho]-glycerol (Cardiolipin), and 1,2-dioleoyl-sn-glycero-3-phosphoethanolamine-N-(lissamine rhodamine B sulfonyl) (ammonium salt) (RhB-PE) were obtained from Avanti Polar Lipids, Inc. (Alabaster, AL). Linolenic acid (LNA), linoleic acid (LLA), oleic acid (OA), 6-Dodecanoyl-N,N-dimethyl-2-naphthylamine (Laurdan) were procured from Sigma-Aldrich (St. Louis, MO). Tryptic soy broth (TSB) broth, Mueller-Hinton (MH) agar and broth were purchased from Becton Dickinson (Sparks, MD). Phosphate-buffered saline (PBS) was purchased from Gibco (Carlsbad, CA). All solutions were prepared using deionized water treated with a Milli-Q system (>18 MΩ·cm) (Millipore, Billerica, MA).

6.2.2 Synthesis and Characterization of Antimicrobial Fatty Acids and Liposomes

Stock solutions of LNA, LLA, and OA were arranged by blending each fatty acid with ethanol at a concentration of 50 mg/ml, with experimental concentrations achieved by dilution with PBS. Liposomes were prepared using the vesicle extrusion technique, incorporating modifications from a previously established protocol [54, 55]. LipoLNA, LipoLLA, LipoOA, and BareLipo were formulated by combining 15 mg of Egg PC, cholesterol, and LNA, LLA, or OA in weight ratios of 5:1:4 and 9:1:0, respectively. These mixtures were mixed with 1 mL chloroform and were dried using nitrogen at 50 °C, followed by overnight storage in a desiccator to eliminate any residual solvents. The dried sample was rehydrated with PBS buffer (3 mL). After hydration, the lipid suspension was vortexed for 15 s, sonicated in a bath sonicator (RS PRO, Kuala Lumpur, Malaysia), and then further tip-sonicated using a 20 kHz ultrasonic probe with a tip diameter of 12 mm (QSonica, Newton, CT) at 20 kHz, 500 W, and 40% amplitude for 5 min to produce small unilamellar vesicles (SUVs). Finally, the suspension underwent extrusion through a polycarbonate (PC) membranes with 400 nm-sized pores, followed by additional extrusion through a 100-nm sized pores using a mini-extruder (Avanti Polar Lipids Inc., Alabaster, AL) 21 times. The hydrodynamic size and surface zeta potential of LipoLNA, LipoLLA, LipoOA, and BareLipo were assessed using dynamic light scattering (DLS) and zeta PALS analyzer (Brookhaven Instruments, Holtsville, NY). BareLipo was utilized as the negative control. All characterization tests were conducted in triplicate at room temperature.

6.2.3 Cryogenic Electron Microscopy (Cryo-EM) Imaging

For Cryo-EM imaging, samples were prepared by placing 3 µl of the sample onto a 400-mesh Tedpella lacey carbon copper grid, which was coated with ultrathin carbon film (Ted Pella, Inc.) and glow-discharged in air for 60 s. Subsequently, the grid was blotted for either 1 s or 2 s (blot force 1) at 22°C and 100% humidity before being rapidly immersed in liquid ethane using an FEI Vitrobot Mark IV. Micrographs were captured with a 300 kV Titan Krios cryo-transmission electron microscope, equipped with a Selectris X imaging filter and a Falcon 4i direct electron detector. Images were acquired at 53,000× magnification, resulting in a pixel size of 2.4 Å/px.

6.2.4 Lipid Preparation for SLB Formation

A Gram-positive lipid membrane consisting of anionic lipid 1-palmitoyl-2-oleoyl-*sn*-glycero-3-phospho-(1′-*rac*-glycerol) (POPG), cationic lipid 1,2-dipalmitoyl-sn-glycero-3-[phospho-rac-(3-lysyl(1-glycerol))] (Lysyl PG), and anionic lipid 1′,3′-bis[1-Palmitoyl-2-oleoyl-sn-glycero-3-phospho]-glycerol (CL) was blended in a molar ratio of 65:30:5 in chloroform to achieve a concentration of 0.3 mg/mL. For SALB experiments, lipid films were desiccated using nitrogen gas and vacuum-stored overnight to confirm elimination of the organic solvent. To enhance solubility, the anionic and cationic lipids were dissolved in ethanol at 70 °C for 1-2 min to achieve a concentration of 1 mg/mL. Prior to each experiment, this solution underwent further dilution in isopropanol.

6.2.5 Quartz Crystal Microbalance with Dissipation (QCM-D) Experiments

To examine the molecular interaction between the liposomes and SLBs, QCM-D experiments were carried out using a four-channel Q-Sense E4 instrument (Q-Sense AB, Gothenburg, Sweden). This technique tracks variations in frequency (Δf) and energy dissipation (ΔD) of an oscillating quartz crystal sensor chip over time. These measurement responses offer insights into the changes in mass and dissipation properties of the film. 5

MHz sensor chips, coated with silicon dioxide (model no. QSX 303, Biolin Scientific), were used. Immediately before the experiment, the chips were washed with 1% SDS, DI water, and ethanol. Subsequently, the chips were dried with nitrogen and treated with oxygen plasma for 1 min using an Expanded Plasma Cleaner (PDC-002, Harrick Plasma, Ithaca, NY). Bacterial model membranes were established using the solvent-assisted lipid bilayer (SALB) technique [57]. Each SLB was used only once per experiment. Initially, stabilization was recorded in an aqueous Tris buffer. The buffer solution was substituted with an isopropanol solution, followed by the introduction of the lipid solution. Subsequently, the solvent was exchanged with TRIS and PBS to form the SLB. After the bilayer formation, test liposome samples in PBS solution were introduced, followed by final PBS wash. All the samples were introduced into the chamber at 50 μL/min. The chamber temperature was maintained at room temperature throughout the experiments. Experimental data collection was performed at the third (n = 3), fifth (n = 5), seventh (n = 7), and ninth (n = 9) overtones using the Q-Soft software program (Biolin Scientific). The results presented were specifically from the fifth harmonic. All data processing was completed using the Q-Tools (Biolin Scientific) and OriginPro (OriginLab, Northampton, MA).

6.2.6 Time-lapse Fluorescence Microscopy

Epifluorescence microscopy was employed to monitor the surface membrane morphology changes in SLBs treated with liposomes containing LNA, LLA, and OA. These experiments were carried out using an Eclipse TI-E inverted microscope (Nikon, Tokyo, Japan) equipped with a 60× magnification (NA = 1.49) oil-immersion objective lens (Nikon). Micrographs were captured using an iXon EMCCD camera (Andor Technology, Belfast, Northern Ireland) featuring a resolution of 512 × 512 pixels and a pixel size of 0.267 × 0.267 μm^2. Illumination was provided by a fiber-coupled mercury lamp (Intensilight C-HGFIE, Nikon) and a TRITC filter to excite the fluorescently labeled bacterial phospholipids. SLBs were fabricated on a glass coverslip substrate contained within a flow-through chamber (sticky slide VI 0.4, Ibidi, Germany) using the SALB method [57-59]. After the SLB formation, the chamber was rinsed with PBS buffer solution,

followed by the introduction of the liposome samples at a flow rate of 50 µL/min. Micrographs were taken every 5 s for a 1 h to examine the time-dependent effects of the LipoFAs on the SLBs. t = 0 s was designated as the starting time of test compound injection. The collected images were analyzed using ImageJ (National Institutes of Health, Bethesda, MD, USA).

6.2.7 Fluorescence Recovery after Photobleaching (FRAP) Measurements

FRAP methodologies were utilized to assess the lateral diffusivity of SLBs labeled with Rhodamine-PE fluorescent lipids before and after exposure to LipoFAs. Photobleaching process was performed using a 532 nm, 100 mW laser (Klastech Laser Technologies, Dortmund, Germany) to generate circular spots with a 20-µm diameter for 5 s. Fluorescence micrographs were taken every 2 s over 120 s to track fluorescence recovery. The lateral diffusion coefficients were computed from the FRAP data using a Hankel transform method [60] implemented in Matlab (MathWorks, USA).

6.2.8 Membrane Fluidity Assay

An overnight culture of *S. aureus* MW2 was diluted 1:100 in 2 mL TSB and then incubated at 37°C until reaching an OD_{600} of 1.0 at 600 nm. Subsequently, the bacteria were co-incubated with 10 µM Laurdan in the absence of light for 10 min. After staining, the bacterial suspension underwent four washes with PBS and was then concentrated two-fold. This concentrated bacterial suspension was combined with equal volumes of PBS, benzyl alcohol (BA), BareLipo, LipoLNA, LipoLLA, and LipoOA, each at double the target concentrations. Following a 1 h incubation in the absence of light at room temperature, Laurdan's fluorescence intensity was evaluated at emission wavelengths of 435 nm 490 nm, upon excitation at 350 nm, using a spectrophotometer (Tecan Spark®, Tecan, Zurich, Switzerland). Membrane fluidity was quantified by the Laurdan generalized polarization (GP) index, which is expressed as $GP = (I_{435} - I_{490})/(I_{435} + I_{490})$. Benzyl alcohol at a concentration of 50 mM was employed as a positive control.

6.2.9 Liposome Fusion with *S. aureus* MW2

The fusion activity of LipoFAs with *S. aureus* MW2 was studied using a fluorescence-based method. To prepare fluorescently labeled LipoLNA, LipoLLA, and LipoOA, RhB-PE (0.5 mol%) was combined with EggPC, cholesterol, and FFA. Then, 1 mL of the LipoFA suspension was combined with 1.5×10^8 CFU/mL of *S. aureus*. After a 30 min incubation, the bacteria were harvested by centrifugation at 17,500 × g for 5 min and fixed with 2% (vol/vol) glutaraldehyde in PBS at room temperature for 20 min. The bacteria were subsequently washed and resuspended in 500 μL of DI water. For imaging purposes, 10 μL of the bacterial suspension was mixed with 10 μL DAPI-containing mounting media (Fluoroshield™ with DAPI, Sigma-Aldrich) and placed on a glass slide. The sample was visualized using a 63× oil immersion objective on a Zeiss Observer II microscope. The experiments were conducted three times independently unless otherwise specified. Statistical analysis was performed using a two-tailed T-test in Microsoft Excel (Microsoft, Redmond, WA, USA), with correlations having a p-value <0.05 considered statistically significant (*$p < 0.05$, **$p < 0.01$, and ***$p < 0.001$).

6.3 Results and Discussion

6.3.1 Synthesis and *In Vitro* Characterization of LipoFAs

The stability of the prepared LipoFAs and FFA micelles was assessed by observing alterations in size and zeta potential over 24 h through dynamic light scattering (DLS). **Figure 6.2A-F** depict the size changes of FFAs and LipoFAs at a concentration of 5 mg/mL in PBS buffer, with samples diluted tenfold for zeta potential measurements. All FFAs demonstrated a significant increase in size over 24 h. For instance, the measured size of LNA increased from 625.7 ± 17.5 nm to 1015.9 ± 67.1 nm, LLA increased from 727.9 ± 35.4 nm to 1314.4 ± 45.2 nm, and OA increased from 885.1 ± 34 nm to 1522.9 ±101.1 nm, indicating rapid aggregation of FFAs. Similarly, the size of LipoFAs loaded with 80% FAs (weight ratio of 1:1:8) also increased markedly overnight, with LipoLNA growing from 212.6 ± 3.6 nm to 812.7 ± 23.5 nm, LipoLLA to 461.4 ± 10.6 nm, and LipoOA to 403.6 ±

9.4 nm. This increase in final liposome sizes was attributed to the structural changes in FAs, with OA showing denser packing with phospholipids than LNA [61]. In contrast, LipoFAs with weight ratios of 8:1:1 and 5:1:4 exhibited better stability, maintaining their sizes within 150 nm over 24 h. The polydispersity indices (PDIs) of FFAs and their corresponding LipoFAs with a weight ratio of 1:1:8 exceeded 0.3 over a 24 h period, whereas the PDIs for LipoFAs with weight ratios of 8:1:1 and 5:1:4 remained below 0.24. This suggests that an excess of FAs results in unstable liposomes [61]. Additionally, the PDIs of the prepared LipoFAs slightly increased overnight, with higher PDIs observed in the less stable groups (**Figure 6.2A-C**).

The zeta potential of the FFAs and LipoFAs was measured at intervals of 0, 6, 12, and 24 h. It was observed that only liposomes with a weight ratio of 5:1:4 exhibited consistent and stable trends in line with their zeta potential stability (**Figure 6.2D-F**) [62]. Zeta potential, indicative of the effective electric charge on liposome surface, is used to determine the stability and aggregation behavior of liposomal formulations [63]. This parameter serves as an indicator of the colloidal stability of liposomes, with higher absolute values suggesting enhanced particle stability [64]. For LipoFAs with a weight ratio of 5:1:4, the surface zeta potential was measured as -38.66 ± 1.2 mV for LipoLNA, -33.85 ± 2.09 mV for LipoLLA, -39.54 ± 2.08 mV for LipoOA, and -4.29 ± 0.4 mV for BareLipo. The marked decrease in surface zeta potential suggests the integration of FAs into the lipid layers, with the carboxylic acid group deprotonating to COO^- at neutral pH [32]. Liposomes with diameters less than 50 nm exhibit significant instability and a tendency to fuse due to high surface tension [40]. Conversely, larger liposomes (>200 nm) tend to be stable but face penetration challenges [65, 66]. Intermediate-sized liposomes (50-200 nm) offer relatively good stability, fusion capability, and penetration efficiency [40]. Thus, the 5:1:4 weight ratio was selected due to its moderate size (~140 nm) and physical stability. The size and shape of the prepared liposomes were further validated through cryogenic-electron microscopy (cryo-EM) (**Figure 6.2G**), revealing both BareLipo and LipoFAs as spherical with clear single or double layers, approximately 100 nm in size. The difference in sizes between cryo-EM and DLS may be due to the surface ions that provides a larger dynamic diameter [67].

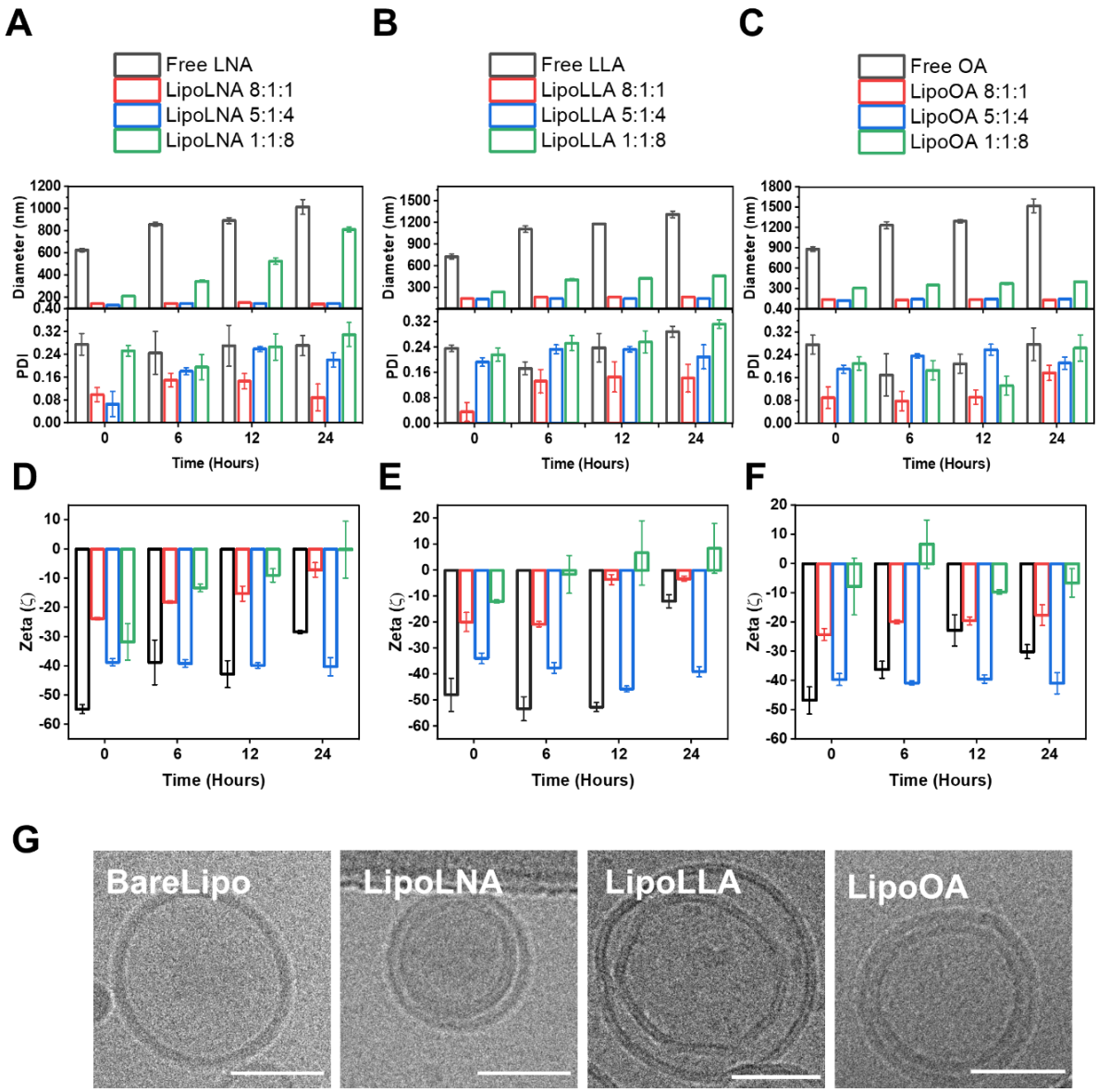

Figure 6.2 Characterization of LipoFAs. (A-C) Change in hydrodynamic size (diameter, nm) and PDI of FFAs and LipoFAs with different compositions measured by DLS. **(D-F)** Change in surface zeta potential (mV) of FFAs and LipoFAs with different compositions measured by DLS over 24 h (n = 3, mean ± SD). **(G)** Representative cryo-EM images of (1) BareLipo, (2) LipoLNA, (3) LipoLLA, and (4) LipoOA. The scale bar is 50 nm.

6.3.2 Frequency and Dissipation Relations (F-D Curves) for LipoFAs on Gram-positive Model Membranes

The frequency and dissipation relations for LipoFAs with the model membrane were derived from the QCM-D analysis (**Figure 6.3**), allowing for real-time tracking of variations in the membrane's mass and viscoelastic properties (**Figure 6.4A-C**).

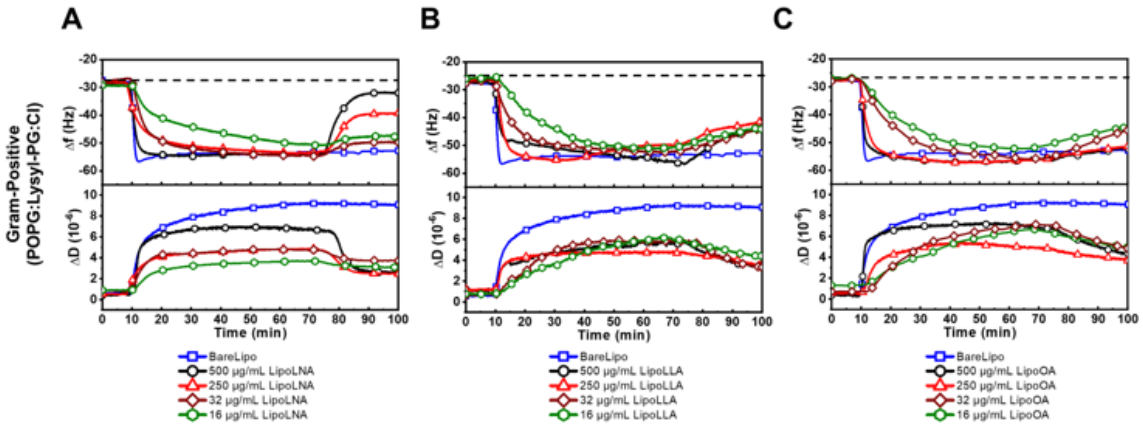

Figure 6.3 QCM-D curves for LipoFAs on Gram-positive model membranes. Δf and ΔD shifts as a function of time. (A-C) Frequency and dissipation shifts of BareLipo and LipoFAs on Gram-positive model membrane at varying concentrations. The dash line in panels (A-C) refer to initial SLB formation baseline.

In **Figure 6.4A**, the introduction of BareLipo to the model membrane surface resulted in adhesion [68-70], evidenced by a decline in frequency decrease and an elevation in dissipation [-f, +D]. This stage indicates the initial adsorption of liposomes onto the membrane surface. In the second stage, a continued rise in dissipation and a slight increase in frequency [+f, +D] were noted, suggesting the incorporation of lipid molecules within the model membrane [71-74]. During buffer washing in stage 3, both frequency and dissipation remained relatively unchanged, indicating that fusion of BareLipo with the membrane had occurred. Overall, the higher dissipation values demonstrated that the phospholipids changed the viscoelasticity of the membrane.

The frequency and dissipation relations for LipoLNA, LipoLLA, and LipoOA are shown in **Figure 6.4B**. Similar to the observations in stage 1 with BareLipo, the initial decrease in frequency indicates the adhesion of LipoFAs to the Gram-positive model membrane, characterized by the shift [-f, +D]. Variations in the $\partial D/\partial f$ ratio among LipoLNA, LipoLLA, and LipoOA were primarily due to differences in the rate of

dissipation increase. LipoOA exhibited the highest *∂D/∂f* values, suggesting a higher degree of incorporation into the model membrane (**Figure 6.4B**), as the viscoelasticity of the membrane increased most rapidly. Furthermore, the consistent *∂D/∂f* ratio for LipoOA indicated that fusion began upon adsorption onto the model membrane. LipoLLA showed a slight increase in the *∂D/∂f* ratio, indicative of a small impediment in liposome fusion and a slower fusion rate compared to LipoOA. Conversely, LipoLNA exhibited a noticeable change in the *∂D/∂f* ratio. The initial *∂D/∂f* ratio for LipoLNA (**Figure 6.4B**) suggests slower incorporation into the model membrane, followed by a significant increase in the *∂D/∂f* ratio, corresponding to a faster rise in dissipation for this sample. This may be attributed to the larger tail volume of LNA, which could impede the fusion rate [76, 77]. After rinsing with buffer at t = 100 min, the endpoints of the f-D curves provided insights of the membrane property changes. In **Figure 6.4C**, the frequency changes of LipoFAs after buffer rinsing were -21.87 ± 0.095 *Hz* for LipoLNA, -8.64 ± 0.049 *Hz* for LipoLLA, and -3.40 ± 0.06 *Hz* for LipoOA, indicating a decreasing trend in mass loss and suggesting more incorporation with the membrane components.

The membrane interactions were less pronounced at a lower concentration of 15.625 µg/ml (**Figure 6.4C**). The adhesion process was less significant due to the lower sample concentration. Given the absence of notable variations in the surface zeta potential of LipoFAs, they should present a similar adsorption ability resulting in similar frequency measurement responses. Interestingly, the frequency endpoints before buffer rinsing were -49.675 ± 0.112 *Hz* for LipoLNA, -51.181 ± 0.034 *Hz* for LipoLLA, and -54.022 ± 0.224 *Hz* for LipoOA, respectively, demonstrating an increase in mass and indicating a stronger incorporation capability of OA into the model membrane. Less change in mass was observed compared to higher LipoFA concentrations after buffer washing, while the final dissipation for LipoOA was the highest, primarily due to the greater incorporation of OA into the model membrane, resulting in the membrane instability.

To complement the fusion activities of LipoFAs, *in vitro* interactions between LipoFAs labeled with lipophilic Rh-PE fluorophore and *S. aureus* MW2 were investigated (**Figure 6.4D**). The bacteria were stained with DAPI (blue)**,** and only DAPI fluorescence was observed in PBS buffer solution. In contrast, upon co-incubation of the bacteria with Rh-PE labeled LipoFAs, distinct red fluorescence signal was detected around the bacteria,

confirming the fusion event with bacteria. Therefore, the fluorescence images are consistent with our QCM-D analysis.

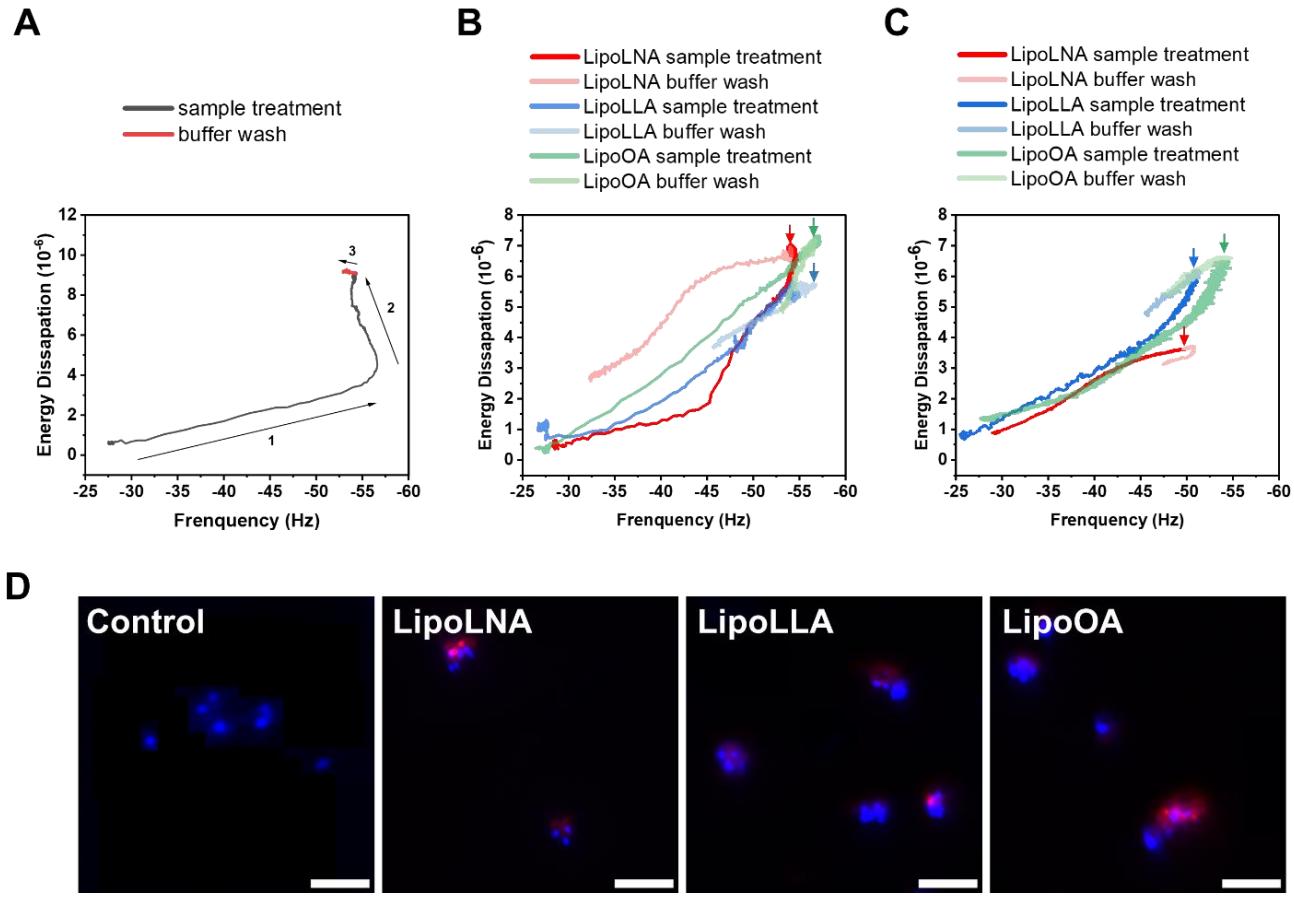

Figure 6.4 Biophysical characterization of membrane interaction and fusion with *S. aureus* MW2. Viscoelastic fingerprints of interactions of LipoFAs with model Gram-positive bacterial SLBs. Frequency-dissipation (F-D) curves for (A) BareLipo, (B) 500 μg/mL LipoFAs, and (C) 15.625 μg/mL LipoFAs. Arrows in panel (A) highlight the stages of interaction, while the downward arrows in panels (B and C) denote the initiation of buffer washing. (D) Fluorescence images illustrating fusion activity between RhB-labeled LipoFAs (red) and DAPI-stained bacteria (blue). Control bacteria were incubated with PBS. The scale bar is 5 μm.

6.3.3 Quantitative Analysis of Particle Formation in Gram-positive Model Membranes

To verify the f-D relation signatures and their corresponding kinetic effects on membrane morphology, fluorescence microscopy was employed to investigate and monitor the direct interactions between LipoFAs and Gram-positive model membranes. These membranes were established using the solvent-assisted lipid bilayer (SALB) method, following the protocol detailed in the experimental section. Freshly prepared LipoFAs were introduced to the formed lipid bilayers, with the introduction time marked as t = 0 min. Evaluations were conducted at concentrations of 500 µg/mL and 15.625 µg/mL.

LipoLNA on Gram-positive bacterial membranes. The interaction of LipoLNA with the Gram-positive model membrane is presented in **Figure 6.5A**. Upon exposure to 500 µg/mL LipoLNA, rapid morphological changes were observed due to the increased local curvature stress on membrane caused by the insertion of FAs [78]. Large dots appeared 10 min after sample introduction, with a total count number of 322 ± 17.4 dots, while the background intensity diminished, indicating the formation of bud structures on the model membrane, causing the background to become off-focus [79]. The formation of these large bud structures validates the impedance of the fusion of LipoLNA with the bacterial membrane, indicating restricted rearrangements of the lipid molecules, as evidenced by the lower $\partial D/\partial f$ ratios of LipoLNA compared to LipoLLA and LipoOA in **Figure 6.4B**. After rinsing with buffer, a significant reduction in the spots was observed, with only 23 ± 5.3 dots remaining, suggesting the removal of the formed structures. In contrast, a 15.625 µg/mL concentration of LipoLNA elicited negligible morphological response, with no significant disturbance observed on the model membrane.

LipoLLA on Gram-positive bacterial membranes. **Figure 6.5A** illustrates the monitoring of visual interactions between the model membrane and LipoLLA. When exposed to 500 µg/mL of LipoLLA, minor morphological changes were observed, evidenced by the presence of 1359 ± 50.4 small dots. The emergence of smaller and denser spots following LipoLLA introduction indicates increased integration and reorganization of lipid molecules within the model membrane, accompanied by formation of flatter bud structures. These morphological changes are consistent with the higher $\partial D/\partial f$ ratio compared to LipoLNA,

as shown in **Figure 6.4B**, which suggests a higher fusion rate and incorporation efficiency. After buffer rinsing, the number of bright dots significantly reduced to 355 ± 21.4 with a 73.8% removal rate. The remaining dots exhibited greater aggregation, implying a rearrangement of the membrane lipid molecules. This is supported by the decreased dissipation leading to a more rigid system. Conversely, introducing a lower concentration of LipoLLA resulted in minimal interactions with the model membrane. Nevertheless, the presence of small dark regions suggests some degree of fusion with the model membrane.

LipoOA on Gram-positive bacterial membranes. LipoOA rapidly induced the formation of numerous small and dense spot protrusions on the model membrane, indicating effective fusion and incorporation of its components. The presence of these dense spots indicated rapid fusion and rearrangement with the model membrane, resulting in higher $\partial D/\partial f$ ratios after sample treatment (**Figure 6.4B**). A total of 1636 ± 71.3 dots were counted on the model membrane, attributed to reduced impediments in incorporation and less local curvature stress of OA. Dark areas emerged after buffer rinsing, revealing defects on the model membrane where curved lipid molecules had been washed away due to changes in surface tension in the affected regions. Following washing, only 388 ± 16.9 dots remained, a count higher than that observed with LipoLNA before rinsing, indicating that LipoOA induced more significant lipid bilayer component rearrangements. Similarly, exposure to 15.625 μg/mL of LipoOA resulted in a greater number of tiny bright spots compared to those observed with LipoLNA and LipoLLA at lower concentrations, indicating more extensive incorporation of LipoOA into the membrane. In comparison to higher concentrations, less membrane change was observed.

The formation of diverse surface changes is attributed to the incorporation of FAs into the membrane. The insertion of non-cylindrical molecules, such as FAs, disrupts the lipid order in bacterial membrane and generate curvature stress and lateral pressure in the surrounding area, likely altering the surface curvature of the membrane [77, 79, 80]. This change in membrane structure results in destabilization of the membranes. Notably, unsaturation degree affects their interaction behaviors. LCFAs with less unsaturated bonds cause a flatter membrane surface morphology due to lower curvature stress, while those with more unsaturated bonds result in a more curved membrane surface.

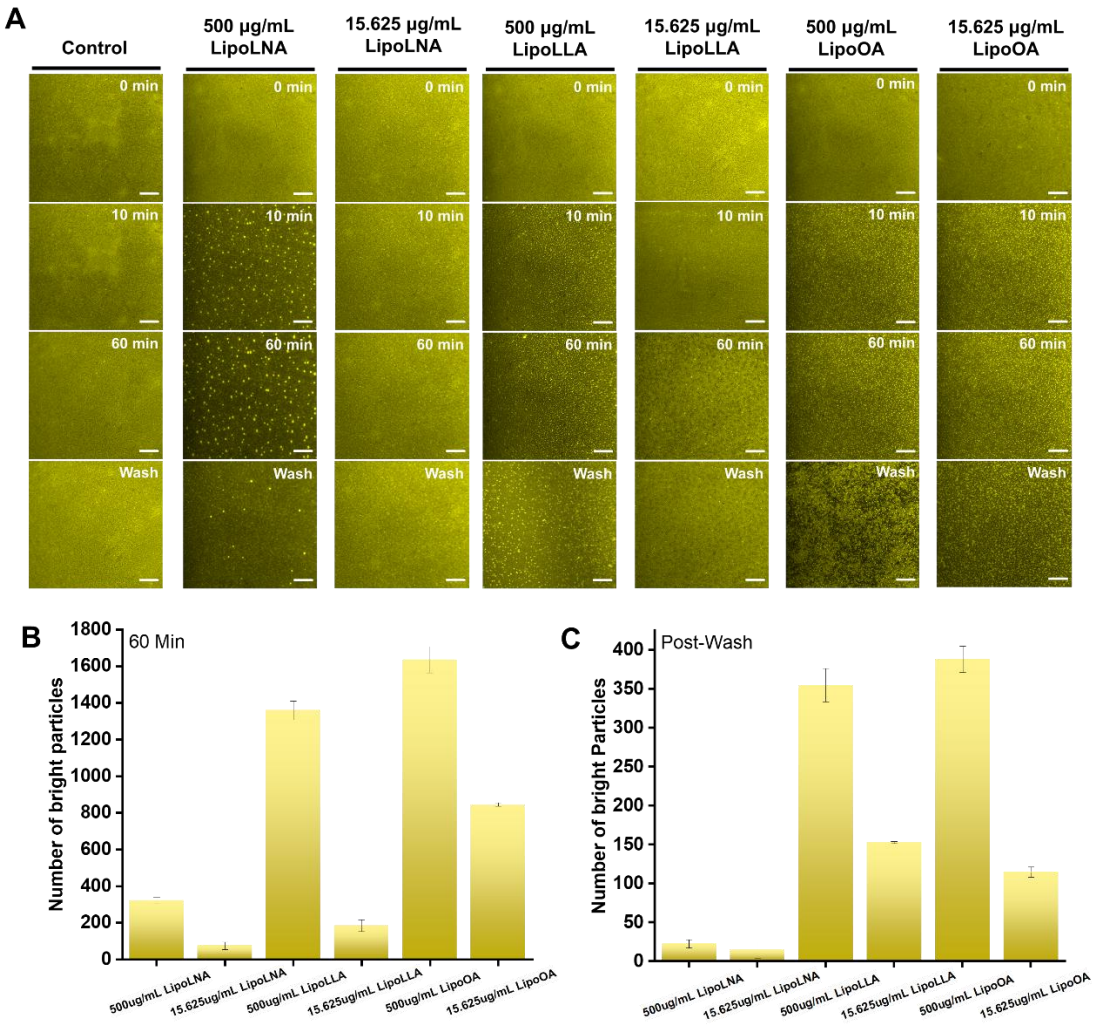

Figure 6.5 Quantitative analysis of particle formation in Gram-positive model membranes. Time-lapse microscopic observation of membrane morphological responses in SLBs induced by BareLipo, LipoOA, LipoLLA, and LipoLNA. **(A)** Sequential image snapshots depicting the morphological changes of SLBs upon interaction with BareLipo and LipoFAs at varying concentrations. The scale bar is 20 µm. The total number of particles **(B)** after sample treatment and **(C)** post-washing (n = 5, mean ± SD).

6.3.4 *In Vitro* Membrane Fluidity Changes Induced by LipoLNA, LipoLLA, and LipoOA on Gram-positive Bacterial Membranes

The incorporation of *cis*-unsaturated FAs in bacterial membranes can affect the membrane fluidity by inducing rearrangements of surrounding lipid molecules, thus

changing the membrane properties [51, 52, 81]. To evaluate these changes in membrane lipid behavior upon exposure to LipoFAs, FRAP measurements were conducted to measure the diffusion coefficient and mobile fraction of lipid molecules in the model membranes. As shown in **Figure 6.6A**, BareLipo increased the diffusion coefficient of the model membrane by 35.2%, LipoLNA by 18.4%, while LipoLLA and LipoOA decreased it by 36.4% and 92%, respectively. Concurrently, the mobile fraction of the lipid molecules was 80.0 ± 3% for LipoLNA, 43.8 ± 0.8% for LipoLLA, and 25.7 ± 2.2% for LipoOA. The reduction in the diffusion coefficient suggests an increase in lipid molecule rearrangement to restore the membrane. A higher degree of unsaturation leads to a more irregular arrangement of lipid molecules, facilitating easier movement within the membrane. Conversely, the mobile fraction of the exposed membrane was calculated to reflect the membrane's recovery rate. LipoOA exhibited the lowest mobile fraction of 25.7 ± 2.2%, indicating that only a quarter of the destabilized membrane was restored. The lower unsaturation degree in LipoOA results in a relatively higher order in the lipid tail arrangements, limiting molecular movement within the membrane [82]. In contrast, the presence of three unsaturated bonds in LipoLNA leads to a more disordered arrangement of lipid molecules in the membrane [83].

To further substantiate the changes in membrane properties after treatment with LipoFAs, the fluidity of the bacterial membrane was assessed using Laurdan Generalized Polarization (GP) intensity (**Figure 6.6F**). The Laurdan GP values for membranes treated with LipoFAs were 0.457 ± 0.017 for LipoLNA, 0.471 ± 0.005 for LipoLLA, and 0.477 ± 0.006 for LipoOA, respectively. In comparison, the Laurdan GP value was 0.448 ± 0.01 after treatment with BareLipo. The results indicated that *S. aureus* MW2 treated with LipoFAs exhibited increased membrane rigidity, consistent with the observations from the FRAP results, suggesting that the incorporation of FAs into the membrane induced changes in fluidity.

A

	diffusion coefficient ($\mu m^2/s$)			
	before treatment	after treatment		mobile fraction
BareLipo	0.71 ± 0.04	0.96 ± 0.11	+35.2%	87.0 ± 1%
500 µg/mL LipoLNA	0.76 ± 0.04	0.90 ± 0.03	+18.4%	80.0 ± 3%
500 µg/mL LipoLLA	0.44 ± 0.03	0.28 ± 0.02	-36.4%	43.8 ± 0.8%
500 µg/mL LipoOA	0.49 ± 0.04	0.04 ± 0.02	-92.0%	25.7 ± 2.2%

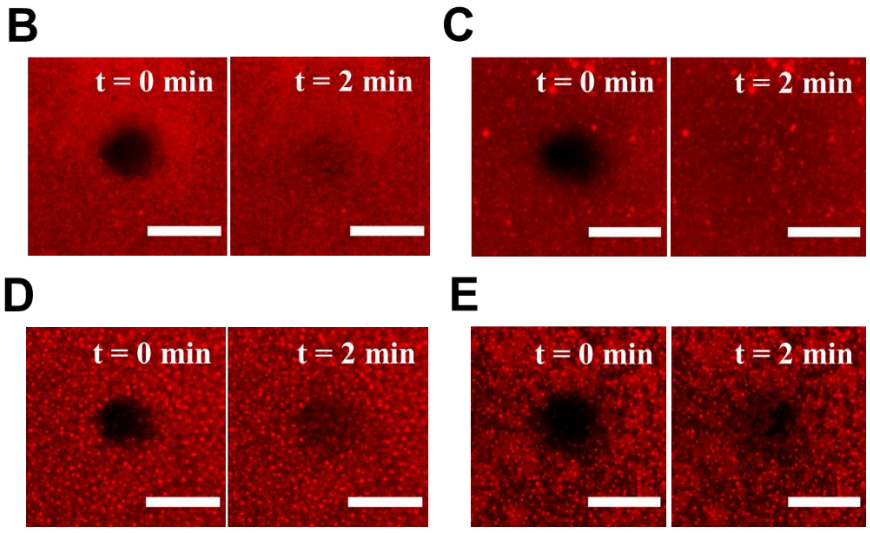

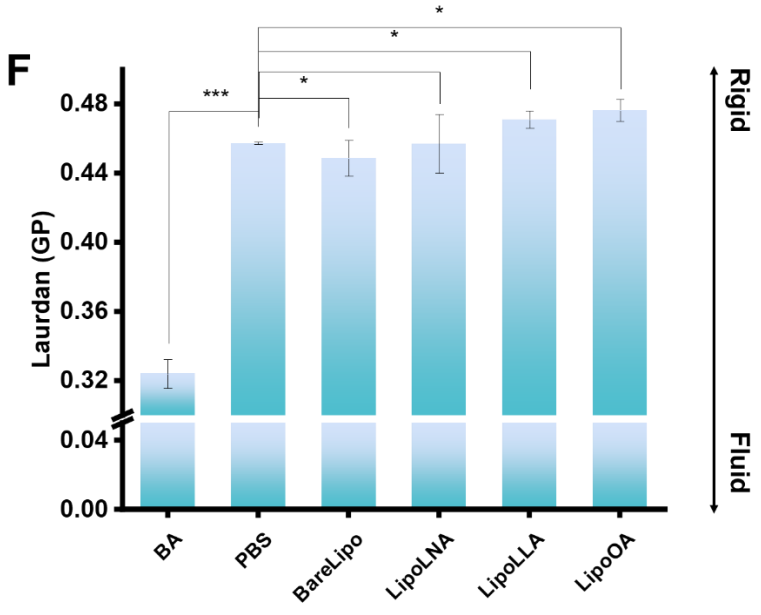

Figure 6.6 Membrane fluidity changes induced by LipoFAs on Gram-positive model membranes and *in vitro* bacterial fusion assays. (A) Summary of diffusion coefficients and mobile fractions for the Gram-positive model membrane before and after treatment with LipoFAs. Fluorescence micrographs at 0 min and 2 min after photobleaching for model membranes treated with **(B)** BareLipo, **(C)** LipoLNA, **(D)** LipoLLA, and **(E)** LipoOA. The scale bar is 20 μm. **(F)** Membrane fluidity of *S. aureus* MW2 treated with LipoFAs and BareLipo for 1h. Laurdan GP index = $(I_{435} - I_{490})/(I_{435} + I_{490})$, where 435 and 490 are the emission intensities at 435 nm and 490 nm, respectively, when excited at 350 nm (n = 3, mean ± SD). Statistical significance was determined with p values <0.05 as significant (*p < 0.05, **p < 0.01, and ***p < 0.001).

6.4 Conclusion

This investigation offers an in-depth examination of the interaction behaviors of LipoFAs with Gram-positive model membranes using various biophysical techniques. The research elucidates how LipoFAs fuse and integrate with phospholipid membrane components and the consequent alterations in the membrane's viscoelastic properties. The prepared LipoFA formulations with the optimal weight ratio demonstrated a significant decrease in zeta potential of around -50 mV and an intermediate size of ~140 nm, suggesting a propensity to fuse with Gram-positive model membranes. The observed changes in membrane fluidity, measured through fluorescence recovery after photobleaching (FRAP) experiments, are strongly correlated with the results of other biophysical assays conducted in this study. FRAP revealed a notable reduction in the lateral diffusivity of supported lipid bilayers (SLBs) mimicking Gram-positive bacterial membranes upon exposure to long-chain unsaturated fatty acids (LNA, LLA, and OA). This observation is consistent with quartz crystal microbalance-dissipation (QCM-D) measurements, which documented significant changes in frequency (Δf) and dissipation (ΔD), reflecting modifications in the mass, thickness, and viscoelastic properties of the SLBs during fatty acid interaction. Specifically, experimental results revealed that a lower degree of saturation in the FA tails impedes their incorporation and rearrangement within the Gram-positive model membrane possibly due to larger local curvature stress surrounding the FAs. In contrast, FAs with fewer unsaturated bonds are more easily incorporated and form less curvature stress. These findings indicate that the structural

characteristics of FAs substantially influence their interaction with model bacterial membranes. Overall, these insights are crucial for understanding the fundamental processes governing FA-membrane interactions and can inform the design of more effective lipid-based therapeutic agents targeting Gram-positive bacterial infections. Future work extending the scope of tested compounds on their biological activities on MRSA could enhance the understanding of how the compounds act against bacterial membrane and further validate the relevance of the *in vitro* model bacterial membrane.

References

[1] H. Fongang, A.T. Mbaveng, V. Kuete. In *Chapter One - Global burden of bacterial infections and drug resistance, in: V. Kuete (Ed.), Advances in Botanical Research*, Academic Press2023, pp. 1-20.

[2] J.H. Kwon, W.G. Powderly. *Science*. **2021**, 373(6554), 471.

[3] G. Casillas-Vargas, C. Ocasio-Malavé, S. Medina, C. Morales-Guzmán, R.G. Del Valle, N.M. Carballeira, D.J. Sanabria-Ríos. *Progress in Lipid Research*. **2021**, 82, 101093.

[4] A.P. Desbois, V.J. *Applied Microbiology and Biotechnology*. **2010**, 85(6), 1629-1642.

[5] C. Borreby, E.M.S. Lillebæk, B.H. Kallipolitis. *FEMS Microbiology Reviews*. **2023**, 47(4).

[6] B.K. Yoon, J.A. Jackman, E.R. Valle-González, N.-J. Cho. *International journal of molecular sciences*. **2018**, 19(4), 1114.

[7] B.K. Yoon, J.A. Jackman, M.C. Kim, N.-J. Cho. *Langmuir*. **2015**, 31(37), 10223-10232.

[8] J.A. Jackman, B.K. Yoon, D. Li, N.-J. Cho. *Molecules*. **2016**, 21(3), 305.

[9] T.-A. Hagve. *Scandinavian Journal of Clinical and Laboratory Investigation*. **1988**, 48(5), 381-388.

[10] H. Galbraith, T.B. Miller, A.M. Paton, J.K. *Journal of Applied Bacteriology*. **1971**, 34(4), 803-813.

[11] J.J. Kabara, R. Vrable. *Lipids*. **1977**, 12(9), 753-9.

[12] F. Kanetsuna. *Microbiology and Immunology*. **1985**, 29(2), 127-41.

[13] D.L. Greenway, K.G. Dyke. *The Journal of General Microbiology*. **1979**, 115(1), 233-45.

[14] B.W. Petschow, R.P. Batema, L.L. Ford. *Antimicrobial Agents and Chemotherapy*. **1996**, 40(2), 302-6.

[15] E. Skrivanová, O.G. Savka, M. Marounek. *Folia Microbiologica*. **2004**, 49(2), 199-202.

[16] A. Kollanoor, P. Vasudevan, M.K.M. Nair, T. Hoagland, K. Venkitanarayanan. *Aquaculture Research*. **2007**, 38(12), 1293-1300.

[17] J.Y. Lee, Y.S. Kim, D.H. Shin. *Journal of Agricultural and Food Chemistry*. **2002**, 50(7), 2193-9.

[18] A.P. Desbois, K.C. Lawlor. *Marine Drugs*. **2013**, 11(11), 4544-57.

[19] H. Arellano, V. Nardello-Rataj, S. Szunerits, R. Boukherroub, A.-L. Fameau. *Advances in Colloid and Interface Science*. **2023**, 318, 102952.

[20] C.Q. Sun, C.J. O'Connor, A.M. Roberton. *FEMS Immunology and Medical Microbiology*. **2003**, 36(1-2), 9-17.

[21] K.T. Yuyama, M. Rohde, G. Molinari, M. Stadler, W.R. Abraham. *Antibiotics*. **2020**, 9(11).

[22] C.J. Zheng, J.-S. Yoo, T.-G. Lee, H.-Y. Cho, Y.-H. Kim, W.-G. Kim. *FEBS Letters*. **2005**, 579(23), 5157-5162.

[23] J.A. Kenar, B.R. Moser, G.R. List. *In Chapter 2 - Naturally Occurring Fatty Acids: Source, Chemistry, and Uses, M.U. Ahmad (Ed.), Fatty Acids*, AOCS Press2017, pp. 23-82.

[24] A.S.H. Ong, S.H. Goh. *Food and Nutrition Bulletin*. **2002**, 23(1), 11-22.

[25] J.E., Kinsella. *Food Technology*. **1974**, 28(5), 58–60.

[26] L. DeBonte, D. Iassonova, L. Liu, W. Loh. *Lipid Technology*. **2012**, 24(8), 175-177.

[27] J.Y.B. Tan, B.K. Yoon, N.-J. Cho, J. Lovrić, M. Jug, J.A. Jackman. *International Journal of Molecular Sciences*. **2021**, 22(18), 9664.

[28] R.T. Holman, O.C. Elmer. *Journal of the American Oil Chemists' Society*. **1947**, 24(4), 127-129.

[29] H. Schulz, In *Chapter 5 Oxidation of fatty acids in eukaryotes, New Comprehensive Biochemistry*, Elsevier2002, pp. 127-150.

[30] X. Fu, F. Feng, B. Huang. *International Journal of Pharmaceutics*. **2006**, 321(1), 171-175.

[31] N. Üstündag-Okur, E.H. Gökçe, S. Eğrilmez, Ö. Özer, G. Ertan. *Journal of Ocular Pharmacology and Therapeutics*. **2014**, 30(4), 319-332.

[32] S. Thamphiwatana, W. Gao, M. Obonyo, L. Zhang. *Proceedings of the National Academy of Sciences*. **2014**, 111(49), 17600-17605.

[33] M.A. Vélez, M.C. Perotti, E.R. Hynes, A.M. Gennaro. *Journal of Food Engineering*. **2019**, 240, 199-206.

[34] P. Pushparaj Selvadoss, J. Nellore, M. Balaraman Ravindrran, U. Sekar, J. Tippabathani. *Artificial Cells, Nanomedicine, and Biotechnology*. **2018**, 46(2), 268-273.

[35] L. Yan, L. Wang, S. Gao, C. Liu, Z. Zhang, A. Ma, L. Zheng. *Food Chemistry*. **2020**, 309, 125717.

[36] L. Mei, D. Zhang, H. Shao, Y. Hao, T. Zhang, W. Zheng, Y. Ji, P. Ling, Y. Lu, Q. Zhou. *ACS Applied Materials & Interfaces*. **2022**, 14(18), 20538-20550.

[37] U. Butt, A. ElShaer, L.A.S. Snyder, A.A. Al-Kinani, A. Le Gresley, R.G. Alany. *Nanomaterials*. **2018**, 8(1).

[38] C. Torres-Luna, N. Hu, X. Fan, R. Domszy, J. Yang, R.M. Briber, A. Yang. *European Journal of Pharmaceutics and Biopharmaceutics*. **2020**, 155, 1-11.

[39] L. Zhang, D. Pornpattananangkul, C.-M. Hu, C.-M. Huang. *Current Medicinal Chemistry*. **2010**, 17(6), 585-594.

[40] C.-M. Huang, C.-H. Chen, D. Pornpattananangkul, L. Zhang, M. Chan, M.-F. Hsieh, L. Zhang. *Biomaterials*. **2011**, 32(1), 214-221.

[41] L.M. Lieb, C. Ramachandran, K. Egbaria, N. Weiner. *Journal of Investigative Dermatology*. **1992**, 99(1), 108-113.

[42] V.P. Torchilin. *Nature Reviews Drug Discovery*. **2005**, 4(2), 145-160.

[43] S.W. Jung, S. Thamphiwatana, L. Zhang, M. Obonyo. *PLoS One*. **2015**, 10(3), e0116519.

[44] L.J. Halverson, M.K. Firestone. *Applied and Environmental Microbiology*. **2000**, 66(6), 2414-2421.

[45] X. Ge, X. Shi, L. Shi, J. Liu, V. Stone, F. Kong, T. Kitten, P. Xu. *PLoS One*. **2016**, 11(3), e0151142.

[46] T. Itoh, T. Takenawa. *Progress in Lipid Research*. **2009**, 48(5), 298-305.

[47] M. Gohrbandt, A. Lipski, J.W. Grimshaw, J.A. Buttress, Z. Baig, B. Herkenhoff, S. Walter, R. Kurre, G. Deckers-Hebestreit, H. Strahl. *The EMBO Journal*. **2022**, 41(5), e109800.

[48] D. Or, B.F. Smets, J.M. Wraith, A. Dechesne, S.P. Friedman. *Advances in Water Resources*. **2007**, 30(6), 1505-1527.

[49] C.M. Huang, C.H. Chen, D. Pornpattananangkul, L. Zhang, M. Chan, M.F. Hsieh, L. Zhang. *Biomaterials*. **2011**, 32(1), 214-21.

[50] M. Obonyo, L. Zhang, S. Thamphiwatana, D. Pornpattananangkul, V. Fu, L. Zhang. *Molecular Pharmaceutics*. **2012**, 9(9), 2677-2685.

[51] D.L.A. Greenway, K.G.H. Dyke. *Microbiology*. **1979**, 115(1), 233-245.

[52] N.R. Chamberlain, B.G. Mehrtens, Z. Xiong, F.A. Kapral, J.L. Boardman, J.I. Rearick. *Infection and Immunity*. **1991**, 59(12), 4332-4337.

[53] S. Murínová, K. Dercová, M. Čertík, K. Lászlová. *Biologia*. **2014**, 69(4), 428-434.

[54] D. Yang, D. Pornpattananangkul, T. Nakatsuji, M. Chan, D. Carson, C.M. Huang, L. Zhang. *Biomaterials*. **2009**, 30(30), 6035-40.

[55] L.D. Mayer, M.J. Hope, P.R. Cullis. *Biochimica et Biophysica Acta (BBA)*. **1986**, 858(1), 161-8.

[56] S.R. Tabaei, J.H. Choi, G. Haw Zan, V.P. Zhdanov, N.J. Cho. *Langmuir*. **2014**, 30(34), 10363-73.

[57] S. Di Leone, M. Kyropoulou, J. Köchlin, R. Wehr, W.P. Meier, C.G. Palivan. *Langmuir*. **2022**, 38(21), 6561-6570.

[58] M.C. Dixon. *Journal of Biomolecular Techniques*. **2008**, 19(3), 151-8.

[59] P. Jönsson, M.P. Jonsson, J.O. Tegenfeldt, F. Höök. *Biophysical Journal*. **2008**, 95(11), 5334-48.

[60] O.G. Mouritsen, Lipids. *European Journal of Lipid Science and Technology*. **2011**, 113(10), 1174-1187.

[61] M. Danaei, M. Dehghankhold, S. Ataei, F. Hasanzadeh Davarani, R. Javanmard, A. Dokhani, S. Khorasani, M.R. Mozafari. *Pharmaceutics*. **2018**, 10(2), 57.

[62] I.L. Dejeu, L.G. Vicaș, T. Jurca, A.C. Teușdea, M.E. Mureșan, L. Fritea, P. Svera, G.A. Gabor, G.E. Dejeu, O.A. Maghiar, A.S. Bodea, A. Pallag, E. Marian. *Processes*. **2021**, 9(6), 912.

[63] N.A. Ramli, N.a. Ali, S. Hamzah. *Journal of Sustainability Science and Management*. **2020**, 15(6), 15-27.

[64] R. Li, L.Y. Zhang, Z.J. Li, C.H. Xue, P. Dong, Q.R. Huang, Y.M. Wang, T.T. Zhang. *Journal of Agricultural and Food Chemistry*. **2019**, 68(2), 642-651.

[65] N. Dragicevic-Curic, S. Gräfe, B. Gitter, S. Winter, A. Fahr. *International Journal of Pharmaceutics*. **2010**, 384(1), 100-108.

[66] N. Dragicevic-Curic, S. Winter, D. Krajisnik, M. Stupar, J. Milic, S. Graefe, A. Fahr. *Journal of Liposome Research*. **2010**, 20(1), 38-48.

[67] S. Peretz Damari, D. Shamrakov, M. Varenik, E. Koren, E. Nativ-Roth, Y. Barenholz, O. Regev. *International Journal of Pharmaceutics*. **2018**, 547(1), 648-655.

[68] I.Y. Hasan, A. Mechler. *Soft Matter*. **2015**, 11(27), 5571-5579.

[69] B. Seantier, C. Breffa, O. Félix, G. Decher. *The Journal of Physical Chemistry B*. **2005**, 109(46), 21755-21765.

[70] M. Deng, Q. Liu, Z. Xu. *Minerals Engineering*. **2013**, 46–47, 6–15.

[71] K.R. Flynn, L.L. Martin, M.L. Ackland, A.A.J. Torriero. *Langmuir*. **2016**, 32(45), 11717-11727.

[72] N. Asai, N. Matsumoto, I. Yamashita, T. Shimizu, S. Shingubara, T. Ito. *Sensing and Bio-Sensing Research*. **2021**, 32, 100415.

[73] M. Wlodek, M. Kolasinska-Sojka, M. Szuwarzynski, S. Kereïche, L. Kovacik, L. Zhou, L. Islas, P. Warszynski, W.H. Briscoe. *Nanoscale*. **2018**, 10(37), 17965-17974.

[74] I.F. Márquez, M. Vélez. *MethodsX*. **2017**, 4, 461-468.

[75] T. Koyanagi, K.J. Cao, G. Leriche, D. Onofrei, G.P. Holland, M. Mayer, D. Sept, J. Yang. *Chemistry – A European Journal*. **2017**, 23(28), 6757-6762.

[76] L.R. Walker, M.T. Marty. In *Lipid Tails Modulate Antimicrobial Peptide Membrane Incorporation and Activity*, bioRxiv2021, pp.2021-08.

[77] A. Arouri, O.G. Mouritsen. *Progress in Lipid Research*. **2013**, 52(1), 130-140.

[78] D. Thid, J.J. Benkoski, S. Svedhem, B. Kasemo, J. Gold. *Langmuir*. **2007**, 23(11), 5878-5881.

[79] H. Jespersen, J.H. Andersen, H.J. Ditzel, O.G. Mouritsen. *Biochimie*. **2012**, 94(1), 2-10.

[80] R.S. Cantor. *Biophysical Journal*. **1999**, 76(5), 2625-2639.

[81] M.S. Lopez, I.S. Tan, D. Yan, J. Kang, M. McCreary, Z. Modrusan, C.D. Austin, M. Xu, E.J. Brown. *Proceedings of the National Academy of Sciences*. **2017**, 114(42), 11223-11228.

[82] K.C. Weng, J.L. Kanter, W.H. Robinson, C.W. Frank. *Colloids and Surfaces B: Biointerfaces*. **2006**, 50(1), 76-84.

[83] M. Ibarguren, D.J. López, P.V. Escribá. *Biochimica et Biophysica Acta (BBA)*. **2014**, 1838(6), 1518-1528.

Chapter 7

Conclusions and Recommendations

Chapter 7 highlights the key outcomes and conclusions derived from the experimental framework, highlighting the extent to which the hypothesis was validated. The fundamental insights gained from this research provide a foundation for potential therapeutic applications and inform strategies for future work.

7.1 Conclusions

Due to the limited comprehension of the underlying mechanisms that contribute to the antimicrobial properties of LCFAs and LipoFAs, an integrative framework was developed in this thesis. This framework aims to establish the connection between CMC values of LCFAs and their antibacterial potency on model membrane SLBs, as well as to elucidate the mechanisms of membrane interactions of antimicrobial FAs and LipoFAs on model SLB membranes. The framework facilitated the characterization of the self-aggregation behaviors of LCFAs, specifically LNA, LLA, and OA. It enabled the acquisition of concentration-dependent FA-membrane interaction activity profiles, an understanding of the magnitude of the membrane morphological changes, and the determination of membrane property alterations, and provided insights into the structure-activity relationships at the molecular level. Additionally, this framework was utilized to test the hypothesis that single-component and multi-component SLBs provide robust screening platforms for characterizing the MOA of antimicrobial LCFAs and LipoFAs against phospholipid membranes in real-time, as these platforms can be integrated with other surface-sensitive techniques. The key design steps to validate the hypothesis are presented along with the key outcomes.

Chapter 4 laid the foundational understanding of how physicochemical properties of LCFAs influence molecular interactions with zwitterionic DOPC lipids and to draw the connection with their respective CMC values. The results revealed that LNA, LLA, and OA displayed membrane-active behavior at concentrations mainly above their CMC values, with negligible effects observed below these concentrations. This observation demonstrated a CMC-dependent activity profile of LCFAs against DOPC lipids. Additionally, it was discovered that the FA with the highest degree of unsaturation induced more significant membrane changes, forming notable tubular morphological changes on the SLB. These findings demonstrate a broadly applicable screening platform for gaining enhanced molecular-level understanding of the MOA of LCFAs, which can be useful for design antimicrobial agents.

In the following chapter, the scope is expanded to develop multi-component SLBs that replicate the plasma membrane of the representative GPB *S. aureus*, using the SALB fabrication method. The model bacterial membrane was compared with the conventional single-component DOPC SLB platform. The results revealed that LCFAs interacted weakly with the charged SLBs compared to the single-component SLBs. It was also discovered that LNA and LLA displayed weaker interactions, while OA penetrated deeper into the bilayer. The findings demonstrated that LCFAs are primarily active against charged SLBs above CMC values, except for OA, which forms vesicles at concentrations below CMC at physiological pH, facilitating attachment to the SLB even at low concentrations. Overall, the results demonstrated that charged SLBs composed of varying ratios of charged lipids could be successfully fabricated and that LCFAs interact differently with these SLBs, indicating different mechanisms of interaction on model bacterial membranes, warranting further research.

In Chapter 6, the mechanisms of interaction of liposomes loaded with FAs with model bacterial membranes are described. Given the low solubility of FAs in aqueous solution, it is imperative to encapsulate the FAs into liposomes to improve delivery and to understand the mechanisms of interaction of LipoFAs. The results revealed that LipoFAs altered the membrane fluidity upon incorporation of the FAs into the SLBs. It also revealed that LNA, with the highest unsaturation degree, inserted less efficiently into the membrane, resulting in decreased membrane rigidity and high local curvature stress. This chapter demonstrated the potential of LipoFAs to fine-tune membrane interactions, providing insights into how formulation strategies can enhance the antimicrobial efficacy of these compounds and enhanced the understanding of the individual mechanisms of FAs from previous chapters.

The progression from Chapters 4 to 6 highlights the layered complexity of LCFA interactions with lipid membranes. Chapter 4 established fundamental structure-activity relationships, emphasizing the role of CMC and unsaturation in determining membrane-active properties. Chapter 5 expanded this knowledge by showing how membrane composition and charge influence these interactions, revealing differences in behavior between model and bacterial-mimetic SLBs. Finally, Chapter 6 demonstrated the potential

of advanced formulations, such as liposomes, to overcome solubility limitations and enhance antimicrobial delivery.

Together, these chapters build a cohesive narrative that bridges fundamental molecular insights with practical applications. The findings provide a roadmap for designing next-generation antimicrobial agents by leveraging the interplay between LCFA structure, lipid bilayer composition, and formulation strategies. This integrative framework not only enhances our understanding of antimicrobial mechanisms but also offers valuable principles for optimizing the therapeutic potential of LCFAs and LipoFAs. Future work should include biological evaluations such as bactericidal kinetics analysis, membrane permeabilization assay, intracellular metabolite leakage assay, and cytoxicity testing to validate the utility of the model membrane platforms and further the application of these antimicrobial agents.

7.2 Future Work

This thesis has provided significant insights into the mechanistic interactions of LCFAs and LipoFAs with single-component and multi-component SLB membranes, laying the groundwork for advancing next-generation antimicrobial agents using the SLB platform as an analytical framework. The proposed future work will build on these findings by including *in vitro* biological experimental data, aiming to translate the fundamental research into practical therapeutic applications.

7.2.1 Antimicrobial Potency of the Membrane-Active Long-Chain Unsaturated Fatty Acids on *S. aureus* MW2

Due to issues related to the solubility of FAs, MIC measurements were not possible in the study. Instead, the study focused on assessing the compounds' bactericidal properties. The observed bactericidal effects against *S. aureus* MW2 generally corresponded with the behaviors observed on our model of Gram-positive membranes, highlighting the

significance of our model bacterial membrane systems in comprehending antimicrobial activities.

To characterize the antimicrobial activity of LNA, LLA, and OA, we evaluated the bactericidal activity of the FAs against *S. aureus* MW2 from the concentration range of 16 μM to 500 μM (**Figure 7.1A**). Treatment with LNA for 4 h led to approximately 4-log reduction in bacterial viability at equal or more than 125 μM. While 4-h treatment with LLA resulted in approximately 4-log reduction in bacterial viability at equal or more than 250 μM, treatment with OA for the same time frame could cause about 3-log decrease in *S. aureus* MW2 viability at 500 μM. The concentrations at which the three FA compounds induced more than 3-log killing is consistent with the concentrations at which those compounds interacted with the model bacterial membranes (**Figure 5.4**, **Figure 5.7**, and **Figure 5.10**). These findings indicate that LNA, LLA, and OA exhibit antimicrobial activity against *S. aureus* MW2 within concentration ranges that align with their biophysical interactions with model bacterial membranes. Notably, the observed bactericidal activity of OA is not directly proportional to the biophysics data. One possible rationale for this phenomenon is that not all neutral OA molecules exhibit membrane activity due to their tendency to self-aggregate at physiological pH, forming self-assembled complexes or dimers that may lack or have reduced antimicrobial efficacy against bacteria [1]. This phenomenon may also be attributed to the CMC-independent behavior exhibited by OA. In addition, an intricate sequence of biological events occurs once an antimicrobial agent interacts with its primary target, which can trigger secondary processes such as the accumulation of reactive oxygen species (ROSs) [2], alterations in metabolisms [3], or damage to cellular components [4], which collectively lead to bacteria demise [5].

To complement this study, we further evaluated the membrane-active ability of LNA, LLA, and OA through membrane permeability and cellular ATP leakage assays (**Figure 7.1B** and **Figure 7.1C**). LNA triggered a swift escalation in SYTOX Green fluorescence at concentrations from 125 μM to 500 μM, LLA from 63 μM to 500 μM, and OA from 31 μM to 500 μM. Antimicrobial agents that disrupt membranes can lead to the leakage of intracellular ATP [1, 6]. To determine whether FA treatment results in ATP leakage from inside the bacterial cells, an ATP luminescence assay was employed. A notable rise in

luminescence was detected in *S. aureus* MW2 cells treated with LNA at concentrations between 125 μM and 500 μM, LLA at concentrations between 63 μM and 500 μM, and OA at concentrations between 31 μM and 500 μM. Overall, the results indicate that the test compounds induce membrane disruption on the bacteria in a CMC-dependent manner [7].

Overall, it is noteworthy that the interaction dynamics of LCFAs on Gram-positive bacterial membranes are relatively in line with the bactericidal efficacy against *S. aureus* MW2. The results of the membrane permeabilization and ATP leakage assay results corresponded closely to their individual CMC values, indicating a CMC-dependent interaction behavior on Gram-positive bacterial membranes. Conversely, OA exhibited bactericidal effects at a concentration exceeding its CMC value, suggesting a CMC-independent interaction with Gram-positive bacterial membranes. The observed bactericidal effects against *S. aureus* MW2 generally aligned with the behaviors observed on the model Gram-positive membrane, reinforcing the relevance of our model bacterial membrane systems in understanding antimicrobial activities. This correlation underscores the importance of utilizing biologically relevant model systems of bacterial membranes in antimicrobial studies.

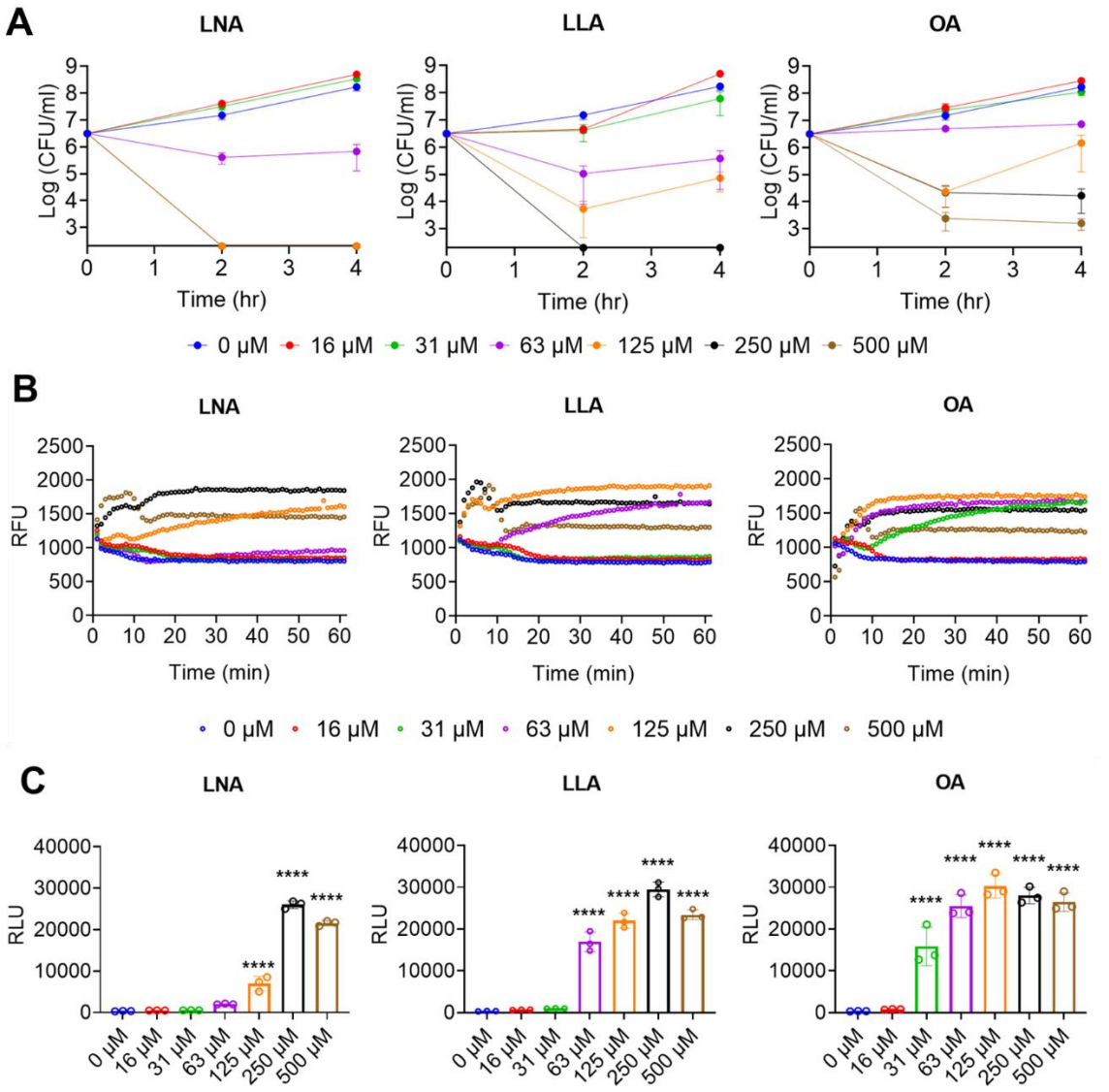

Figure 7.1 LNA, LLA, and OA penetrate the cell membrane bilayers of *S. aureus* MW2, demonstrating antimicrobial activity. (A) Exponential-phase *S. aureus* MW2 cells were treated with concentrations ranging from 16 µM to 500 µM for 4 h. Surviving cells were quantified by determining CFU (Colony Forming Units) counts through serial dilution and plating on MH agar plates every 2 h (n = 5, mean ± SD). Data points below the detection limit (2×10^2 CFU/mL) are indicated on the x-axis. (B) Membrane permeabilization was assessed after a 60 min treatment of *S. aureus* MW2 with LNA, LLA, and OA using SYTOX Green fluorescence (Ex 485 nm, Em 525 nm). The data represent the mean of three independent experiments. (C) Intracellular ATP leakage from *S. aureus* MW2 cells treated with LNA, LLA, and OA for 20 min was measured using an ATP luminescence assay. Individual data points are displayed, with error bars representing mean ± SD

(n = 3). Statistical differences were analyzed using one-way ANOVA followed by Tukey's multiple comparisons test (**** $p < 0.0001$).

7.2.2 Antimicrobial Potency of the Membrane-Active Liposomal Long-Chain Fatty Acids on *S. aureus* MW2

The antimicrobial activity of LipoFAs was evaluated through a minimum inhibitory concentration (MIC) assay against *S. aureus* MW2 (**Figure 7.3A**). The study found that LipoLNA had the lowest MIC at 125 µg/mL, followed by LipoLLA at 500 µg/mL, while LipoOA did not exhibit any MIC even at 500 µg/mL. Since MIC measurements are determined based on an OD_{600} reading below 0.1, the MICs for LNA and LLA among the LCFAs could not be determined due to their solubility issues. Under identical MIC measurement conditions, without bacterial addition, the OD_{600} values for LNA and LLA at 250 µg/mL remained above 0.1, thus they were deemed unreadable. OA did not show an MIC even at 500 µg/mL. Therefore, as shown in **Figure 7.3B**, further evaluation was performed through a time-kill kinetic analysis. Bacterial counts were recorded as log CFU. After treatment with all FFA and LipoFAs, a decreasing trend was observed at 16 µg/mL. In particular, after 4 h of treatment, LipoLNA reduced bacterial counts by more than 2-Log at 63 µg/mL and inhibited bacterial growth to detection limits at 125 µg/mL. LipoLLA achieved a reduction of more than 2-Log at 31 µg/mL and inhibited bacterial growth to detection limits at 125 µg/mL. LipoOA reduced bacterial counts by 1-Log at 500 µg/mL. LNA reduced bacterial counts by more than 2-Log at 16 µg/mL and inhibited bacterial growth to detection limits at 31 µg/mL. LLA achieved a reduction of more than 3-Log at 16 µg/mL and inhibited bacterial growth to detection limits at 31 µg/mL. OA inhibited bacterial growth to detection limits at 16 µg/mL.

A

Pathogen	Strain	LipoLNA	LipoLLA	LipoOA	BareLipo	LNA	LLA	OA	Vancomycin
S. aureus	MW2	125	500	>500	>500	unreadable	unreadable	>500	1

(μg/mL)

B

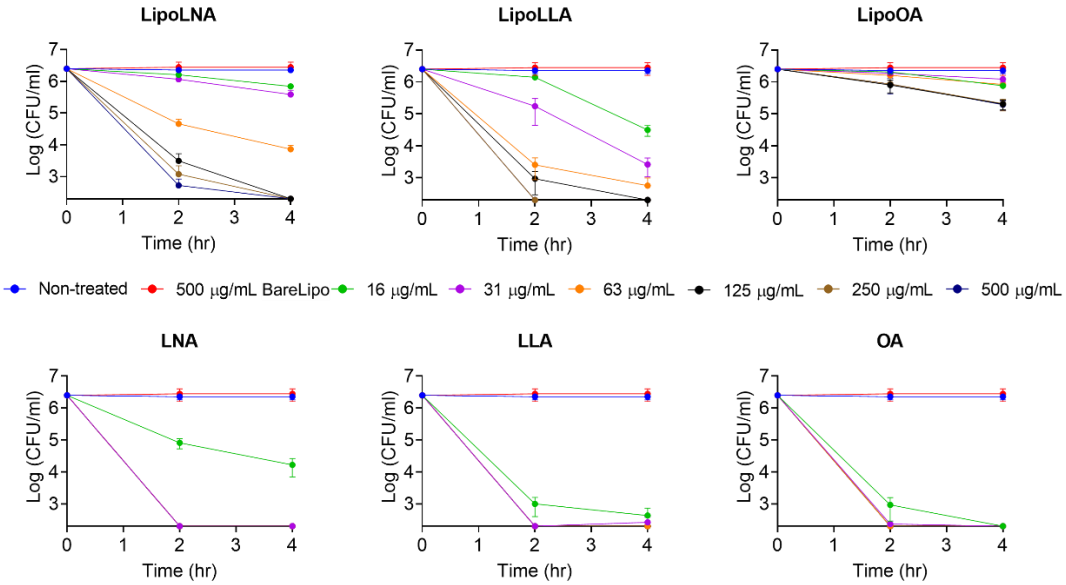

Figure 7.2 *In vitro* bactericidal activity of LCFAs and LipoFAs against *S. aureus* MW2. (A) A table showing the MIC values against *S. aureus* MW2. (B) CFU-time curves of liposomes against *S. aureus* MW2 plotted using exponential phase bactericidal kinetics analysis. Data are presented as mean ± standard deviation (n = 3), and data points on the x-axis fall below the detection limit of 2×10^2 CFU/mL.

The evaluation of the effects of LipoFAs and LCFAs on the membrane permeability and ATP leakage in *S. aureus* MW2 revealed that the introduction of LipoFAs induced significant changes in bacterial membrane permeability. Specifically, in the membrane permeability assay, *S. aureus* treated with LipoLNA showed a concentration-dependent increase in relative fluorescence units (RFU) over time, with a particularly marked increase observed at concentrations of 125 μg/ml or higher. This indicates that LipoLNA significantly enhances bacterial membrane permeability. Similarly, the LipoLLA-treated group also exhibited a substantial increase in membrane permeability, with RFU notably

rising at higher concentrations (>63 μg/ml). In contrast, LipoOA demonstrated a relatively lower effect on increasing permeability, and the concentration-dependent changes were less pronounced compared to LipoLNA and LipoLLA. In the BareLipo control group, almost no change in permeability was observed, suggesting that bacterial membranes remain stable in the absence of FAs. Additionally, when treated with LNA and LLA, an increase in permeability was observed at higher concentrations, though the effect was significantly reduced in the OA-treated group.

Further evaluation of the extent of bacterial membrane disruption induced by LipoFAs was conducted via ATP leakage assays. LipoLNA-treated cells exhibited a concentration-dependent increase in ATP leakage, with a particularly significant increase at concentrations of 250 μg/ml or higher. This suggests that LipoLNA disrupts bacterial membranes, leading to the external release of ATP. The LipoLLA-treated group showed a similar pattern to LipoLNA, with a significant increase in ATP leakage at higher concentrations. In contrast, LipoOA induced relatively lower ATP leakage, but significant differences were observed at concentrations of 63 μg/ml or higher. In the BareLipo group, ATP leakage was minimal, indicating no membrane disruption in the absence of FAs. When treated with LCFAs, ATP leakage was also observed in a concentration-dependent manner, albeit at lower levels compared to liposomes. These findings indicate that LipoFAs, particularly LipoLNA and LipoLLA, significantly increase the permeability of the *S. aureus* MW2 membrane, promoting ATP leakage and leading to bacterial membrane disruption. This suggests that the unsaturated bond structures of LCFAs exert high local stress on the membrane, potentially enhancing bactericidal effects by increasing membrane permeability and ATP leakage.

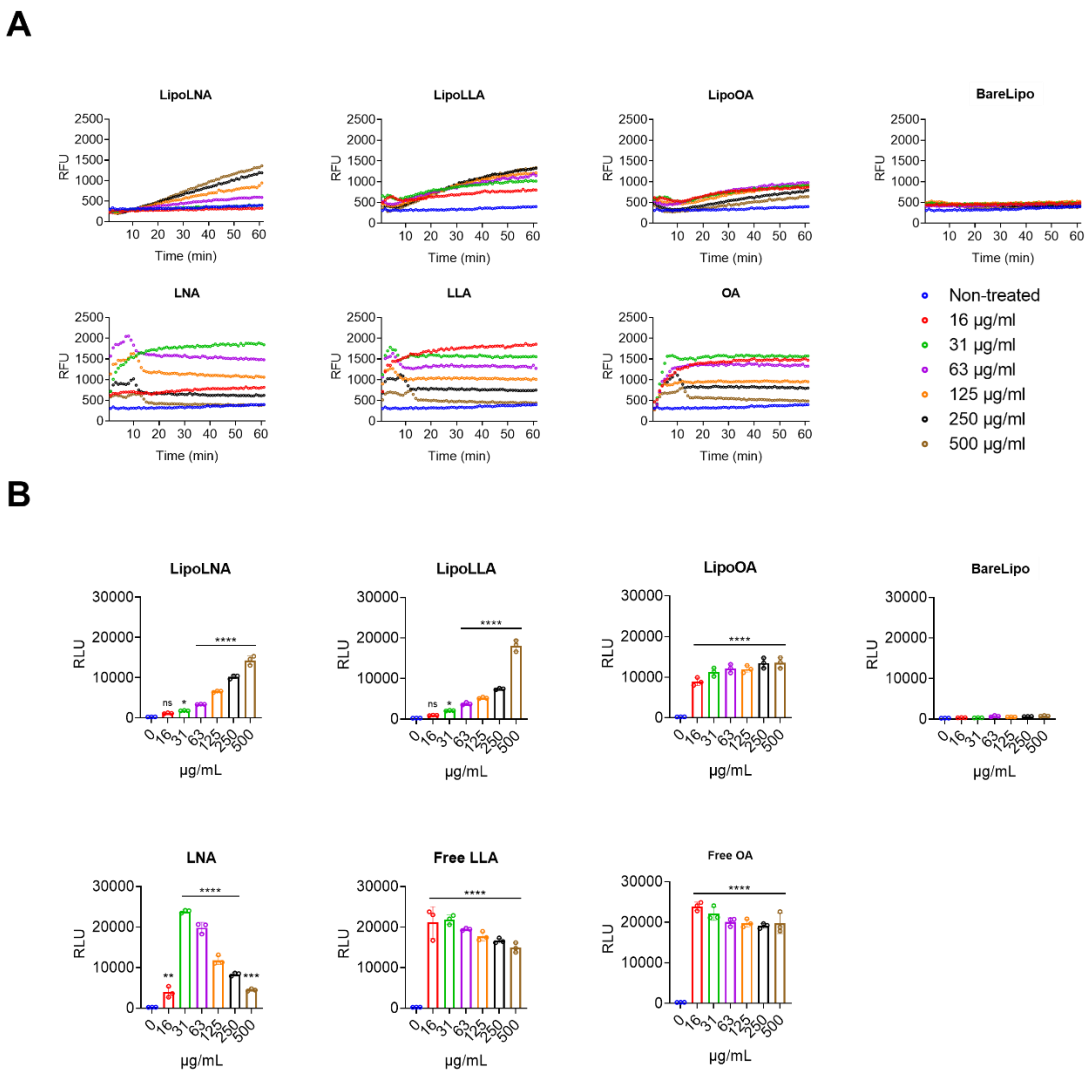

Figure 7.3 Membrane permeability analysis and ATP leakage in bacterial cells. (A) Membrane permeability of *S. aureus* MW2 was assessed following treatment with LCFAs and LipoFAs for 60 min, using SYTOX Green (Ex 485 nm, Em 525 nm). Results represent the mean of three independent experiments. (B) ATP leakage from *S. aureus* MW2 was monitored for 10 min after treatment with LCFAs and LipoFAs, using an ATP luminescence assay. Individual data points are displayed, and error bars indicate the mean ± standard deviation (n = 3). Statistical differences were determined by one-way ANOVA followed by Tukey's multiple comparison test (* $p < 0.1$, ** $p < 0.001$, *** $p < 0.0001$, **** $p < 0.0001$).

7.2.3 *In Vitro* Cytotoxicity Evaluation of Long-Chain Fatty Acids and Liposomal Fatty Acids

In addition to the solubility challenges associated with FAs, their inherent cytotoxicity represents a significant drawback that limits their application as antimicrobial agents. The cytotoxic effects of FAs have been well documented in numerous research investigations. Literature reports have linked FAs to cell toxicity through various pathways like apoptosis, autophagy, and disruption of cellular pathways [8-10]. This aspect hampers the utilization of FAs as antimicrobial agents, emphasizing the need to address this issue for further development of effective therapeutic strategies. To investigate the *in vitro* cytotoxic effects of LCFAs and LipoFAs, mouse fibroblast cells (L-929) and human keratinocyte cells (HaCat) were employed as test models.

Cell viability assays were performed on L-929 and HaCat cells (**Figure 7.2A** and **Figure 7.2B**). Both FFAs and LipoFAs exhibited cytotoxicity at 128 µg/mL, with cell viability dropping below 40%. In contrast, LipoFAs significantly improved cell viability to approximately 100% across all tested concentrations, indicating little toxicity at this concentration. In contrast, LCFAs demonstrated lower viability on L-929 cells, with values of 10.7% for free LNA, 25.7% for free LLA, and 60.9% for free OA. HaCat cells showed no significant decrease in viability when exposed to FFAs, potentially due to their higher resistance. These findings indicate that LipoFAs do not induce increased cytotoxicity, supporting their potential as effective antibacterial agents with improved biocompatibility compared to LCFAs. Looking forward, these findings emphasize the value of using SLBs as an experimental model to further investigate the antibacterial effects of LCFAs and LipoFAs. This approach will help to uncover the mechanisms of these agents and establish connections between their biophysical interactions and biological impacts.

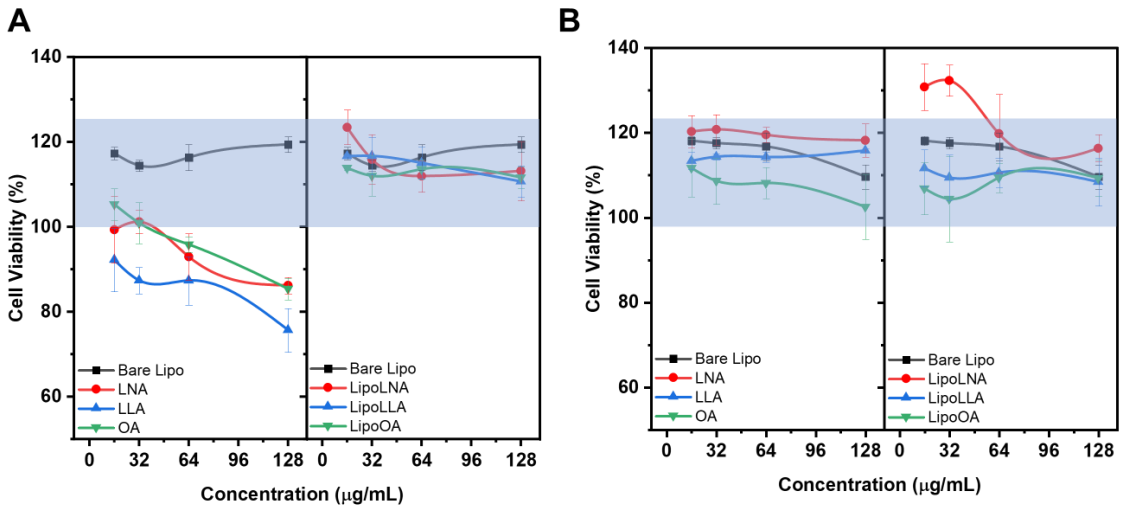

Figure 7.4 *In vitro* cell viability assays for *S. aureus* MW2 after treatment with LCFAs and LipoFAs. (A) Cell viability analysis on (B) mouse fibroblast cells (L-929) and (C) human keratinocyte cells (HaCat) treated with LCFAs, BareLipos, and LipoFAs (n = 3, mean ± SD).

References

[1] M. Lackinger, W.M. Heckl. *Langmuir*. **2009**, 25(19), 11307-21.

[2] Y. Hong, J. Zeng, X. Wang, K. Drlica, X. Zhao. *Proceedings of the National Academy of Sciences*. **2019**, 116(20), 10064-10071.

[3] W.F. Wong, M. Santiago. *Microbial Biotechnology*. **2017**, 10(5), 1047-1053.

[4] C.S. Lunde, S.R. Hartouni, J.W. Janc, M. Mammen, P.P.A. Humphrey, B.M. Benton. *Antimicrobial Agents and Chemotherapy*. **2009**, 53(8), 3375-3383.

[5] H.-J. Lee, J.S. Hwang, D.G. Lee. *Journal of Microbiology and Biotechnology*. **2021**, 31(2), 189-196.

[6] H.Y. Heo, G. Zou, S. Baek, J.-S. Kim, E. Mylonakis, F.M. Ausubel, H. Gao, W. Kim. *Advanced Science*. **2024**, 11(9), 2306112.

[7] S. Shin, H. Tae, S. Park, N.-J. Cho. *International Journal of Molecular Sciences*. **2023**, 24(11), 9639.

[8] S. Mei, H. Ni, S. Manley, A. Bockus, K.M. Kassel, J.P. Luyendyk, B.L. Copple, W. Ding. *Journal of Pharmacology and Experimental Therapeutics*. **2011**, 339(2), 487-498.

[9] A.M. Engelbrecht, J.-L.d. Toit-Kohn, B. Ellis, M. Thomas, T. Nell, R. Smith. *Apoptosis*. **2008**,13(11), 1368-1377.

[10] L. Zheng, S. Srivastava, X. Yang, S. Mittal, P. Norton, J.H. Resau, B.B. Haab, C. Chan. *BMC Systems Biology*. **2007**, 1(1).